Universidade de São Paulo
Instituto de Física

Instabilidades de Disruptura em Tokamaks

Alvaro Vannucci

Tese submetida ao Instituto de Física da Universidade de São Paulo para a obtenção do título de Livre Docente

Controlled Fusion,

Bringing the Power Source of the Stars...

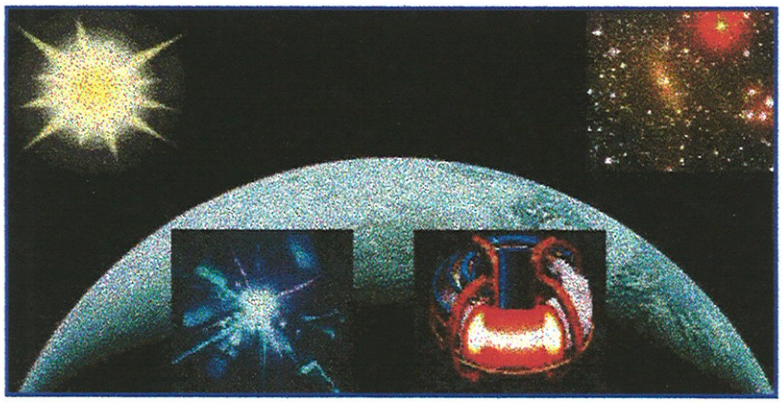

http://FusEdWeb.pppl.gov/

...Down to Earth!

São Paulo
1998

FICHA CATALOGRÁFICA
Preparada pelo Serviço de Biblioteca e Informação
do Instituto de Física da Universidade de São Paulo

Vannucci, Álvaro

Instabilidades de Disruptura em Tokamaks.
São Paulo, 1998.

Tese Livre Docência - Universidade de São Paulo.
Instituto de Física - Departamento de Física Aplicada.

Área de Concentração: Física Nuclear

Unitermos: 1. Plasma; 2. Tokamak; 3. Fusão Nuclear;
4. Redes Neurais; 5. Instabilidades MHD.

USP/IF/SBI-018/98

"A mente centralizada na oração pode ser comparada a uma flor estelar que se abre ante o Infinito, absorvendo-lhe o orvalho nutriente de vida e de luz"

André Luiz

À Fátima, com todo o meu amor e carinho, pelo esforço e dedicação constantes.

À Marina, ao Bruno e à Camilla pelas alegrias de todos os momentos.

Aos meus pais, pela minha formação e incentivo dado em todas as etapas da minha vida.

Aos meus espíritos protetores e amigos do plano espiritual, pela inspiração e suporte através dos caminhos da vida.

AGRADECIMENTOS

Fico bastante contente em poder expressar aqui os meus agradecimentos às várias pessoas que contribuiram de forma direta ou indireta com este trabalho, o qual basicamente retrata a minha formação de pesquisador.

Muitos chegaram e foram-se, deixando a lembrança da amizade e do companheirismo. Outros, ainda permanecem presentes em nosso dia a dia, estimulando a nossa jornada e participando de nossos esforços.

Desculpando-me desde já por algum esquecimento imperdoável, gostaria de agradecer em particular:

- Ao Prof. Ivan C. Nascimento pelo convite que me foi formulado para entrar no Grupo de Física de Plasmas do IFUSP, pela sua orientação durante o meu trabalho de doutorado e também pelo apoio dado em inúmeras ocasiões.
- Aos Profs. Ricardo M.O. Galvão e Iberê L. Caldas pela amizade, pelo incentivo constante e pelas muitas discussões científicas (e também pelas discussões não-científicas, tão importantes para o fortalecimento do espírito de grupo que sempre procuramos estabelecer em nosso laboratório).
- Ao Prof. Ruy Pepe da Silva, companheiro de sala desde há alguns anos, pela paciência e gentileza natural (próprias de uma grande alma) com que envolve a todos aqueles que o procuram.
- Aos Profs. Aluísio N. Fagundes e José Henrique Vuolo, pelas sugestões e ajuda que nos foram dados em várias ocasiões, e pelo interesse demonstrado em todos os momentos que precisamos de auxílio.
- À Dra. Ing H. Tan e à Profa. Mutsuku Kucinski pelas conversas amigas e pela amizade sincera.
- Às Profas. Vilma S.W. Vuolo e Maria Vittória Heller, e aos Profs. Hugo Franco e Delton de Oliveira Campos pelo companheirismo e apoio dado em vários momentos.

• Aos "meus estudantes" de Mestrado e Doutorado: Mauro, Kênya, Regina e Erich, pela confiança e pelo clima de amizade que sempre reinou em nossas relações.

• À todo o pessoal de suporte técnico-científico do nosso laboratório, cujo trabalho é de fundamental importância, em especial ao Banzai, André, Tadeu, Ablício, Wanderley, Juan, Nélio, Nelson, Rogério e Ivan.

• Aos Drs. Yuri, Leonid e Artour que, vindos de muito longe, transformaram-se em um reforço científico de grande importância para o nosso laboratório.

• À Eleonora, Lia e Sylvia (apesar de ter "abandonado o barco" por duas vezes) pelo eficiente trabalho de secretaria e também pelo bom humor com que sempre tem nos recebido.

• À todos estudantes de Mestrado e Doutoramento do Laboratório de Física de Plasmas.

• Aos muitos professores, funcionários e alunos do IFUSP que tem nos prestigiado com a sua amizade e dedicação.

• À FAPESP, CNPq, FINEP a CAPES pelos auxílios financeiros prestados.

Resumo

A origem das instabilidades de disruptura foi investigada. Trabalhos realizados em três tokamaks diferentes, um pequeno (TBR-1), outro médio (TEXT-U) e outro de grande porte (JET), mostraram que o acoplamento entre os modos MHD m = 2 e m = 1 constituiria o principal mecanismo de desencadeamento das disrupturas maiores. Os resultados obtidos indicam que este tipo de processo de desencadeamento das disrupturas possuiria um caráter universal, isto é, valeria para todos os tokamaks com baixo β e alta razão de aspecto.

Neste trabalho são discutidos também alguns resultados envolvendo mecanismos de controle das instabilidades de disruptura. No TBR-1, como conseqüência da aplicação de campos magnéticos externos criados por um conjunto de malhas helicoidais e por um sistema de limitador ergódico magnético, uma forte atenuação da atividade MHD pôde ser obtida.

Finalmente, em um trabalho bastante inédito na área de fusão, redes neurais foram utilizadas para se tentar prever, com a maior antecedência possível, o instante de ocorrência de uma disruptura nas descargas de plasma do tokamak TEXT. Utilizando-se sinais de oscilações magnéticas de Mirnov na rede neural, pôde-se realizar a previsão da ocorrência de uma disruptura com mais de 1 ms de antecedência.

Mais recentemente, este tempo de previsão pôde ser quase triplicado, através da utilização de sinais de raios-X de baixas energias provenientes da região central da coluna de plasma em lugar dos sinais de Mirnov. Comparações realizadas entre os sinais experimentais destes dois sistemas de diagnóstico, nos instantes finais do pulso de plasma, indicaram que o processo disruptivo inicia-se em torno da região central da coluna de plasma e somente depois afeta a parte mais externa do plasma, onde localiza-se a superfície magnética correspondente ao fator de segurança q = 2.

Abstract

The origin of the disruptive instabilities was experimentally investigated. The research was carried out in three tokamaks of different sizes and characteristics: the small TBR-1, the medium size TEXT-U, and JET, which is one of the largest devices that have been constructed and put in operation. For all of them, the $m = 2$ and $m = 1$ mode coupling was found to be the main triggering mechanism for the major disruptions analyzed. These results indicate, therefore, that this triggering mechanism may be considered rather universal in a sense that it would be valid for tokamaks with low-β and low aspect ratio.

Also, some controlling mechanism for disruptions were investigated. In the TBR-1 tokamak a strong attenuation of the MHD activity was obtained when external magnetic fields were applied. These external perturbing fields were produced by a set of helical windings and also by an ergodic magnetic limiter.

Finally, the results obtained with neural networks to forecast the onset of disruptions in TEXT discharges are discussed. This original work was done by using Mirnov magnetic signals to feed the neural net and predictions greater than 1 ms could be obtained.

More recently, it was possible to increase the forecasting time (for almost three times longer) by using the central soft X-rays signal instead of the Mirnov magnetic signal in the neural networks. A comparison between the experimental data of both diagnostic systems, close to the disruption time, was made and indications were found that the disruptive process initiates around the central part of the plasma column and, only afterwards, it disturbs the plasma around the region where the $q = 1$ magnetic surface is located.

Índice

Apêndice 3 - Artigo publicado sobre a investigação das instabilidades de disruptura no tokamak TEXT-U

Apêndice 4 - Artigos publicados sobre a investigação da atuação de campos magnéticos externos no tokamak TBR-1

Apêndice 5 - Artigos publicados sobre a utilização de redes neurais na previsão das instabilidades de disruptura no tokamak TEXT

Capítulo 1

Introdução

1.1 - *A fusão termonuclear controlada*

O crescente consumo mundial de energia vem sinalizando, para futuro não muito distante (Fig.1), a necessidade de se viabilizar, o quanto antes, a utilização de fontes alternativas de energia [1-3]. Em particular, os combustíveis fósseis, largamente empregados, certamente têm duração limitada (apesar das possíveis novas jazidas que poderão ser descobertas), além de serem causadores diretos ou indiretos de graves problemas ambientais.

Dentre as possíveis alternativas para a produção de energia em larga escala destaca-se a fusão termonuclear controlada que, se for realmente viabilizada, poderá suprir definitivamente as necessidades básicas na área de energia; isto porque, além de ser bastante segura (não há o perigo de que possa escapar de controle) e razoavelmente "limpa" (reduz enormemente o problema de lixo radiativo quando comparada com o processo de fissão nuclear, por exemplo), é uma fonte praticamente inesgotável de energia haja visto que, em reações do tipo deutério-deutério, todo material combustível pode ser retirado da água do mar [2, 3].

http://ep.llnl.gov/informal_science/fusion/red6.html

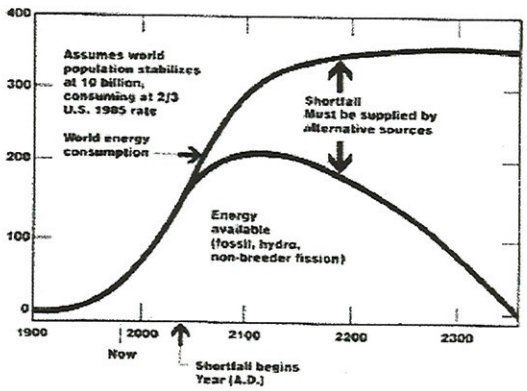

Fig. 1 - Estimativas sobre o consumo mundial de energia mostram que há uma necessidade urgente da descoberta de novas fontes de energia.

Neste contexto, dois processos distintos apresentam-se como os mais promissores para a viabilização da fusão controlada: 1°) o que envolve o confinamento inercial por laser e 2°) o que envolve o confinamento magnético por tokamaks [4]. Em ambos os casos, as pesquisas que vêm sendo desenvolvidas utilizam-se de uma mistura combustível contendo os dois isótopos do hidrogênio, o deutério ($^2H_1$) e o trítio ($^3H_1$), já que a reação $D + T = n + {}^4He$ (Fig.2) é a que possui maior seção de choque de fusão.

http://www-lasers.llnl.gov/lasers/nif/nif_ife.html#fusion

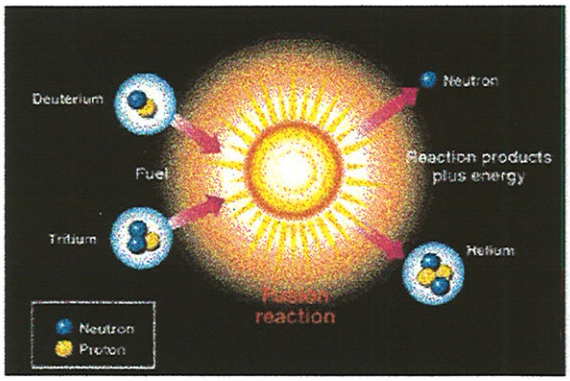

Fig. 2 - A reação de fusão envolvendo os isótopos de deutério e trítio é a que possui maior seção de choque. Como sub-produto da reação obtêm-se um núcleo de ^4He e um nêutron rápido, com 14,1 MeV de energia.

No processo de confinamento inercial, feixes de laser de altíssimas potências (da ordem de algumas centenas de Tera Watts) incidem simultânea e simetricamente sobre uma pastilha contendo uma mistura congelada (temperaturas abaixo de 14 K) de deutério-trítio, aquecendo-a e comprimindo-a a altíssimas temperatura e densidade, provocando sua ignição e conseqüente combustão [5, 6]. O diagrama da figura 3 exemplifica detalhadamente o processo. Os feixes de laser, ao incidirem sobre uma pastilha com aproximadamente 5 mg de uma mistura eqüitativa de deutério-trítio, elevam rapidamente a temperatura na superfície da pastilha, vaporizando quase que instantaneamente o material localizado naquela região e formando, nas imediações, uma camada de plasma. A subseqüente expansão repentina desta camada na direção radial comprime o material combustível de forma que, em intervalos de tempo da ordem de 10^{-9} s, sua densidade aumenta para cerca de 20 vezes a densidade do chumbo e sua temperatura atinge um valor da

http://www.lasers.llnl.gov/lasers/nif/nif_ife.html#fusion

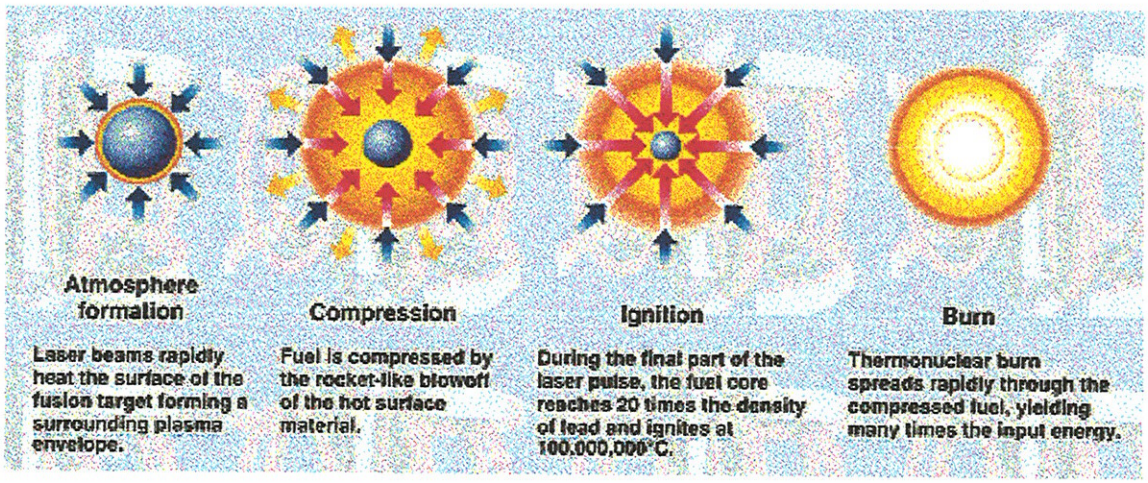

Fig. 3 - Diagrama ilustrativo de como se processa a fusão pelo método de confinamento inercial por laser.

ordem de 10^8 °C, fazendo com que entre em ignição. A "queima" do material ocorre em aproximadamente 10^{-10} s, tempo suficientemente grande para que praticamente todos os núcleos de deutério-trítio sofram o processo de fusão, gerando enorme quantidade de energia. Em um futuro reator, no qual este processo possa ser reproduzido 6 vezes por segundo, será possível produzir da ordem de 1000 MW de energia elétrica, já levando-se em consideração a ineficiência intrínseca do processo de conversão de energia [6].

No processo de fusão em reatores tokamaks, por outro lado, um plasma com quantidades iguais de deutério e trítio deve ser formado e mantido confinado através de campos magnéticos intensos que possuem, basicamente, simetria helicoidal. Estas linhas magnéticas helicoidais possuem duas componentes distintas (Fig. 4), a toroidal (formada por um conjunto de bobinas distribuídas ao longo da câmara de vácuo toroidal) e a poloidal (criada pela própria corrente de plasma). O objetivo principal a ser alcançado nos futuros reatores tokamaks será o de manter um plasma razoavelmente denso (com pelo menos 10^{20} partículas x m^{-3}) confinado pelo maior tempo possível e aquecê-lo a uma temperatura suficientemente alta (acima de 100 milhões de graus Celsius), para que os íons consigam adquirir energia cinética suficientemente grande de forma a vencerem a barreira de repulsão coulombiana e sofrerem o processo de fusão [7, 8].

http://www.pppl.gov/oview/pages/fusion_tokamak

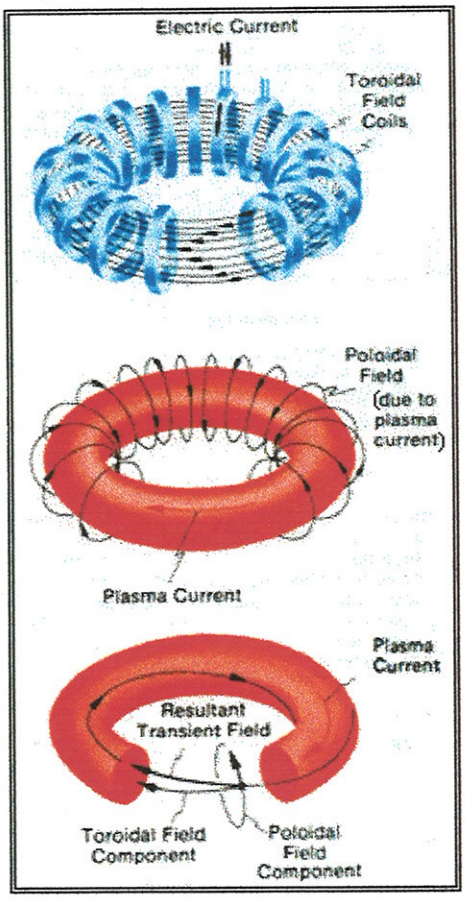

Fig. 4 - Diagrama esquemático do plasma confinado por um tokamak, mostrando a forma pela qual as linhas de campo helicoidais são formadas a partir de suas componentes poloidal e toroidal.

No entanto, dentre as várias máquinas de grande porte já construídas, somente o TFTR (*Tokamak Fusion Test Reactor*) dos EUA e, mais recentemente, o JET (*Joint European Torus*) da Comunidade Européia, foram operados até o momento com descargas onde se introduziu uma mistura eqüitativa de deutério e trítio. No seu melhor desempenho, antes de ser desativado em abril de 1997, o TFTR conseguiu produzir até 10,7 MW de potência de fusão, trabalhando com um campo magnético toroidal $B_T = 5,6$ T e corrente de plasma $I_P = 2,7$ MA. Nestas condições, os parâmetros básicos do plasma alcançados pelo TFTR foram: densidade de elétrons $n_e = 1 \times 10^{20}$ m^{-3}, temperatura de elétrons $T_e = 13,5$ keV e temperatura de íons $T_i = 32$ keV [9, 10]. No JET, porém, resultados mais impressionantes ainda foram alcançados. No final de 1997, 16 MW de potência de pico (de fusão) foi obtida, o que corresponde a uma razão de

65% entre a energia de fusão produzida em relação à energia total consumida para manter o tokamak em operação.

Atualmente, tanto o processo de confinamento inercial quanto o de confinamento

http://picard.iterus.org/iter_picture/new_overall_96.gif

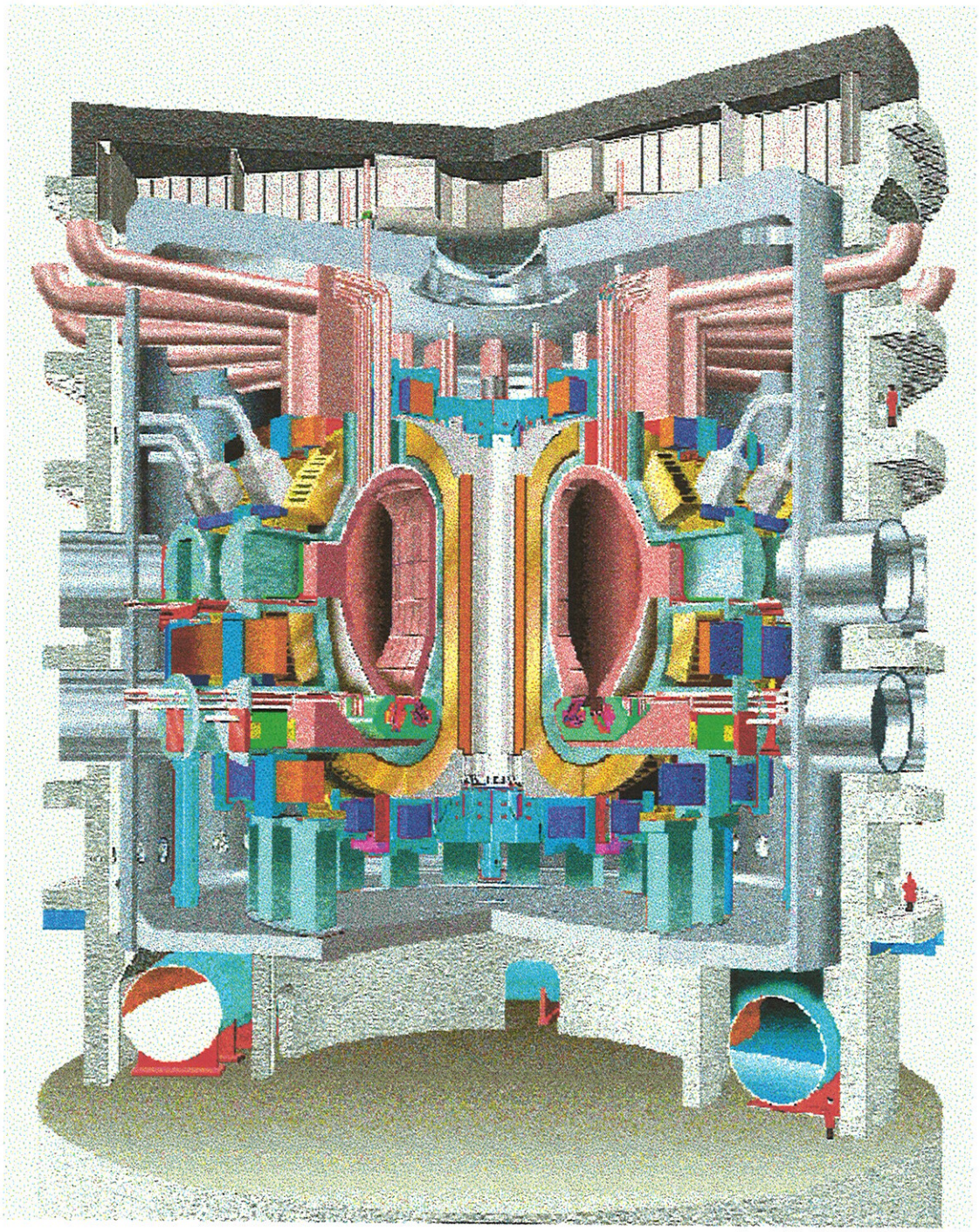

Fig. 5 - Desenho artístico da estrutura básica do tokamak ITER.. As gigantescas proporções desta máquina tornam-se evidentes quando comparadas com as dimensões dos homens desenhados (ao lado direito) no andar térreo e também no 1^0 e no 4^0 pavimento.

magnético continuam sendo objetos de pesquisas intensas e grandes projetos, com custos superiores a um bilhão de dólares cada um, já se encontram em desenvolvimento [5, 8]. Com respeito ao processo de fusão por confinamento magnético, por exemplo, o projeto ITER (*International Thermonuclear Experimental Reactor*) constitui-se em um empreendimento internacional (envolvendo basicamente os EUA, a comunidade européia, a Rússia e o Japão) que pretende demonstrar, de forma definitiva, a viabilidade da fusão termonuclear para fins pacíficos de produção de energia [11, 12]. Atualmente o ITER, que corresponderá a um tokamak de gigantescas proporções (Fig. 5), encontra-se na fase de detalhamento técnico, o qual é realizado simultaneamente por três grupos distintos de cientistas e engenheiros. Estes grupos, que estão incubidos de executar tarefas específicas, encontram-se localizados nas cidades de Garching (Alemanha), Naka (Japão) e San Diego (Estados Unidos). Estima-se que a decisão final quanto ao local e também quanto à data de início da construção deverá ser tomada, provavelmente, em um ou dois anos.

1.2 - Instabilidades de disruptura

Desde as primeiras pesquisas realizadas, envolvendo plasmas magneticamente confinados, tem-se observado que vários são os fenômenos que surgem durante o confinamento do plasma, interferindo no seu equilíbrio. Muitos destes fenômenos decorrem de perturbações nos parâmetros macroscópicos do plasma que se propagam através de ondas e são usualmente estudadas através das equações da magnetohidrodinâmica (modelo MHD) que descrevem o plasma como um sistema de grande escala, não se importando com os aspectos microscópicos do meio. Em tokamaks, estas instabilidades, quando surgem, degradam o confinamento, provocam a perda de partículas e energia e chegam até mesmo a destruir rápida e completamente a coluna de plasma, como no caso das disrupturas maiores [13, 14].

http://www.jet.uk/tour.html

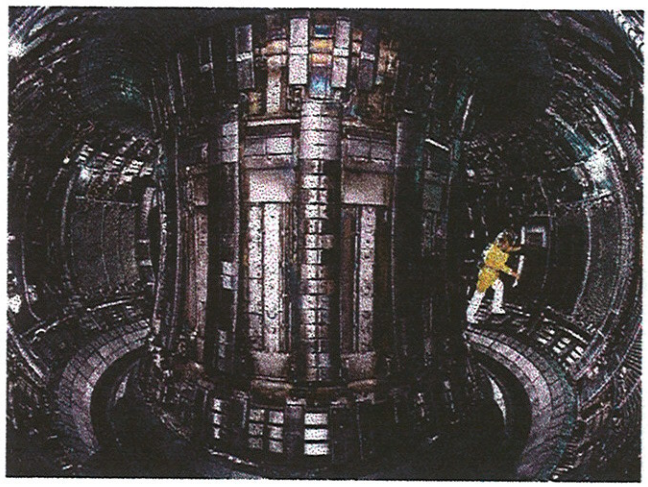

Fig. 6 - Parte interna da câmara toroidal de vácuo do tokamak JET.

O rápido aniquilamento da corrente de plasma, provocado por uma disruptura maior, acarreta a indução de altas tensões elétricas nos diversos componentes eletro-mecânicos do tokamak, podendo causar-lhe sérios danos. No tokamak JET (*Joint European Torus*), por exemplo, já foram constatado deslocamentos de alguns milímetros de toda a imensa estrutura da máquina (Fig.6) devido `a

ocorrência de alguma disruptura maior mais violenta [15]. Para o ITER, por outro lado, prevê-se que a ocorrência de uma disruptura maior poderá exercer, comparativamente, tensões mecânicas na câmara de vácuo e seus componentes da ordem de 10^4 toneladas-força. Isto irá requerer, conseqüentemente, que suas estruturas mecânicas sejam muito mais robustas e bastante reforçadas (encarecendo enormemente, desta forma, os custos de construção) para que possam suportar tensões desta magnitude [16].

Por esta razão, os mecanismos físicos que desencadeiam as instabilidades de disruptura têm sido objeto de estudos bastante intensos já que, caso consigam ser adequadamente compreendidos, talvez possibilitem o controle destas instabilidades ou, pelo menos, permitam que seus efeitos sejam amenizados. Isto certamente contribuiria significativamente para que ao menos seja mantido o avanço das conquistas já efetuadas na área da fusão controlada, no ritmo indicado pela Fig. 7, com vistas à obtenção dos parâmetros necessários para se atingir a condição de ignição, em futuro não muito distante.

Porém, muito embora diversos trabalhos tanto teóricos quanto experimentais já tenham sido realizados nas últimas décadas [17-30], uma compreensão detalhada de como as instabilidades de disruptura se desenvolvem e de como se processa o decaimento do plasma, logo a seguir, infelizmente ainda não foi obtida. Mecanismos que envolvem a perda por irradiação [17, 18], ergodização das linhas de campo magnético [19, 20], emissão assimétrica de radiação da periferia do plasma (MARFES) [21] e mesmo microturbulências [22] já foram consideradas como sendo as principais causas da degradação do confinamento magnético que levam ao desencadeamento das disrupturas maiores. Aspectos que assinalam para uma possível interação das ilhas magnéticas localizadas em q = 2 com o limitador [23, 24] ou que envolvem o acoplamento da componente $m = 2$ com outras perturbações MHD, de maior [25, 26] ou menor [27-30] m, ainda requerem maiores esclarecimentos.

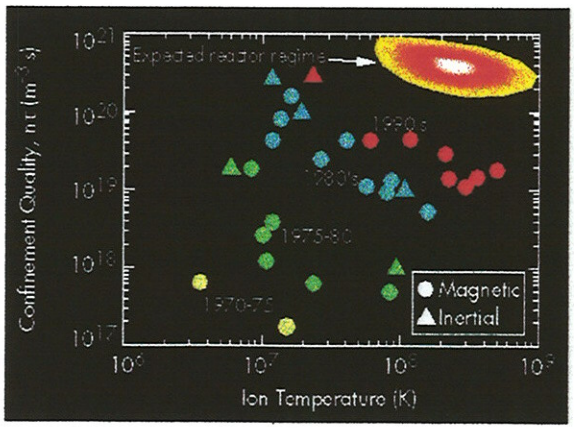

Fig. 7 - Evolução temporal dos parâmetros básicos que são necessários para a conquista da fusão termonuclear controlada.

1.3 -Tokamaks investigados

Neste trabalho estarão sendo discutidos, em conjunto, os resultados das investigações realizadas por este autor sobre as instabilidades de disruptura que ocorrem em três tokamaks

distintos: o TBR-1 (tokamak de pequeno porte do Instituto de Física da Universidade de São Paulo), o TEXT-U (tokamak de médio porte do Fusion Research Center - Universidade do Texas) e o tokamak JET (empreendimento europeu na área de fusão, localizado na Inglaterra, como já mencionado anteriormente). A título de comparação, na Tabela I são mostrados os principais parâmetros destas máquinas, juntamente com os do TCA/BR (que já se encontra em funcionamento no Instituto de Física da USP), do TFTR e também com os previstos para o ITER. Basicamente serão discutidos, no decorrer deste trabalho, os dados experimentais obtidos nestes três tokamaks, mostrando-se que eles dão suporte à interpretação de que o acoplamento entre os modos MHD $m = 2$ e $m = 1$ corresponde ao principal mecanismo físico responsável pelo desencadeamento de uma instabilidade de disruptura maior.

Um outro aspecto importante, que também será abordado em detalhes, envolve dois possíveis métodos, que temos investigado pessoalmente, de controle das instabilidades de disruptura: 1^0) através da aplicação de campos magnéticos ressonantes (no TBR-1 um significativo amortecimento da atividade MHD precursora de disrupturas foi obtido utilizando-se um conjunto de malhas helicoidais e um limitador ergódico magnético) e 2^0) através da utilização de redes neurais para se tentar prever, com a maior antecedência possível, quando ocorreria uma disruptura maior durante uma descarga e, conseqüentemente, permitir que providências possam ser tomadas no sentido de interromper uma disruptura que esteja se formando, ou pelo menos, amenizar os graves danos que ela possa causar. No tokamak TEXT, previsões de disupturas em intervalos de tempo maiores que 3 ms puderam ser feitas ao utilizarem-se sinais de raios-X de baixas energias para alimentar a rede.

PARÂMETROS	TBR-1	TEXT-U	JET	TFTR	ITER	TCA/BR
Raio Maior, R_0 (m)	0,3	1.05	2,96	2,6	8,14	0,61
Raio Menor, a (m)	0,08	0.27	1,25 x 2,1	0,8 - 1,96	2,80	0,18
Campo Toroidal, B_T (T)	0,4	3.0	3,8	6,0	5,7	1,2
Corrente de Plasma, I_P (MA)	0,012	0.4	7	3	21	0,12
Duração das Descargas, τ_D (s)	0,012	0.5	60	5	1300	0,1

Tabela I - Dados comparativos dos parâmetros básicos dos tokamaks TBR-1 *e* TCA/BR *(Brasil),* JET *(Comunidade Européia), TEXT-U e* TFTR *(E.U.A.), e* ITER *(Colaboração Internacional).*

Capítulo 2

Instabilidades MHD

2.1 - Tipos de instabilidades

Várias são as instabilidades macroscópicas que surgem durante o confinamento magnético do plasma por tokamaks. No entanto, de forma geral, estas instabilidades podem ser agrupadas em duas categorias distintas, as *ideais* e as *resistivas*.

As instabilidades do tipo *ideal* são usualmente estudadas através da teoria MHD que considera o plasma como sendo um fluido condutor perfeito e que pode ser desenvolvida através das equações de fluido [31-35]:

(conservação do momento) $$\rho\frac{d\vec{v}}{dt} = -\vec{\nabla}P + \vec{j}\times\vec{B} \quad (1)$$

(equação da continuidade) $$\frac{\partial\rho}{\partial t} + \vec{\nabla}\cdot\left(\rho\vec{v}\right) = 0 \quad (2)$$

(conservação de energia p/ processos adiabáticos) $$\frac{d}{dt}\left(P\rho^{-\Gamma}\right) = 0 \quad (3)$$

conjuntamente com as equações de Maxwell:

(lei de Ohm ideal) $$\vec{E} + \vec{v}\times\vec{B} = 0 \quad (4)$$

(lei de Faraday) $$\vec{\nabla}\times\vec{E} = -\frac{\partial\vec{B}}{\partial t} \quad (5)$$

(lei de Ampère) $$\vec{\nabla} \times \vec{B} = \mu_0 \vec{j} \tag{6}$$

(inexistência de monopolos magnéticos) $$\vec{\nabla} \cdot \vec{B} = 0 \tag{7}$$

sendo que $\frac{d}{dt} = \frac{\partial}{\partial t} + \vec{v} \cdot \vec{\nabla}$ é a derivada convectiva e Γ é a razão dos calores específicos.

Uma maneira de se estudar a estabilidade do sistema é considerando-se inicialmente o plasma em equilíbrio estático (velocidade do fluido nula) e estudar, a partir daí, como ocorre a evolução temporal de pequenas perturbações que possam então surgir. Para isto, efetua-se a linearização das equações acima associando, a cada um dos parâmetros físicos pertinentes, uma componente de equilíbrio e uma perturbação de primeira ordem, do tipo:

$$f = f_0(\vec{r}) + f_1(\vec{r}) \tag{8}$$

de forma que, após considerar-se somente os termos de primeira ordem, tem-se:

$$\rho_0 \frac{d^2 \vec{\xi}}{dt^2} = \vec{F}(\vec{\xi}) \tag{9}$$

onde $\vec{\xi}$ corresponde a deslocamentos infinitesimais do fluido perturbado e

$$\vec{F}(\vec{\xi}) = \vec{\nabla}\left(\Gamma P_0 \vec{\nabla} \cdot \vec{\xi} + \vec{\xi} \cdot \vec{\nabla} P_0\right) + \left(\vec{\nabla} \times \vec{B}_1\right) \times \vec{B}_0 + \left(\vec{\nabla} \times \vec{B}_0\right) \times \vec{B}_1 \tag{10}$$

sendo que $\vec{B}_1 = \vec{\nabla} \times \left(\vec{\xi} \times \vec{B}_0\right)$ corresponde ao campo magnético de perturbação.

Um determinado equilíbrio será instável se a amplitude da solução dependente do tempo da equação (9) crescer, a partir de uma perturbação $\vec{\xi}(r,0)$ inicial. Os modos normais do sistema podem ser obtidos ao se expressar os elementos de deslocamento $\vec{\xi}$ através de uma expansão do tipo:

$$\vec{\xi}(\vec{r}, t) = \sum_{\alpha} \vec{\xi}_{\alpha}(\vec{r}) e^{i\omega_{\alpha} t} \tag{11}$$

de forma que, pela equação (9):

$$\vec{F} = -\rho \omega_{\alpha}^2 \vec{\xi}_{\alpha} \tag{12}$$

Para modos instáveis, tem-se que $\omega_\alpha^2 < 0$ e as taxas de crescimento de suas amplitudes, no tempo, são dadas por $\gamma_\alpha = |\omega_\alpha|$.

A avaliação de ω_α^2, para uma configuração particular de campo magnético que não se restrinja a geometrias simples, pode tornar-se bastante complexa. Porém, existe um outro critério que determina as condições de instabilidades resultantes, sem que haja a necessidade de se calcular as auto-funções e os auto-valores das equações linearizadas. Este critério denomina-se *princípio de energia* e está basicamente relacionado com a variação da energia potencial sofrida pelo sistema, mediante uma perturbação inicial [31-35]:

$$\delta W(\vec{\xi}) = -\frac{1}{2}\int \vec{\xi}^* \cdot \vec{F}(\vec{\xi}) d^3r \tag{13}$$

Desta forma, para um dado deslocamento $\vec{\xi}$, se a variação da energia potencial for positiva ($\delta W > 0$) o equilíbrio será estável. Caso ocorra uma perturbação $\vec{\xi}$ que provoque uma variação negativa na energia potencial ($\delta W < 0$), então o equilíbrio será instável.

Utilizando-se a aproximação cilíndrica para tokamaks correspondente às configurações de grande razão de aspecto ($\varepsilon = a/R_0 << 1$), as condições macroscópicas que devem ser respeitadas para que não surjam instabilidades podem ser facilmente obtidas se ε for utilizado como um parâmetro de expansão para a variação da energia potencial do sistema. Constatando-se que o primeiro termo da expansão resulta em uma variação nula para a energia potencial, o segundo termo é que deve então ser considerado na análise das condições de estabilidade o qual, para um deslocamento radial $\vec{\xi}(\vec{r})$, pode ser expresso na forma [34, 35]:

$$\delta W = \pi^2 R_0 \int_0^b \left[B_1^2 + B_{0\theta}\left(1 - \frac{nq}{m}\right)\frac{dj_\phi}{dr}\xi^2 \right] r dr \tag{14}$$

onde R_0 e b são o raio maior e menor da câmara toroidal de vácuo, respectivamente, q é o *fator de segurança* da máquina e j_ϕ a densidade de corrente de plasma.

Pode-se mostrar que o deslocamento que minimiza δW, para o caso mais simples de corrente uniforme, é dado por $\xi(r) = \xi_a(r/a)^{m-1}$. A taxa de crescimento da amplitude das instabilidades correspondentes a este caso, usualmente denominadas *instabilidades de dobra* ("*kink instabilities*"), são determinadas pela expressão [34, 35]:

$$\gamma^2 = \frac{2mB_{\theta a}^2}{\rho a^2}\left(1 - \frac{nq_a}{m}\right)\left[1 - \frac{m - nq_a}{1 - (a/b)^{2m}}\right] \tag{15}$$

onde ρ é a densidade de partículas, suposta constante, a é o raio do plasma e $B_{\theta a}$ é o valor do campo magnético poloidal na borda do plasma. Em geral, muitas destas instabilidades podem ser evitadas se forem respeitados os limites de operação dos tokamaks.

No entanto, se o plasma for considerado de forma mais realista, como um meio condutor não-ideal, faz-se então necessário introduzir uma resistividade finita nas equações da magnetohidrodinâmica, o que acaba gerando outras condições de instabilidade do plasma. Estas novas instabilidades são usualmente chamadas de *instabilidades de ruptura* ("*tearing instabilities*") porque, devido ao efeito resistivo, elas estão intrinsecamente relacionadas com o rompimento e conseqüente reconecção das linhas de força do campo magnético [31-40]. Este processo ocorre principalmente em uma estreita região em torno de superfícies racionais onde $\vec{K} \cdot \vec{B} = 0$, sendo $\vec{K}$ o vetor de onda da perturbação. Em decorrência da recombinação destas linhas de força, estruturas denominadas *ilhas magnéticas* são formadas, como será detalhadamente explicado a seguir.

2.2 - *Recombinação magnética*

Em tokamaks, uma linha de força helicoidal do campo magnético pode descrever várias e várias voltas ao longo do toroide sem retornar ao ponto inicial de partida, acabando por formar, desta maneira, uma *superfície magnética* no interior do plasma. Cada uma destas superfícies é geralmente caracterizada por um valor do parâmetro q, denominado *fator de segurança*, que encontra-se basicamente relacionado com o valor médio do passo da hélice representada pela linha de campo correspondente.

Na aproximação cilíndrica, pode-se facilmente mostrar que [31-33]:

$$q = \frac{rB_\phi}{R_0 B_\theta} \qquad (16)$$

onde B_ϕ e B_θ correspondem às componentes toroidal e poloidal do campo magnético, e R_0 e r correspondem aos raios maior (do tokamak) e menor (da superfície magnética em consideração), respectivamente (fig. 8).

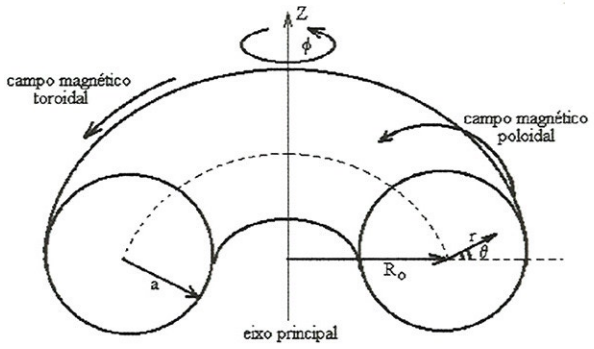

Fig. 8 - Na figura, R e a correspondem aos raios maior e menor do toroide. Estão também indicadas as coordenadas cilíndricas (R, ϕ, Z) e as pseudo-toroidais (r, ϕ, θ), além do eixo de simetria Z.

Pode-se mostrar também que o fator de segurança q está relacionado com os números m e n ($q = m/n$), que correspondem ao número de voltas que uma linha de campo magnético descreve ao longo das direções

toroidal (ϕ) e poloidal (θ), respectivamente, até retornar ao ponto de partida, em uma mesma seção transversal da coluna de plasma. Se *m* e *n* forem números inteiros, então o número de voltas que uma linha de campo magnético percorre até retornar ao ponto de partida será finito e a superfície magnética por eles definida é chamada de *ressonante*. Estas superfícies desempenham um importante papel no estudo das instabilidades em tokamaks porque a propagação de uma perturbação qualquer do plasma, com uma determinada freqüência ω, pode ser representada por [31-33]:

$$\tilde{\xi} \;\alpha\; \xi_0 \, e^{i(m\theta - n\phi + \omega t)} \tag{17}$$

onde *m* e *n*, já introduzidos acima, correspondem agora aos números de onda (poloidal e toroidal) da perturbação.

Uma maneira bastante ilustrativa de se entender a recombinação das linhas de campo magnético é através de um equilíbrio bi-dimensional (Fig. 9) cujo campo magnético é dado por [36, 37]:

$$\vec{B}_0 = B_{z0}\hat{e}_z + B_{y0}\hat{e}_y \tag{18}$$

sendo que B_{y0} muda de sentido no plano x = 0, conforme mostrado na figura 9a.

Neste modelo, é considerada uma perturbação B_{x1} do campo magnético com uma dependência espaço-temporal da forma:

$$B_{x1} = B_{x1}(x)\, e^{(\gamma t + iky)} \tag{19}$$

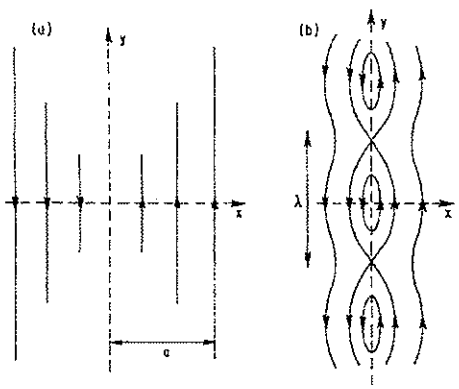

Fig. 9 - Regiões do plasma onde as linhas de campo invertem de sentido (a) podem gerar a formação de ilhas magnéticas (b), frente a alguma perturbação transversal.

sendo que $B_{x1} = ikA_z$, onde A_z é a componente *z* do potencial vetor $\vec{A}$.

Escrevendo-se a lei de Ohm na forma resistiva:

$$\vec{E} + (\vec{v} \times \vec{B}) = \eta \vec{j} \tag{20}$$

onde η é a resistividade do plasma na região de análise, a linearização desta equação fornece, para a componente A_z, a expressão [36]:

$$\frac{-\partial A_z}{\partial t} + v_x B_{y0} = \frac{-\eta}{\mu_0} \nabla^2 A_z \tag{21}$$

A equação de movimento (eq. 1), desta forma, torna-se:

$$\rho_0 \frac{d\vec{v}}{dt} = -\vec{\nabla} P_1 + \vec{j}_1 \times \vec{B}_0 + \vec{j}_0 \times \vec{B}_1 \tag{22}$$

a qual, escrita em termos de sua componente z e considerando-se ainda que o fluido é incompressível ($\vec{\nabla} \cdot \vec{v}_0 = 0$), resulta na expressão [36]:

$$\frac{\rho_0}{k^2} \frac{\partial}{\partial t} \nabla_\perp^2 v_x = -B_{0y} \nabla_\perp^2 A_z + A_z \frac{dj_{z0}}{dx} \tag{23}$$

onde $\nabla_\perp^2 = \frac{\partial}{\partial x^2} - k^2$.

É interessante observar, pela expressão (21), que na ausência de resistividade a instabilidade não cresce (γ é nulo) porque $B_{y0} = 0$ em $x = 0$. Ou seja, este modelo planar é estável com relação às perturbações ideais. Desta forma, no estudo das instabilidades, é sempre conveniente dividir o plasma em duas regiões distintas: uma que abrange apenas uma estreita faixa δ onde $|x| \leq \delta << a$ na qual a resistividade seria considerada, provocando rupturas e reconecções das linhas de campo magnético, e outra ($|x| >> \delta$) onde as equações ideais se aplicariam. Com relação à esta última região, tem-se que [36]:

$$\nabla_\perp^2 A_z \frac{-\mu_0}{B_{y0}(x)} \frac{dj_{z0}}{dx} A_z = 0 \tag{24}$$

cuja solução deve ser assintoticamente ligada com a solução correspondente à região resistiva. Isto feito, obtém-se que a largura da região resistiva, na qual as ilhas magnéticas são formadas, é dada pela expressão [36]:

$$\delta \approx \left(\frac{\gamma \rho \eta}{k^2 B_{y0}} \right)^{1/4} \tag{25}$$

sendo que a taxa de crescimento para as perturbações pode ser escrita como [36]:

$$\gamma = 0.5(ka)^{2/5} (\Delta' a)^{4/5} \tau_A^{-2/5} \tau_R^{-3/5} \tag{26}$$

Nesta última equação, $\tau_A = a\,(\mu_0\rho)^{1/2}/B_y$ é o tempo característico de propagação de uma onda de Alfvén e $\tau_R = \mu_0 a^2/\eta$ o tempo característico de difusão das linhas de campo no plasma.

O parâmetro Δ', por outro lado, é dado por:

$$\Delta' = \frac{1}{A_z(0)}\left[\frac{dA_z}{dx}\right]_{x=0} \tag{27}$$

e quantifica a descontinuidade das soluções em torno da camada resistiva. Vale a pena ressaltar que, neste modelo, as ilhas magnéticas se formam sempre nas vizinhanças da superfície correspondente a x = 0, que é justamente onde B_{y0} muda de sentido (e onde $\vec{k}\cdot\vec{B}_0 = 0$, uma vez que $\vec{k} = k\hat{e}_y$ e $\vec{B}_0(x=0) = B_{z0}\hat{e}_z$). Finalmente, esta característica, de existir uma componente do campo magnético que inverte de sinal na região onde $\vec{k}\cdot\vec{B}_0 = 0$, também é própria de plasmas confinados por tokamaks, originando a formação de ilhas magnéticas.

Conforme já mencionado anteriormente, as linhas de campo magnético de equilíbrio em tokamaks correspondem às hélices coaxiais, caracterizadas pelo parâmetro *q(r)*. Considerando-se uma superfície racional qualquer localizada a uma distância r_s do eixo magnético, as linhas de campo pertencentes às superfícies adjacentes a ela possuirão componentes que lhes são paralelas e que mudam de sentido justamente em r_s, onde finalmente se anulam. Se uma perturbação radial existir na forma:

$$B_r = B_r(r)e^{i(m\theta - n\phi + \omega t)} = B_r(r)e^{i(\vec{k}\cdot\vec{r} + \omega t)} \tag{28}$$

então ilhas magnéticas se formarão nas vizinhanças de superfície ressonante onde $\vec{k}\cdot\vec{B}_0 = 0$, ou seja, em $q(r_s) = m/n$.

De maneira análoga ao modelo bidimensional, já discutido, as ilhas surgem em uma estreita região em torno da superfície ressonante, fora da qual a teoria MHD ideal pode ser aplicada. Soluções assintóticas que satisfaçam a condição de sua continuidade em todo o sistema devem ser obtidas, muito embora uma descontinuidade em suas derivadas, na região da superfície ressonante, deva ser tolerada. O parâmetro Δ' que abrange esta condição, no caso de um plasma com geometria cilíndrica, é dado por [33, 37]:

$$\Delta' = \frac{1}{\psi}\frac{d\psi}{dr}\Big|_{r_s-\varepsilon}^{r_s+\varepsilon} \quad , \quad \text{com } \varepsilon \to 0 \tag{29}$$

onde

$$\psi = \frac{iB_\theta(m - nq)}{r}\xi_r \tag{30}$$

corresponde ao fluxo magnético perturbado.

É possível mostrar, através do princípio de energia, que a condição de estabilidade das perturbações resistivas é dada por [36, 37]:

$$\Delta' \leq 0 \tag{31}$$

e as taxas de crescimento das instabilidades correspondentes a $m \geq 2$, quando Δ' for positivo, serão [33, 38]:

$$\gamma \approx 0{,}55\left(\frac{a}{R_0} n \frac{aq'}{q}\right)^{2/5} \tau_R^{-3/5} \tau_A^{-2/5} (\Delta' a)^{4/5} \tag{32}$$

onde q'("*shear*") $\equiv dq/dr$. O critério de estabilidade estabelece que uma determinada perturbação com números de onda m e n específicos, para ser estável, basta que $q(a) < m/n$; ou seja, a superfície magnética onde se origina deve estar situada fora do plasma.

Muito embora a abordagem linear das perturbações que ocorrem em plasmas confinados por tokamaks tenha resultado em valiosas contribuições ao entendimento dos processos de instabilidades que são experimentalmente observadas, uma compreensão mais abrangente só é obtida com a introdução de efeitos não lineares nas equações MHD básicas, tais como resistividade, inércia e viscosidade do fluido. Como exemplo significativo desta observação vale citar o desenvolvimento de modos normais resistivos que, em vez de crescerem exponencialmente com o tempo, têm, muitas vezes, suas taxas de crescimento atenuadas e acabam por atingir um estado de *saturação* [39]. Este comportamento é, muitas vezes, experimentalmente verificado durante as descargas de plasma.

Finalmente, deve-se mencionar que perturbações magnéticas correspondentes a diferentes modos poloidais podem interagir entre si. Vários estudos já têm sido realizados [40-45] responsabilizando estas interações, originadas devido à própria geometria toroidal do sistema ou mesmo devido à existência de campos magnéticos de erro que surgem em resposta a possíveis desalinhamentos das bobinas do tokamak, por vários fenômenos que surgem no plasma. Dentre estes fenômenos podem-se destacar as sensíveis modificações que ocorrem nos processos de transporte de partículas e energia e o próprio desencadeamento das violentas instabilidades de disruptura. Em particular, a ação de campos de erro provocando o surgimento dos chamados *modos travados* ("*locked modes*") podem ser um grande obstáculo para o funcionamento dos futuros reatores de fusão.

2.3 - Fenomenologia dos *modos travados*

Como ficará bastante claro, no transcorrer deste trabalho, a componente $m = 2$ em particular desempenha um papel bastante importante no processo de desencadeamento de instabilidades de disruptura em tokamaks. Experimentalmente pode-se observar, quase que invariavelmente, que a amplitude das flutuações do campo magnético poloidal associada a este modo MHD cresce rapidamente momentos antes da ocorrência de uma disruptura. Como já discutido anteriormente, a teoria MHD resistiva permite que se associe, a esta componente, ilhas magnéticas que se localizam na superfície magnética correspondente a $q = 2$. A interpretação usualmente aceita é que as flutuações do campo magnético poloidal seriam causadas, basicamente, pela rotação destas ilhas ao longo da direção toroidal do tokamak.

Em muitos casos, porém, tem sido observado que, em um dado momento, estas ilhas param de girar, apesar de continuarem a aumentar de tamanho. Daí o nome sugestivo de *modo travado* que é geralmente dado a este fenômeno. Quando ocorre o *travamento do modo*, é muito grande a possibilidade de uma disruptura desenvolver-se logo a seguir. Deve-se ressaltar, no entanto, que a constatação do modo travado é geralmente feita apenas em tokamaks de médio e grande porte, provavelmente devido às velocidades mais baixas de movimento das partículas do plasma ao longo da direção toroidal, em comparação com as máquinas de pequeno porte.

A primeira tentativa de se idealizar um modelo que pudesse explicar a formação e as características básicas dos modos travados baseou-se na interação dos modos MHD com as paredes condutoras da câmara toroidal do tokamak [46, 47].

Posteriormente, no entanto, um modelo considerado mais plausível foi proposto no qual a diminuição da rotação do plasma nas proximidades das superfícies ressonantes seria devido a um torque sobre o plasma causado, provavelmente, por campos magnéticos de erro. [48-52].

Basicamente, as ilhas magnéticas no plasma são consideradas, neste modelo, como sendo pequenos obstáculos imersos em um fluido viscoso incompressível. Desta forma, adotando-se a abordagem de fluido único para o plasma e utilizando-se algumas condições de contorno apropriadas para o eixo magnético e para a região da borda, o cálculo do torque exercido sobre as ilhas, pelo plasma situado externamente à superfície magnética, pode então ser realizado. Para que a intensidade do torque seja significativa, levando o sistema à condição de modo travado, é necessário que as dimensões das ilhas magnéticas sejam razoavelmente grandes. Conseqüentemente, a velocidade do plasma localizado nas regiões das superfícies magnéticas ressonantes diminui rapidamente para próximo de zero, conforme já verificado experimentalmente, ao mesmo tempo que a taxa de crescimento das ilhas magnéticas acentua-se ainda mais.

Para a aproximação de geometria cilíndrica, pode-se mostrar que a razão entre o campo magnético perturbado e o campo toroidal, para que o processo de *travamento do modo* se inicie é dada por [52]:

$$\left.\frac{B_{r,mn}}{B_T}\right|_a = 1{,}1\left(\frac{r_s}{a}\right)^{2-m}\left[\frac{(-\Delta' r_s)^{3/5} S^{1/5}}{n^{4/5}}\left(\frac{r_s}{R_0}\right)^{1/5}\right]\left(\frac{f_s \tau_H^2}{\tau_M}\right)^{2/5} \qquad (33)$$

onde r_s é o raio da superfície ressonante, $\Delta' r_s$ é o parâmetro adimensional que representa a descontinuidade da região ideal/resistiva do plasma em torno de r_s, f_s corresponde à rotação toroidal do modo, $\tau_H = (R_0/B_T)(\mu_0 n m_i)^{1/2}$ é o tempo de Alfvén para íons de massa m_i, e τ_M é o tempo de confinamento relacionado com o momento do plasma na direção toroidal.

Comparações com resultados experimentais já realizadas [49], mostraram que a expressão (33) fornece resultados válidos para confinamentos de baixo β (parâmetro que fornece a razão entre as pressões cinética e magnética do plasma).

Capítulo 3

Diagnósticos Relevantes

Apesar de diversos diagnósticos diferentes já terem sido utilizados para a investigação das várias instabilidades que surgem em plasmas confinados por tokamaks [53-59], o sistema de deteção de raios-X de baixas energias e o sistema que mede a derivada temporal do campo magnético flutuante de perturbação são os que mais se destacam no estudo das disrupturas. Isto porque são estes os sistemas de diagnósticos que possibilitam a monitoração dos modos m = 1 e m = 2, respectivamente, e, conforme já mencionado, diversos trabalhos tanto experimentais quanto teóricos têm sugerido que o desencadeamento das instabilidades de disruptura maior seria causada por um possível acoplamento entre estas duas componentes MHD [26-30, 60-62].

3.1 - *Bobinas magnéticas de Mirnov*

As bobinas magnéticas de Mirnov são assim chamadas em homenagem ao cientista russo S.V. Mirnov, por ter sido ele o primeiro a medir as flutuações do campo magnético através de um conjunto de pequenas espiras instaladas ao redor do tokamak T-3 em 1969 [63]. A interpretação usualmente aceita para a existência destas oscilações é que elas estariam relacionadas com estruturas espaciais helicoidais da forma $e^{i(m\theta - n\phi)}$, consistentes com a rotação de modos de ruptura (modos "*tearing*") resistivos; sendo que os números de onda m e n, como já visto anteriormente, definem a helicidade dessas estruturas. Geralmente, a faixa de freqüência das oscilações de Mirnov varia de 1 a 20 kHz para tokamaks de grande e médio porte e de 20 a 60 kHz para pequenos tokamaks. O grande interesse existente quanto à deteção e estudo destas flutuações reside justamente no fato delas poderem fornecer informações sobre os mecanismos

físicos que desencadeiam os fenômenos disruptivos. Próximo a uma disruptura maior, por exemplo, tem sido observado que a amplitude do campo magnético poloidal de perturbação cresce exponencialmente, podendo alcançar até 4% do campo poloidal total produzido pela corrente de plasma [28].

Para a determinação experimental do número de onda poloidal *m*, várias bobinas magnéticas são usualmente distribuídas internamente à câmara de vácuo e ao longo de uma única seção transversal da câmara toroidal. Para a determinação da componente *n*, outras bobinas são distribuídas ao longo da direção toroidal do tokamak. De forma que, quando se deseja investigar as instabilidades que ocorrem em um certo instante de tempo qualquer, durante um determinado pulso de plasma, os sinais de todas estas bobinas são conjuntamente analisados em termos de suas amplitudes relativas e da variação de fase que apresentam entre si.

Em termos operacionais, o sinal induzido em cada bobina, após ter sido digitalizado, é armazenado em módulos de memória para ser, posteriormente, reconvertido em um sinal analógico e adequadamente analisado. Esta análise é realizada, basicamente, através da decomposição em séries de Fourier do sinal experimental obtido, através de um programa computacional que consiste em se obter os coeficientes a_0, a_m e b_m da equação:

$$\tilde{\dot{B}}_\theta(\theta) = \frac{a_0}{2} + \sum_{m=1}^{N-1}\left[a_m \cos(m\theta) + b_m \sin(n\theta)\right] + \frac{a_N}{2}\cos(N\theta) \qquad (34)$$

onde:

$$a_m = \frac{2}{N}\left[\sum_{k=0}^{N-1} \tilde{\dot{B}}(k)\cos(ksm)\right] \qquad \text{e} \qquad b_m = \frac{2}{N}\left[\sum_{k=0}^{N-1} \tilde{\dot{B}}(k)\sin(ksm)\right] \qquad (35)$$

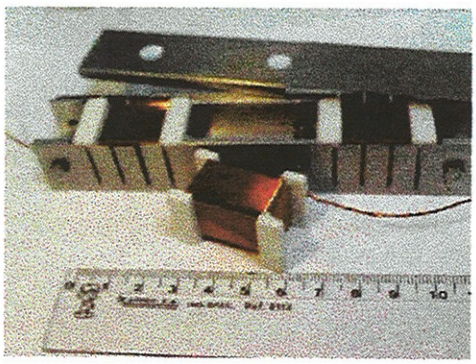

Fig. 10 - Bobinas de Mirnov que serão utilizadas no tokamak TCA/BR do Laboratório de Física de Plasmas do IFUSP.

Nestas equações, *N* corresponde ao número de bobinas magnéticas utilizadas e *s* representa o espaçamento entre as bobinas. Os coeficientes $c_m = ½ (a_m^2 + b_m^2)^{1/2}$, resultantes desta análise, quantificam a amplitude dos números de onda *m* presentes em um certo instante considerado durante uma descarga do plasma. Deve-se mencionar também que outras abordagens, como as que efetuam a análise dos sinais magnéticos por "*wavelets*", por exemplo, também têm sido utilizadas com sucesso e resultados bastante interessantes já foram obtidos [64, 65].

No tokamak TCA/BR do Instituto de Física da USP, que está entrando em operação neste ano de 1998, quatro conjuntos de bobinas magnéticas poloidais já estão sendo construídos, cada um deles constituído por 22 bobinas de Mirnov (Fig. 10). Além destas, outras 30 bobinas estarão também sendo distribuídas ao longo da direção toroidal. A utilização deste número bastante grande de bobinas faz parte de um trabalho original que tem como principal objetivo o de investigar possíveis comportamentos assimétricos das estruturas resistivas presentes no plasma antes, durante e após a ocorrência de uma disruptura maior. Certamente, todas estas bobinas estarão sendo instaladas internamente à câmara de vácuo para evitar-se, ao máximo, a atenuação do campo magnético de perturbação antes que ele possa ser finalmente medido. É interessante observar ainda que, em cada conjunto poloidal, as bobinas magnéticas estarão espaçadas entre si de forma a já se levar em conta o efeito da geometria toroidal do sistema (Fig. 11). O sistema de aquisição de dados e digitalização dos sinais magnéticos será baseado em módulos VME, recentemente importados de Portugal.

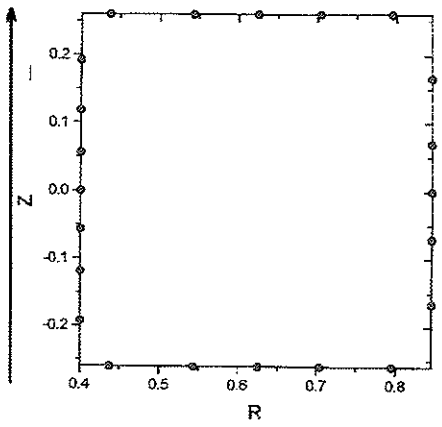

Fig. 11 - Posicionamento das bobinas magnéticas de Mirnov no interior da câmara de vácuo do TCA/BR.

3.2 - *Raios-X de baixas energias*

Os raios-X de baixas energias (ou *raios-X moles*, como também são usualmente denominados) constituem-se em emissões situadas na faixa de freqüência eletromagnética de 100 eV a 10 keV, aproximadamente. O espectro de emissão de raios-X moles, devido a plasmas confinados por tokamaks, é basicamente formado por um contínuo, com picos característicos superpostos. A componente contínua é formada por radiação de "*bremsstrahlung*" produzida em decorrência das interações dos elétrons energéticos com os isótopos de hidrogênio e íons de impurezas, e também devido aos processos de recombinação elétron-íon. Em ambos os casos, a produção de radiação nesta faixa de freqüência é fortemente proporcional à temperatura de elétrons (T_e), da forma [66, 67]:

$$\frac{\Delta W}{\Delta E} \propto \sum_i n_e n_i Z_i^2 T_e^{-1/2} e^{-\frac{h\nu}{T_e}} \qquad (36)$$

Nesta expressão, ΔW é a potência irradiada por unidade de volume do plasma correspondente aos fótons de energias pertencentes ao intervalo ΔE, n_e e n_i são as densidades de elétrons e íons, respectivamente, Z_i correspondem aos números atômicos dos íons do plasma e $h\nu$ é a energia do fóton emitido. Esta forte e predominante dependência da emissão de raios-X de baixas energias com a temperatura de elétrons indica que a emissão de radiação será tanto mais intensa quanto mais próximo do centro da coluna de plasma estiver sendo considerado um determinado elemento de volume do plasma. Também, pelo fato de se poder supor o plasma confinado por tokamaks como um meio opticamente transparente aos raios-X de baixas energias, nas condições usuais de trabalho, o diagnóstico de raios-X moles tem-se revelado uma excelente ferramenta para a investigação das instabilidades que ocorrem na região central da coluna de plasma.

Os picos superpostos ao contínuo, por outro lado, correspondem basicamente aos decaimentos espontâneos dos íons excitados para um estado de menor energia. Assim sendo, os comprimentos de onda dos fótons emitidos situam-se predominantemente na região espectral do ultra-violeta distante (VUV) [68]. Por esta razão, filtros que são geralmente colocados no caminho óptico dos detetores absorvem uma grande parte destas emissões e somente uma pequena parcela de fótons com energias mais altas, emitidos por impurezas de alto Z altamente ionizadas, não são totalmente filtrados.

Em tokamaks, sistemas de deteção de raios-X moles têm sido, algumas vezes, utilizados para medir a temperatura de elétrons através do método dos absorvedores [69, 70]. Porém, a maior contribuição deste diagnóstico reside no seu potencial de *observar* o centro da coluna de plasma e, desta forma, auxiliar na investigação das instabilidades que se desenvolvem nesta região em particular.

As flutuações *dentes de serra*, neste contexto, são sem dúvida as mais interessantes de serem discutidas. Elas recebem este nome justamente pelo formato que possuem e tem-se observado que elas estão intrinsecamente associadas a um processo de expansão e contração cíclica da região central da coluna de plasma.

Em seu trabalho pioneiro, Von Goeler e colaboradores [71], após terem instalado convenientemente alguns detetores de raios-X moles ao longo das direções toroidais e poloidais do tokamak PLT, puderam observar que uma perturbação MHD do tipo m/n = 1/1, localizada nas imediações da superfície magnética q = 1, seria a responsável direta pela formação das instabilidades dentes de serra. Pouco tempo depois, um modelo fenomenológico foi proposto por Kadomtsev [72] para explicar os mecanismos físicos que dariam origem aos dentes de serra. Neste modelo, ainda bastante aceito nos dias de hoje, durante a fase de crescimento de um dente de serra a região central da coluna de plasma estaria sendo gradualmente aquecida pelo transformador ôhmico em decorrência a uma redução da resistividade local. Esse processo teria continuidade até que q(0) se torne menor que um, possibilitando o surgimento da

perturbação resistiva m/n = 1/1 no instante t_1 da Fig. 12. A ilha magnética nas imediações da superfície ressonante q = 1, associada a esta perturbação, passaria então a crescer devido à recombinação sucessiva das linhas de campo (instantes t_2 e t_3 da Fig. 12) até que, quando todas tiverem sido recombinadas, o centro magnético da ilha seria o novo centro magnético da coluna de plasma. Neste ponto (instante t_4 da Fig. 12), o sistema retorna à sua configuração original e todo o processo se repetiria então novamente.

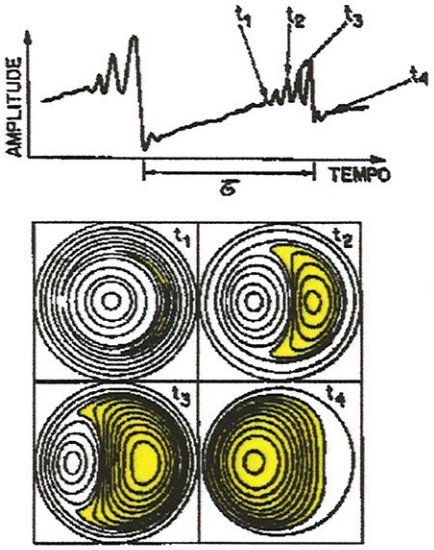

Fig. 12 - Várias fases da formação de um dente de serra, associadas com o crescimento de uma ilha magnética em torno da superfície q=1.

Talvez seja interessante mencionar que dentes de serra, com diferentes períodos, têm sido experimentalmente observados em uma mesma descarga de plasma. Isto pode ser considerado como um indício de que a parte central da coluna de plasma é bastante susceptível às mudanças que possam ocorrer com os parâmetros físicos do plasma nesta região da coluna.

3.2 - *Bobinas de deteção de modos travados*

Conforme explicado anteriormente, os modos travados estão intrinsecamente relacionados com o fato das ilhas magnéticas, em determinadas circunstâncias, pararem de girar durante uma descarga do plasma. Conseqüentemente, nenhum sinal é induzido nas bobinas magnéticas de Mirnov, apesar das dimensões das ilhas continuarem aumentando. Desta maneira, faz-se necessário que várias outras espiras sejam instaladas no tokamak para poder-se medir a variação do campo magnético radial associado ao crescimento das ilhas magnéticas, especialmente neste caso em que elas param de girar.

Este campo magnético radial, por ser geralmente muito pequeno, impõe que as espiras de modos travados tenham um área efetiva razoavelmente grande. Também, de forma a se evitar que outras componentes do campo magnético possam interferir nas medidas, é normalmente adotado o procedimento de se instalar duas destas bobinas separadas entre si de 180°, na direção toroidal. Os sinais das duas bobinas são, então, subtraídos entre si de forma que o sinal resultante seja diretamente proporcional às dimensões das ilhas, localizadas na superfície correspondente a q = 2. Instalando-se duas outras bobinas, conforme mostrado na Fig. 13, tanto a componente seno quanto a componente cosseno do modo podem então ser obtidas, possibilitando que a amplitude e a fase do modo travado sejam determinadas. Também, para que haja o cancelamento adequado dos campos magnéticos produzidos pelas espiras

verticais, toroidais e ôhmicas, as áreas efetivas das bobinas devem ser as mesmas (dentro de um erro menor que 1%) e cuidados especiais têm que ser tomados quanto ao alinhamento de cada par destas bobinas.

No TCA/BR, um sistema de bobinas de deteção de modos travados deverá ser construído e instalado para auxiliar no estudo das instabilidades de disruptura. Uma estimativa quanto a área efetiva para cada bobina pode ser feita considerando-se que, no JET, o travamento dos modos ocorrem quando $\widetilde{B}_\theta$ (parede) ~ 10 Gauss e o campo magnético radial é de 0,25 a 1,5 Gauss. Então o modo cresce até que, um pouco antes de uma disruptura ocorrer, $\widetilde{B}_r/\widetilde{B}_\theta$ (parede) ~ 0,6 - 1,2 x 10^{-2} o que corresponde a uma intensidade de campo magnético radial de 30 a 60 Gauss [50].

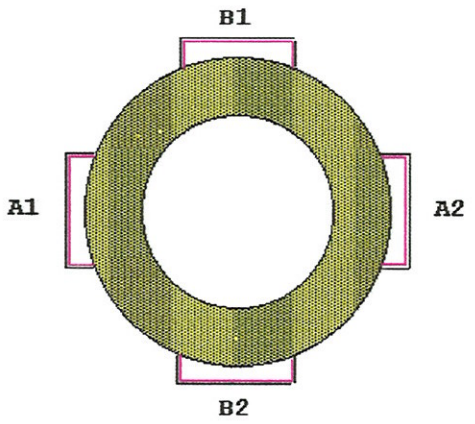

Fig. 13 - Posicionamento adequado das espiras de deteção de modos travados, ao redor do tokamak.

Para o TCA/BR, considerando-se descargas de I_p ~ 100 kA e que a distância do centro do plasma até a parede externa da câmara toroidal é de b ~ 22 cm, então a intensidade do campo magnético radial na região da parede, instantes antes de uma disruptura maior, será de 0,5 a 1,0 Gauss, aproximadamente. Por esta análise, a área efetiva das espiras a serem instaladas no TCA/BR deveria, a princípio, ser muito maior que a área efetiva das espiras utilizadas no JET (da ordem de 4 m^2). No entanto, como estas espiras são usualmente posicionadas fora da câmara de vácuo e uma vez que as paredes de aço do tokamak JET são muito mais espessas que a do TCA/BR, a diferente atenuação do campo nos dois casos indica que uma área efetiva da mesma ordem poderia também ser utilizada no TCA/BR.

Capítulo 4

Mecanismos de Desencadeamento das Instabilidades de Disrupturas

Durante uma descarga em tokamaks, são vários os processos já conhecidos que podem levar o confinamento do plasma à sua total destruição. No entanto, se por um lado a compreensão exata de alguns destes mecanismos é ainda objeto de controvérsias, por outro, tem-se observado que grande parte dessas disrupturas pode ser facilmente evitada ao operar-se o tokamak dentro de certos limites razoavelmente bem estabelecidos, que envolvem alguns de seus parâmetros básicos como densidade de partículas e intensidade da corrente de plasma, por exemplo. Assim, quando algum desses limites é violado, torna-se bastante grande a probabilidade de que alguma disrupturas ocorra. Um procedimento usualmente adotado é o de identificar as disrupturas segundo o tipo de limite que tenha sido violado, ou então segundo algum sistema de controle particular que tenha falhado durante o confinamento do plasma. Desta forma, têm-se as disrupturas de *limite de densidade* ("*density limit disruption*"), as disrupturas de *baixo q* ("*low-q disruption*"), as disrupturas de *alto* β ("*high-*β *disruption*"), as disrupturas ocasionadas por *deslocamentos verticais* da coluna de plasma ("*vertical displacement disruption*"), etc. [73,74]. Neste sentido, espaços operacionais para tokamaks, como o ilustrado na Fig. 14, muitas vezes são construídos para que sejam estabelecidas as condições experimentais de trabalho mais adequadas de forma a minimizar a probabilidade de uma destas disrupturas ocorrer.

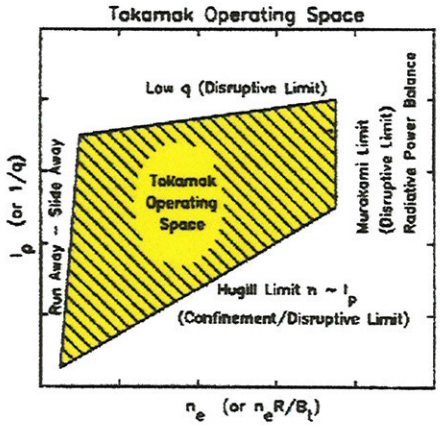

Fig. 14 - Espaço operacional típico de tokamaks (ref. [73]), conhecido como diagrama de Hugill

De um modo geral, quando uma disruptura surge, ela provoca uma rápida perda da energia interna do plasma, uma abrupta expansão do raio menor e um deslocamento da coluna como um todo em direção às paredes internas da câmara de vácuo (diminuição do seu raio maior), além de um transiente característico (*pico negativo*) na tensão de enlace. Estas características são mais ou menos típicas das disrupturas maiores, independentemente do "tipo de disruptura" ocorrido.

No transcorrer do presente capítulo serão discutidos os mecanismos físicos que dão surgimento às instabilidades de disruptura que ocorrem em três tokamaks distintos, investigados por este autor em ordem cronológica: o pequeno tokamak TBR-1 do IFUSP - Instituto de Física da USP, o tokamak JET, de grande porte, da Comunidade Européia - Inglaterra e o tokamak TEXT, de médio porte, da Universidade do Texas - EUA. Estes trabalhos, onde investigaram-se disrupturas que geralmente não seguiam uma classificação específica segundo a discussão acima, deram origem a alguns artigos publicados em revistas internacionais que encontram-se anexados na forma de apêndices.

4.1 - *Acoplamento entre os modos m = 1 e m = 2*

O principal resultado obtido nos três tokamaks investigados, TBR-1, JET e TEXT, foi a constatação de que o acoplamento entre os modos m = 1 e m = 2 qualifica-se como a causa mais provável do desencadeamento das instabilidades de disruptura maior observadas. Este resultado torna-se ainda mais interessante pelo fato destes tokamaks investigados, apesar de serem bastante diferentes um do outro em termos de dimensão, razão de aspecto, forma da coluna de plasma, etc., ainda assim, o desenvolvimento das disrupturas processa-se basicamente através de um acoplamento entre modos MHD.

Com relação ao tokamak TBR-1, por exemplo (ver apêndice 1), a origem das instabilidades de disruptura foi investigada comparando-se os sinais de campo magnético detetados por bobinas de Mirnov (16 delas distribuídas ao longo da direção poloidal e 4 bobinas na direção toroidal), com o sinal de raios-X moles provenientes da região central da coluna de plasma. Tipicamente, a intensidade da atividade MHD precursora das disrupturas maiores, medida pelas bobinas de Mirnov, mostrou um crescimento exponencial de forma que, no instante da disruptura, o campo magnético poloidal de perturbação alcançou, em relação ao campo magnético poloidal de equilíbrio, um valor razoavelmente grande, de até $\widetilde{B}_\theta / B_\theta \sim 4\ \%$. A constatação do provável acoplamento entre os modos m/n = 2/1 e m/n = 1/1, como sendo a principal causa de desencadeamento das disrupturas maiores, pode ser feita observando-se o comportamento destes modos e verificando que eles passam a oscilar em fase instantes antes da

ocorrência do pico negativo característico da tensão de enlace, conforme mostrado nas Figs. 15 e 16, para duas descargas de plasma distintas.

Quanto às disrupturas menores no TBR-1, estas, por outro lado, foram identificadas como sendo causadas pelo acoplamento entre os modos m/n = 2/1 e m/n = 3/1. Análises realizadas mostraram que este acoplamento produziria uma ergodização das linhas de campo magnético na região do plasma situada entre as superfícies magnéticas com fator de segurança q = 2 e q = 3, levando o plasma a uma condição de rápida perda de energia e partículas da região da borda, o que caracterizaria a disruptura menor.

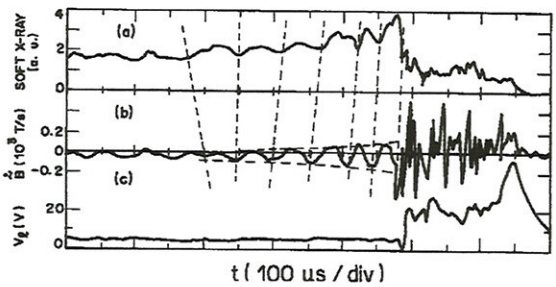

Fig. 15 - As oscilações correspondentes aos modos m/n =1/1 (a) e m/n = 2/1 (b) crescem em amplitudes e exibem a mesma frequência antes da disruptura, sugerindo um provável acoplamento entre eles.

Já no tokamak JET, a investigação das disrupturas (ver apêndice 2) pode ser realizada posteriormente de forma mais minuciosa e precisa devido à grande quantidade de sistemas de diagnósticos existentes em operação, simultaneamente, junto àquela máquina (Fig. 17). Dentre os resultados obtidos, talvez o mais significativo foi o que levou à constatação de que a maioria das disrupturas estudadas não eram desencadeadas devido a uma contração da coluna de plasma, em decorrência de uma intensa potência irradiada (por ter-se atingido o limite de densidade), como era o pensamento corrente dos cientistas do JET naquela época [53]. Além disso, foi verificado também que estas não se tratavam de disrupturas de baixo *q* porquanto, em muitas descargas, observou-se que o fator de segurança manteve-se sempre acima de três durante todo o período de confinamento. Por outro lado, o acoplamento entre os modos m = 2 e m = 1 mostrou-se novamente como sendo o mecanismo mais provável de desencadeamento das instabilidades de disruptura maior analisadas. Na Fig. 18 é mostrada uma descarga de plasma com corrente Ip ≈ 6,3 MA (Fig. 18a), que sofreu uma disruptura em t ≈ 13,28 s, e que exemplifica bem a afirmativa feita. Para esta descarga em particular, foi observado em um certo instante o valor da potência radiada alcançando quase 100% da potência injetada (Fig. 18b), devido a um influxo grande de impurezas para o interior da coluna de plasma, em t ≈ 13,16 s. Este influxo intenso de impurezas, pelo menos aparentemente, determinou o acoplamento entre os modos m = 2 e m = 1 (Figs. 19a e 19c) o

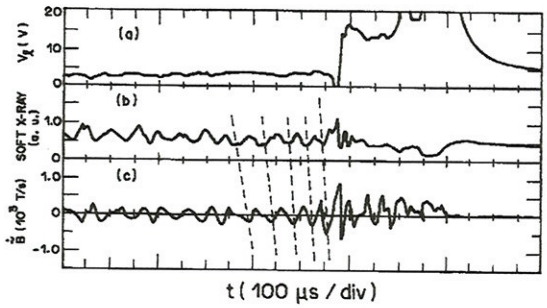

Fig. 16 - Descarga de plasma onde o acoplamento entre os modos m/n = 1/1 e m/n = 2/1 é novamente identificado através da mesma frequência que exibem *momentos antes da disruptura.*

que causou, conseqüentemente, o início de um processo de modos travados em t ≈ 13,24 s (Fig. 19b). O surgimento do pico negativo característico no sinal da tensão de enlace ocorre logo depois, em t ≈ 13,26 s, e o colapso da coluna de plasma é então finalmente observado.

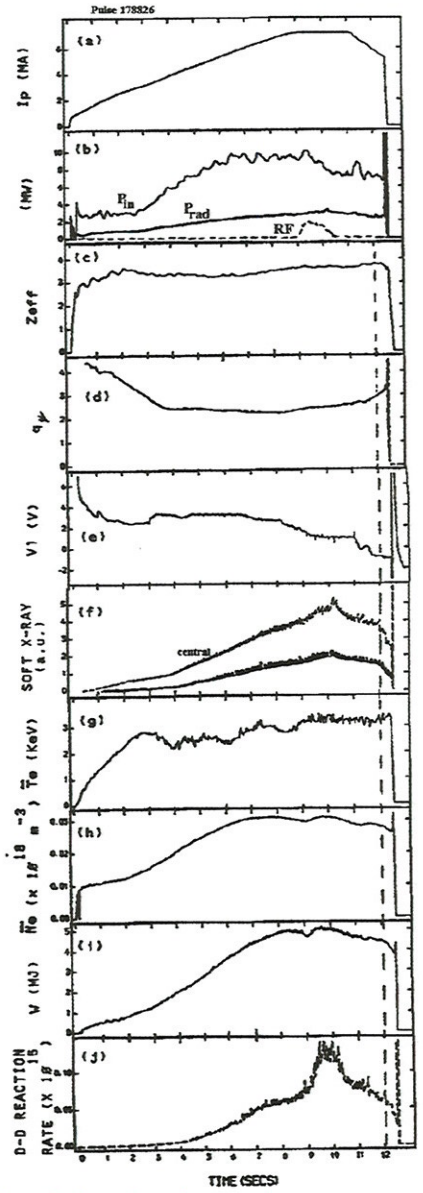

Fig. 17 - Pulso de plasma disruptivo com $I_p \approx 7{,}1$ MA (a) onde vários sistemas de diagnósticos encontravam-se simultaneamente em operação. Note que nesta, como em outras descargas, a potência irradiada (P_{rad}) manteve-se bem abaixo da potência injetada (P_{in}) durante todo o período de confinamento (b).

Deve-se salientar, neste ponto, que tanto para estas disrupturas maiores investigadas no tokamak JET quanto para as do TBR-1 e do TEXT-U, o cálculo das taxas de crescimento dos modos MHD foi realizado e os baixos valores obtidos sugeriram que estas perturbações possuíam, para todos os casos, caráter resistivo.

Durante o processo de investigação das disrupturas que ocorrem no JET foi possível ainda, utilizando-se todas as disrupturas analisadas, determinar um espaço operacional de funcionamento para esta máquina válido, ao menos, para as disrupturas com correntes de plasma $I_p \geq 5$ MA. Foi observado, por exemplo, que a construção de um diagrama de Hugill (semelhante ao mostrado na Fig. 14) não indicava com confiabilidade quais as fronteiras proibidas de serem alcançadas durante o processo de confinamento do plasma. Por outro lado, construindo-se um gráfico do valor da indutância interna do plasma (L_i) em função do fator de segurança (q_ψ) relacionado com a última superfície magnética do plasma, pode-se observar a existência de uma fronteira mais ou menos bem definida para o plasma (Fig. 20) que não poderia ser ultrapassada durante o confinamento sem que uma disruptura maior viesse a ocorrer. É interessante observar ainda que este limite foi determinado utilizando-se descargas em diferentes condições quanto ao tipo de limitador material utilizado (carbono ou berílio) e também quanto ao tipo de aquecimento empregado, i. e., puramente ôhmico ou com aquecimento adicional (RF e NB).

Lembrando que a indutância do plasma pode ser relacionada com o campo magnético poloidal segundo a expressão:

$$L_i = \frac{2}{\mu_0^2 R_0 I_P^2} \int B_\theta^2 dV \qquad (37)$$

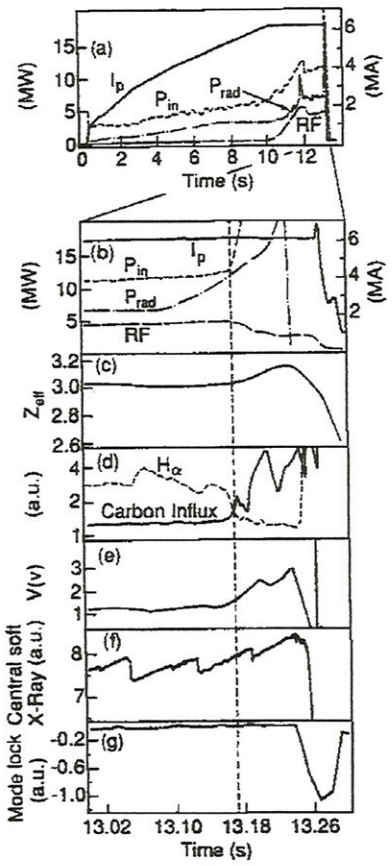

Fig. 18 - Descarga de plasma na qual a potência radiada quase alcança 100% da potência injetada, devido a um influxo de impurezas na coluna de plasma.

onde a integral é realizada sobre todo o volume de plasma, então o comportamento exibido pelo diagrama da Fig. 20, obtido experimentalmente, indicaria talvez que há uma quantidade limite de energia magnética poloidal que o plasma confinado pode armazenar, para um dado valor de corrente. Alcançando este limite, o sistema se encontraria em uma condição de equilíbrio instável de forma que uma pequena perturbação qualquer poderia provocar o desencadeamento de uma disruptura maior.

Finalmente, com relação aos mecanismos que dão origem às disrupturas maiores no tokamak TEXT-U da Universidade do Texas (apêndice 3) pode-se igualmente observar, através da análise dos sinais de Mirnov e de raios-X moles, que eles também estão intrinsecamente relacionados com o acoplamento entre os modos m = 2 e m = 1. Isto pode ser verificado, por exemplo, analisando-se descargas de plasma como a da Fig. 21. Pode-se observar que a potência irradiada mantêm-se sempre bem menor que a potência injetada (Fig. 21c) e o fator de segurança cilíndrico parece não variar muito, possuindo o valor de $q_{cil} \approx 2{,}8$ no instante da disruptura (Fig. 21b). Por outro lado, observando-se o sinal correspondente à densidade média de elétrons desta descarga (Fig. 21d) poder-se-ia até supor que a disruptura do plasma teria ocorrido pelo fato do limite de densidade ter sido atingido. No entanto, acompanhando-se a trajetória desta descarga no espaço de fase correspondente ao diagrama de Hugill (Fig. 22) verifica-se que este não é bem o caso, já que a disruptura acabou ocorrendo em um ponto distante do limite de densidade.

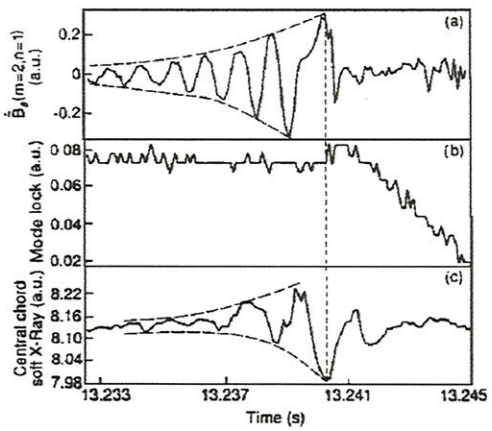

Fig. 19 - O crescimento e o acoplamento dos modos m/n = 2/1 e m/n = 1/1(a) e (b) dão o início a um processo de modos travados (c) e levam então o plasma a sofrer uma disruptura maior.

Analisando-se, no entanto, os sinais dos diversos diagnósticos correspondentes à parte final desta descarga (Fig. 23), verifica-se que o

pico negativo na tensão de enlace (Fig. 23b) foi precedido por um crescimento da atividade MHD (Fig. 23c) que, ao alcançar determinada amplitude (em t ≈ 307 ms) começa a modificar o formato das oscilações dentes de serra observados nos sinais de raios-X moles (Fig. 23d). A partir deste instante é observado então um crescimento do sinal de H_α (Fig. 23e), concomitantemente a uma diminuição perceptível do valor da corrente de plasma (Fig. 23a). Esta deformação dos sinais de raios-X moles, em particular, que sempre parece começar no momento em que a atividade MHD atinge uma determinada amplitude, dando lugar a uma flutuação periódica com a mesma freqüência do modo m = 2, sugere a existência de um acoplamento desta componente com o modo m = 1. Após o acoplamento, ocorrem no plasma duas disrupturas menores não muito intensas e finalmente, em t ≈ 320 ms, é observada a destruição total do confinamento devido à disruptura maior. Deve-se mencionar aqui que as oscilações "tipo dente de serra", observadas no sinal de Mirnov desta descarga, correspondem unicamente a ruídos eletromagnéticos externos captados pelas bobinas magnéticas posicionadas fora da câmara de vácuo, e que não existe nenhuma correlação destas com as oscilações dentes de serra observadas nos sinais de raios-X moles. No que se refere à escala de tempo necessária para que ocorra o colapso total da corrente de plasma, após a observação do pico negativo característico no sinal da tensão do tokamak TEXT-U, foi constatado que existe uma variação bastante significativa abrangendo um intervalo de aproximadamente cinco a algumas dezenas de milisegundos.

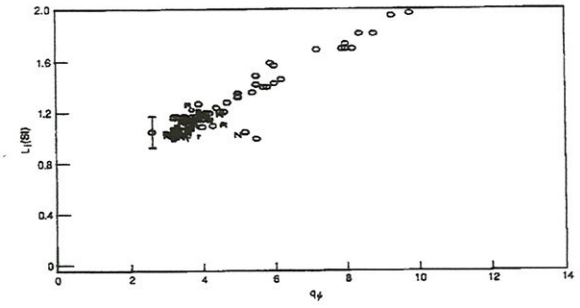

Fig. 20 - Diagrama construído com os valores da indutância do plasma (L_i) e fator de segurança relativo à última superfície magnética q_ψ obtidos nos instantes anteriores à disruptura maior.

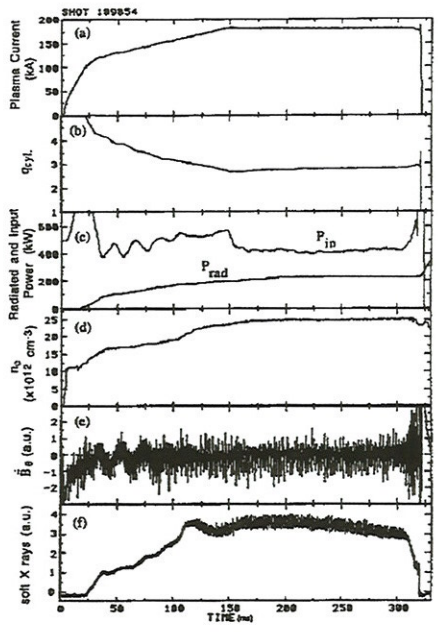

Fig. 21 - Descarga disruptiva do TEXT-U, em t ≈ 320 ms, na qual Prad > Pin durante todo o período de confinamento.

Os pulsos de plasma das Figs. 24 e 25, por exemplo, mostram as características básicas de uma descarga onde a corrente de plasma decai rapidamente para zero após a disruptura maior e uma outra onde a corrente decai de forma bem mais lenta, respectivamente. Com relação à descarga mostrada na Fig. 25, após o acoplamento dos modos m = 1 e m = 2 em t ≈ 427 ms (Figs. 25c e 25d), é observada a ocorrência de uma disruptura menor que acaba provocando uma queda

significativa na intensidade de raios-X de baixas energias emitidos pelo plasma. Logo em seguida, a amplitude da atividade MHD decresce enquanto a emissão de raios-X moles começa a crescer. Porém, logo depois, duas outras disrupturas menores acabam ocorrendo seqüencialmente, degradando seriamente o confinamento. A coluna de plasma continua a deslocar-se em direção às paredes internas da câmara de vácuo (região de valores menores do campo toroidal), conforme mostrado na Fig. 25e, e o sistema de posicionamento eletrônico da coluna (sistema de *"feed-back"*) torna-se incapaz de manter o plasma centrado. Finalmente, uma disruptura maior ocorre em t ≈ 435 ms provocando o pico negativo no sinal da tensão de enlace (Fig. 25b). A partir daí a intensidade da corrente de plasma vai decaindo gradativamente para zero (Fig. 25a).

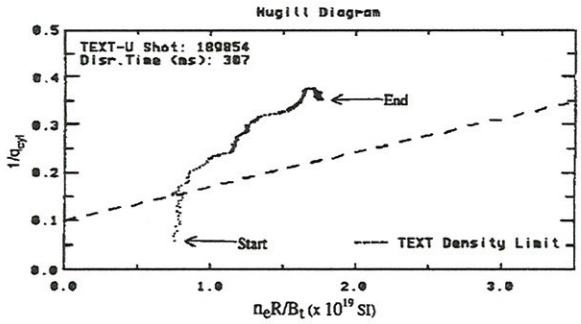

Fig. 22 - Trajetória no espaço de fase de Hugill correspondente ao pulso da Fig. 21.

Deve-se também ressaltar que, durante a queda final da corrente de plasma da descarga mostrada na Fig. 25, várias protuberâncias são observadas no sinal da corrente de plasma (Fig. 25a), que também são identificadas através dos vários outros diagnósticos (Figs. 25b, 25c, 25d, 25e e 25f). Este comportamento indica, muito provavelmente, que a coluna de plasma acabou interagindo diversas vezes com o limitador material e as paredes da câmara de vácuo. Tem-se a impressão de que, durante cada interação, a parte mais externa e fria da coluna de plasma é perdida e logo a seguir o sistema ainda tenta recuperar-se das conseqüências do processo, com parcial sucesso, conforme pode-se concluir ao compararem-se as quedas observadas no sinal de H_α com os correspondentes crescimentos identificados no sinal de raios-X moles. Entretanto as condições gerais do confinamento apresentam-se drasticamente mudadas. Os resultados do processo disruptivo tornaram-se, desta forma, irreversíveis e o fim do confinamento é então verificado.

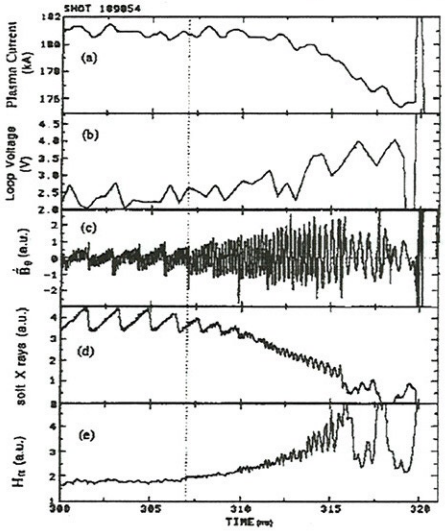

Fig. 23 - Sinais experimentais correspondentes ao pulso de plasma da Fig. 21, nos instantes finais da descarga.

Comparativamente, os pulsos de plasma disruptivos que apresentam uma queda rápida na intensidade da corrente de plasma são, certamente, bem mais perigosos para o tokamak, devido às altas tensões eletro-mecânicas que são induzidas em todos os seus sistemas e componentes. No caso da descarga disruptiva apresentada na Fig. 24, por exemplo, após a ocorrência do pico negativo no sinal da tensão de enlace em t ≈ 435 ms é observado que a corrente de plasma

decai em apenas 5 ms, aproximadamente. Neste caso, muito provavelmente devido à rapidez do processo, tanto o sistema que mede o perfil temporal da corrente de plasma quanto o que monitora a posição horizontal da coluna de plasma (Figs. 24a e 24c, respectivamente) não conseguem acompanhar adequadamente as modificações ocorridas durante os instantes finais da descarga. Como pode ser visto através das Figs. 24d e 24e, o acoplamento entre os modos

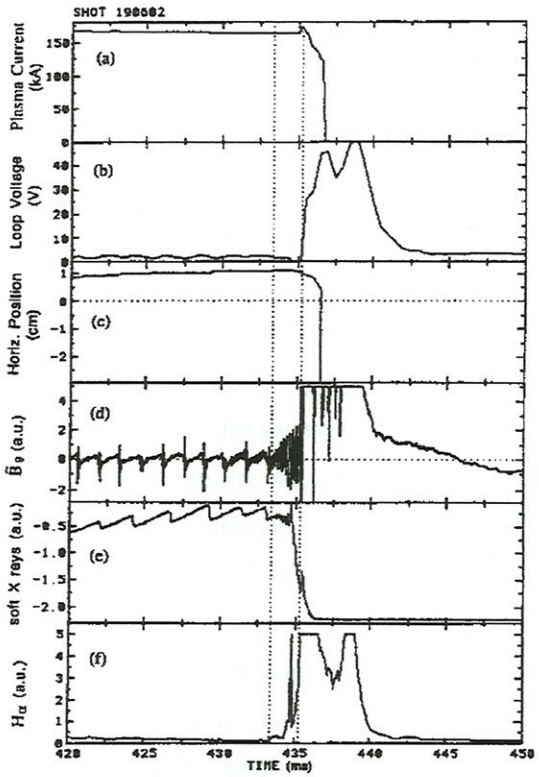

Fig. 24 - Pulso de plasma que exibe um decaimento rápido da corrente de plasma, em consequência da ocorrência de uma instabilidade de disruptura maior.

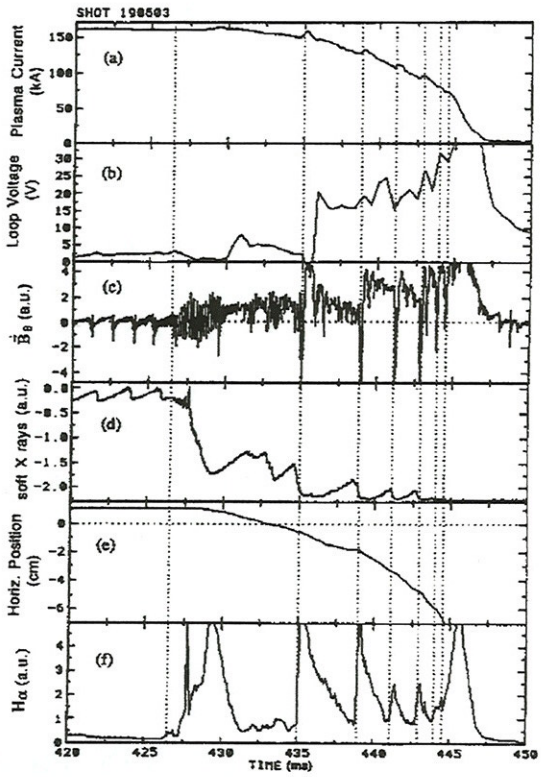

Fig. 25 - Exemplo de um pulso no qual a corrente de plasma decai mais lentamente, após a disruptura maior. Várias disrupturas menores ocorrem durante o decaimento.

m = 2 e m = 1, que acabou desencadeando a disruptura maior, aconteceu apenas alguns milisegundos antes, em t ≈ 433 ms.

É interessante observar, neste ponto da discussão, que este pulso de plasma com decaimento rápido da corrente (pulso N° 190602) corresponde justamente ao antecessor do pulso de decaimento lento da corrente de plasma já discutido antes (pulso N° 190603 da Fig. 25), de forma que os parâmetros básicos correspondentes a ambos são bastantes semelhantes. Talvez a diferença mais significativa resida no fato de que, geralmente, uma grande quantidade de impurezas é arrancada das paredes de aço do tokamak devido à ocorrência de uma disruptura maior e que muitas vezes estas impurezas persistem na câmara de vácuo durante as descargas seguintes. Baseando-se nesta observação, seria razoável levantar a hipótese de que o fator determinante para que a corrente de plasma de um pulso disruptivo venha a decair rápida ou lentamente talvez pudesse estar diretamente relacionado com o valor do *Z*-efetivo do plasma

durante o seu processo de confinamento. No entanto, análises semelhantes realizadas posteriormente, utilizando outros pulsos disruptivos também consecutivos, mostraram que esta hipótese não é verdadeira já que o contrário do que observou-se para estes dois pulsos pode ser verificado.

4.2 - Bobinas de deteção de modos travados do tokamak TEXT-U

Como sistema de diagnóstico auxiliar para a investigação dos processos disruptivos no TEXT-U, dois pares de bobinas de deteção de modos travados foram por nós projetados, construídos e instalados externamente à câmara de vácuo do tokamak. As bobinas foram afixadas em portas radiais do tokamak, distanciadas angularmente entre si de 90°, aproximadamente, sendo que um par foi construído com 12 espiras em cada bobina (1,8 ± 0,3 m^2 de área efetiva) e as bobinas do outro par com 24 espiras (3.6 ± 0,4 m^2 de área efetiva). Experimentalmente, os sinais de campo magnético radial detetados pelos dois pares de bobinas não se mostraram afetados por perturbações electromagnéticas externas de qualquer espécie durante a operação do TEXT-U, de forma que nenhum tipo de compensação adicional nos sinais fez-se necessário. Para cada par de bobinas os sinais correspondentes foram subtraídos diretamente, conforme mostrado na Fig. 26, e digitalizados a uma freqüência de 20 kHz.

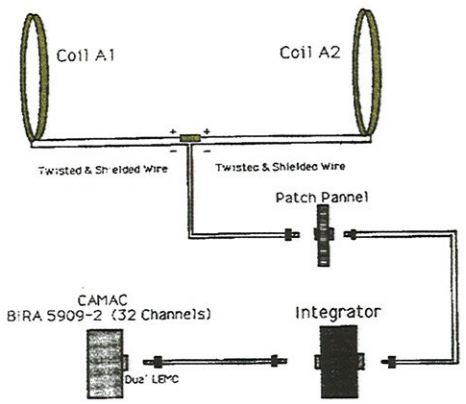

Fig. 26 - Arranjo experimental das bobinas de deteção de modos travados construídas para o tokamak TEXT-U.

De forma geral, o campo magnético radial de perturbação medido pelas bobinas de modos travados demonstrou crescer em amplitude durante os instantes finais que antecediam a ocorrência de uma disruptura maior. Estas oscilações precursoras mostraram-se variando no tempo de alguns poucos milisegundos até várias dezenas de milisegundos. É interessante observar que, praticamente para todas as descargas investigadas, as oscilações nos sinais das bobinas de modos travados surgiam no mesmo instante em que se observava o acoplamento entre os modos MHD m = 2 e m = 1. Uma análise detalhada dos sinais dos vários diagnósticos mostraram que as oscilações do campo magnético radial perturbado, presentes nos sinais das espiras de deteção de modos travados, seria mais uma conseqüência do acoplamento entre os modos m = 2 e m = 1 que o fator responsável pelo desencadeamento da disruptura maior.

Um exemplo de uma disruptura na qual foi bastante importante ter-se em operação as bobinas de deteção de modos travados é apresentada na Fig. 27. Trata-se dos momentos finais de uma descarga na qual o acoplamento característico dos modos m = 2 e m = 1, ocorrido em t $\approx$ 401 ms, mostra-se como a principal causa da disruptura maior que destrói completamente o confinamento, aproximadamente 40 ms depois. Uma vez mais, logo após o acoplamento dos modos, identificado através do aumento da atividade MHD (Fig. 27c) concomitantemente à deformação característica das oscilações dentes de serra (Fig. 27b), observa-se uma queda no valor da corrente de plasma (Fig. 27a). Analisando-se o sinal do sistema de deteção de modos travados (Fig. 27d) nota-se que um campo magnético radial de perturbação surge a partir do momento em que ocorre o acoplamento entre os modos MHD. A partir deste instante, o sinal cresce em amplitude e diminui em freqüência ao mesmo tempo que as flutuações observadas na bobina de Mirnov decrescem tanto em freqüência quanto em amplitude. O comportamento exibido por estes dois sinais é explicado em função da diminuição da velocidade de giro das ilhas magnéticas (menor freqüência das oscilações) ao mesmo tempo que continuam a aumentar de tamanho. Observando-se os sinais de raios-X moles e bobina de Mirnov durante os últimos dez milisegundos da descarga verifica-se que as oscilações nestes sinais praticamente desaparecem. Este comportamento é geralmente entendido como sendo devido às ilhas nas superfícies magnéticas q = 1 e q = 2 que param completamente de girar (ocorrência de "modo travado"). No entanto, comparando-se os sinais integrados dos dois pares de bobinas de deteção de modos travados (Figs. 27e e 27f) pode-se concluir que as ilhas magnéticas em q = 2 continuam a girar ao longo da direção toroidal mas só que com uma freqüência muito baixa, de aproximadamente 50 Hz. Cálculos realizados envolvendo esta e outras descargas de plasma semelhantes mostraram que o desaparecimento das oscilações nos sinais de raios-X moles e bobina de Mirnov, sinalizando a ocorrência de um processo de "modo travado", acontece quando a razão entre o campo magnético radial de perturbação e o campo poloidal na borda do plasma alcança o valor de $\tilde{B}_r / B_\theta \approx 0.4 - 0.5\%$.

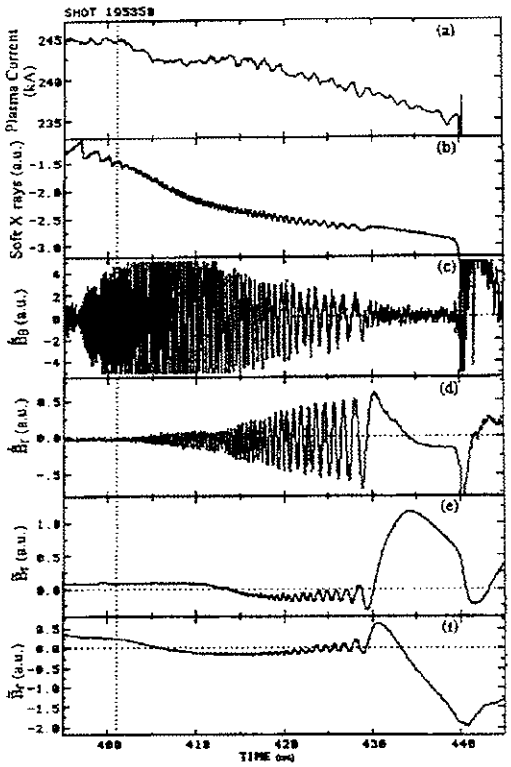

Fig. 27 - Momentos antes da destruição total do confinamento as oscilações nos sinais de raios-X (b) e bobina de Mirnov (c) desaparecem. Porém os sinais integrados das bobinas de deteção de modos travados indicam que as ilhas em q = 2 continuam a girar com frequência de ~ 50 Hz.

Finalmente, baseando-se nos resultados discutidos neste capítulo, referentes às investigações realizadas em tokamaks tão distintos quanto às dimensões e características básicas como o TBR-1, JET e TEXT-U, pode-se concluir que o acoplamento dos modos $m = 2$ e $m = 1$ seria o maior responsável pelas instabilidades de disrupturas que surgem durante o confinamento magnético do plasma e, principalmente, que este mecanismo de desencadeamento de disrupturas possui um caráter basicamente universal. Desta maneira, estes resultados podem ser utilizados como uma forma de suporte quanto ao que se pode esperar com respeito aos processos disruptivos que provavelmente surgirão durante a operação dos tokamaks da próxima geração, como o ITER.

Capítulo 5

Mecanismos de Controle das Instabilidades de Disrupturas

Diversos mecanismos e sistemas têm sido utilizados com o objetivo de tentar exercer algum tipo de controle sobre as instabilidades de disruptura, e seus perigosos efeitos, durante o confinamento do plasma por tokamaks. A aplicação de campos magnéticos externos [23, 75-81], injeção de "pellets" [55], injeção adicional de gás [82], deposição localizada de feixe de partículas neutras [82] e ondas de RF [83], por exemplo, são alguns dos métodos que já foram investigados com esta finalidade.

No presente capítulo, duas abordagens bastante distintas, relacionadas com trabalhos já desenvolvidos nos tokamaks TBR-1 e TEXT estarão sendo apresentadas e discutidas. Na primeira parte, serão abordados os trabalhos realizados utilizando campos magnéticos externos (apêndice 4) criados por um conjunto de malhas helicoidalmente enroladas ao redor da câmara de vácuo do TBR-1 [76, 77] e também por um sistema de limitador ergódico magnético [78]. Na segunda parte, serão discutidos os resultados dos trabalhos, bastante inovadores na área de fusão (apêndice 5), envolvendo a previsão da ocorrência das instabilidades de disruptura no TEXT utilizando-se redes neurais [84, 85].

5.1 - Campos magnéticos externos de perturbação no tokamak TBR-1

5.1.1 - Campos helicoidais ressonantes

Desde o trabalho pioneiro de Karger e colaboradores [75], Campos Helicoidais Ressonantes (CHR) têm sido aplicados em vários tokamaks na tentativa de controlar o surgimento das instabilidades de disruptura, através do amortecimento da atividade MHD do plasma. No tokamak TBR-1, a investigação de como estes campos atuam durante o confinamento (apêndice 4) foi realizada utilizando-se campos ressonantes de perturbação relativos às componentes m/n = 2/1, m/n = 3/1 e m/n = 4/1. Experimentalmente, a indução de campos relacionados com estas componentes foi feita através de um conjunto de malhas condutoras, externamente enroladas na superfície da câmara de vácuo (Fig. 28), com helicidades correspondentes aos modos que se pretendiam criar.

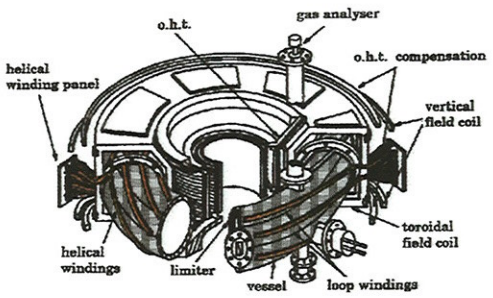

Fig. 28 - Desenho esquemático do tokamak TBR-1, com destaque para o posicionamento das malhas helicoidais.

De forma geral, a ativação dos enrolamentos helicoidais, utilizando-se correntes de intensidade $I_{hel} \leq 200$ A, acabaram produzindo forte atenuação da atividade MHD observada através das bobinas magnéticas de Mirnov. Valores mais elevados de corrente nos enrolamentos muitas vezes desestabilizavam o confinamento, provocando a ocorrência de uma disruptura maior. Um exemplo bastante claro da atenuação produzida por estes campos na atividade MHD, utilizando-se o enrolamento m/n = 2/1 com uma corrente $I_{hel} \approx 260$ A, é mostrado na Fig. 29. O pulso de corrente helicoidal foi aplicado após a subida da corrente de plasma, por um período de tempo $\Delta t \approx 0{,}7$ ms (Fig. 29b). Como pode-se observar, a atenuação da atividade MHD é bastante evidente durante o intervalo de tempo em que há corrente fluindo nas espiras do enrolamento helicoidal (Fig. 29c). Com o término do pulso helicoidal, após a influência do CHR no plasma ter cessado, a intensidade inicial das flutuações MHD é prontamente restabelecida. Deve-se notar que a defasagem temporal entre o início do pulso de CHR e o conseqüente amortecimento efetivo da atividade

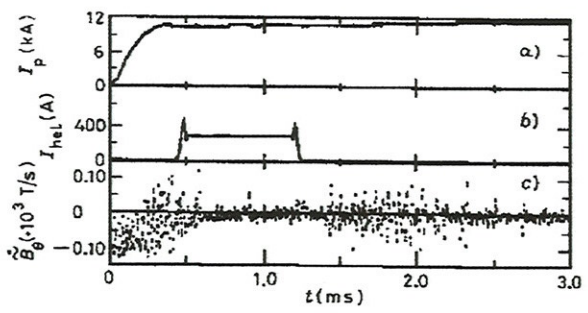

Fig. 29 - A aplicação de campos magnéticos ressonantes externos resultaram em uma atenuação eficientemente do modo MHD m/n = 2/1.

MHD observado nos sinais de Mirnov, de $\tau \approx 150$ - 200 microsegundos, é compatível com o cálculo do tempo necessário para que ocorra a penetração do campo magnético através das paredes de aço inoxidável do TBR-1 (espessura de 3,1 mm).

Analisando-se a composição de modos presentes na descarga de plasma da Fig. 29 antes, durante e após a aplicação do campo CHR, constatou-se a presença efetiva do modo m/n = 2/1 somente antes e após a aplicação do pulso de CHR. Durante o período em que ocorreu a aplicação do pulso, o modo presente era puramente m/n = 3/1. Isto indica que, através da ativação do enrolamento helicoidal m/n = 2/1 pode-se atuar de maneira eficaz sobre as ilhas magnéticas localizadas na superfície magnética q = 2, fazendo com que diminuam de tamanho. Resultados semelhantes a este foram também obtidos analisando-se outras descargas do TBR-1, para as quais foram calculados os respectivos espectros de potência, como mostrado na Fig. 30. Através dos diagramas desta figura, correspondentes aos períodos anteriores (Fig. 30a), durante (Fig. 30b) e posteriores (Fig. 30c) à aplicação do CHR, fica bastante nítido o efeito atenuador do campo magnético ressonante sobre a atividade MHD, resultando na supressão quase que completa do modo m/n = 2/1.

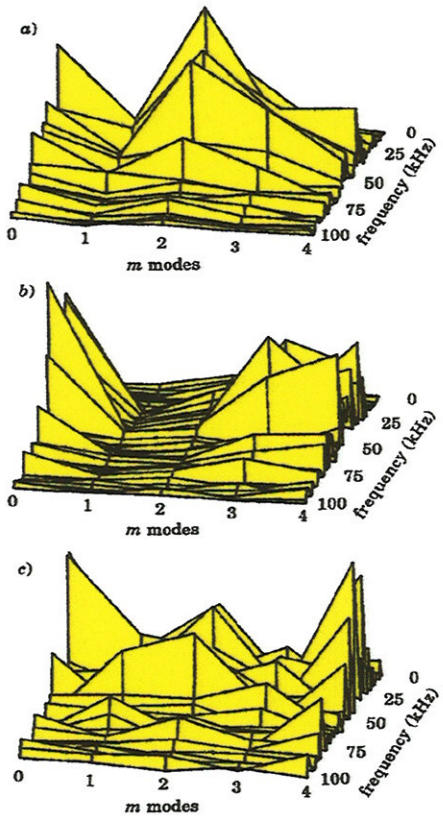

Fig. 30 - Espectros de potência calculados nos períodos (a) anterior, (b) durante e (c) posterior à aplicação do CHR m/n = 2/1.

5.1.2 - Limitador ergódico magnético

Sistemas de Limitadores Ergódicos Magnéticos (LEM) têm sido utilizados em diversos tokamaks com o objetivo de criar perturbações magnéticas de pequena amplitude no plasma, principalmente na região periférica da coluna. De forma geral, tem-se observado, por exemplo, que estas perturbações externas são capazes de diminuir a temperatura do plasma na região da borda e modificar a interação plasma-parede, causando, conseqüentemente, uma diminuição na perda de partículas e uma queda na taxa de influxo de impurezas provenientes da câmara de vácuo do tokamak [78, 86-90]. Isto acaba produzindo uma melhora no confinamento global do plasma, podendo inclusive beneficiar as condições de operação do tokamak, uma vez que o seu limite de densidade é expandido.

O sistema LEM para o TBR-1 é composto por um conjunto de quatro anéis, construídos e instalados externamente ao redor da câmara de vácuo. A configuração

geométrica destes anéis (Fig. 31) foi escolhida de forma a produzir uma perturbação dominante m/n = 7/2 na região periférica do plasma. Os anéis possuem 8 cm de largura cada e o diferente espaçamento existente entre os vários segmentos de cada anel foi calculado de forma a levar em consideração a geometria toroidal do sistema, segundo a expressão [78]:

$$\theta_\ell = \frac{\ell\pi}{7} + 0{,}38\sin\left(\frac{\ell\pi}{7}\right) \qquad (38)$$

onde θ_ℓ representa o posicionamento angular do segmento de cada anel e o parâmetro ℓ, que varia de 0 a 13, representa cada um dos 14 segmentos do arranjo utilizado. O número 7, nesta equação, representa o valor do modo poloidal escolhido para a perturbação criada, de forma que ela atue preferencialmente sobre a superfície magnética $q = m/n = 7/2$. O valor 0,38 corresponde ao inverso da razão de aspecto para o TBR-1, na região onde os anéis encontram-se instalados.

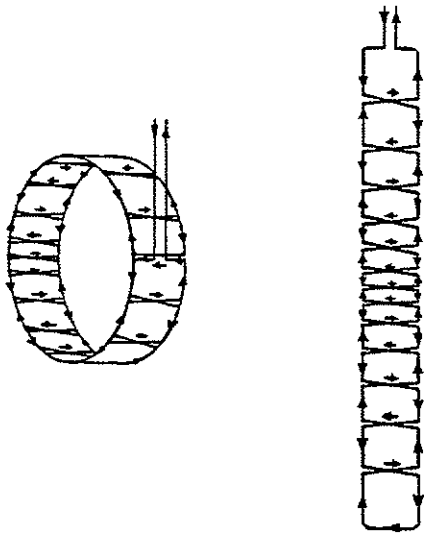

Fig. 31 - Configuração geométrica de um dos anéis que compõe o sistema de Limitador Ergódico Magnético do TBR-1.

Investigando-se, experimentalmente, como atuam estas perturbações criadas pelo limitador ergódico sobre o plasma confinado pelo TBR-1, foi possível comprovar que os valores de temperatura e densidade de elétrons na região da borda diminuíam quando o LEM era ativado. Além disto, observou-se também que a atividade MHD diminuía de intensidade sob a influência das perturbações criadas pelo LEM, de maneira semelhante ao que se obtém utilizando CHR, conforme mostrado na Fig. 32. Uma vez mais, a diferença temporal observada entre os instantes de aplicação do campo produzido pelo LEM e sua efetiva atuação na atividade MHD do plasma é compatível com o cálculo do tempo de penetração do campo através da câmara de vácuo, de aço inox.

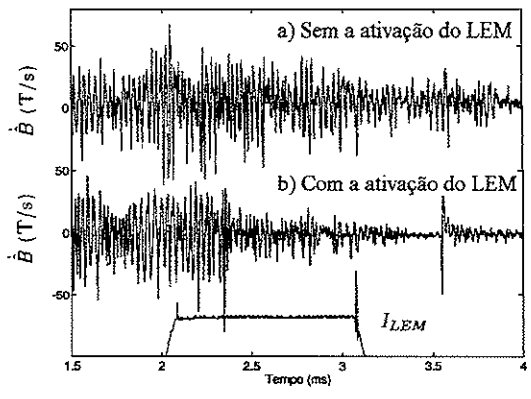

Fig. 32 - Atividade MHD no tokamak TBR-1, correspondentes a descargas (a) normais e (b) sob a influência de campos perturbativos criados pelo LEM.

Na Fig. 33, é mostrado o efeito que os campos criados pelo Limitador Ergódico Magnético causam sobre a frequência e composição dos modos MHD, em comparação com uma situação de operação normal do tokamak, sem a presença de campos perturbativos. Como pode-se observar, anteriormente à aplicação do LEM os modos MHD apresentam um espectro

de modos geralmente dominado pela presença das componentes m = 2, 3 e 4, com frequências características concentradas no intervalo 40 - 70 kHz (Fig. 33a). Durante a ativação do LEM, no entanto, observa-se que além de ocorrer um amortecimento bastante significativo da amplitude, a composição dos modos MHD é também tipicamente mais abrangente, além de exibir um espectro bem mais largo de frequência (Fig. 33b).

Em vista destas investigações, realizadas utilizando-se campos magnéticos externos perturbativos para tentar modificar algumas condições do plasma e influenciar de alguma forma no processo de formação das instabilidades de disruptura, pode-se concluir que tanto o sistema CHR como o LEM são igualmente eficientes. Porém, na escolha entre um e outro, o LEM leva ligeira vantagem sobre o CHR se for considerado que é um sistema de mais fácil instalação e também pelo fato de sua atuação não perturbar demasiadamente o confinamento do plasma, haja visto terem sido raras as disrupturas provocadas pela atuação deste sistema mesmo nas situações onde utilizavam-se correntes nos condutores do LEM de valores bastante elevados (até 500 A).

a) Antes da aplicação do LEM

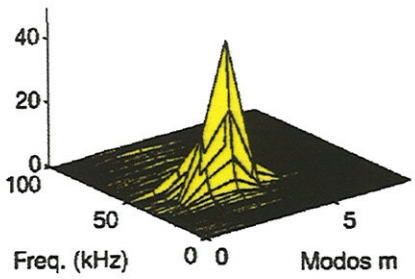

b) Após a aplicação do LEM

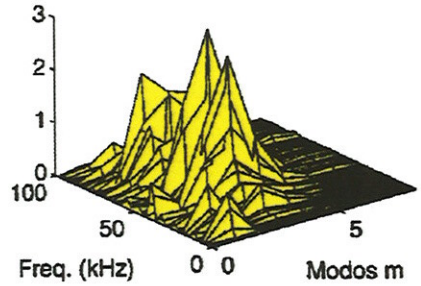

Fig. 33 - Composição de modos e espectro de frequências tipicamente observados em trechos de uma descarga antes e após a ativação do LEM.

5.2 - Previsão da ocorrência de instabilidades de disruptura no tokamak TEXT através da utilização de redes neurais

Um método bastante promissor e original de abordar o problema da ocorrência de instabilidades de disruptura em tokamaks, foi desenvolvido durante as investigações dos processos disruptivos realizadas junto ao tokamak da Universidade do Texas (apêndice 5). Este novo método baseia-se na utilização de redes neurais para tentar prever, com a maior antecedência possível, o instante em que uma disruptura ocorreria de forma a ter-se tempo para que mecanismos de defesa, caso estejam disponíveis, possam ser acionados com a finalidade de abortar a disruptura iminente ou, pelo menos, minimizar seus efeitos danosos.

Conforme já discutido anteriormente, o modo m = 2 desempenha um papel muito importante no processo de desencadeamento das instabilidades de disruptura em tokamaks. Nas disrupturas maiores, em particular, a desestabilização deste modo e seu acoplamento com o modo m = 1 é que causaria o início do processo disruptivo. Desta forma, foi natural a opção de

utilizar-se, inicialmente, os dados experimentais relativos ao campo magnético poloidal de perturbação para alimentar o programa de rede neural. Os resultados obtidos foram muito bons e bastante animadores, apesar da rede prever a disruptura em um intervalo de tempo não tão longo quanto seria desejável. Mais recentemente, no entanto, sinais de raios-X moles da região central da coluna de plasma foram utilizados para alimentar a rede neural e os resultados obtidos foram, comparativamente, muito melhores.

5.2.1 - Princípios básicos das redes neurais

As redes neurais constituem-se de algoritmos computacionais que procuram simular, de maneira bastante simplificada, o funcionamento dos neurônios cerebrais [91-94]. Neste processo, cada neurônio é matematicamente representado por uma *unidade binária* que dispara um sinal sempre que um certo "potencial" específico é atingido. Mais especificamente falando, em cada unidade da rede neural todos os sinais recebidos das demais unidades com as quais encontra-se ligada são somados e um *sinal de excitação* ou um *sinal inibitório* é emitido caso esta soma tenha ou não atingido, respectivamente, um determinado valor limite.

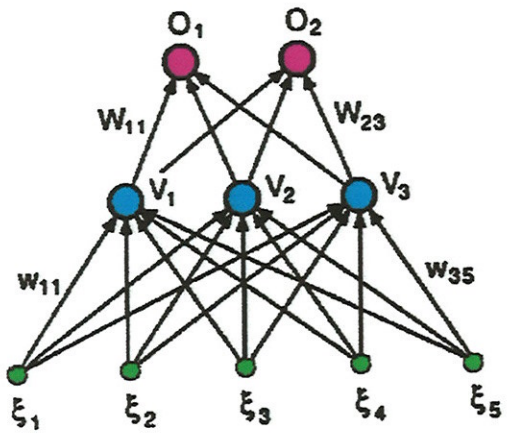

Fig. 34 - Rede neural do tipo "alimentação para a frente", com apenas uma camada escondida, mostrando as conecções e os pesos estatísticos existentes entre as várias unidades neurais.

Em uma rede neural as unidades neurais encontram-se distribuídas em camadas. O número de camadas e a quantidade de unidades neurais que cada uma possui, define a *arquitetura* da rede. As redes são usualmente constituídas por uma *camada de entrada*, uma *camada de saída* e uma ou mais *camadas escondidas*. Na figura 34, por exemplo, encontra-se esquematizada uma rede com três camadas apresentando 5 unidades neurais (ξ_k) na camada de entrada, três unidades (V_j) na camada escondida e duas unidades (O_i) na camada de saída. Este tipo de rede neural, na qual cada unidade neural encontra-se ligada com todas as unidades neurais existentes tanto na camada anterior como na camada posterior, é chamada de *rede de alimentação para a frente* ("*feed forward network*"). As ligações conectando as unidades neurais localizadas nas diversas camadas estão relacionadas com pesos estatísticos próprios.

Em cada unidade neural da rede os sinais de entrada (V_j), provenientes da camada anterior àquela na qual a unidade encontra-se localizada, após serem somados segundo seus pesos estatísticos correspondentes (W_{ij}), são processados segundo uma *função ativação*, g(x),

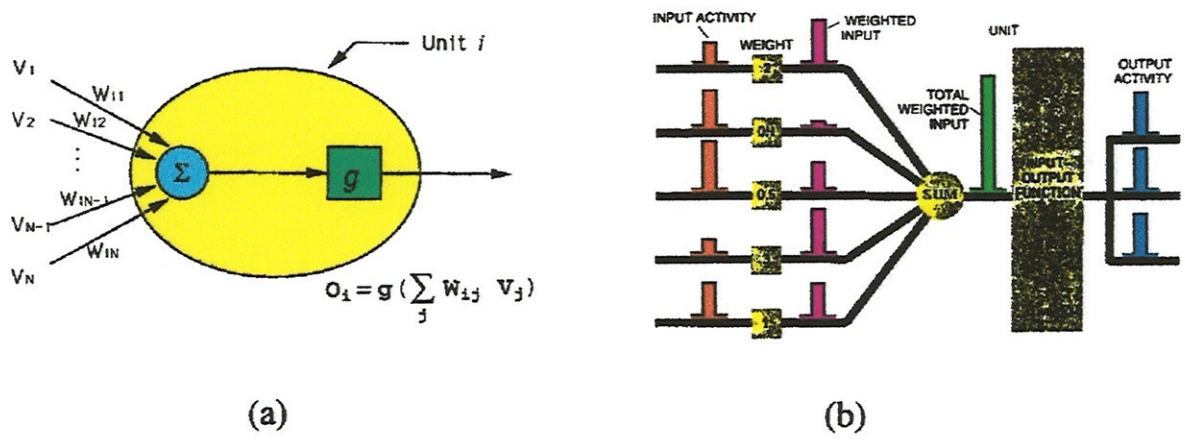

Fig. 35 - Ilustrações esquemáticas de funcionamento de cada elemento (unidade neural) da rede neural.

e são então transmitidos (O_i) para as unidades neurais da camada seguinte. Este processo, ilustrado através dos diagramas da figura 35, pode ser matematicamente representado pela equação:

$$O_i = g\left(\sum_j W_{ij}\, V_j\right) \tag{39}$$

5.2.2 - Utilização de redes neurais para a previsão das instabilidades de disruptura

O procedimento básico de utilização de uma rede neural para prever a ocorrência de uma instabilidade de disruptura, consiste em alimentar a rede com uma sequência de valores temporais (passados) de algum sinal experimental, como a derivada temporal do campo magnético poloidal medido por uma das bobinas magnéticas de Mirnov, por exemplo:

$$V = \dot{\tilde{B}}_\theta(t),\ \dot{\tilde{B}}_\theta(t-\tau),\ \dot{\tilde{B}}_\theta(t-2\tau),\ \ldots,\ \dot{\tilde{B}}_\theta(t-n\tau), \tag{40}$$

e supor a existência de uma função não-linear P de forma que o valor do campo magnético, no instante futuro $(t+\tau)$, possa ser obtido (predito) de acordo com:

$$\dot{\tilde{B}}_\theta(t+\tau) = P(V) \tag{41}$$

A rede neural é então utilizada para a realização deste cálculo de $\dot{\tilde{B}}_\theta$ no instante $(t+\tau)$ (e instantes posteriores), já que a função não-linear P é desconhecida. Porém, para que a rede neural possa desempenhar esta função com sucesso, é preciso primeiro *treiná-la*, ou seja, é

necessário determinar corretamente os pesos estatísticos de todas as conexões entre as unidades neurais através de um algoritmo chamado de *propagação reversa* ("*back propagation algorithm*") [95]. Neste treinamento os sinais experimentais, obtidos ao longo de uma descarga de plasma, são introduzidos na rede para serem processados e os sinais gerados (previstos) são então comparados com os sinais reais (obtidos experimentalmente). Esta "comparação" é realizada através de uma *função-erro* ("*cost function*"), usualmente definida por:

$$\varepsilon(W) = \frac{1}{2}\sum_{j}\left(Oj - \hat{O}j\right)^2 \tag{42}$$

onde Oj e $\hat{O}j$ representam os sinais medidos pela bobina de Mirnov e os fornecidos pela rede neural, respectivamente. O processo é ilustrado pelo diagrama da figura 36.

A função do algoritmo de propagação reversa é de, primeiramente, alterar os valores dos pesos estatísticos das conexões e, depois, comparar os novos resultados gerados pela rede com o sinal real. Este processo é realizado de uma forma interativa e a rede é considerada "treinada" quando a diferença entre os sinais que ela gera (prevê), e os medidos experimentalmente, encontra-se minimizada. Operacionalmente, este ajuste nos pesos estatísticos é realizado a partir das últimas conexões (que envolvem as unidades neurais da camada de saída), passando pelas conexões das camadas escondidas e, finalmente, envolvendo as unidades neurais da camada de entrada. Daí o nome de "*back propagation algorithm*". Matematicamente, esta variação nos pesos estatísticos das várias conexões é feita através das equações:

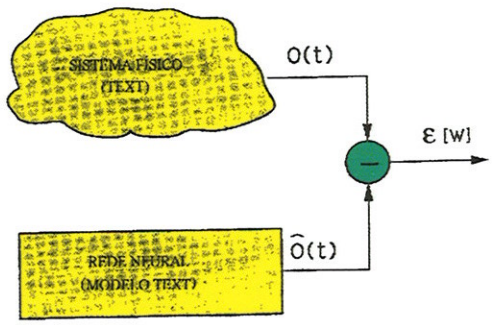

Fig. 36 - A minimização da função-erro $\varepsilon(W)$ através do algoritmo de propagação reversa corresponde ao treinamento da rede.

$$\Delta W_{ij} = -\eta\frac{\partial\varepsilon}{\partial W_{ij}} + \alpha W_{ij} \tag{43}$$

sendo que:

$$W_{ij}^{novo} = W_{ij}^{antigo} + \Delta W_{ij} \tag{44}$$

onde η e α, que correspondem à *taxa de aprendizado* e ao *termo inercial*, respectivamente, são utilizados para acelerar a convergência do processo de treinamento da rede.

5.2.3 - *Utilizando sinais magnéticos de Mirnov nas redes neurais*

Para a previsão das instabilidades de disruptura que ocorrem nas descargas do tokamak TEXT da Universidade do Texas, utilizando sinais experimentais de uma bobina magnética de Mirnov, foi inicialmente utilizada uma rede neural com arquitetura ***15 - 9 - 3 - 1*** (quinze unidades neurais de entrada, duas camadas escondidas com nove e três unidades neurais cada, e uma unidade neural de saída). A função ativação escolhida foi g(x) = tanh (x) para todas as unidades neurais, exceto para unidade neural de saída, quando g(x) = x (uma função linear, para

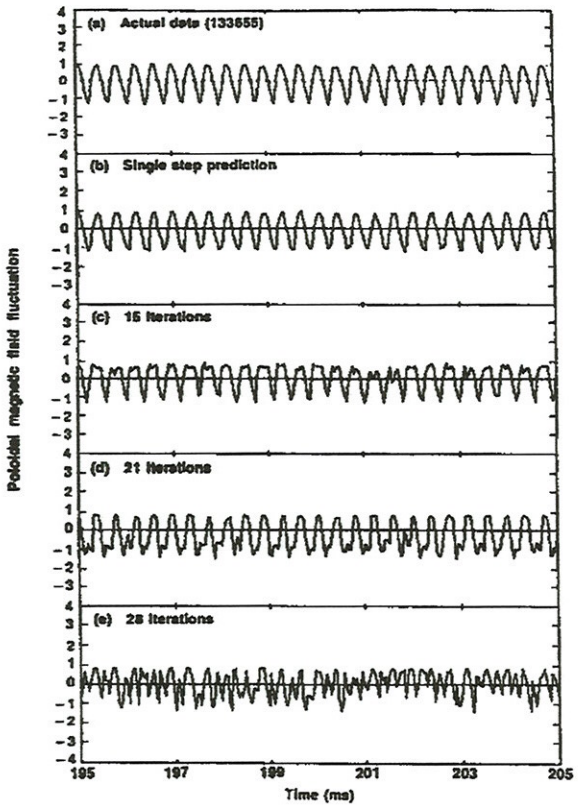

Fig. 37 - Comparando-se a parte oscilatória do sinal experimental (a) com os resultados previstos pela rede (b → e) constata-se o bom desempenho da rede mesmo para um número elevado de interações.

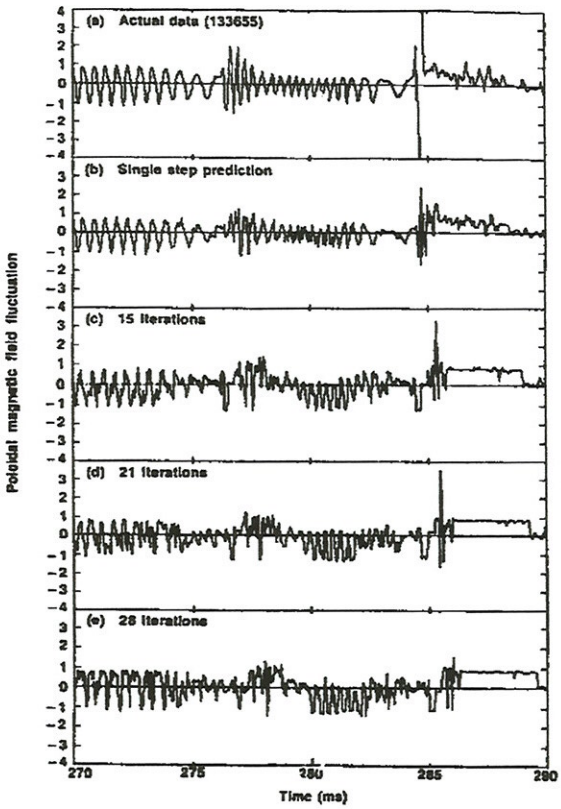

Fig. 38 - Previsões fornecidas pela rede (b → e) em comparação com o sinal experimental (a), durante a ocorrência de uma disruptura menor em t ≈ 277 ms e uma disruptura maior em t ≈ 285 ms.

propiciar um espectro largo de resposta).

Para o treinamento da rede foram utilizados dois pulsos de plasma, um disruptivo e um não-disruptivo, e uma terceira descarga disruptiva foi utilizada como pulso de validação (que serve para monitorar o processo de treinamento da rede). Após ter-se obtido um treinamento adequado, a rede foi aplicada a um outro pulso disruptivo (diferente daqueles utilizados para treinamento e validação) com a tarefa de prever os valores dos sinais experimentais de campo

magnético poloidal, com uma antecedência temporal que variou de $\tau = 0{,}04$ ms até $\tau = 1.12$ ms. Os resultados obtidos, para as partes oscilatória e disruptiva da descarga, são mostrados nas figuras 37 e 38, respectivamente.

Como pode-se perceber da Fig. 38, apesar de existirem algumas discrepâncias quanto à forma do sinal em relação ao sinal experimental, a rede neural foi capaz de prever com sucesso os transitórios no sinal de campo magnético poloidal devido às ocorrências das disrupturas menor (em $t \approx 277$ ms) e maior (em $t \approx 285$ ms), com uma antecedência de até $\Delta t \approx 1.12$ ms. Outro fato evidente, observado nos resultados da rede neural mostrados na Fig. 38, refere-se ao atraso temporal existente entre o instantes previstos para a ocorrência das disrupturas e os instantes de tempo em que elas de fato ocorreram. Este atraso, indesejável, mostrou-se ser tanto maior quanto maior o número de interações requisitadas à rede para efetuar o trabalho de predição.

Apesar de muito animadores, tais resultados certamente não podem ser considerados suficientemente bons, de forma a possibilitar uma ação efetiva sobre o plasma, em tempo real, de forma a abortar ou pelo menos atenuar as conseqüências causadas por uma disruptura maior que estivesse por surgir. No entanto, se for conseguido que a previsão da ocorrência de disruptura pela rede neural seja feita em um intervalo de tempo consideravelmente maior e se também for adequadamente configurado um sistema de realimentação baseado em um circuito integrado que pudesse rodar o programa de previsão por redes neurais em tempo real, os efeitos nocivos de algumas instabilidades de disruptura maior talvez pudessem ser de alguma forma evitados ou pelo menos amenizados, por exemplo, através da aplicação de campos magnéticos externos, injeção rápida de gás no interior da câmara de vácuo ou através de lançamento de "*pellets*" [55, 76-78, 82].

5.2.4 - Alimentando as redes neurais com sinais de raios-X de baixas energias

Muito recentemente, a utilização do sinal de raios-X emitidos da região central da coluna de plasma foi utilizado para alimentar uma rede neural, na tentativa de se expandir o intervalo temporal de previsão da ocorrência de disrupturas no tokamak TEXT, em relação ao que já se havia obtido anteriormente através do uso de um sinal da bobina de Mirnov. Os resultados obtidos, que agora serão discutidos, constituem-se na contribuição original para esta tese.

Utilizando-se a mesma arquitetura de rede do trabalho anterior (***15 - 9 - 3 - 1***), os pesos estatísticos para todas as conecções entre as unidades neurais foram obtidos utilizando-se dois pulsos de plasma disruptivos: o de treinamento e o de validação. A rede neural, após ter sido convenientemente treinada utilizando os últimos 200 ms de cada descarga, foi então utilizada

no processo de previsão da ocorrência de disrupturas utilizando-se duas outras descargas disruptivas, diferentes daquelas usadas para treinamento e validação. Na Fig. 39 são mostrados os sinais experimentais relativos à primeira destas descargas utilizadas para a previsão. Trata-se de um pulso com $I_p \approx 170$ kA cujo término ocorreu em $t \approx 470$ ms. No entanto, aproximadamente 18 ms antes da disruptura maior destruir o confinamento do plasma, um crescimento abrupto na atividade MHD é observado (Fig. 39c) concomitantemente às quedas ocorridas na densidade de elétrons (Fig. 39f) e na emissão de raios-X moles da região central da coluna (Fig. 39d). Estes são indícios claros de que uma disruptura menor ocorreu em $t \approx 452$ ms. É importante ressaltar que as descargas utilizadas para treinamento e validação da rede também apresentavam esta característica de uma disruptura menor ocorrer um pouco antes do colapso da corrente de plasma devido ao desencadeamento de uma disruptura maior.

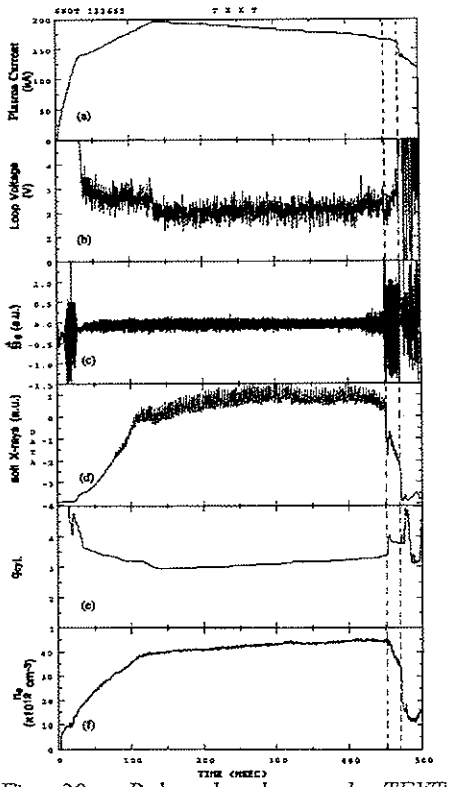

Fig. 39 - Pulso de plasma do TEXT utilizado pela rede neural para o processo de previsão dos instantes em que as disrupturas ocorrem.

Os resultados de previsão das disrupturas fornecidos pelo programa de rede neural para a descarga da Fig. 39 são mostrados na Fig. 40. Como pode ser observado, para uma interação (um "*time-step*") a rede reproduz (Fig. 40b) quase que perfeitamente o sinal experimental de raios-X moles experimental (Fig.40a). Aumentando progressivamente o tempo de previsão (números de interações) verifica-se que os sinais dentes de serra vão se deformando (Fig. 40c) mas a rede mostra-se capaz de prever de modo preciso o momento em que a disruptura ocorre, em $t \approx 452$ ms. O tempo mais longo de predição pela rede, do instante em que a disruptura ocorre, corresponde a $\tau_P = 2{,}52$ ms (63 interações). Para tempos mais longos (maior número de interações) a rede continua determinando o instante em que a disruptura menor ocorre, só que com um atraso temporal, como mostrado na Fig. 40d para 90 interações.

Examinando com mais detalhe o melhor resultado de previsão efetuado pela rede neural, para 63 interações (Fig. 40c), constata-se que os 15 pontos experimentais utilizados pela rede para realizar esta previsão, localizam-se na região oscilatória correspondente à penúltima flutuação dente de serra, em $t \approx 449{,}5$ ms. É interessante perceber que nesta região, para nossos olhos, não há qualquer evidência de alterações no comportamento do sinal de raios-X moles que pudessem indicar que uma disruptura já estaria sendo desencadeada. Somente após o término deste penúltimo dente de serra, quando uma intensa atividade MHD é

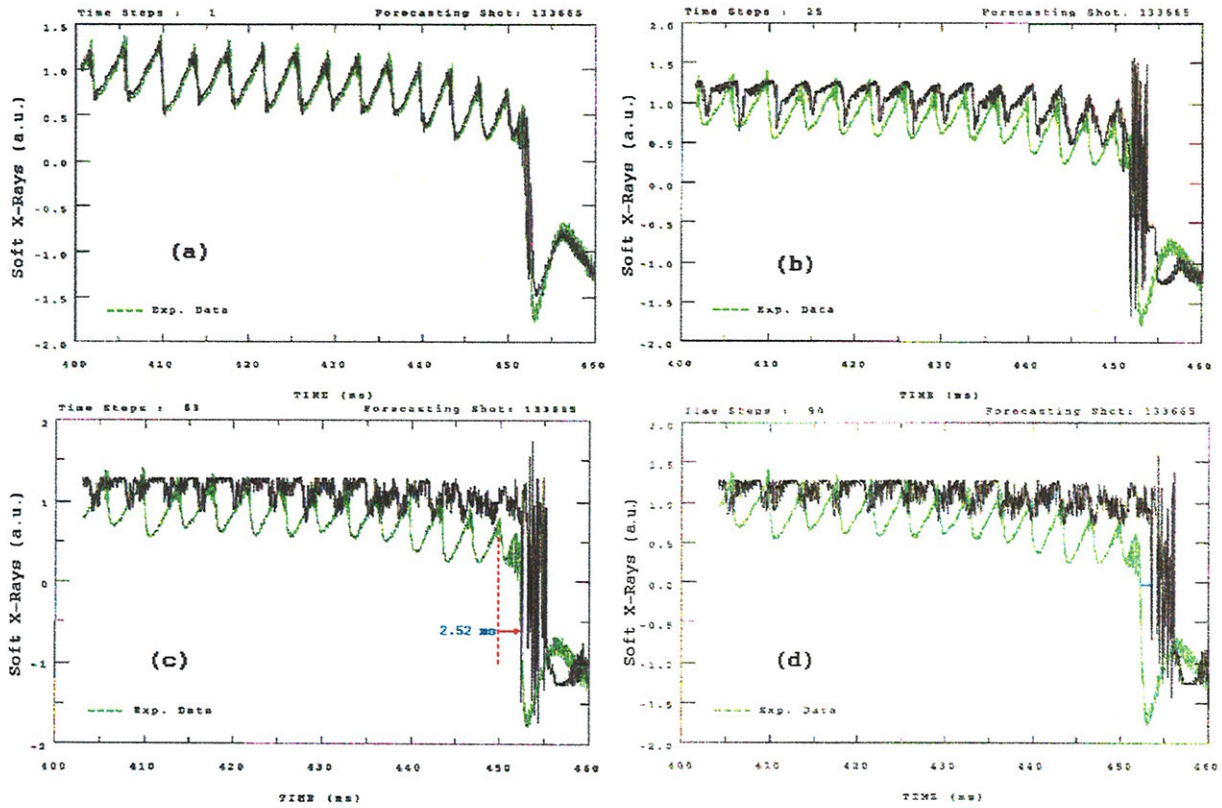

Fig. 40 - Resultados fornecidos pela rede neural para o pulso de plasma da Fig. 39. No seu melhor desempenho (c) a rede prevê o instante exato de ocorrência da disruptura com uma antecedência de 2,52 ms. Para tempos maiores (d) é observado um deslocamento temporal.

observada no sinal de raios-X, poderia alguém afirmar que uma disruptura estaria em desenvolvimento.

Posteriormente, como uma forma de testar o funcionamento da rede, o mesmo conjunto de pesos estatísticos utilizados pela rede para realizar as previsões da Fig. 40 foi utilizado no processo de previsão de disruptura para um outro pulso de plasma do TEXT (Fig. 41). Trata-se de uma descarga com corrente de plasma $I_P \approx 170$ kA que terminou em $t \approx 424$ ms. Para esta descarga, diferentemente dos outros pulsos de plasma utilizados para treinamento e validação, a disruptura maior não foi precedida pela ocorrência de uma disruptura menor.

Os resultados de previsão da disruptura fornecidos pela rede neural são mostrados na Fig.42. Novamente pode-se observar o pleno acordo existente entre os sinais da rede neural e o experimental para o caso de apenas uma interação, inclusive no instante exato de ocorrência da disruptura maior (Fig. 42a). Aumentando o número de interações, a rede consistentemente aponta antecipadamente o instante da disruptura até o intervalo de tempo $\tau_P = 3.12$ ms, correspondente a 78 interações (Fig. 42b). Este intervalo de tempo é praticamente o triplo daquele conseguido utilizando-se um sinal magnético de uma bobina de Mirnov para alimentar a rede neural. Para previsões realizadas em intervalos temporais maiores, novamente observa-se um deslocamento entre o instante da disruptura previsto pela rede e o experimentalmente

medido. Analisando-se com mais detalhe o melhor resultado da rede, para 78 interações (Fig.42b), observa-se que a rede neural, para efetuar esta previsão, utilizou novamente pontos experimentais localizados na penúltima flutuação dente de serra, correspondentes a t ≈ 420,6 ms.

Fazendo-se uma comparação entre os sinais de raios-X moles e da bobina magnética de Mirnov, correspondentes aos dois pulsos de plasma do TEXT utilizados para a previsão de disrupturas, Fig. 43 e Fig. 44 respectivamente, observa-se que os pontos experimentais dos sinais de raios-X que a rede utilizou nos dois casos para fazer as predições dos instantes em que as disrupturas iriam ocorrer, estão localizados no tempo em instantes anteriores ao crescimento em amplitude da atividade MHD. Este interessante comportamento sugere, talvez, que o desencadeamento das disrupturas analisadas não foi iniciado pela desestabilização do modo m = 2 que, fazendo as ilhas magnéticas localizadas na superfície magnética ressonante q = 2 crescerem, acaba por interferir com a ilha em q = 1. O processo provavelmente ocorreria de maneira inversa, isto é, alguma perturbação interferiria inicialmente com a região mais interna do plasma (visualizada pelo detetor central de raios-X moles) e só então a região do plasma nas proximidades da superfície q = 2 seria perturbada, desestabilizando o modo m = 2. Esta análise preliminar vai ao encontro de observações experimentais já publicadas as quais sugerem que as instabilidades de disruptura ocorrem devido ao deslocamento de uma bolha fria ("cold bubble") para a região central da coluna de plasma [96, 97]. No entanto, análises mais cuidadosas devem ser realizadas antes que alguma conclusão definitiva possa ser formulada.

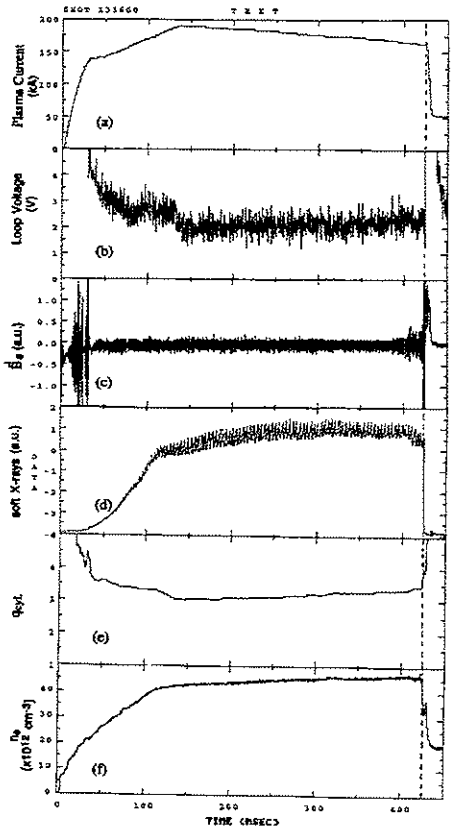

Fig. 41 - Pulso de plasma utilizado pela rede com os mesmos pesos estatísticos do caso anterior, só que agora a disruptura maior não foi precedida por uma menor.

Finalmente, um outro teste foi realizado com as redes neurais. Conforme mencionado anteriormente, os resultados de previsão de disrupturas acima apresentados foram obtidos utilizando-se somente os últimos 200 ms dos pulsos de plasma analisados. Quando tentou-se realizar a previsão utilizando os dados experimentais correspondentes à descarga toda, distorções bastante grandes foram obtidas quanto às formas dos sinais de raios-X fornecidos pela rede. Isto, no entanto, já era esperado uma vez que, na obtenção do conjunto de pesos estatísticos utilizado para as previsões, também foram utilizados somente os pontos correspondentes aos últimos 200 ms das descargas de treinamento e validação.

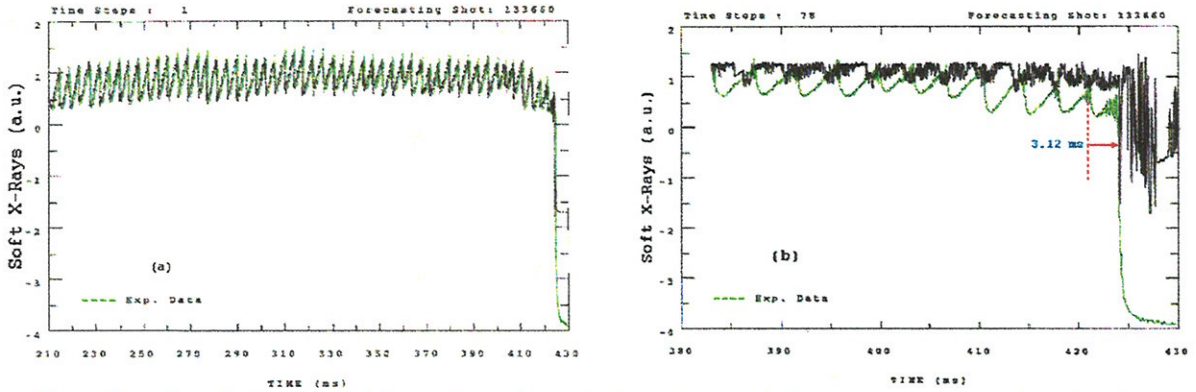

Fig. 42 - Resultados fornecidos pela rede neural, correspondentes ao segundo pulso de plasma analisado, para (a) uma única interação e (b) para 78 interações.

Assim, para realizar a previsão de disrupturas usando todos os pontos experimentais da descarga de plasma deve-se também, necessariamente, treinar a rede utilizando-se o mesmo intervalo para os pulsos de treinamento e validação. Isto foi efetivamente realizado. Para a obtenção do novo conjunto de pesos estatísticos, dois pulsos de plasma disruptivos foram utilizados para treinamento e um outro para a validação. Conforme mostrado na Fig. 45 o

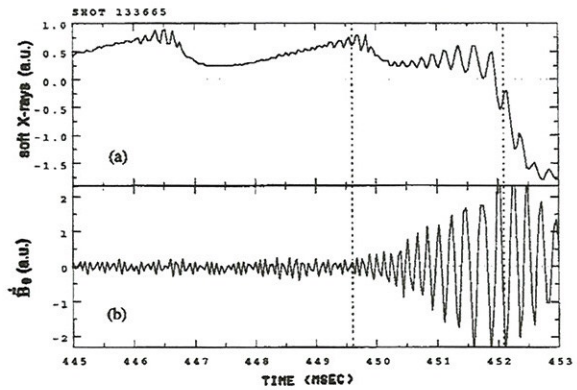

Fig. 43 - Sinais experimentais de raios-X moles e da bobina magnética de Mirnov do pulso de plasma da Fig. 39.

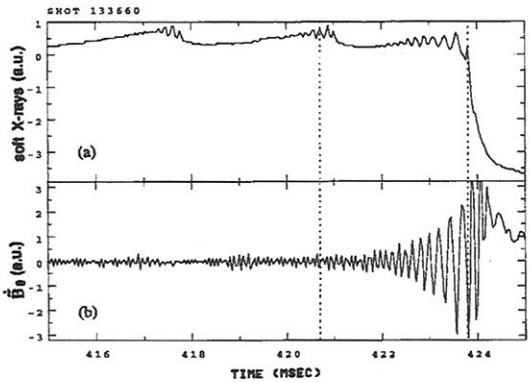

Fig. 44 - Sinais experimentais de raios-X moles e da bobina de Mirnov correspondente à descarga de plasma da Fig. 41.

resultado fornecido pela rede neural, correspondente a uma interação, reproduz fielmente o sinal experimental (Fig. 45a). Aumentando-se o número de interações obtêm-se, como melhor resultado, o diagrama da Fig. 45b correspondente a 13 interações. Pode-se observar na figura a existência de alguns picos espúrios que surgem no início do sinal produzido pela rede, além de fortes oscilações após a disruptura menor. No entanto, ainda assim a rede consegue determinar o instante exato de ocorrência da disruptura em $t \approx 454$ ms, conforme mostrado na Fig. 46. As previsões realizadas impondo um número maior de interações resultaram novamente em uma discrepância quanto ao instante da disruptura previsto pela rede e aquele medido medido experimentalmente. Este resultado de previsão obtido, de certa forma não tão bom quanto o mostrado anteriormente, indica apenas que a rede ainda não se encontra devidamente treinada.

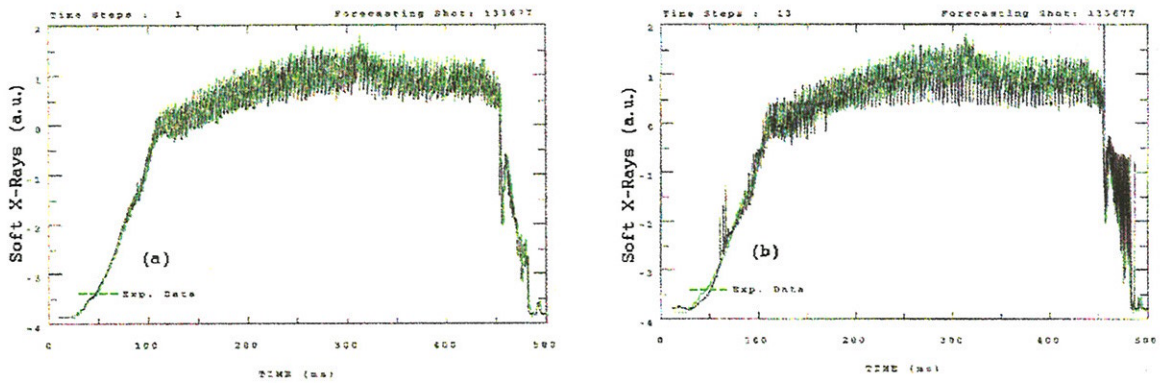

Fig. 45 - Utilizando dois pulsos de plasma disruptivos para treinar a rede, com todos os pontos da descarga, um novo conjunto de pesos estatísticos foi obtido com o qual a rede forneceu os resultados acima para (a) uma interação e (b) 13 interações.

Para isto, talvez seja necessário que se escolha uma arquitetura mais apropriada para a rede neural ou, até mesmo, se faça uso de uma quantidade maior de dados experimentais obtidos conjuntamente a partir de diferentes sistemas de diagnósticos.

De qualquer maneira, estes trabalhos realizados junto ao TEXT demostraram a viabilidade de se utilizar redes neurais para a previsão da ocorrência de instabilidades disruptivas em tokamaks. É importante observar que tokamaks de dimensões maiores que o TEXT possuem escalas de tempo maiores e, portanto, o intervalo de tempo de previsão de disrupturas fornecido por uma rede também deve ser conseqüentemente maior. Isto faz com que os resultados obtidos adquiram grande importância uma vez que abrem a possibilidade de construírem-se futuramente sistemas de realimentação baseados em redes neurais, para serem utilizados no controle do surgimento e desenvolvimento das instabilidades de disruptura durante o processo de confinamento do plasma.

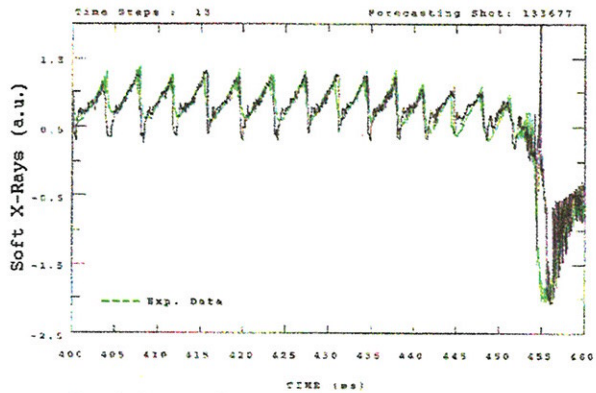

Fig. 46 - Sinal fornecido pela rede (para 13 interações) e sinal experimental correspondentes aos instantes finais da descarga mostrada na Fig. 45.

Capítulo 6

Conclusões

As instabilidades de disruptura maior que ocorrem em plasmas magneticamente confinados por tokamaks, por provocarem uma abrupta e completa destruição da coluna de plasma, constituem-se em um dos mais sérios obstáculos a ser vencido para o avanço efetivo das conquistas futuras na área de fusão termonuclear controlada. Desta forma, é de grande importância que esforços sejam despendidos no sentido de se conseguir alguma forma de controle sobre estas instabilidades e/ou de se entender os mecanismos físicos que levam ao seu desencadeamento.

No presente trabalho, foram apresentados e discutidos os resultados obtidos em três diferentes tokamaks: o TBR-1 do instituto de Física da USP, o JET da Comunidade Européia - Inglaterra e o TEXT da Universidade do Texas - EUA. Nesses estudos foi investigada a origem da disruptura maior e algumas possíveis formas de se obter o seu controle.

Apesar dos tokamaks investigados possuírem características e dimensões muito diferentes entre si, pode-se constatar, em todos eles, que o acoplamento entre os modos MHD $m = 2$ e $m = 1$ mostra-se como o maior responsável pela ocorrência das disrupturas analisadas. A identificação do acoplamento entre estes modos pode ser realizada analisando-se conjuntamente os sinais de raios-X de baixas energias e as oscilações magnéticas de Mirnov, nos instantes que antecedem a ocorrência da disruptura maior. É claramente observado um crescimento exponencial da amplitude da componente $m = 2$ ao mesmo tempo em que o formato das flutuações dentes de serra modifica-se, dando vez a um sinal senoidal (algumas vezes saturado) com freqüência idêntica às das oscilações de Mirnov.

O cálculo da taxa de crescimento dos modos, realizado nos três tokamaks, indicou que os modos MHD precursores possuíam um caráter resistivo, sugerindo a existência de ilhas

magnéticas no plasma. O crescimento das ilhas associadas ao modo m = 2, em particular, pode ser diretamente identificado, no tokamak TEXT-U, através de um sistema de deteção de modos travados que foi por nós projetado e construído. Em alguns pulsos de plasma disruptivos, observou-se que as oscilações características nos sinais de Mirnov e nos de raios-X moles cessavam durante os instantes que antecediam a disruptura maior, indicando uma ocorrência do fenômeno de modos travados. No entanto, análises mais detalhadas mostraram que as ilhas magnéticas não paravam completamente, como se poderia pensar, mas continuavam a girar na direção toroidal, só que com uma freqüência bem baixa, da ordem de 50 Hz.

No tokamak TBR-1, estudos também foram realizados com o objetivo de analisar a atuação de campos magnéticos externos de perturbação sobre o plasma confinado, como uma forma de controle do surgimento das disrupturas maiores. Estes campos foram criados de duas maneiras diferentes: 1°) através de malhas condutoras enroladas helicoidalmente ao redor da câmara de vácuo do tokamak (CHR) e 2°) através de um limitador ergódico magnético (LEM). Em ambos os casos foi possível identificar experimentalmente uma forte atenuação produzida na atividade MHD durante os instantes em que os campos externos eram aplicados. Em alguns casos foi possível, inclusive, verificar o pronto restabelecimento da amplitude original da atividade MHD, assim que os campos magnéticos externos foram desligados.

Finalmente, utilizando-se dados experimentais do tokamak TEXT, redes neurais foram empregadas no processo de previsão dos instantes de ocorrência das instabilidades de disruptura. A idéia básica é de que, caso as ocorrências das disrupturas possam ser previstas antecipadamente, em um intervalo de tempo suficientemente grande, sistemas defensivos talvez possam ser acionados com o objetivo de se tentar abortar a disruptura eminente ou, pelo menos, atenuar seus efeitos nocivos. Em uma primeira tentativa, sinais da derivada temporal do campo magnético poloidal de perturbação foram empregados na rede neural. Foi então possível constatar o bom desempenho da rede neural, que demonstrou ser capaz de prever a ocorrência de disrupturas, com razoável precisão, com uma antecedência de até 1,12 ms.

Em um trabalho mais recente, porém, resultados muito melhores que estes foram obtidos alimentando-se a rede neural com sinais de raios-X de baixas energias provenientes da região central da coluna de plasma. Neste caso, as disrupturas puderam ser previstas com uma antecedência de até 3,12 ms, o que corresponde a um intervalo de tempo quase três vezes maior que o obtido anteriormente. Comparações envolvendo os sinais de Mirnov e de raios-X moles, quanto a localização dos pontos experimentais utilizados pela rede para efetuar a previsão de disrupturas, mostraram que o processo disruptivo não se iniciaria na região do plasma onde localiza-se a superfície magnética correspondente a q = 2. Os resultados obtidos sugerem, contrariamente ao pensamento corrente, que a disruptura teria inicio na região central da coluna de plasma e só depois a parte mais externa seria afetada.

Como uma continuação natural deste trabalho sobre as instabilidades de disruptura em tokamaks, que já vem sendo desenvolvido por nós há vários anos, pretende-se investigar mais profundamente o uso de redes neurais no processo de previsão de disrupturas, de forma a tentar melhorar ainda mais os resultados até agora obtidos. Isto deverá ser feito testando-se redes neurais com outras arquiteturas e, principalmente, introduzindo-se concomitantemente na rede neural sinais experimentais de diferentes diagnósticos. Espera-se, inclusive, que uma parte deste trabalho possa ser realizado, em futuro bem próximo, utilizando-se sinais experimentais obtidos junto ao tokamak TCA/BR do Laboratório de Física de Plasmas do Instituto de Física da USP. Em seguida, pretende-se desenvolver um sistema de realimentação de injeção de "pellets", com acionamento monitorado por redes neurais em tempo real, para tentar estabelecer algum controle sobre o desencadeamento e/ou desenvolvimento das instabilidades de disruptura maior.

Com respeito aos mecanismos físicos envolvidos que dão início ao surgimento das disrupturas maiores, pretende-se ainda, futuramente, investigar os pulsos de plasma de tokamaks com baixa razão de aspecto. O grande interesse despertado quanto a este tipo de geometria específica advém do fato de já existirem evidências experimentais de que este tipo de máquina possui a capacidade natural de impedir o surgimento destas disrupturas durante o confinamento do plasma. Uma avaliação mais fundamentada quanto a este comportamento ser ou não universal (isto é, valer tanto para pequenos quanto para grandes tokamaks), poderá ser feita em futuro não muito distante, quando várias máquinas deste tipo que encontram-se em construção, como o tokamak MAST da Inglaterra e o tokamak ETE do INPE, por exemplo, entrarem em funcionamento.

Bibliografia

[1] - ORNSTEIN L.T.M. - Trans. of Fusion Technol. **25** (1994) 7.

[2] - FIDDLER N.F., NASCIMENTO I.C. - Ciência Hoje **7** (1988) 44.

[3] - Internet - "*http://ep.llnl.gov/informal_science/fusion/red3.html*".

[4] - WEYNANTS R.R. - Trans. of Fusion Technol. **25** (1994) 19.

[5] - PAISNER J.A., CAMPBELL E.M., HOGAN W.J. - Fusion Technol. **26** (1994) 755.

[6] - Internet - "*http://ishmael.nmh.northfield.ma.us/~eric/fusion/IC.html*".

[7] - LASHE G.P. - The Phys. Teacher (1981) 234.

[8] - Internet - "*http://www.cnie.org/nle/eng-22.html*".

[9] - BELL M.G., McGUIRE K.M., ARUNASALAM V., et al. - Nucl. Fusion **35** (1995) 1429.

[10] - Internet - "*http://www.pppl.gov/oview/pages/TFTR_MajorAccomp.html*".

[11] - REBUT P.H. - Trans. Fusion Technol. **27** (1995) 3.

[12] - Internet - "*http://iter.ucsd.edu*".

[13] - WESSON J. - Phys. Rev. Lett. **44** (1980) 1215.

[14] - WESTERHOF E. - Trans. of Fusion Technol. **25** (1994) 152.

[15] - NOLL P., SONNERUP L., FROGER C., et al. - Fusion Technol. **15** (1989) 259.

[16] - GRUBER O., LACKNER K., PAUTASSO G., et al. - Plasma Phys. and Control. Fusion **35** (1993) B191.

[17] - VERSHKOV V.A., MIRNOV S.V. - Nucl.Fusion **14** (1974) 383.

[18] - GIBSON A. - Nucl. Fusion **16** (1976) 546.

[19] - HICKS H.R., HOLMES J.A., CARRERAS B.A., et al. - Proc. 8th IAEA Int. Conf. On Plasma Phys. and Contr. Nuclear Fusion Res., Brussels (1981) 259.

[20] - DIAMOND P.H. - Phys. Fluids **27** (1984) 1449.

[21] - STABLER A., McCORNICK K., MERTENS V., et al. - Nucl. Fusion. **32** (1992) 1557.

[22] - BROWER D.L., YU C.X., BRAVENEC R.V., et al. - Phys. Rev. Lett. **67** (1991) 200.

[23] - KARGER F., LACKNER K., FUSSMAN G., et al. - Plasma Phys. Contr. Nucl. Fusion Res. (Proc. 6th IAEA Int. Conf., Berchtesgarden, 1976) Vol. **1** (1977) 267.

[24] - ROBERTS D.E., De VILLIERS J.A.M., FLETCHER J.D., et al. - Nucl. Fusion. **26** (1986) 785.

[25] - McGUIRE K.M., ROBINSON D.C. - Phys. Rev. Lett. **44** (1980) 1666.

[26] - PIETRZYK Z.A., POCHELON A., BEHR R., et al. - Nucl. Fusion. **32** (1992) 1735.

[27] - TSUJI S., NAGAYAMA Y., MIYAMOTO K., et al. - Nucl. Fusion. **25** (1985) 305.

[28] - VANNUCCI A., NASCIMENTO I.C., CALDAS I.L. - Plasma Phys. Contr. Fusion. **31** (1989)147.

[29] - VANNUCCI A. , GILL, R.D. - Nucl. Fusion. **31** (1991) 1127.

[30] - VANNUCCI A., McCOOL S.C. - Nucl. Fusion **37** (1997) 1229.

[31] - BATEMAN G. - "*MHD Instabilities*", MIT Press (1978).

[32] - WESSON J. - "*Tokamaks*", Clarendon Press - Oxford (1987).

[33] - CALDAS I.L., VANNUCCI A. - "*Equilíbrio e Instabilidades do Plasma em Tokamaks*", Report IFUSP/P-523 (1985).

[34] - CALDAS I.L., TASSO H. - Plasma Phys. **20** (1978) 1299.

[35] - COPPI B., GALVÃO R.M.O., PELLAT R., et al. - Sov. Journ. Plasma Phys. **2** (1976) 533.

[36] - ROSENBLUTH M.N., RUTHERFORD P.H. - "*Tokamak Plasma Stability*", Fusion, vol.**1** - part A, Academic Press (1981).

[37] - WESSON J. - Nucl. Fusion **18** (1978) 87.

[38] - RUTHERFORD P.H. - "*Tearing Modes in Tokamaks*" - Proc. Int. School ofPlasma Phys., Varena - Itália (1979) 129.

[39] - RUTHERFORD P.H. - Phys. Fluids **16** (1973) 1903.

[40] - FINN J.M. - Nucl. Fusion **15** (1975) 845.

[41] - FERNANDES A.S., HELLER M.V.A.P., CALDAS I.L. - Plasma Phys. Control. Fusion **30** (1988) 1203.

[42] - ITOH K., ITOH S.I. - Nucl. Fusion **32** (1992) 1851.

[43] - FITZPATRICK R., HASTIE R.J., MARTIN T.J., ROACH C.M. - Nucl. Fusion **33** (1993) 1533.

[44] - REIMAN A., MONTICELLO D. - Phys. Fluids B **3** (1991) 2230.

[45] - YOKOYAMA M., CALLEN J.D., HEGNA C.C. - Nucl. Fusion **36** (1996) 1307.

[46] - PERSSON M., BONDESON A. - Nucl. Fusion **29** (1989) 989.

[47] - NAVE M.F.F., WESSON J.A. - Nucl. Fusion **30** (1990) 2575.

[48] - FISHPOOL G.M., HAYNES P.S. - Nucl. Fusion **34** (1994) 109.

[49] - La HAYE R.J., HYATT A.W., SCOVILLE J.T. - Nucl. Fusion **32** (1992) 2119.

[50] - SNIPES J.A., CAMPBELL D.J., HAYNES P.S., HENDER T.C., et al. - Nucl. Fusion **28** (1988) 1085.

[51] - FITZPATRICK R. - Nucl. Fusion **33** (1993) 1049.

[52] - FITZPATRICK R., HENDER T.C. - Phys. Fluids B **3** (1991) 2230.

[53] - WESSON J.A., GILL R.D., HUGON M., et al. - Nucl. Fusion **29** (1989) 641.

[54] - KADOMTSEV B.B. - Plasma Phys. Control. Fusion **26** (1984) 217.

[55] - PAUTASSO G., BÜCHL K., FUCHS J.C., et al. - Nucl. Fusion **36** (1996) 1291.

[56] - TAN I.H., CALDAS I.L., NASCIMENTO I.C., et al. - IEEE Trans. Plasma Sci. **PS-14** (1986) 279.

[57] - HUTCHINSON I.H. - Phys. Rev. Lett. **37** (1976) 338.

[58] - SAUTHOFF N.R.. Von GOELER S., STODIEK W. - Nucl. Fusion **18** (1978) 1445.

[59] - JACOBSEN R.A. - Plasma Phys. **17** (1975) 547.

[60] - SAVRUKHIN P.V., LYADINA E.S., MARTYNOV D.A., et al. - Nucl. Fusion **34** (1994) 317.

[61] - HOWARD J., PERSSON M. - Nucl. Fusion **32** (1992) 361.

[62] - BONDESON A., PARKER R.D., et al. - Nucl. Fusion **31** (1991) 1695.

[63] - MIRNOV S.V. - Nucl. Fusion **9** (1969) 57.

[64] - FRANCO H., RIBEIRO C., SILVA R.P., et al. - Rev. Sci. Instrum. **63** (1992) 3710.

[65] - DOSE V., VENUS G., ZOHM H. - Phys. Plasmas **4** (1997) 323.

[66] - Von GOELER S., STODIEK W., EUBANK H. et al. - Nucl. Fusion **15** (1975) 301.

[67] - MICHELIS C., MATTIOLI M. - Nucl. Fusion **21** (1981) 677.

[68] - Von GOELER S. - "*Diagnostics for Fusion Experiments*", Pergamon Press, N.Y. (1979) 79.

[69] - Equipe TFR - Nucl. Fusion **17** (1977) 213.

[70] - VANNUCCI A., NASCIMENTO I.C., OLIVEIRA I.C., et al. - Nucl. Instr. Meth. in Phys. Res. **A280** (1989) 593.

[71] - Von GOELER S., STODIEK W., SAUTHOFF N., et al.- Phys. Rev. Lett. **33** (1974) 1201.

[72] - KADOMTSEV B.B. - Sov. Journ. Plasma Phys. **1** (1975) 389.

[73] - GREEWALD M., TERRY J.L., WOLFE S.M., et al - Nucl. Fusion. **28** (1988) 2199.

[74] - YOSHINO R., et al. - Journal of Plasma and Fusion Res. **70** (1994) 1081.

[75] - KARGER F., LACKNER K., FUSSMAN G., et al. - Plasma Phys. Contr. Nucl. Fusion Research (Proc. 5th IAEA Int. Conf., Tokio, 1973) Vol. **1** (1974) 207.

[76] - VANNUCCI A., BENDER O.W., CALDAS I.L., NASCIMENTO I.C., et al. - Il Nuovo Cimento, vol. **10D** (1988) 1193.

[77] - ARAUJO M.S.T., VANNUCCI A., CALDAS I.L. - Il Nuovo Cimento **18D** (1996) 807.

[78] - ARAUJO M.S.T., VANNUCCI A., OLIVEIRA K.A., CALDAS I.L. - referente ao trabalho de tese de doutorado do Sr. M.S.T. Araújo, a ser submetido para publicação na revista *Physics of Plasmas*.

[79] - VALLET J.C., POUTCHY M.S., et al. - Phys. Rev. Lett. **67** (1991) 2662.

[80] - HENDER T.C., FITZPATRICK R., MORRIS A.W., et al. - Nucl. Fusion **32** (1992) 2091.

[81] - CHEN J., XIE J., HUO Y., et al. - Nucl. Fusion **30** (1990) 2271.

[82] - YOSHINO R., NEYATANI Y., HOSOGANE N., et al. - Nucl. Fusion **33** (1993) 1599.

[83] - KISLOV D.A., ALIKAEV V.V., ESIPCHUK Yu.V., et al. - Nucl. Fusion **37** (1997) 339.

[84] - HERNANDEZ J.V., VANNUCCI A., TAJIMA T., et al. - Nucl. Fusion **36** (1996) 1009.

[85] - VANNUCCI A., OLIVEIRA K.A., TAJIMA T. - submetido para publicação na revista *Nuclear Fusion*.

[86] - OHYABU N., de GRASSIE J.S., BROOKS N.H., et al. - Nucl. Fusion **25** (1985) 1684.

[87] - TAKAMURA S., OHNISHI N., YAMADA H., OKUDA T. - Phys. Fluids **30** (1987) 144.

[88] - McCOOL S.C., WOOTTON A.J., AYDEMIR A.Y., et al. - Nucl. Fusion **29** (1989) 547.

[89] - YAMADA H., YOSHIDA Z., INQUE N., UCHIDA T. - Jap. Journal Appl. Physics **23** (1984) 1107.

[90] - BRETON C., De MICHELIS C., MATTIOLI M., et al. - Nucl. Fusion **31** (1991) 1774.

[91] - HINTON, G. - Scientific American **Sept.** (1992) 145.

[92] - HERTZ J., KROGH A., PALMER R.G. - "*Introduction to Theory of Neural Computation*", Addison - Wesley, Reading, MA (1991).

[93] - REILLY D., COOPER L. - "*An Introduction to Neural and Electronic Networks*", Academic Press Inc. (1990) cap. 11.

[94] - EKMAN J.P., RUELLE D. - Rev. Mod. Phys. **57** (1985) 617.

[95] - RUMELHART D.E., HINTON G.E., WILLIAMS R.J. - Nature **323** (1986) 533.

Apêndice 1

Artigo publicado sobre a investigação das instabilidades de disruptura no tokamak TBR-1

Plasma Physics and Controlled Fusion, Vol. 31, No. 2, pp. 147 to 156, 1989
Printed in Great Britain.

0741-3335/89 $3.00 + .00
IOP Publishing Ltd. and Pergamon Press plc

DISRUPTIVE INSTABILITIES IN THE DISCHARGES OF THE TBR-1 SMALL TOKAMAK*

A. VANNUCCI, I. C. NASCIMENTO and I. L. CALDAS
Instituto de Fisica, Universidade de Sao Paulo, C.P. 20.516, 01498 Sao Paulo, SP, Brazil

(*Received* 14 *July* 1988)

Abstract—Minor and major disruptions as well as sawteeth oscillations (internal disruptions) were identified in the discharges of the small Tokamak TBR-1, and their main characteristics were investigated. The coupling of a growing $m = 2$ resistive mode with an $m = 1$ perturbation seems to be the basic process for the development of a major disruption, while the minor disruption could be associated with the growth of a stochastic region of the plasma between the $q = 2$ and $q = 3$ islands. Measured sawteeth periods were compared with those predicted by scaling laws and good agreement was found. The time necessary for the sawteeth crashes also agrees with the values expected from KADOMTSEV's model. However, there are some sawteeth oscillations, corresponding to conditions of higher plasma Z_{eff}, which showed longer crashes and could not be explained by this model.

1. INTRODUCTION

ENERGY DISSIPATION and the complete loss of confinement of the plasma are the most harmful characteristics of disruptive instabilities, which are usually classified as internal (sawteeth) and external (minor and major), accordingly to their global features. In spite of the intensive efforts expended since the last decade, the mechanisms that lead to any one of these disruptions are far from being well understood.

The sawteeth oscillations, having been discovered by VON GOELER *et al.* (VON GOELER *et al.*, 1974) were, in many aspects, explained by KADOMTSEV's model (KADOMTSEV, 1975), which was further supported by numerical simulations (WADDELL *et al.*, 1976; SYKES and WESSON, 1976) and even by experimental observations (JAHNS *et al.*, 1978). Later on, experimental evidence was pointed out which no longer supported this model. This evidence involved, for example, the detection of internal disruptions without any precursor oscillation and the $m/n = 1/1$ mode only after the sawtooth crash (CAMPBELL *et al.*, 1986), the appearance of "giant" and "monster" sawteeth (CAMPBELL *et al.*, 1987) and, more recently, the evidence that $q(0)$ remains below unity throughout the sawtooth phenomenon (WEST *et al.*, 1987). Although alternative theories were formulated (DUBOIS *et al.*, 1983; WESSON, 1986), the exact phenomenological mechanism that leads to an internal disruption is not completely known.

The external disruptive instabilities, called minor and major disruptions depending on the intensity with which they disturb the plasma column (MIRNOV, 1979), have also been intensively investigated. Their main characteristics are: negative spikes in the loop voltage signal, rapid loss of confined energy, and sudden expansion of the minor radius with a diminution of the major radius. It is furthermore typically verified

* This paper is an expanded version of material which originally was a contributed presentation at the 15th EPS Plasma Physics Division Conference, Cavtat, Yugoslavia, May 1988.

that there is an intense MHD activity with a frequency decrease and a fast (sometimes explosive) growth in amplitude, associated with the occurrence of an external disruption.

The major disruption, since it naturally leads to the complete destruction of the plasma confinement, is the one which deserves more attention. Knowledge of the processes through which a major disruption is created (so that controlling mechanisms can therefore be developed) is very important for the reliability of future fusion reactors.

Several explanations have already been proposed to clarify the external disruption occurrence; almost all of them involving the $m/n = 2/1$ amplitude increase as the main factor responsible for the disruption. The interaction of the $q = 2$ islands with the limiter, the coupling between the $m/n = 2/1$ and $m/n = 1/1$ modes (KARGER *et al.*, 1976) and the destabiliziation of odd m-value modes such as $m/n = 3/2$, 5/3, etc. by the growing $q = 2$ islands (WADDELL *et al.*, 1978) are some of the more accepted mechanisms for the development of a major disruption. The minor disruption, on the other hand, could be explained by considering the existence of secondary magnetic islands between the principal islands. The superposition of these small islands would create an ergodic region inside the plasma. As the perturbation grows, the ergodic region becomes larger until the whole system is affected and the collapse occurs (FINN, 1975; RECHESTER and STIX, 1976).

Experimental evidence has already been reported, supporting each one of these models. While the presence of $m/n = 2/1$, 3/2 and 5/3 modes was detected right before a major disruption event (MCGUIRE and ROBINSON, 1980), in other experiments the interaction of $q = 2$ islands with the limiter (ROBERTS *et al.*, 1986) and the coupling of the $m/n = 2/1$ and 1/1 modes (EQUIPE TFR, 1977) were clearly identified. On the other hand, it was also observed that the perturbation which leads to a major disruption begins between the $q = 1$ and $q = 2$ magnetic surfaces (HUTCHINSON, 1976); this would therefore be favourable to the magnetic lines braiding model.

Since the present knowledge about the disruptive phenomena is still inconclusive in many aspects, it seems that any further contribution to this "status-quo" would be welcome. Considering this point of view, the plasma disruptions in the small size and low β TBR-1 discharges were therefore investigated and reported here.

2. EXPERIMENTAL SET-UP AND MEASUREMENTS

The TBR-1 basic parameters are: $R_0 = 0.30$ m, $a = 0.08$ m, $B_\phi \sim 0.4$ T, $T_e \sim 200$ eV, $6 \leqslant I_p \leqslant 12$ kA and discharge duration ranging up to 7 ms. The two main diagnostics used in this work were a soft x-ray detection system and a set of 20 Mirnov coils. The soft x-ray flux from the plasma was measured by an array of six surface barrier detectors (ORTEC model CR 019-50-100) placed inside an imaging camera. Each detector viewed a different plasma volume through a solid angle delimited by a polypropilene covered slot. The output signals, after having been properly amplified, were digitalized and recorded through a PC-microcomputer.

The poloidal magnetic field perturbation was measured by 16 pick-up coils equally spaced in the poloidal direction and four in the toroidal direction. All these coils were positioned inside the toroidal camera to avoid field attenuation by the wall of the vessel (TAN *et al.*, 1986).

We consider now each type of disruption investigated, internal and external (minor and major), and present and analyse the experimental results obtained separately.

2.1. *Internal disruption*

Operating the TBR-1 device with high plasma current ($I_p \sim 12$ kA) and $3.0 \lesssim q(a) \lesssim 3.5$, the presence of sawteeth events was identified in $\lesssim 10\%$ of the discharges. A typical example is shown in Fig. 1b. The period and amplitude of the sawteeth are seen to change slightly with time. The average frequency is about 7.5 kHz and no transients were verified in the loop voltage signal (Fig. 1c) during the sawteeth activity. It was also observed that they show the expected $m = 1$ oscillation superimposed on them.

Temporal expansion of soft x-ray and magnetic pick-up coil signals of this discharge are shown in Fig. 2. An inverted sawtooth is observed (Fig. 2b) for each sawtooth crash (Fig. 2a). Observing, furthermore, the pick-up coils' signals, a fast increase in amplitude of the perturbed poloidal magnetic field associated with the sawteeth crashes is usually seen (Fig. 2c). This would be related to the energy transport from the inner to the outer region of the $q = 1$ magnetic surface.

In respect to the superimposed $m/n = 1/1$ oscillations it was indeed verified, many times, that their amplitudes increased just before the sawteeth crashes. This could suggest that the $q = 1$ growing magnetic island would be responsible for the internal disruptions' development through the reconnective field lines model. However, examples in which the amplitude did not exhibit any growth at all were observed more often. In some cases even an intensity decrease was verified. These aspects are well exemplified in Fig. 3, where some sawteeth events from three different discharges are grouped. The average growth rate of the oscillations denoted by (*) is $2.6 \times 10^4\ s^{-1}$.

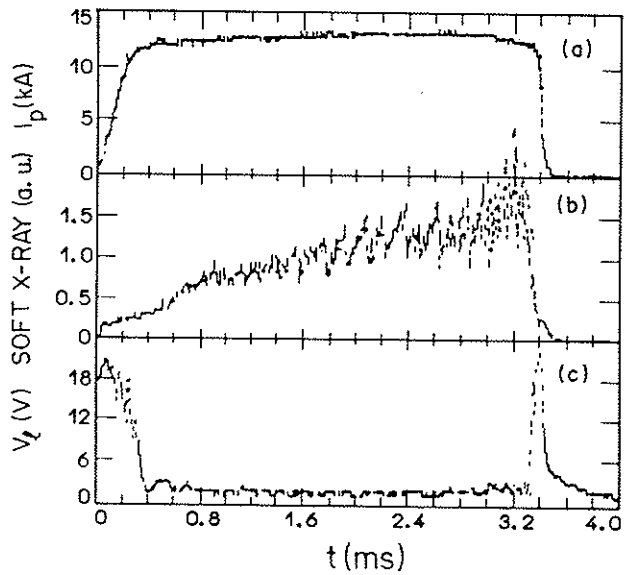

FIG. 1. Plasma current (a), soft x-ray signal (central chord) showing sawteeth oscillations (b) and loop voltage (c) in a typical TBR-1 discharge.

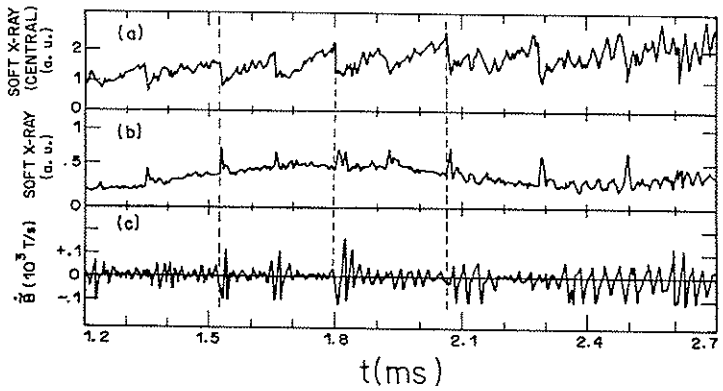

FIG. 2.—X-rays and MHD activity signals in expanded time scale corresponding to the discharge shown in Fig. 1. No increase in the MHD activity prior to each sawtooth crash is observed.

Another interesting experimental feature is related to the observation of a sawtooth relaxation, occurring always more to the end of the discharges. This was usually accompanied by a stronger and saturated MHD activity. In Fig. 4, where the central soft x-ray and perturbed magnetic field signals are temporarily expanded, this aspect can be better evaluated.

The average time for the sawteeth crashes, in several discharges, was measured in the interval 13 μs $\leqslant \tau_c \leqslant$ 26 μs. However, when the sawteeth were preceded by minor disruptions, which deteriorated the confinement and increased the plasma's Z_{eff}, the crashes no longer showed a rapid and sharp decay as in Figs 3a and 3b. Now, the decay times almost increased 3-fold and $m/n = 1/1$ oscillations were detected during this period (Fig. 3c).

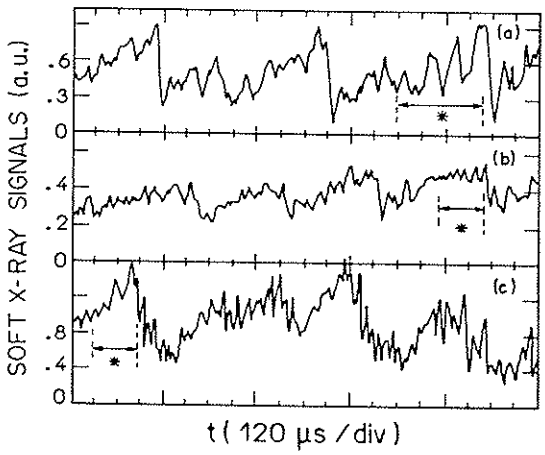

FIG. 3. Examples of sawteeth fluctuation from three different discharges. The $m/n = 1/1$ oscillation amplitude does not always increase in a sawtooth period. The crashes are longer for discharges with high Z_{eff} (c). The events designated by (*) had their growth rate measured to be 2.6×10^4 s^{-1}, on average.

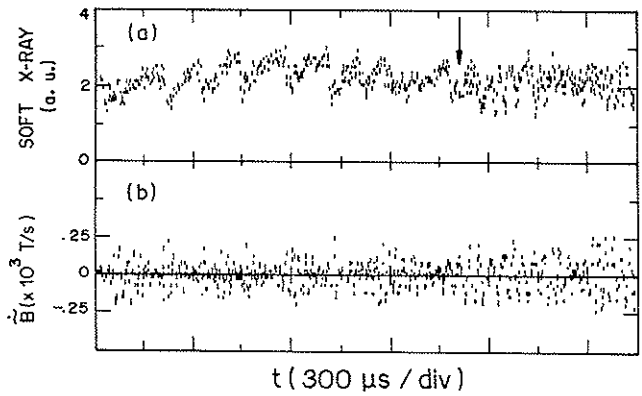

FIG. 4.—Soft x-ray (a) and MHD activity (b) temporal evolution. The arrow indicates the beginning of the sawteeth relaxation giving place to a strong $m/n = 1/1$ oscillation, accompanied by a saturated MHD oscillation.

Concerning the sawteeth periods, the experimental values obtained ranged from 100 to 170 μs. We did not notice any influence of the plasma's Z_{eff} on this parameter.

2.2 *Minor disruption*

This type of disruptive instability was very commonly observed in the TBR-1 Tokamak. In Fig. 5 we observe a sequence of minor disruptions all along the discharge. The negative spikes in the loop voltage show the exact instants each disruption took place. The slow rises and fast decays in the soft x-ray signals (Fig. 5c) are similar and simultaneous for all detectors. The MHD activity (Fig. 5e) exhibit a fast growth in amplitude prior to the negative spikes (Fig. 5d). The plasma current and column position also exhibit slight discontinuities in their signals (Figs 5a and 5b, respectively), suggesting a rather agitated and unstable plasma.

Different initial field adjustments lead to other equilibrium conditions which usually make the discharges longer and minor disruptions are therefore identified only at the beginning. Figure 6, for example, shows a discharge in which minor disruptions are followed by sawteeth fluctuations.

Fourier analysis indicated that the dominant $m/n = 2/1$ and $3/1$ modes are the dominant precursor modes associated with the minor disruptions. The average MHD growth rate was $5 \times 10^4\ s^{-1}$ and $\tilde{B}_\theta/B_\theta \sim 2\%$, typically.

Taking the measured perturbation amplitude, corresponding to the $m = 2$ and $m = 3$ modes of a particular minor disruption event, and calculating the locations and half-widths of the magnetic islands, the corresponding stochasticity parameter S clearly indicated an overlapping between them. The associated Poincaré maps for the field lines' distribution were obtained by integrating the magnetic field line equations determined by FERNANDES *et al.* (1988). The resulting diagrams for two different times, 50 μs before and at the exact instant of the negative spike appearance in the loop voltage, are shown in Figs 7a and 7b, respectively. In this example the disruption took place while the plasma column was centered.

2.3. *Major disruption*

The major disruptions in TBR-1 discharges with $3.0 \leqslant q(a) \leqslant 4.0$ are usually characterized by a noticeable growing precursor activity, a negative spike in the loop

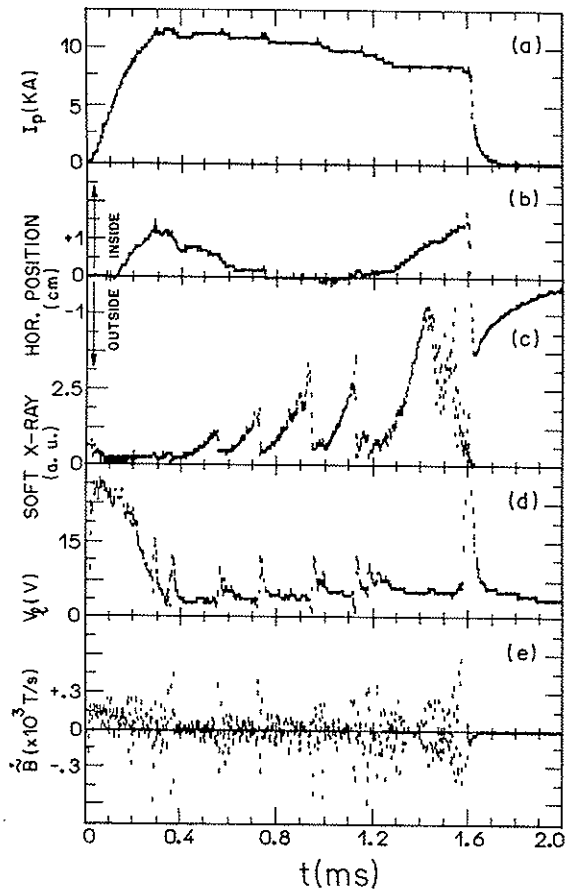

FIG. 5.—Plasma current (a), horizontal position (b), soft x-ray emission (c), loop voltage (d) and MHD activity (e) evolution during a discharge in which successive minor disruptions occurred.

voltage signal and a small displacement of the plasma column towards the inner part of the torus. The duration of the major disruptive events detected was $\tau_D \sim 200$ μs, typically.

The perturbed poloidal field ratio, right before the appearance of the negative spike, was $\tilde{B}_\theta/B_\theta \sim 4\%$ and the precursor oscillation growth rate ranged from 1.4×10^3 to 8.9×10^4 s^{-1}. Fourier analysing the MHD signals it was observed that the $m/n = 2/1$ was always the dominant and responsible mode for the major disruptions observed.

Calculations regarding the $q = 2$ resonant magnetic surface localization and the half-width of its corresponding islands (FERNANDES *et al.*, 1988) showed that there was no possibility of an island–limiter interaction. On the other hand, the coupling of the $m/n = 2/1$ and $1/1$ modes could be a realistic mechanism through which the disruption could occur. This interpretation is based upon the observation of the soft x-ray and MHD signals in Figs. 8a and 8b, respectively. The frequencies of these two modes change and finally assume the same values right before the occurrence of the negative spike in the loop voltage (Fig. 8c), indicating an interaction between them.

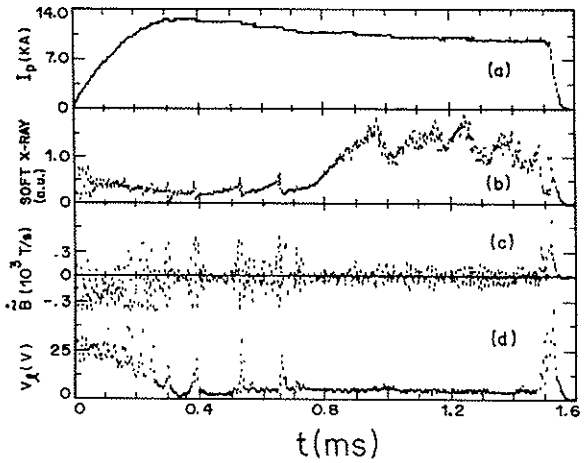

FIG. 6.—Minor disruptions are initially observed but afterwards the equilibrium conditions change and sawteeth fluctuations are then identified.

In other discharges again the $m/n = 1/1$ and $2/1$ modes assume the same frequencies before a major disruption, as shown in Fig. 9, but now there is no amplitude growth of the $m/n = 1/1$ mode (Fig. 9b). This behaviour strengthens the idea that the $q = 2$ islands are, in fact, those most responsible for the major disruptions.

Another interesting aspect concerning some TBR-1 discharges is the interaction between the plasma column and the wall (or limiter) of the vessel, due to the lack of feedback control. If the plasma column moves towards the inner part of the toroidal chamber, the interaction simply annihilated the confinement. The time-lag between the interaction and the complete destruction of the plasma is on average about 100 μs. This value is one half of the plasma destruction time in a major disruption, indicating that the former is an even more violent phenomenon than the latter. The absence of negative spikes in the loop voltage and a lack of MHD growing modes prior to the plasma–limiter interaction are other observed characteristics of the end of this type of discharge.

On the other hand, when the interaction happens in the outer side of the vessel, the confinement is not lost. A fast plasma cooling is verified through the soft x-ray emission and the loop voltage is strongly affected by the event. Afterwards, an increase of the plasma temperature accompanied by strong $m/n = 1/1$ oscillations or even sawteeth fluctuations is usually observed.

3. DISCUSSION AND CONCLUSIONS

The data presented in this paper show that even a small-scale device like the TBR-1 exhibits similar behaviour to larger-sized Tokamaks, as far as disruptive instabilities are concerned.

The experimental values obtained for the sawteeth periods (100–170 μs) were compared with those expected from scaling laws. Reasonable agreement was achieved by using the expressions from McGUIRE and ROBINSON (1980) and KADOMTSEV (1984), which gave 87 and 210 μs, respectively.

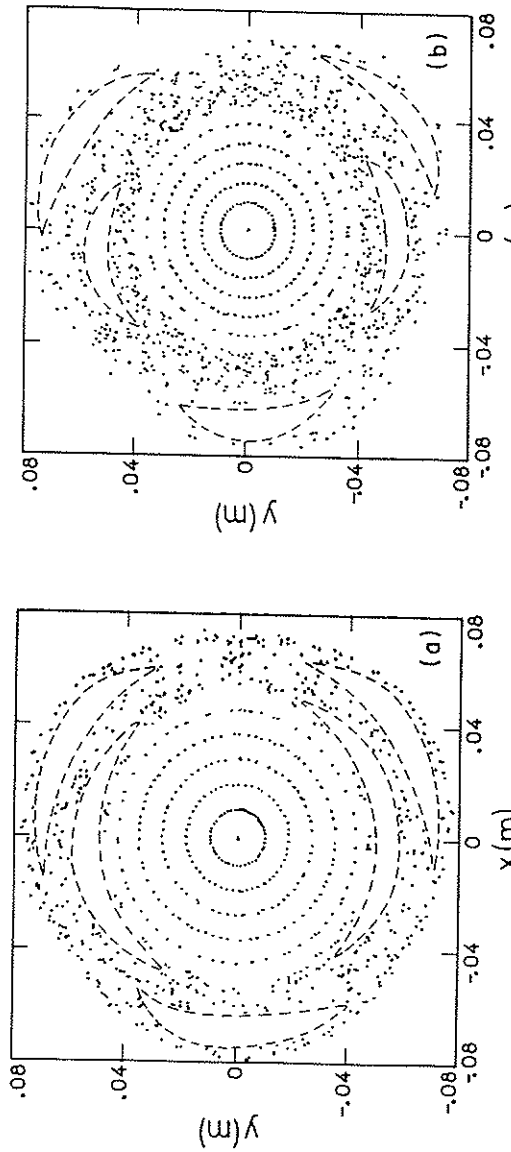

FIG. 7.—Intersection of magnetic field lines with a poloidal plane 50 μs before (a) and at the instant (b) of a minor disruption occurrence. The islands shrink as the chaotic region between them increases.

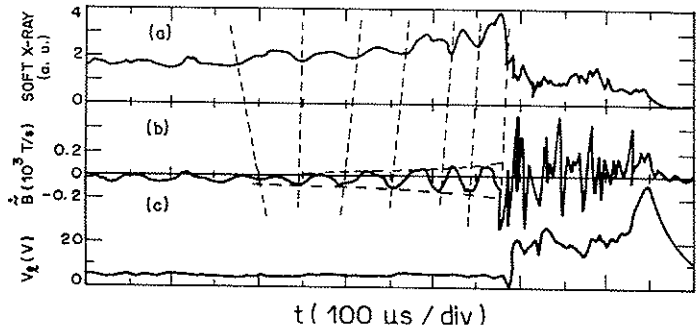

FIG. 8.—The $m/n = 1/1$ oscillation in the soft x-ray signal (a) and the $m/n = 2/1$ dominant MHD mode (b) have the same frequency just prior to a major disruption indicating mode coupling.

The sawteeth relaxation previously mentioned is an interesting phenomenon which has also been observed by the EQUIPE TFR (1977). The explanation proposed, based upon the existence of two $m/n = 1/1$ modes with different frequencies, one of them being directly responsible for the internal disruptions, could not be confirmed in this work.

The predicted sawtooth crash-time from KADOMTSEV's model using the TBR-1 parameters was estimated to be $\tau_c \sim 18\ \mu s$. This value is comparable to those measured in normal discharges, where $13\ \mu s \lesssim \tau_c \lesssim 26\ \mu s$. The values obtained for high Z_{eff} discharges, on the other hand, are too large to be explained by this model. Furthermore, the observation of internal disruptions without the growing $m/n = 1/1$ precursor oscillation is another indication that the reconnective model is not fully appropriate for describing the sawtooth instability and new explanations have to be formulated for a complete understanding of this phenomenon.

When the plasma is well formed and the column centered, it was verified that the minor disruptions in TBR-1 could be explained in terms of a superposition of the

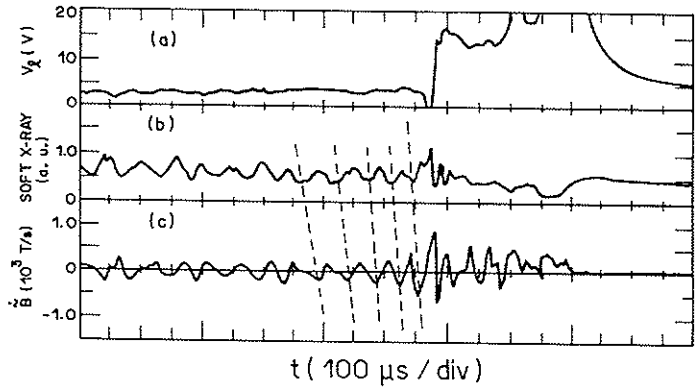

FIG. 9.—The $m/n = 1/1$ and $2/1$ mode coupling is again identified [(b) and (c)] but now the $m/n = 1/1$ oscillation amplitude no longer increases before the major disruption [(a) and (b)].

$m = 2$ and $m = 3$ MHD modes. The amplitude of the poloidal magnetic field perturbation, as mentioned before, is $\tilde{B}_\theta/B_\theta \sim 2\%$, typically.

The construction of Poincaré maps 50 μs before and at the instant of the disruption, Figs 7a and 7b, illustrates well the ergodization of the magnetic field lines between the principal islands. Near the magnetic axis a circle-like closed line pattern is formed. Outwards, near the magnetic islands, the intersecting points no longer form a closed line. They are displaced almost randomly and this effect is stronger for higher amplitude perturbations. Comparing the pictures in Figs 7a and 7b it can be seen that the islands shrink and the chaotic region increases as the perturbation amplitude grows. The destruction of magnetic surfaces seems to trigger the observed minor disruptions. This behaviour is consistent with the theory proposed by FINN (FINN, 1975) and others (RECHESTER and STIX, 1976).

Finally, it was observed that the coupling between the $m/n = 1/1$ and $m/n = 2/1$ modes would be the mechanism through which a major disruption would be developed. This was concluded because these two modes exhibit the same frequency just before the disruption event. The associated poloidal field ratio is $\tilde{B}_\theta/B_\theta \sim 4\%$.

Calculations regarding the localizations and half-widths of the magnetic islands showed that any interaction between the islands and the limiter can be discarded. No evidence of the $m/n = 3/2$ mode predicted in some theories (WADDELL *et al.*, 1978) was, in the same way, found prior to the major disruptions.

Acknowledgement—The authors would like to thank Dr. M. V. A. P. HELLER for the computer code used in the construction of the Poincaré maps.

REFERENCES

CAMPBELL D. J. *et al.* (1986) *Nuclear Fusion* **26**, 1085.
CAMPBELL D. J. *et al.* (1987) in the 11th *International Conf. on Plasma Physics and Controlled Fusion Research*, Kyoto, IAEA-CN-47/A-VII-5, 433.
DUBOIS M. A., PECQUET A. L. and REVERDIN C. (1983) *Nuclear Fusion* **23**, 147.
EQUIPE TFR (1977) *Nuclear Fusion* **17**, 1283.
FERNANDES A. S., HELLER M. V. A. P. and CALDAS I. L. (1988) *Plasma Phys. Contr. Fusion* **30**, 1203.
FINN J. M. (1975) *Nuclear Fusion* **15**, 845.
HUTCHINSON I. H. (1976) *Phys. Rev. Lett.* **37**, 338.
JAHNS G. L. *et al.* (1978) *Nuclear Fusion* **18**, 609.
KADOMTSEV B. B. (1975) *Sov. J. plasma Phys.* **1**, 389.
KADOMTSEV B. B. (1984) *Plasma Phys. Contr. Fusion* **26**, 217.
KARGER F. *et al.* (1976) in 6th *International Conf. on Plasma Physics and Controlled Fusion Research*, Berchtesgaden, IAEA-CN-35/A-7.
MCGUIRE K. and ROBINSON D. C. (1980) *Phys. Rev. Lett.* **44**, 1666.
MIRNOV S. V. (1979) in *IAEA Symp. on Current Disruptions in Toroidal Devices*, Garching, B-1.
RECHESTER A. B. and STIX T. H. (1976) *Phys. Rev. Lett.* **36**, 587.
ROBERTS D. E. *et al.* (1986) *Nuclear Fusion* **26**, 785.
SYKES A. and WESSON J. A. (1976) *Phys. Rev. Lett.* **37**, 140.
TAN I. H. *et al.* (1986) *IEEE Trans. Plasma Sci.* **PS-14**, 279.
VON GOELER S. *et al.* (1974) *Phys. Rev. Lett.* **33**, 1201.
WADDELL B. V. *et al.* (1976) *Nuclear Fusion* **16**, 528.
WADDELL B. V. *et al.* (1978) *Phys. Rev. Lett.* **41**, 1386.
WESSON J. A. (1986) *Plasma Phys. Contr. Fusion* **28**, 243.
WEST W. P. *et al.* (1987) *Phys. Rev. Lett.* **58**, 2758.

Apêndice 2

Artigo publicado sobre a investigação das instabilidades de disruptura em descarga de altas correntes no tokamak JET

HIGH CURRENT ($I_p^{max} \gtrsim 5$ MA) DISRUPTIVE PULSES IN JET

A. VANNUCCI*, R.D. GILL (JET Joint Undertaking, Abingdon, Oxfordshire, United Kingdom)

ABSTRACT. High current ($I_p^{max} \gtrsim 5$ MA) and low beta disruptive pulses in JET have been investigated. No association was found between the disruptions and a possible triggering when the radiated power (P_{rad}) equalled the input power (P_{in}), as was reported previously for disruptions in discharges with a lower plasma current. Often, P_{rad} remained well below P_{in} throughout the discharge, but a disruption did occur, even though $q_\psi \gtrsim 3$. These pulses were well away from the limiting boundaries associated with the high density and low-q limits in the Hugill diagram. There was evidence of MHD mode interaction as the mechanism triggering a major disruption. The m/n = 1/1 perturbation played an important role in this process. Also, a limit for these high current disruptive pulses was found by plotting the internal inductance of the plasma versus q_ψ; when this limit was reached, there was a very high probability for the plasma to disrupt through an MHD mode coupling process.

1. INTRODUCTION

Despite intensive investigations [1–9], major disruptions in tokamaks are not yet completely understood. Since future thermonuclear fusion reactors will most probably operate at very high plasma currents, a precise understanding of the physical causes of major disruptions is essential. The induced forces and stresses at the vessel can be as high as several tens of meganewtons; the whole JET structure, for example, would be displaced several millimetres by such forces [10].

* Instituto de Física, Universidade de São Paulo, C.P. 20516, 01498 São Paulo, Brazil.

Although many ideas have been proposed to explain these disruptions, it was not possible to describe all the different experimental observations. Nevertheless, it is generally accepted that radiative processes [1–4] and MHD perturbations (mainly involving the m/n = 2/1 mode, either by direct contact with the limiter [5] or by coupling with other MHD modes, such as m/n = 1/1 [6, 7] or m/n = 3/2 [8, 9]) may play important roles at some stage of the disruption triggering process.

In a recent paper [11], where only pulses with a plasma current below 3 MA or of the order of 3 MA were analysed, density limit disruptions in JET were identified to be initially caused by impurity radiation, which makes the plasma temperature profile contract, leading to an unstable MHD configuration of the system. Also, low-q disruptions were found to be triggered just when q_ψ reached a value of two. The behaviour of the energy quench and the current decay was found to be very similar in both cases.

In this paper, we investigate only high current ($I_p^{max} \gtrsim 5$ MA) and low beta disruptive pulses in JET, almost all of them with $q_\psi \gtrsim 3$ at the time of disruption. The experimental set-up and the diagnostics used are described in detail in Refs [11, 12].

2. DISRUPTION TRIGGERING PROCESSES

The idea that a disruption could be initiated when the radiated power level increases considerably with respect to the input power is not new [1, 2] and it was supported by experimental results obtained in different tokamaks [3, 4]. For JET low current pulses ($I_p \lesssim 3$ MA), for example, major disruptions were identified to be triggered when the radiated power P_{rad} reached ~100% of the input power P_{in} [11]. This caused a contraction of the temperature profile, leading to an unstable plasma configuration, which finally collapsed in a disruption.

We have investigated the behaviour of the P_{rad} and P_{in} signals of all high current disruptive discharges in JET. Although for many of them P_{rad} equalled or exceeded P_{in} at some stage of the pulse, in several cases it was found that P_{rad} remained well below P_{in} throughout the discharge, but a disruption did take place.

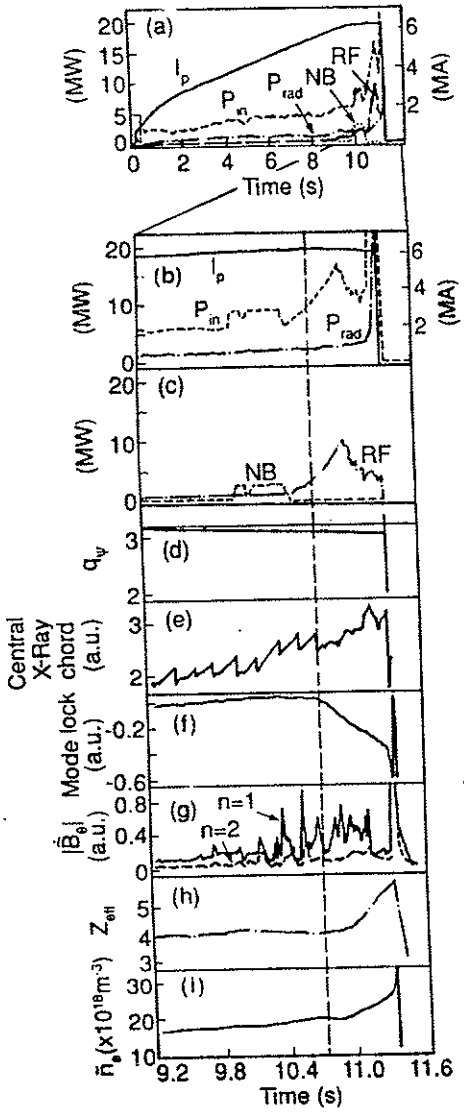

FIG. 1. Plasma behaviour for pulse No. 17857. (a) Overall characteristics of the total input power P_{in}, the radiated power P_{rad} and the contributions from neutral beam (NB) and radiofrequency (RF) heating. An expanded part of this pulse is shown in (b) to (i): (b) and (c) power balance and plasma current I_p; (d) safety factor q_ψ; (e) X-ray signal; (f) amplitude of the locked mode. (g) variation of the poloidal magnetic field B_θ; (h) effective charge Z_{eff}; (i) average electron density.

The pulse presented in Fig. 1 is a typical example of this situation. It corresponds to a 6.2 MA flat-top disruptive discharge where, near the end, some additional RF and NB heating was applied. At the time of disruption, just before the abrupt increase of the input power signal, $P_{rad} \leq 40\%\ P_{in}$, no contractions in the electron temperature profile were observed, and $q_\psi \geq 3$ (Figs 1(b) and 1(c)). Therefore, the occurrence of this disruption could not be explained by radiative emission nor could it be considered a low-q disruption. This means that other triggering mechanisms have to be studied in order to understand the disruptions in JET, at least for the high current disruptive pulses.

The corresponding time expanded soft X-ray signal for this pulse is presented in Fig. 1(e). It is interesting to observe that the sawtooth activity is disturbed at the same time as a mode lock process starts (Fig. 1(f)) at ~ 10.75 s. Only later is a strong impurity influx identified from the Z_{eff} and $\bar{n}_e$ signals (Figs 1(h) and 1(i)). It seems reasonable to assume that the major disruption is initiated at 10.75 s, leading to the collapse of the plasma column 600 ms later.

If the m/n = 1/1 perturbation is the basic cause of the sawteeth, then the observed disturbance, exactly at the time when the mode lock is initiated, may indicate that this particular mode is a factor in the mechanism that initiates the disruption. The contribution of other MHD perturbations can be investigated by analysing the main components of the perturbed poloidal magnetic field measured by the pick-up coils. Figure 1(g) shows the corresponding rectified signals; they do indicate a stronger MHD activity (mainly related to the n = 1 components) at the time when the sawtooth oscillations change and the mode lock starts.

These overall characteristics, indicating mode coupling as the triggering mechanism for the major disruption, were also identified in several other pulses under different conditions, such as in purely Ohmic discharges, with carbon or beryllium as first wall materials.

For some shots, this coupling was apparently enhanced by a mechanism which involved, earlier in time, a considerable increase in the P_{rad} level. The whole disruptive process then took place very rapidly, as shown in Fig. 2. This is an interesting situation where, with an increase of P_{rad} almost up to 100% P_{in} (Fig. 2(b)), there was an impurity influx (Figs 2(c) and 2(d)) which made the plasma more resistive (Fig. 2(e)), while the sawteeth did not suffer any apparent changes (Fig. 2(f)). However, after a very short period (~ 80 ms), at t ~ 13.24 s, the sawtooth activity suddenly came to an end, just before the

appearance of the negative spike in the loop voltage signal, and, at the same time, a mode lock process was initiated (Figs 2(e), 2(f) and 2(g)). A further expansion in time of the central soft X-ray, the mode lock and the magnetic coil signals (Fig. 3) shows that the amplitude of the m/n = 1/1 and 2/1 components increased and reached a maximum exactly at the moment when mode locking started. The corresponding growth rates were calculated to be $\gamma_{m1}^{-1} = 0.75$ s and $\gamma_{m2}^{-1} = 1.33$ s; these values suggest a resistive character for these perturbations. Thus, the respective magnetic islands are probably participating in the disruption process.

Finally, it should be noted that the mode lock process itself did not always lead directly to a major disruption. Unlockings were sometimes observed, with no further consequences. Only when, later, another mode lock took place and when the described mode coupling occurred was a disruption actually triggered.

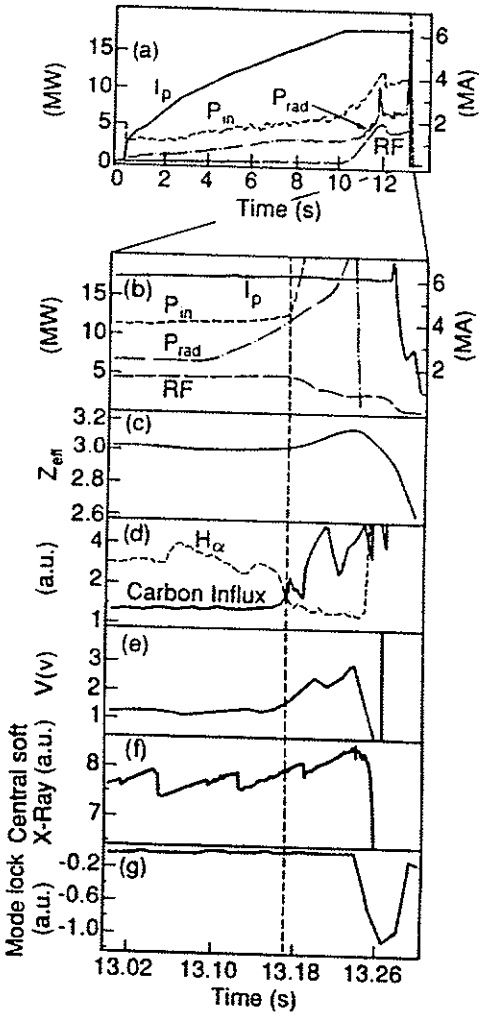

FIG. 2. Plasma behaviour for pulse No. 18040. The nomenclature is the same as for Fig. 1. The H_α and carbon influx intensities are shown in (d) and the loop voltage is shown in (e).

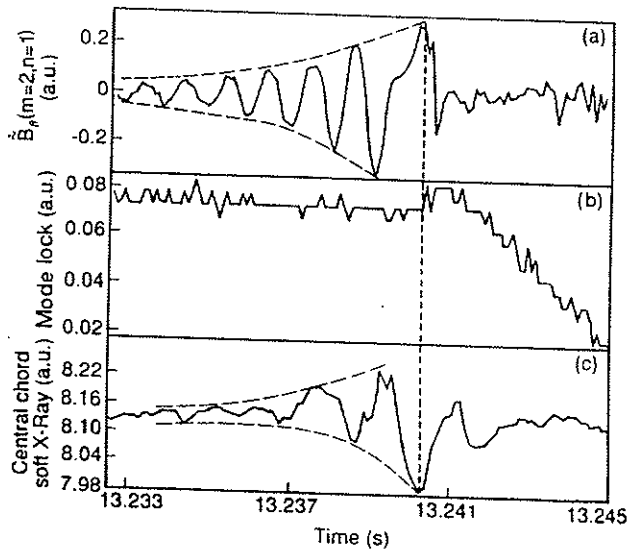

FIG. 3. Expanded view of the central soft X-ray channel, the mode lock and the magnetic coil signals, showing the mode growth until the time of mode locking.

3. LIMITING CONDITIONS AND GLOBAL FEATURES

The operational space of tokamaks is believed to be restricted by certain limiting conditions, involving macroscopic parameters, which must be controlled in order to avoid the occurrence of a major disruption. We have investigated the general aspects of these limits in JET by experiments in high current disruptive discharges.

In Fig. 4, for example, all pulses with $I_p \geq 5$ MA, up to shot No. 20910, were used to construct a Hugill diagram ($\bar{n}_e R/B$ versus $1/q_{cyl}$). They were discriminated by the limiter material (carbon or beryllium) and also by the type of additional heating used at (or very close to) the disruption time. The data for each point of the plot were taken just before the disruption started. This figure shows that major disruptions most likely occur in a fairly restricted region of the Hugill space, between curves A and B (which only delineate the experimental points). The lower boundary A corresponds to density limit disruptions [13], while curve C corresponds to low-q ($q_\psi \sim 2$) disruptions [11].

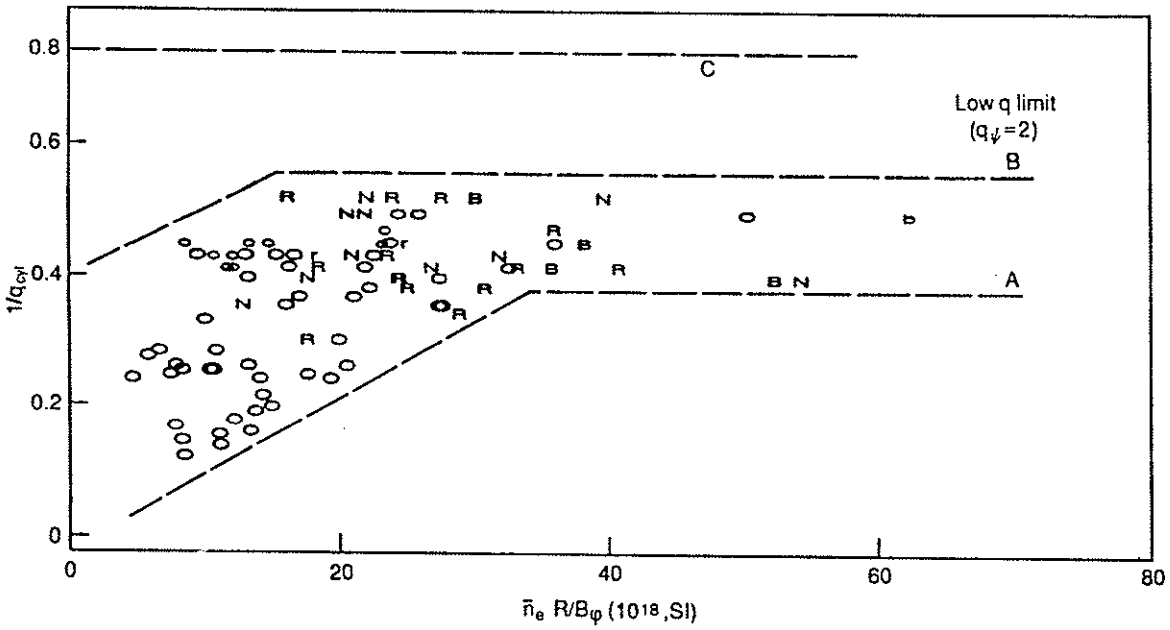

FIG. 4. Hugill diagram (reciprocal of cylindrical q values versus Murakami parameter $\bar{n}_e R/B_\varphi$). Line A corresponds to the density limit and line C to the low q-limit. Line B just delineates the points. Legend: O — Ohmic heating; R — RF heating with C limiter; N — neutral beams with C; B — both additional heating systems with C; o — Ohmic heating with Be; r — RF heating with Be; b — both additional heating systems with Be.

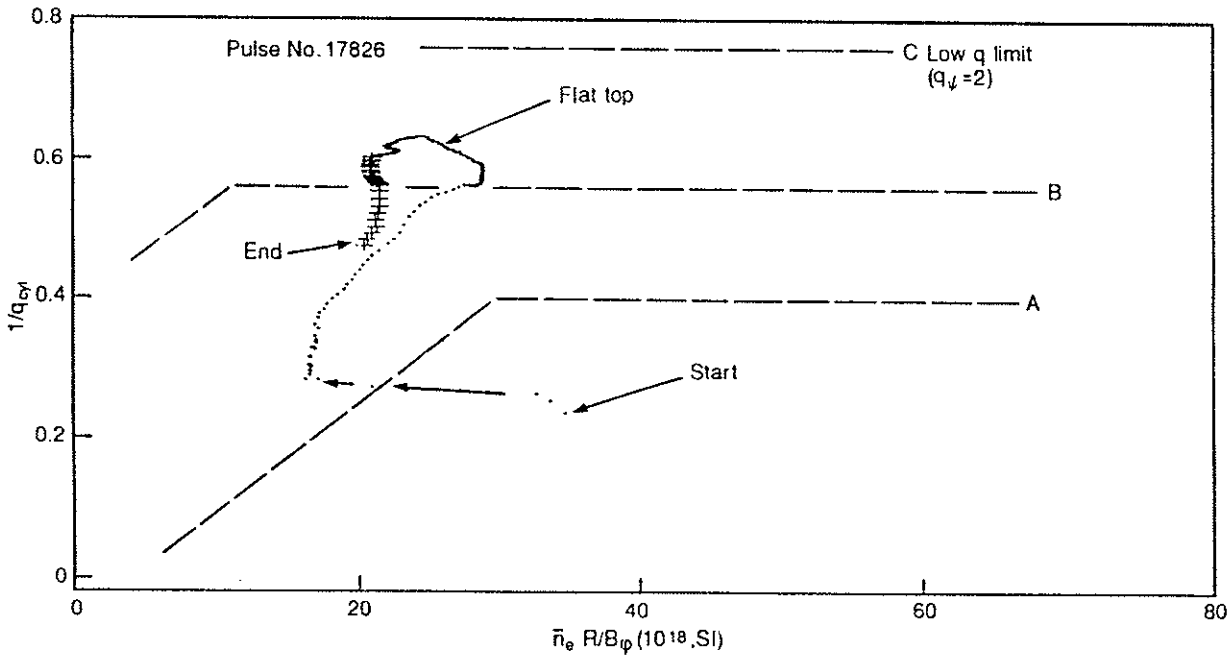

FIG. 5. Trajectory of a pulse with $I_p(max) = 7$ MA on the Hugill diagram.

Since the points in Fig. 4 are much more concentrated in the region near curve A, the high current disruptions investigated may be density limit disruptions (in which case the disruption process would be expected to be triggered by a large amount of radiated power), or a new low-q limit should be considered in order to explain the disruptions in these high current pulses (the boundary B, for example). However, neither of these two alternatives can satisfactorily explain the experimental observations, for two reasons: (1) The time evolution of the corresponding Hugill values for a single pulse is, in some cases, such that they enter the region between curves B and C (Fig. 5). Only when boundary B is crossed again does the disruption finally take place, indicating that the low-q limit has not been reached. (2) For many disruptions, no large amount of radiation was detected at any time during the discharge. These particular pulses were usually found to be located closer to line C in the Hugill plot.

Another significant and interesting diagram which indicates the most important limiting condition, at least for the JET high current discharges, is obtained by plotting the internal inductance (L_i) of the plasma against the corresponding q_ψ values (Fig. 6). It is clear from the figure that, for a given plasma equilibrium, there is a certain value of L_i which cannot be exceeded without a major disruption developing. The relationship between the parameters L_i and q_ψ for JET has been observed previously [11]; we study this relationship here for high current pulses.

Since the inductance is related to the poloidal field by the expression (see Ref. [11])

$$L_i = \frac{2}{\mu_0^2 R I^2} \int B_\theta^2 \, d\tau \qquad (1)$$

where the integral is taken over the entire plasma volume, the behaviour exhibited by the experimental points in Fig. 6 suggests that there is a limited amount of poloidal magnetic energy which can be stored in the plasma for a given plasma current. On reaching the limiting value of L_i, however, the system would be in such an unstable equilibrium that even small perturbations could trigger a disruption.

4. DISCUSSION AND CONCLUSION

In this work, all the available JET high current ($I_p^{max} \geq 5$ MA) and low beta disruptive pulses were analysed. The processes observed were different from those occurring in lower current disruptions ($I_p \leq 3$ MA) reported in a previous paper [11]. The disruptions investigated could not be directly related

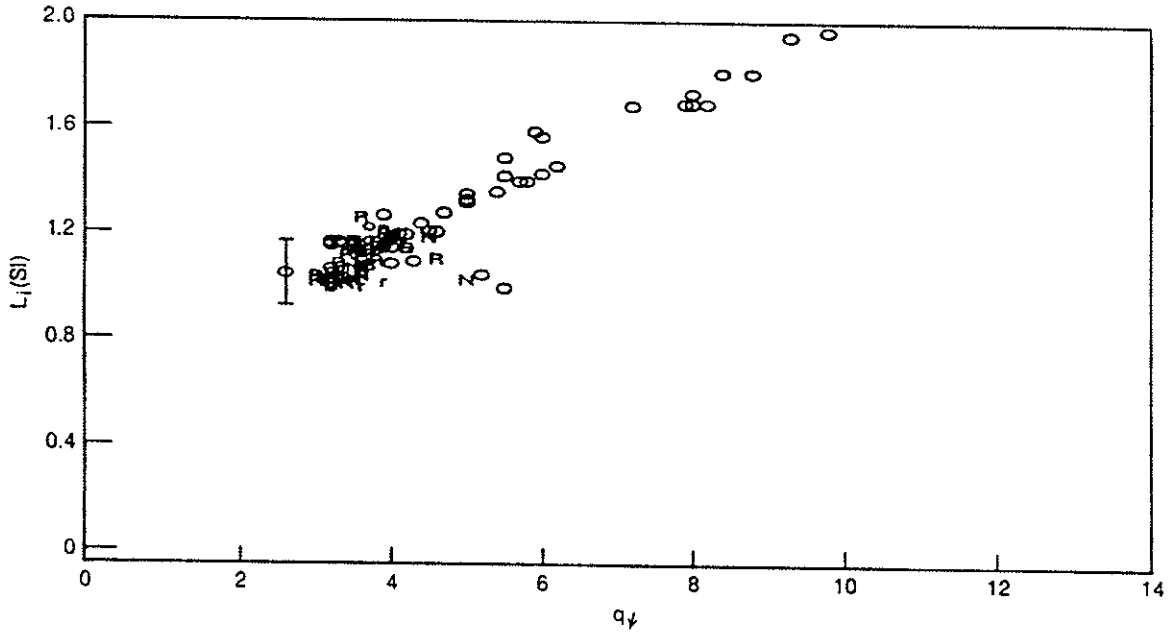

FIG. 6 Plasma inductance versus q_ψ for those pulses which disrupt.

with a certain P_{rad}/P_{in} ratio. For many pulses, the P_{rad} signal remained well below the P_{in} level throughout the discharges, but a disruption did take place.

These pulses, in particular, could not be generally related with the usual low-q or high density limiting boundaries in the Hugill diagram. On the other hand, the L_i versus q_ψ diagram (Fig. 6) brings some light into this rather puzzling situation. The plotted points, which represent the experimental data taken at the disruption time, clearly indicate the existence of a limiting condition for all high current pulses. On reaching this limit during a discharge, there was a very high probability of plasma disruption. The same diagram as in Fig. 6, but for non-disruptive high current shots (with $I_p > 4$ MA), is presented in Fig. 7, which confirms the existence of such a limit.

The L_i parameter, however, is related to the poloidal magnetic energy, as shown by Eq. (1). Therefore, the limitation in L_i, for a certain q_ψ value, suggests that there is a finite and fairly well determined amount of magnetic energy that the plasma can store. If this limiting threshold is reached, the system comes into a marginally stable equilibrium such that any perturbations lead to a major disruption (these perturbations are caused, for example, by pellets, impurity influx from the RF antenna, temperature profile contractions, marfes and additional heating systems which are switched on or off). It is interesting to note that all pulses in Fig. 7 located in the region of high L_i and q_ψ values disrupted during the decay phase, while flat-top disruptions generally occurred at low values of L_i and q_ψ.

Finally, we discuss the possible mechanisms through which the major disruption is triggered. The low q_ψ and the high radiation emission cannot be regarded as being responsible for several disruptions in high current pulses because, for many of them, the radiated power remained much below the input power, the value of q_ψ was more than three and no contractions in the electron temperature profile were identified, but a major disruption did take place. Also, in these pulses there was no indication of a mode lock during the plasma current rise phase which would persist throughout the discharge, causing the disruption to occur later, in the flat-top period. On the other hand, there was evidence that the disruptions could be triggered by an interaction between MHD modes. The m/n = 1/1 perturbation interacted with other components (mainly with the n = 1 mode and often with the m = 2 mode) through a mode locking process and later caused a loss of confinement. Several pulses were observed in which the sawtooth oscillation was quite strongly disturbed at the time when an increase in the amplitude of the radial magnetic field occurred and an increase in the

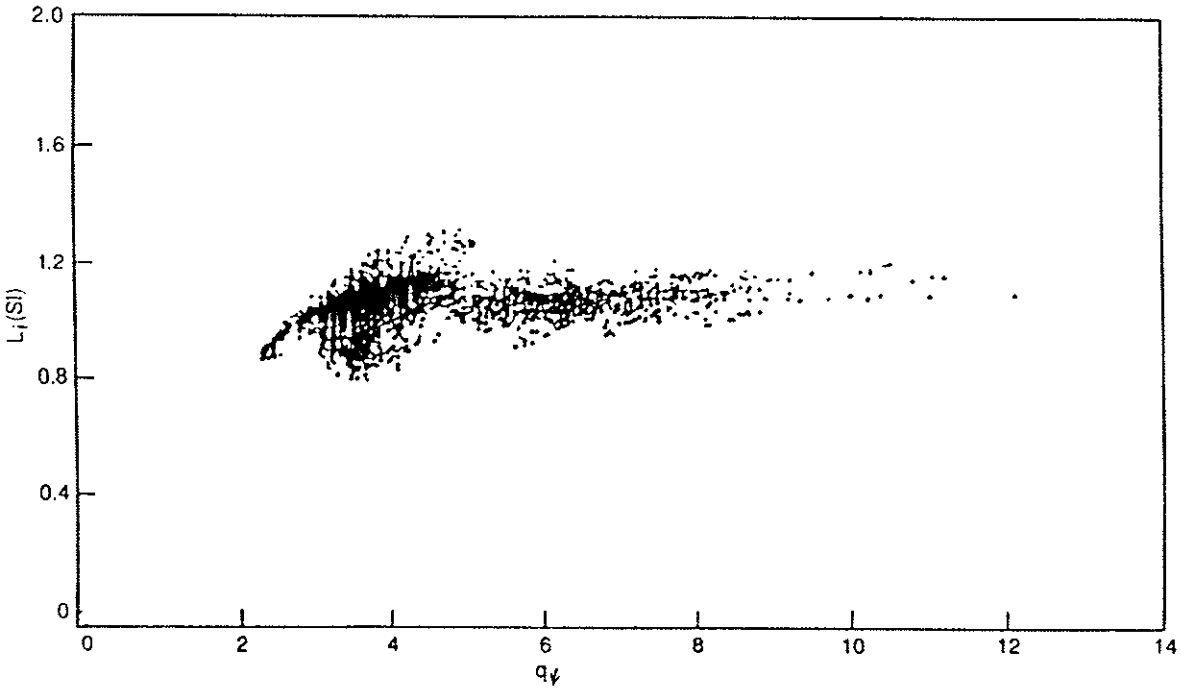

FIG. 7. Plasma inductance versus q_ψ for all non-disruptive pulses with $I_p \geq 4$ MA.

measured magnetic signals was detected. These observations were made in Ohmic discharges as well as in RF and NB discharges, with either carbon or beryllium as covering materials for the first wall.

Furthermore, since in a number of cases the resistive nature of the MHD perturbations was identified by calculating the corresponding growth rates, the overall experimental picture can probably be explained by the coupling between the associated magnetic islands, leading to a mode lock process. Only after this coupling were other characteristic symptoms sometimes observed, such as electron temperature decrease, impurity influx, density rise and loss of stored energy, indicating that the confinement was strongly affected. Still later, after a period of time varying from less than one hundred milliseconds to more than one second, the final plasma collapse occurred. We come to the conclusion that the plasmas in JET disrupt because of a too high density, a too low value of q_ψ or a too high inductance for a particular value of q_ψ. In this letter, we have drawn attention to the latter possible cause of a disruption.

ACKNOWLEDGEMENTS

The authors would like to thank Drs. J.T. Mendonça, M.F.F. Nave, D.J. Ward and J.A. Wesson for helpful suggestions and useful discussions.

REFERENCES

[1] VERSHKOV, V.A., MIRNOV, S.V., Nucl. Fusion **14** (1974) 383.
[2] GIBSON, A., Nucl. Fusion **16** (1976) 546.
[3] STOTT, P.E., Nucl. Fusion **28** (1988) 1469.
[4] ALLADIO, F., in The Density Limit in Tokamaks, Rep. RT/FUS/85/18, ENEA, Frascati (1985).
[5] ROBERTS, D.E., De VILLIERS, J.A.M., FLETCHER, J.D., O'MAHONY, J.R., JOEL, A., Nucl. Fusion **26** (1986) 785.
[6] TSUJI, S., NAGAYAMA, Y., MIYAMOTO, K., KAWAHATA, K., NODA, N., TANAHASHI, S., Nucl. Fusion **25** (1985) 305.
[7] VANNUCCI, A., NASCIMENTO, I.C., CALDAS, I.L., Plasma Phys. Control. Fusion **31** (1989) 147.
[8] WADDELL, B.V., CARRERAS, B., HICKS, H.R., HOLMES, J.A., Phys. Fluids **22** (1979) 896.
[9] McGUIRE, K., ROBINSON, D.C., Phys. Rev. Lett. **44** (1980) 1666.
[10] NOLL, P., SONNERUP, L., FROGER, C., HUGUET, M., LAST, J., Fusion Technol. **15** (1989) 259.
[11] WESSON, J.A., GILL, R.D., HUGON, M., et al., Nucl. Fusion **29** (1989) 641.
[12] STOTT, P.E., in Basic and Advanced Diagnostics Techniques for Fusion Plasmas (Proc. Course and Workshop Varenna, 1986), Vol. 3, CEC, Brussels, and Monotypia Franchi, Città di Castello (1987) 845.
[13] GREENWALD, M., TERRY, J.L., WOLFE, S.M., et al., Nucl. Fusion **28** (1988) 2199.

(Manuscript received 27 September 1990
Final manuscript received 13 March 1991)

Apêndice 3

Artigo publicado sobre a investigação das instabilidades de disruptura no tokamak TEXT-U

DISRUPTIVE INSTABILITIES IN THE TEXT-U TOKAMAK

A. VANNUCCI*, S.C. McCOOL
Fusion Research Center,
The University of Texas at Austin,
Austin, Texas, United States of America

* Instituto de Física,
Universidade de São Paulo,
São Paulo, Brazil

ABSTRACT. Disruptive instabilities in TEXT-U circular plasmas have been investigated. Hugill diagrams have been constructed for some single and consecutive disruptive shots, and the results indicated that the density limit boundary did not depend solely on plasma impurity content. Since the average radiated power intensity was typically only 30% of the input power, it is unlikely that major disruptions resulted from strong edge cooling and subsequent contraction of the plasma column. However, strong indications are found that a coupling between the $m = 1$ and $m = 2$ MHD modes could be the main triggering mechanism for the disruptions analysed, independently of where they occur in the Hugill operating space. After a major disruption has been triggered, the plasma current was observed to decay on a time-scale that varied considerably from one plasma discharge to another. This discrepancy was not found to depend, at least directly, on average quantities such as Z_{eff}, plasma current, stored energy or plasma density. Finally, the installation of a set of locked mode detecting coils, for measuring the time derivative of the radial magnetic field associated mainly with the growth of the $m = 2$ magnetic island, made it possible to observe that both minor and major disruptions were almost always preceded by a growth in $\dot{\tilde{B}}_r$. In particular, for some plasma discharges with long duration precursors, the characteristic fluctuations in the Mirnov coil signals and the soft X ray sawtooth oscillations are observed to disappear, which could suggest that a complete mode lock occurs before the disruption takes place. However, detailed investigation showed that the MHD modes were still rotating in the toroidal direction but with a very low frequency of about 50 Hz.

1. INTRODUCTION

Although several aspects of disruptive instabilities have already been pointed out in many different papers, an exact understanding of how the disruptive instabilities are triggered and how the plasma decays afterwards has not been completely achieved yet.

Radiation losses [1, 2], magnetic field line ergodization [3, 4], multifaceted asymmetric radiation from the edges (MARFES) [5] and even microturbulence [6] have been considered as potentially the primary cause of degraded confinement conditions, which lead to plasma disruptions. Questions concerning whether or not the magnetic islands associated with the $m = 2$ instability touch the limiter [7, 8] or whether the $m = 2$ mode interacts with other MHD perturbations (of either higher [9, 10] or lower [11–13] m values), for example, require clarification.

In this paper, several interesting observations regarding disruptions in TEXT-U circular plasmas are presented and discussed. The investigations have focused on some particular characteristics of major disruptions, by analysing single discharges, and also on some general aspects, by compiling data from several different plasma pulses. Some old TEXT plasma discharges, i.e. data taken before the upgrading of the machine [14], were also used for comparisons.

Furthermore, the use of a set of locked mode detecting coils, specially constructed for this work, provided some new results that are also very intriguing. As is already known, an increase of radial magnetic field perturbations during tokamak plasma discharges, usually related to slowed rotation of magnetic islands resulting from MHD mode locking, has already been reported to be correlated with several changes in the confined plasmas [15–18]. In particular, before a major disruption, this increase may start either well before or almost simultaneously with the characteristic loop voltage spike [2, 11]. However, disruptions are not the only case where such precursors are observed. They were also associated with the large amplitude quasi-stationary modes that follow the injection of a pellet, or occur after a large sawtooth collapse [15]. Furthermore, these perturbations of the radial magnetic field sometimes occur during the plasma current rise, lasting for a long period of

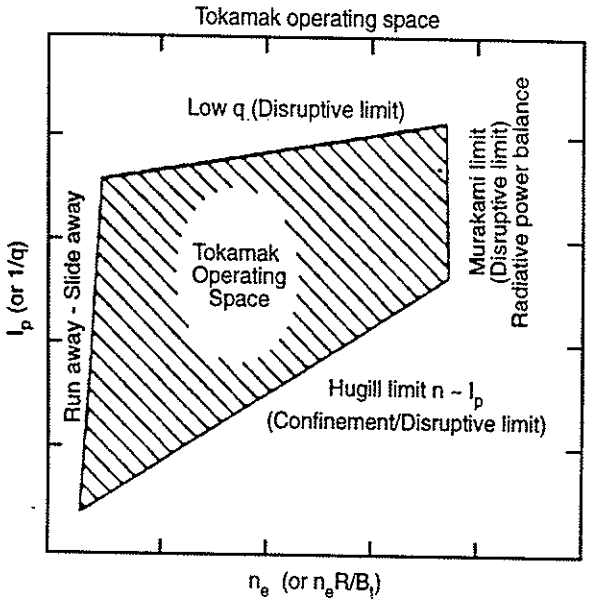

FIG. 1. Diagram taken from Ref. [24] showing the typical tokamak operating space in a I_p versus n_e ($1/q$ versus n_eR/B_t) diagram.

time (as long as 3 s in JET). In some cases the plasma would subsequently disrupt, but in others the mode would unlock, allowing a normal discharge duration [2].

Generally, once a locked mode is present in a plasma, a degraded plasma confinement is concurrently observed. The global stored energy decreases significantly as transport increases, and even the electron cyclotron heating (ECH) efficiency is reduced. These effects have been attributed to a slowing of central plasma ion rotation [19].

Theoretical studies have attempted to explain how the locked modes are formed. The two most accepted models are:

(a) The locked mode is a result of an interaction of MHD modes with the tokamak conducting vessel wall [20, 21].

(b) Magnetic error fields (either pre-existing or purposely imposed) can in some circumstances cause a torque on the plasma, slowing the rotation of the plasma near the rational magnetic surfaces [22, 23].

In Section 2, the construction of the locked mode detecting diagnostic is described. In Section 3, the TEXT-U operating space is analysed, in relation to the results that had been previously obtained, i.e. before the modifications constituting the tokamak upgrade. In Sections 4 and 5, the major disruption characteristics are discussed in detail, and, in Sections 6 and 7, the degradation of the confinement, as a result of an MHD mode coupling, and the way in which the plasma current decays, after a major disruption, are considered. Finally, in Section 8 the conclusions of this work are presented.

2. THE LOCKED MODE DETECTION SYSTEM

Two pairs of locked mode detecting coils have been constructed and installed on the TEXT-U tokamak. They were used along with other diagnostics to investigate how locked modes affect the confined plasma and to better understand how major disruptions are triggered. The coils of each pair were located 180° apart toroidally and the two sets of coils had a toroidal separation of approximately 90° from each other. The coils of one pair were constructed with 12 turns while the other had 24 turns, which results in estimated effective areas of 1.8 ± 0.3 and 3.6 ± 0.4 m^2, respectively. All the coils were externally wound around the vacuum chamber radial ports, made of stainless steel (SS304) with resistivity $\rho = 72\ \mu\Omega \cdot$ cm. Note that the 1/e attenuation frequency of the vacuum chamber was found experimentally to be 0.75 kHz for $m = 2$, with the cut-off frequency being proportional to m.

Experimentally, the locked mode signals were not observed to be strongly affected by extraneous magnetic fields during the tokamak operation and, therefore, no compensation signals have been used. The signals generated by the coils of each pair were directly subtracted and were sampled at a frequency of 20 kHz.

3. TEXT-U TOKAMAK OPERATING SPACE

It is already well known that tokamaks can only operate within a limited space on an I_p versus n_e (or $1/q$ versus n_eR/B_t) diagram. The boundaries are generally accepted to be set, as shown in Fig. 1, by a low-q limit at the top, a low density (or runaway) limit at the left, a radiative (or Murakami) limit at the right and a high density (or Hugill) limit at the bottom [24].

In the TEXT-U tokamak, the plasma pulses were highly reproducible, and major disruptions did not occur very frequently under normal plasma operating conditions. However, when they do occur, interesting aspects of the disruption triggering mechanism and of how the plasma evolved afterwards could be studied.

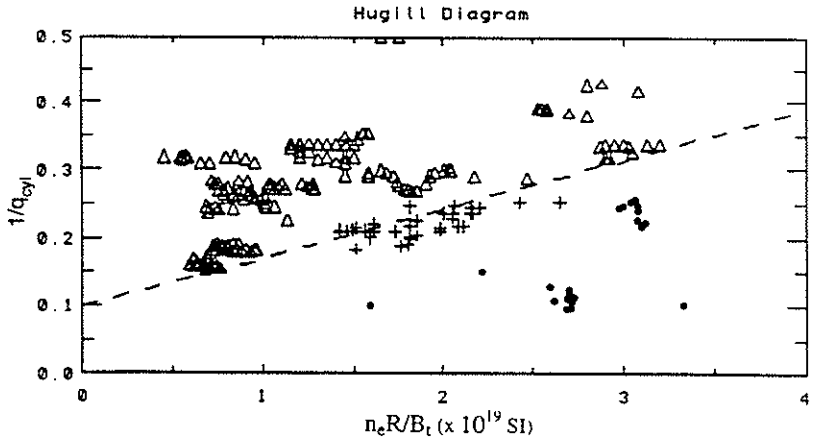

FIG. 2. Experimental data taken before (triangles) and after (crosses) the tokamak upgrading, showing that the plasma confinement has improved. The dashed line indicates the empirically obtained density limit boundary for the old TEXT tokamak. The circles represent TEXT discharges in which pellets were injected, followed by disruptions.

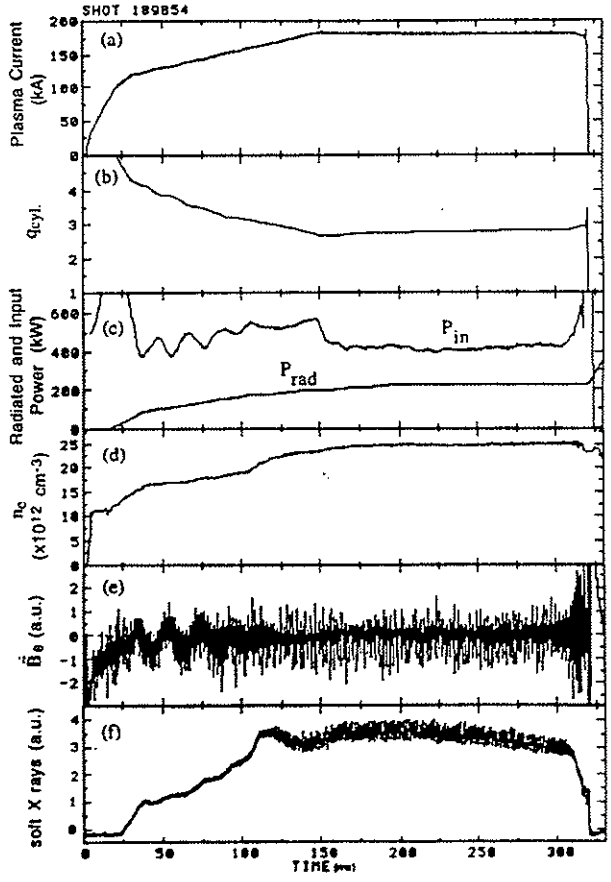

FIG. 3. Typical TEXT-U disruptive plasma pulse. The signals shown are: (a) plasma current, (b) cylindrical safety factor, (c) ohmic power and radiated power, (d) electron density, (e) time derivative of the fluctuating poloidal magnetic field, (f) central soft X ray intensity.

Concerning the machine density limits, before and after the upgrade that has been carried out, it can be seen from Fig. 2 that a significant improvement was achieved, probably as a result of the vacuum chamber and limiter modifications. Note that all the data presented here were taken before the implementation of the TEXT-U boronization system. The triangles correspond to the old TEXT disruption pulses and the dashed line indicates the empirically obtained density limit boundary. The crosses represent the new TEXT-U data, taken just prior to the disruption time. The circles in this figure correspond to TEXT pulses where pellets were injected (either H_2 or carbon), followed by disruptions [25, 26].

The questions to be addressed now concern the basic differences between the so-called density limit disruptions and the disruptions that occurred well below this limit, represented in Fig. 2 by the crosses and triangles located in the upper part, above the dashed line. These pulses, which disrupted before reaching the density limit boundary, in general, were not found to result from the radiated power exceeding the input power, as already reported elsewhere [2]. On the other hand, MHD perturbations, through a mode coupling mechanism, seem to be a good candidate for explaining the major disruptions in TEXT-U, for all cases.

4. TEXT-U DISRUPTIONS

The plasma pulse shown in Fig. 3 is a typical example of how major disruptions are triggered in TEXT-U discharges. It corresponds to an

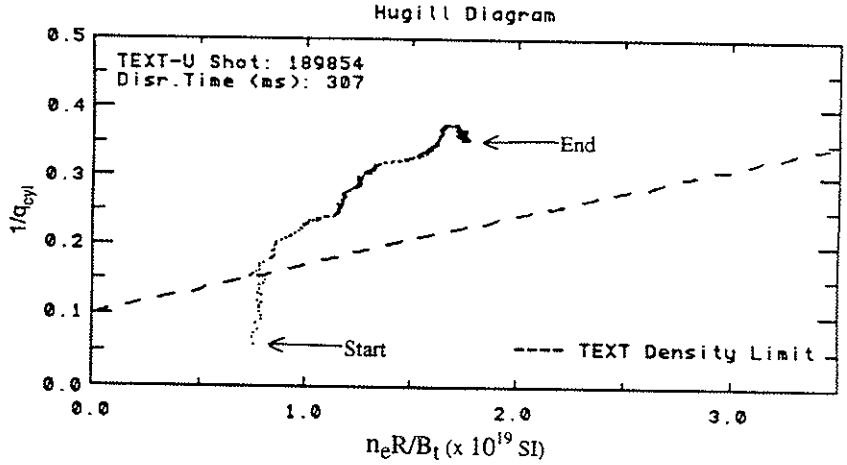

FIG. 4. Trajectory corresponding to the disruptive plasma pulse shown in Fig. 3.

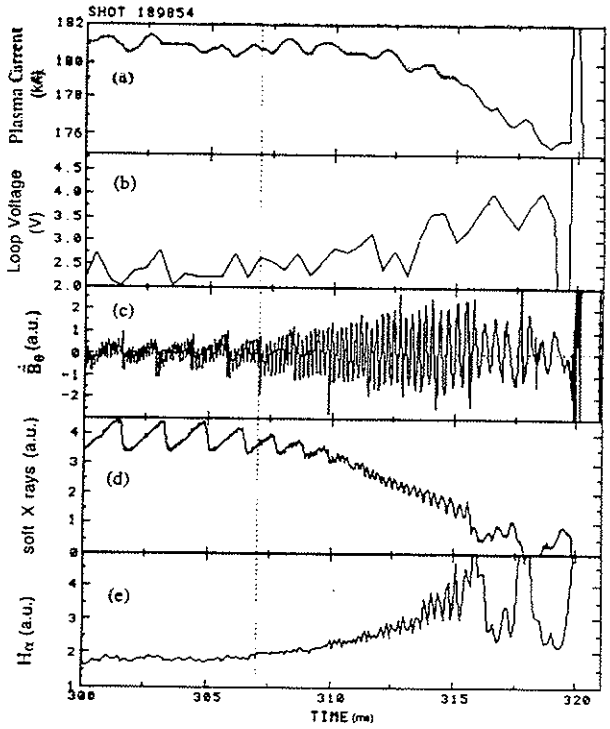

FIG. 5. Some of the experimental data taken for the discharge shown in Fig. 3, in an expanded view, close to the disruption time. The signals correspond to: (a) plasma current, (b) loop voltage, (c) time derivative of the fluctuating poloidal magnetic field (note that the sawtooth-like oscillations in this signal are only externally produced noise picked up by the coils located outside the vacuum chamber and have no correlation with the sawtooth oscillations), (d) soft X ray intensity, (e) H_α signal.

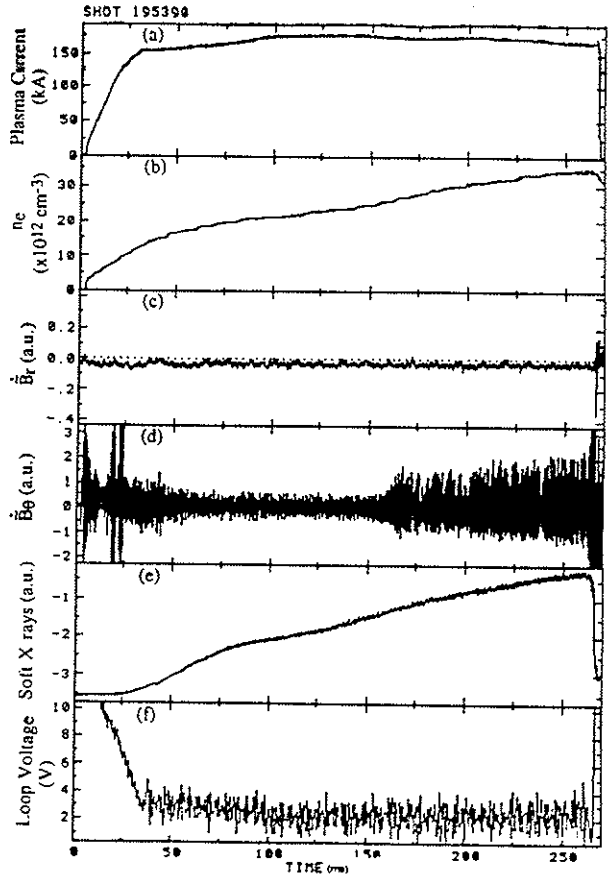

FIG. 6. Plasma behaviour for pulse No. 195 390. The nomenclature is the same as that for Fig. 3. The signal generated by one pair of the constructed locked mode detecting coils is shown in (c).

$I_p \approx 180$ kA (Fig. 3(a)) plasma discharge that disrupted at $t \approx 320$ ms. The cylindrical safety factor q_{cyl} did not vary significantly during the flat-top phase and its value, at the disruption time, was approximately 2.8 (Fig. 3(b)). The radiated power stayed well below the input power level all through the discharge (Fig. 3(c)). Therefore, a plasma detachment from the wall, as a result of edge cooling, could not be implicated as the main disruption triggering mechanism in this case. Although the average electron density did exhibit a smooth maximum close to the disruption time (Fig. 3(d)), this shot did not represent a density limit disruption case in the normal sense, since the disruption occurred well above the dashed line (density limit boundary) of the Hugill diagram, as shown in Fig. 4. Also, the value of the safety factor being quite close to 3.0, in this case, could suggest that the plasma was possibly destabilized by the $q = 3$ resonant magnetic surface that would be located at the edge of the plasma. However, this consideration is not of great significance if we consider that many other disruptive plasma pulses were observed to exhibit similar behaviour to this one but q remained greater than 4.0 throughout the entire discharge duration.

On the other hand, if we focus on the final part of the plasma pulse shown in Fig. 3, we can observe that the growing amplitude of the poloidal magnetic field time derivative (Fig. 3(e)), seems to be strongly correlated with a significant drop in the soft X ray emission (Fig. 3(f)). This might indicate that MHD perturbations in the plasma have played an important role in triggering this disruption.

Plotting some of these experimental data on an expanded scale close to the disruption time (Fig. 5), it can be observed that the major disruption was triggered approximately at $t \approx 307$ ms, 12 ms before the negative loop voltage spike is observed (Fig. 5(b)). Around that instant of time the MHD perturbation, which we will assume to have a dominant $m = 2$ structure (due to the impossibility of doing any detailed Fourier analysis over the Mirnov oscillations obtained for these experiments and because this component has already been observed to play an important role in relation to similar disruptive processes in the TEXT tokamak [25]), is growing rapidly (note that the sawtooth-like oscillations in this signal are only externally produced noise picked up by the coils located outside the vacuum chamber and have no physical meaning) and the sawtooth oscillations are strongly affected (Figs 5(c) and (d)).

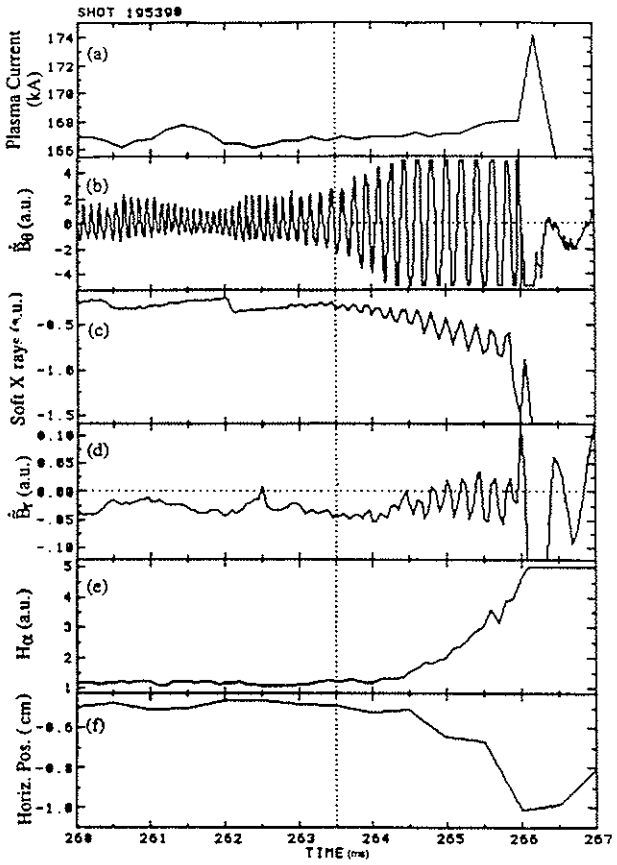

FIG. 7. Experimental signals related to the pulse shown in Fig. 6, close to the disruption time. The plasma is observed to disrupt soon after the mode coupling has taken place, at $t \approx 263.5$ ms.

As is already well known, the $m = 1$ mode is mainly responsible for the sawtooth oscillations. Therefore, the observed disturbance in the sawtooth activity, concurrently with the growth in amplitude of the MHD activity, may suggest that the $m = 2$ and $m = 1$ MHD modes are interacting. As a consequence of this interaction, the plasma current is observed to decrease shortly afterwards (Fig. 5(a)), while both the loop voltage and the H_α signal start to increase (Figs 5(b) and (e)). The small plasma current decrease (about 3%) and the considerable increase in the loop voltage signal (about 60%) are indications that the plasma resistivity has increased significantly, probably owing to an impurity influx. The disruptive process seems to have started in the plasma region between the $q = 1$ and $q = 2$ magnetic surfaces, as indicated by the soft X ray signals from inside and outside the $q = 1$ resonant surface, and to have rapidly affected, afterwards, the whole plasma column. The assumption that an

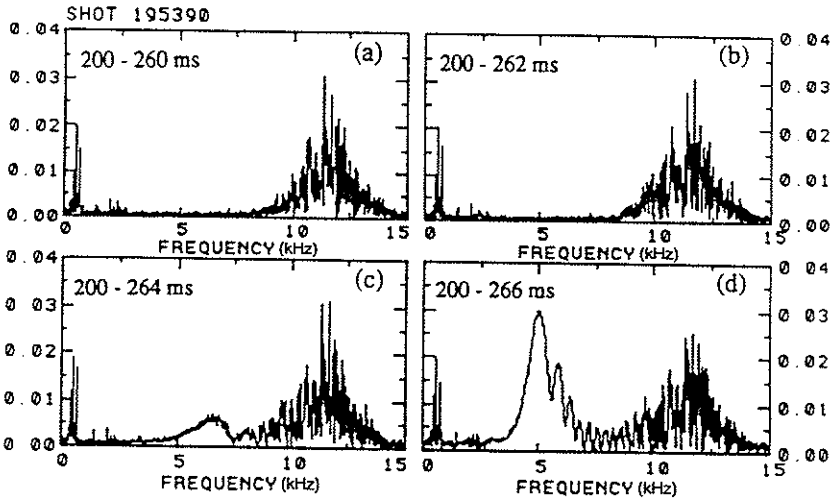

FIG. 8. Fourier spectrum diagrams showing the frequency decrease of the Mirnov oscillations for plasma pulse 195 390 during the last moments before the major disruption takes place. The 200 ms lower limit was arbitrarily chosen, in order to increase the graphic resolution. The time interval considered for each diagram is shown at the left top.

$m = 1$ and $m = 2$ mode interaction occurred and consequently triggered this disruption is reinforced by the fact that the soft X ray and poloidal magnetic field signal fluctuations exhibited the same frequency values during the entire disruption phase. The frequency was found to be around 6 kHz at the beginning of the process, and, as the disruption developed, its value continuously decreased until a fast drop in the soft X ray emission was observed at the instant $t \approx 316$ ms, associated with the occurrence of a minor disruption. Immediately afterwards, the oscillation frequency was measured to be only approximately 3 kHz. Another minor disruption and another drop in the soft X ray emission occurred 2 ms later. At this point the signal frequency has decreased to only about 2 kHz and, immediately afterwards, a large negative loop voltage spike was measured. It is interesting to note, furthermore, that the H_α signal (Fig. 5(e)) fully reflected the soft X ray emission changes and even exhibited the growing amplitude oscillations with the same frequency values as observed on the magnetic coils and the X ray signals. This means that the rapid changes in the plasma core were somehow tightly linked with changes at the plasma boundary.

5. INVESTIGATING DISRUPTIONS WITH THE LOCKED MODE DETECTION COILS

In TEXT-U discharges, the fluctuating radial magnetic field, measured by the locked mode coils, usually shows an increase in amplitude prior to the occurrence of a disruption. The time duration of these precursor oscillations varied significantly, from a few milliseconds to several tens of milliseconds. For nearly all the plasma pulses analysed, the oscillations on the locked mode coil signals started at about the same time as an interaction between the $m = 1$ and $m = 2$ MHD modes. This mode interaction, which is initiated by the growth of the $m = 2$ resistive mode (apparently after it has reached a certain threshold amplitude), as has been described above, seems to be an important mechanism for triggering major disruptions in TEXT-U. An analysis done on the relative timing of the event on the various diagnostic signals, and the way the plasma was affected, suggested that the presence of perturbed radial magnetic fields prior to major disruptions was more a consequence of the mode coupling than the actual trigger of the disruptive instability. The experimental results obtained, which will be presented in the following, will provide qualitative support to this statement.

5.1. Fast disruptions

Major disruptions in TEXT-U can occur on a very fast time-scale when comparing, for example, the frequency and the number of oscillations observed on the magnetic signals between the instants of time the disruption is triggered and the occurrence of the total plasma current collapse. The discharge shown in Fig. 6 is a typical example with $I_p \approx 170$ kA

(Fig. 6(a)) disrupting at $t \approx 266$ ms, when the average electron density has reached its maximum (Fig. 6(b)) and $q_{cyl} \approx 4.5$. The raw signal from one set of locked mode coils is shown in Fig. 6(c). Although noticeable MHD activity is detected by the internal Mirnov coils throughout the discharge (Fig. 6(d)), only near the disruption time is a perturbed radial magnetic field detected by the locked mode coils. This discharge is shown on an expanded time-scale, just before the disruption, in Fig. 7. As has already been mentioned, many major disruptions in TEXT-U are believed to be triggered by the growth of the $m = 2$ mode, which somehow couples to the $m = 1$ mode, causing the characteristic disturbance on the sawtooth oscillations. During this coupling phase, the frequency of the Mirnov oscillations almost always drops from 10–12 kHz to 4–6 kHz. From this point on, the fluctuations observed on the various experimental signals exhibit the same frequency, which in many cases continues to decrease even further.

For the particular plasma pulse under discussion, the coupling is observed to begin at $t \approx 263.5$ ms (Figs 7(b), (c) and (d)). The Fourier spectrum of the poloidal magnetic oscillations (Fig. 8) shows that the frequency of the MHD activity decreases from about 12 kHz (200 ms $\leq t \leq$ 260 ms, the 200 ms limit was arbitrarily chosen) to approximately 5 kHz (200 ms $\leq t \leq$ 266 ms, Fig. 8(d)) during the last few milliseconds of the discharge. Only after this decrease in frequency is the fluctuating radial magnetic field picked up by the locked mode coils. This is due to the conducting tokamak vacuum chamber, which completely shields the locked mode coils, preventing them from detecting internal magnetic oscillations with frequencies above about 6 kHz. Figure 7(d) shows that the oscillations on the locked mode coil signals grow rapidly in amplitude, coincident with an increase in the H_α signal (Fig. 7(e)) and an inward plasma position shift, towards the high toroidal magnetic field side (Fig. 7(f)). Approximately two milliseconds later the plasma collapses.

5.2. Disruptions with long duration precursors

The physical mechanism that triggers TEXT-U disruptions with long duration precursors apparently does not differ very much from that responsible for fast disruptions. The same disturbance of sawtooth oscillations after an increase of MHD activity seen on Mirnov coils is observed. At the same time, oscillations on H_α and other experimental signals are detected. The discharge shown in Fig. 9, with

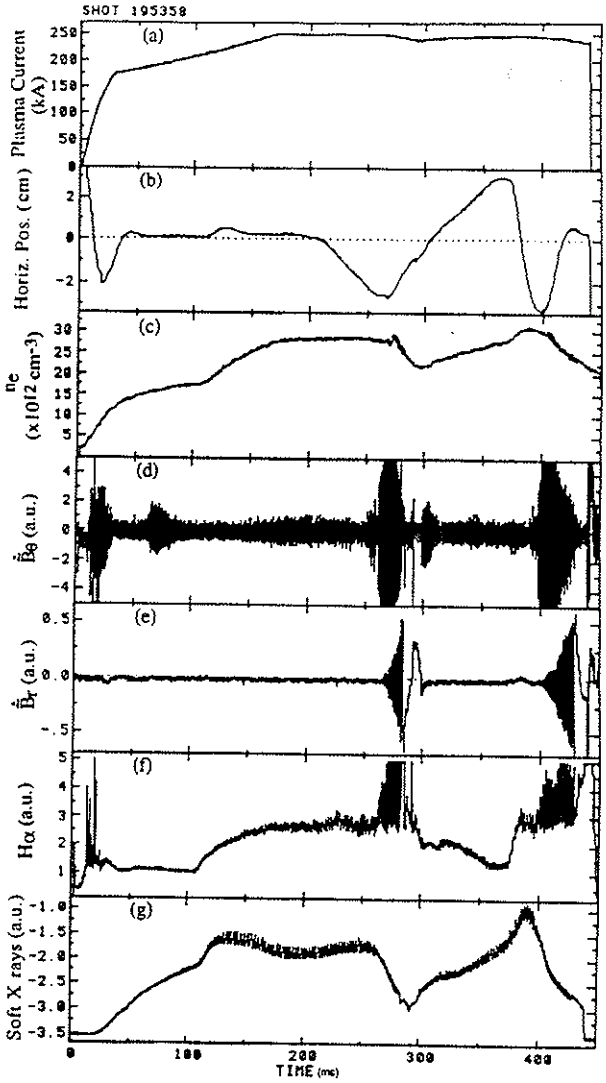

FIG. 9. A TEXT-U disruptive discharge with long duration precursors. The signals correspond to: (a) plasma current, (b) plasma horizontal position, (c) electron density, (d) Mirnov oscillations, (e) fluctuating radial magnetic field, (f) H_α, (g) soft X ray intensity.

$I_p \approx 245$ kA, $B_\phi = 2.28$ T and plasma radius $a = 26.8$ cm, exemplifies these characteristics. The plasma horizontal position, after being deliberately shifted by a few centimetres with a prescribed waveform (Fig. 9(b)), is believed to have caused the boundary of the plasma to interact with the limiter (Figs 9(c) and (g)), destabilizing the $m = 2$ mode (Fig. 9(d)) and originating the minor and major disruptions occurring at $t \approx 290$ ms and $t \approx 440$ ms, respectively. In both situations, the plasma current decreases slightly (Fig. 9(a)), and the locked mode coils begin to detect the increasing radial magnetic

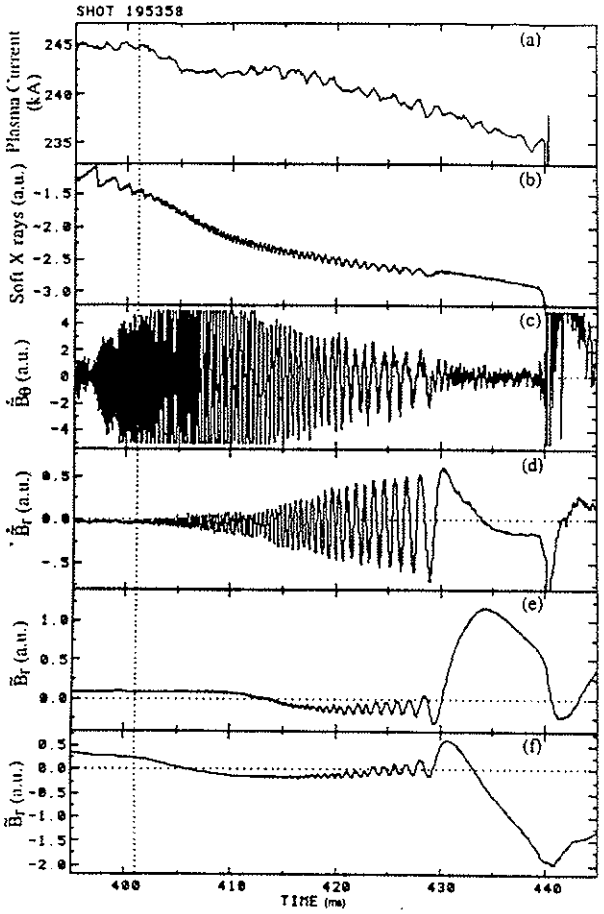

FIG. 10. Signals related to the plasma pulse shown in Fig. 9, in an expanded view, close to the disruption time. The integrated signals generated by the two pairs of locked mode detecting coils are shown in (e) and (f).

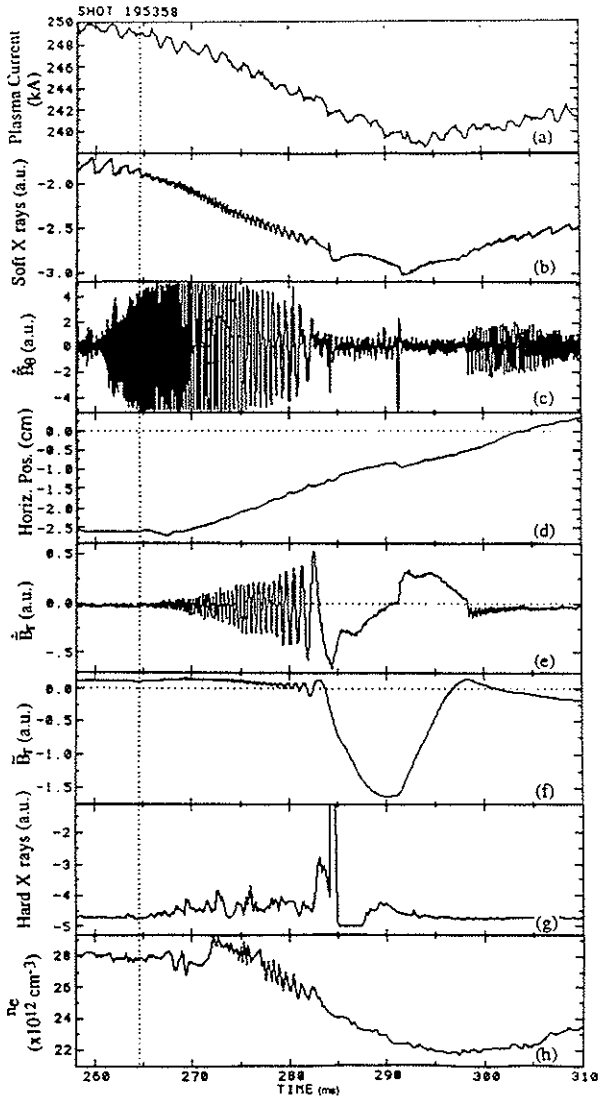

FIG. 11. Expanded view of some of the experimental signals taken for the plasma pulse shown in Fig. 9, during the occurrence of the minor disruption. The integrated signal generated by one pair of locked mode detecting coils is shown in (f).

field perturbation (Fig. 9(e)). Also, large fluctuations appear on the H_α signal (Fig. 9(f)). The oscillations on the various diagnostic signals again all have the same frequency just prior to the disruption.

For most of the major disruptions with long duration precursors that were analysed, the oscillation frequency typically decreases from 10–12 kHz at the time of mode coupling to 1–2 kHz when the plasma current collapses. Less frequently observed, however, are cases in which the mode seems to completely lock some time before the negative loop voltage spike occurs. The plasma pulse shown in Fig. 9 is one such case. In this discharge the MHD frequency before mode coupling was about 12 kHz and continuously dropped until the plasma collapse took place. Looking at the soft X ray and $\dot{\tilde{B}}_\theta$ signals in more detail (Figs 10(b) and (c)), one can see that there are virtually no oscillations on these signals during the last 10 ms of the discharge. This signature is usually interpreted as a complete cessation of magnetic island rotation. However, if the experimental signals from the two pairs of locked mode coils are integrated numerically and compared (Figs 10(e) and (d)), one can see that the modes are still rotating in the toroidal direction, but now with a frequency of only about 50 Hz.

The amplitude of the odd-n ($n = 1$) radial magnetic field measured by the locked mode detecting coils at $t \approx 430$ ms, i.e. just before the oscillations in the soft X rays and the fluctuating magnetic signals decrease to the noise level, was estimated to be

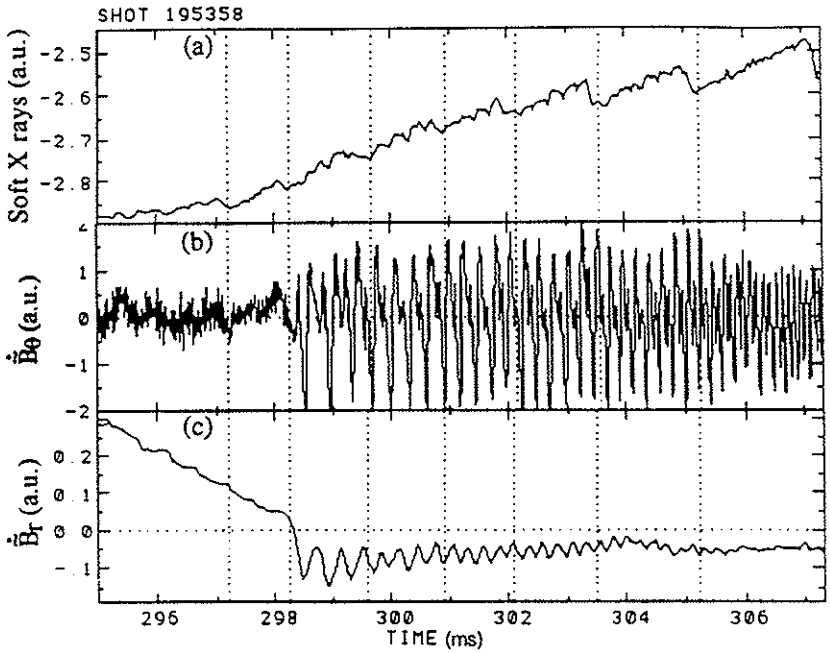

FIG. 12. After the minor disruption has taken place, it seems that sawteeth are observed again on the central soft X ray signal even before the mode unlocking occurs.

$\tilde{B}_{r(\mathrm{wall})} \approx 8.8$ G, which results in $\tilde{B}_r/B_\theta \approx 0.5\%$. In these estimates, the experimental signals have been corrected to take into account the wall penetration effect. Also, the resistive MHD perturbation growth rate was calculated, using the locked mode coils integrated signals, to be $\gamma = (2.7 \pm 0.5) \times 10^2\ \mathrm{s}^{-1}$.

Assuming a cylindrical geometry model for the equilibrium, a parabolic profile for the plasma current distribution and $q(0) \approx 0.9$, the position of the $q = 2$ magnetic surface for this plasma discharge was estimated [27] to be at $r_s^{(q=2)} \approx 22.3$ cm, while the soft X ray signals indicated the $q = 1$ magnetic surface to be located at $r_s^{(q=1)} = 8.2 \pm 2$ cm. The half-width of the magnetic island at the $q = 2$ resonant magnetic surface was calculated using the following expression [27, 28]:

$$\Delta_{m,n=1} = 2\sqrt{\frac{r_s \tilde{B}_r}{m\Psi_0''}\left(\frac{r_{\mathrm{coil}}}{r_s}\right)^{m+1}} \qquad (1)$$

where $r_{\mathrm{coil}} \approx 32$ cm corresponds to the position of the locked mode detectors, and $\Psi_0'' = \partial^2\Psi_0/\partial r^2$, $\Psi_0(r)$ being the unperturbed flux. When the mode 'locked' ($t \approx 430$ ms), we calculated $\Delta_{2,1} \approx 2.6$ cm. However, at the disruption time (i.e. just before the plasma collapse at $t \approx 440$ ms), the amplitude of the radial magnetic signal was measured to be $\tilde{B}_r/B_\theta \approx 1.1\%$, which corresponds to an island at the $q = 2$ resonant surface with half-width $\Delta_{2,1} \approx 3.6$ cm.

Interestingly, these principal characteristics were also observed during the minor disruption that occurred earlier in this discharge. As shown in Fig. 11, after the usual disturbance of the sawtooth activity caused by the $m = 2$ MHD mode at $t \approx 264$ ms (Figs 11(b) and (c)), the plasma current started decreasing (Fig. 11(a)) while the plasma horizontal position started moving towards the centre (Fig. 11(d)). The MHD frequency seen on the Mirnov coils (Fig. 11(c)) continuously decreased from 12 kHz at $t \approx 255$ ms until the 'locking' occurred at $t \approx 283$ ms. At this time, the amplitude of the corrected radial magnetic field was estimated to be $\tilde{B}_{r(\mathrm{wall})} \approx 5.8$ G ($\Delta_{2,1} \approx 2.1$ cm), which results in $\tilde{B}_r/B_\theta \approx 0.4\%$. The precursor MHD activity amplitude growth was $\gamma = (3.6 \pm 0.3) \times 10^2\ \mathrm{s}^{-1}$. At that point the frequency of the mode was as low as 40 Hz, as estimated from the integrated locked mode coil signals (Fig. 11(f)). During this period of time, increased hard X ray emission was observed (Fig. 11(g)), despite a continuous movement of the plasma column away from the vacuum vessel outer wall, towards the torus centre (Fig. 11(d)).

Nevertheless, the plasma did not completely quench. At $t \approx 294$ ms, the plasma current

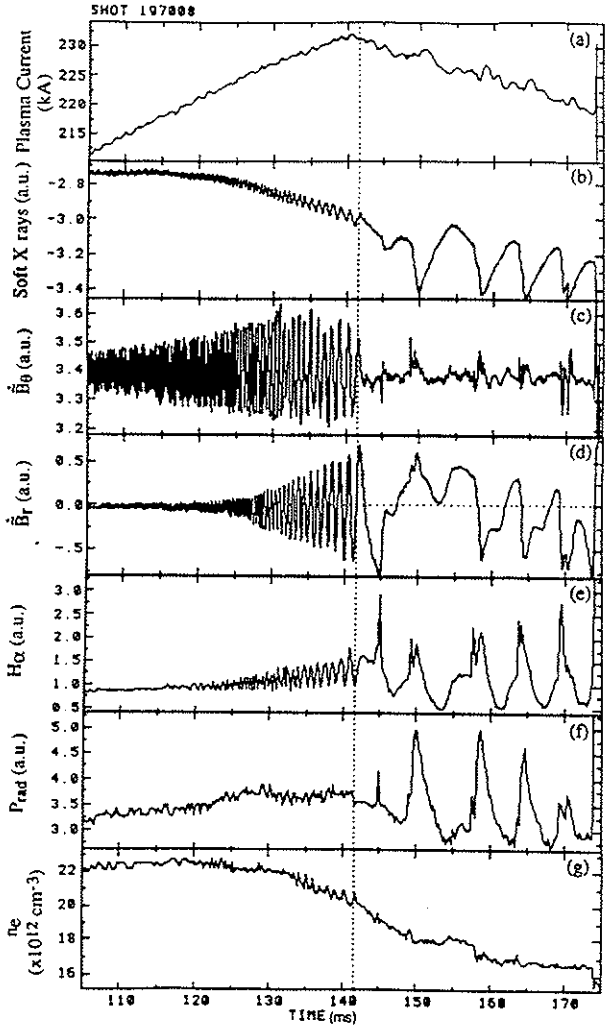

FIG. 13. Example of a discharge where a sequence of minor disruptions occurs while the plasma undergoes a mode locking process, leading the way to a major disruption.

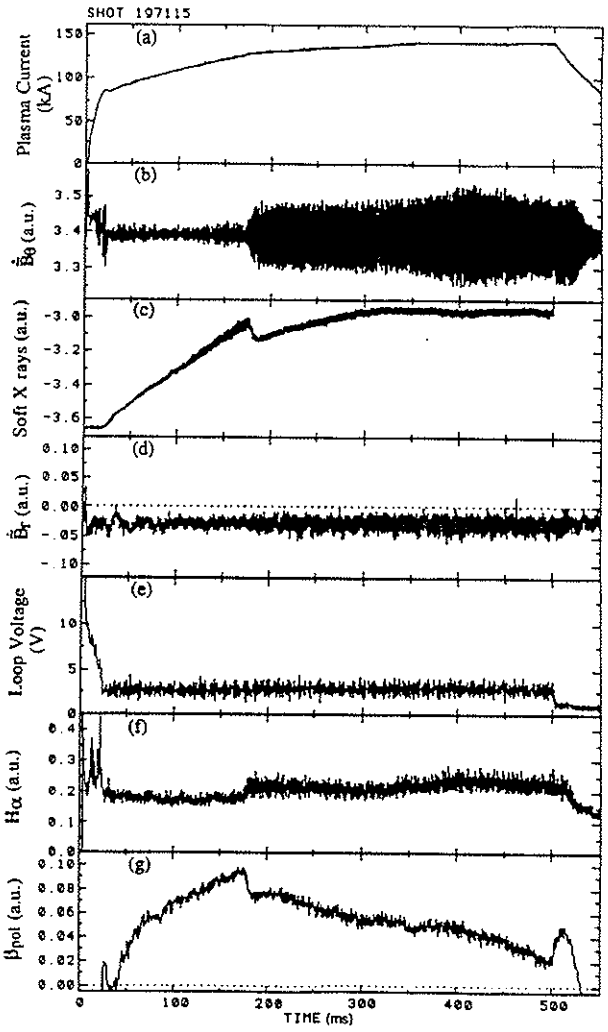

FIG. 14. Example of a plasma discharge that did not end in a major disruption but in which, as a result of a mode interaction that occurred at $t \approx 177$ ms, the confinement was considerably degraded, as observed in the H_α and β_{pol} signals ((f) and (g), respectively).

(Fig. 11(a)) and also the soft X ray emission (Fig. 11(b)) started increasing again. Soon afterwards, oscillations with increasing frequency were seen on the Mirnov coils (Fig. 11(c)). Expanding the time-scale of these experimental signals (Fig. 12), it is apparent that sawteeth are observed again on the central soft X ray signal (Fig. 12(a)) even before the 'unlocking' occurs (Figs 12(b) and (c)) at $t \approx 298.2$ ms.

By measuring the amplitude of the radial magnetic field just before the minor disruption at $t \approx 292$ ms ($\tilde{B}_r/B_\theta \approx 1.2\%$) and just before the plasma once again starts sawtoothing at $t \approx 298.1$ ms ($\tilde{B}_r/B_\theta \approx 0.4\%$), it could be observed that the size of the $q = 2$ island half-width had decreased significantly from $\Delta_{2,1} \approx 3.8$ cm to $\Delta_{2,1} \approx 2.2$ cm, allowing the recovery of the inner region of the plasma column. Only afterwards would the plasma within the $q = 2$ magnetic surface region begin rotating faster, possibly owing to a change in the radial electric field, and would oscillations with increasing frequency consequently be detected by the Mirnov coils.

The plasma pulse shown in Fig. 13 is another example of mode locking that is preceded by long duration precursors. In this case, however, the $m = 1$ and $m = 2$ mode interaction has occurred during the plasma current ramp-up phase (Fig. 13(a)). Soon after the plasma current has reached a plateau, about 30 ms before the end of the discharge, the oscillations on the soft X ray and $\tilde{B}_\theta$ signals

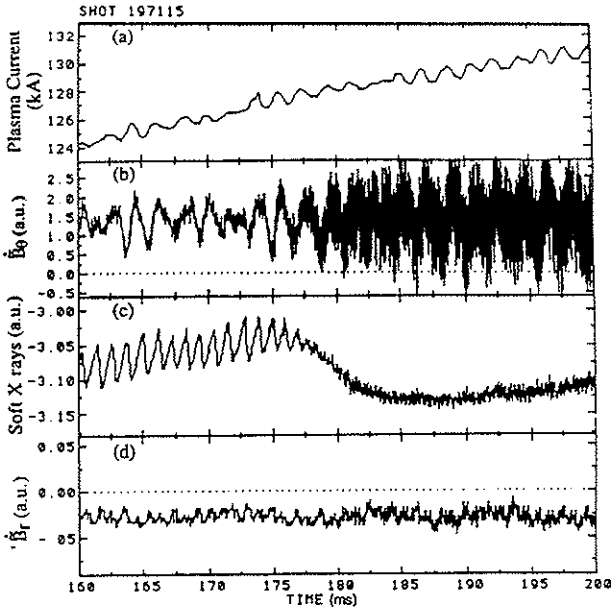

FIG. 15. Expanded view of some of the signals shown in Fig. 15. Note the disturbance in the soft X ray signal (c) concomitantly with the amplitude increase of the Mirnov oscillations (b), indicating that a mode interaction probably has taken place at $t \approx 177$ ms.

disappear (Figs 13(b) and (c)). During this interval the cylindrical safety factor is about 2.7. While 'locked', several partial disruptions occur before the plasma fully collapses, as indicated by the spikes in the loop voltage and by the structures observed in the diagnostic signals. The growth rate of the MHD oscillations that preceded the mode 'lock' was calculated to be $\gamma = (2.7 \pm 0.5) \times 10^2\ s^{-1}$. Finally, it is interesting to note that a few oscillations are observed on $\tilde{B}_\theta$ and H_α (Figs 13(c) and (e)) near the time of these partial disruptions, indicating perhaps that at least one $m \geq 3$ mode is still rotating.

6. CONFINEMENT DEGRADATION

Figure 14 shows a plasma discharge that did not end in a major disruption, but which suffered a mild partial disruption at $t \approx 177$ ms as a result of the mode interaction that occurred earlier. Coincident with the rapid growth of MHD activity (Fig. 14(b)), a relatively small decrease in central soft X ray emission is observed (Fig. 14(c)) and a slight radial magnetic field perturbation increase is detected by the locked mode coils (Fig. 14(d)). Although no change was observed in the loop voltage (Fig. 14(e)), increased H_α emission was detected (Fig. 14(f)) and poloidal beta, β_{pol}, subsequently decreased (Fig. 14(g)), indicating a confinement degradation. Details of this pulse at the time of the mode interaction, when the sawtooth oscillations in the soft X ray signal give place to a strong $m = 1$ fluctuation, are shown in Fig. 15. Note, once more, that the low frequency oscillations on the internal Mirnov coil signal (Fig. 15(b)) are just spurious pick-up from external power supplies. The Fourier spectrum of the poloidal magnetic oscillations (Fig. 16) shows the frequency of the MHD activity for particular time intervals before ($\approx$12 kHz), during ($\approx$7 kHz) and after MHD mode coupling ($\approx$6.5 kHz). Note that the frequency remains near 6.5 kHz until the end of the discharge.

7. PLASMA CURRENT COLLAPSE PHASE

The collapse of the plasma current in TEXT-U, due to major disruptions, did not follow a unique pattern. It was observed, for example, that after the typical loop voltage negative spike the current decayed to zero on a time-scale that varied over one order of magnitude, from less than 5 ms to more than 50 ms. The pulse shown in Fig. 17 is a case where the plasma current decayed in about 12.5 ms, when $q_{cyl} \approx 4.4$. After an initial interaction between the $m = 2$ and $m = 1$ modes at $t \approx 427$ ms (Figs 17(c) and (d)), a partial disruption occurred causing the soft X ray emission to decrease to approximately one quarter of its initial value. Following that, the amplitude of the $m = 2$ perturbation decreased while the X ray emission increased. Shortly after, however, the perturbation increased again and a second and a third partial disruption occurred. By this point, the confinement had already been strongly degraded. The plasma kept moving towards the high B_t side, as shown in Fig. 17(e), and the feedback system was unable to control the plasma position. Finally, at $t \approx 435$ ms, a major disruption took place and both the characteristic bump on the plasma current and the loop voltage negative spike were detected (Figs 17(a) and (b)). The plasma current then slowly decayed to zero. It is interesting to note, however, that during the decay several bumps can be identified on the plasma current signal (Fig. 17(a)), which are correlated with structures observed on several other diagnostic signals (Figs 17(b) to (f)). It seems that the plasma column interacted very strongly, several times, with the limiter and vacuum chamber walls, during the plasma current decay. During each interaction, the external and colder region of the plasma column is presumably lost. The increase of soft X ray

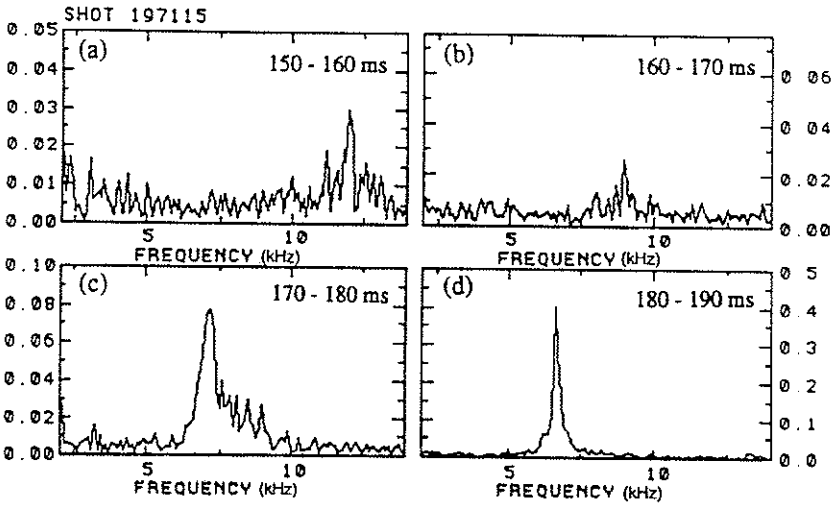

FIG. 16. Fourier spectrum analysis of the pulse presented in Figs 14 and 15, showing that the frequency of the Mirnov fluctuations decreases from approximately 12 kHz (before the mode coupling) to about 6.5 kHz (after the mode coupling). The time interval considered for each diagram is shown at the right top.

emission and the decrease of the H_α signal that followed indicate that the system partially recovers. However, the overall confinement conditions have changed dramatically and the disruptive process is, consequently, irreversible. At $t \equiv 444.5$ ms, the plasma current is about half of its original value, the X ray emission indicates that the plasma temperature is extremely low, and the column displacement towards the inside is very large. Thus, about 3 ms later the pulse ended, with the plasma current decaying to zero.

Although similar observations have been made both for pulses that disrupted either very close to or far away from the density limit, many other pulses were observed to decay on a significantly shorter time-scale. Certainly, the faster the plasma decays, owing to a disruption, the higher are the induced voltages and stresses on the tokamak electromechanical components. Therefore, if the mechanisms that lead the plasma current to decay can be understood and possibly controlled, safer tokamak operation can be obtained.

In Fig. 18, the basic characteristics of the fast current decay disruptive pulses are shown. After the typical disruption signals are observed, i.e. the bump on the plasma current (Fig. 18(a)) and the negative loop voltage spike (Fig. 18(b)) at $t \approx 435$ ms, when $q_{cyl} \approx 4.3$, the plasma current then decays in no more than 5 ms. Probably owing to the abruptness of the event, neither the plasma current nor horizontal position (Figs 18(a) and (c)) diagnostics could accurately track these changes. The mode coupling that probably triggered the disruption occurred at $t \approx 433.5$ ms (Figs 18(d) and (e)). Soon afterwards, the soft X ray emission rapidly dropped to zero, while a strong increase was observed on the H_α signal (Fig. 18(f)).

It is worth noting that the above fast disruption shot (No. 190 602) just preceded the slow one discussed previously (No. 190 603), so the gross parameters of the plasma were about the same for both of them. Maybe one important difference is that after a disruption, impurities are often released from the walls in a greater quantity, and there are indications that they remain within the vacuum chamber until the next pulse. Only after several discharges do the vacuum chamber walls become clean. Therefore, considering that the discharge shown in Fig. 17 would have a higher Z_{eff} than the one that just preceded it, possibly the higher Z_{eff} of the plasma could result in a slower plasma current decay following a major disruption. Analysing, however, other disruptive discharges, it was verified that in some cases where two consecutive shots disrupted the second one had a faster plasma current decay. So the wall condition after a major disruption does not solely determine the plasma current decay rate. Another possible explanation for the variation in plasma current decay rates involves the energy stored in the system at the disruption time; i.e. the greater the energy stored,

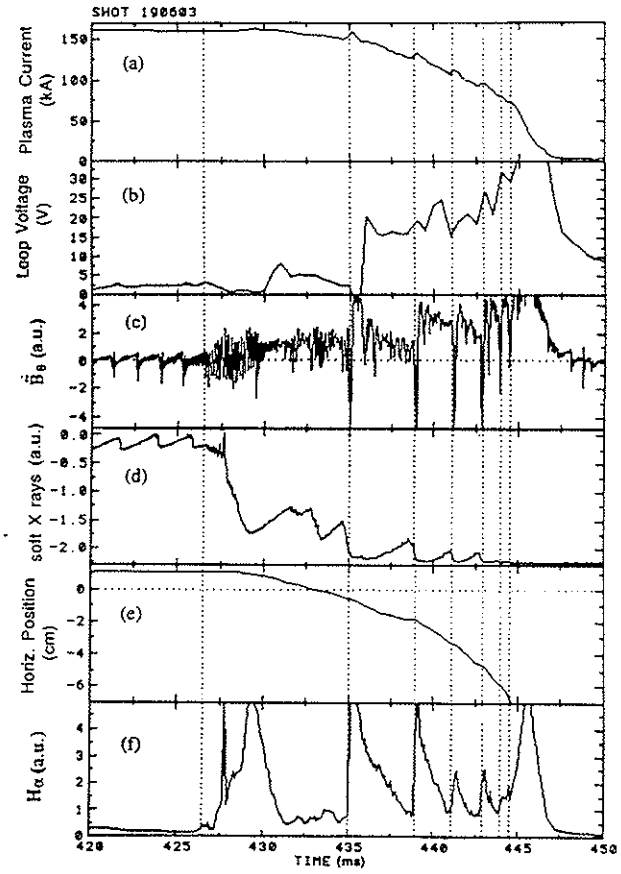

FIG. 17. Long plasma current decay, following a major disruption. Several partial disruptions can be observed to take place during the last moments of this discharge.

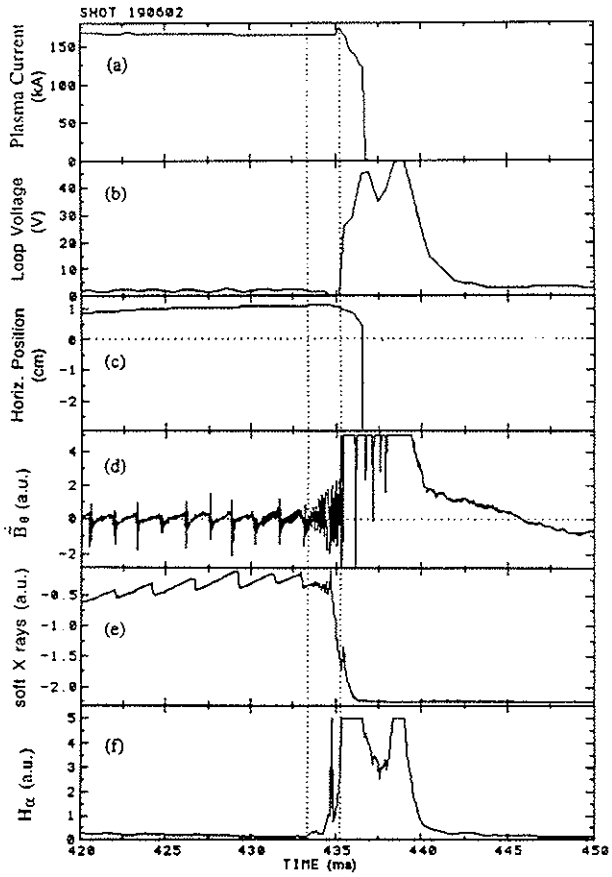

FIG. 18. Example of a plasma discharge that exhibits a very fast plasma current decay following a major disruption. Note that, as already mentioned in the text, the sawtooth-like structures observed in some of the $\tilde{B}_\theta$ signals presented are only externally produced noise picked up by the coils located outside the vacuum chamber.

the longer the disruption time-scale. This possibility was investigated but no strong evidence was found to support it; discharges with the same plasma current and about the same amount of stored energy were observed to disrupt on completely different time-scales. On the other hand, studies carried out on fast current decay disruptive pulses in JET have raised the possibility that a high impurity influx, which would penetrate to the interior of the plasma as a narrow propagating front, could be the cause of the fast electron temperature drop that was observed just before the negative loop voltage spike [29]. Calculations have been performed which showed that such a high level of impurity release by the limiter or wall surfaces could only result from an asymmetric power deposition [29]. Perhaps a similar mechanism, involving the process by which impurities are released from the plasma facing components and the way in which they propagate into the plasma, could explain the TEXT-U observations reported in this paper. However, this study would undoubtedly require taking more appropriate and specific data during the disruptive process.

Finally, it is worth mentioning that in TEXT-U, contrary to what has been suggested elsewhere [30], different plasma impurity conditions do not always directly restrict the tokamak operating space in a Hugill diagram. This was concluded after obtaining Hugill plots for pairs of consecutive discharges, as in Fig. 19. It is quite clear from this case, for example, that the density limit for the discharge with higher Z_{eff} (No. 190 603) did not degrade, but even improved slightly with respect to the pulse with lower Z_{eff} (No. 190 602). Furthermore, the assessment that the plasma density limit is not simply related to the Z_{eff} value is also corroborated by observations made in different devices (TEXT and JET) for helium

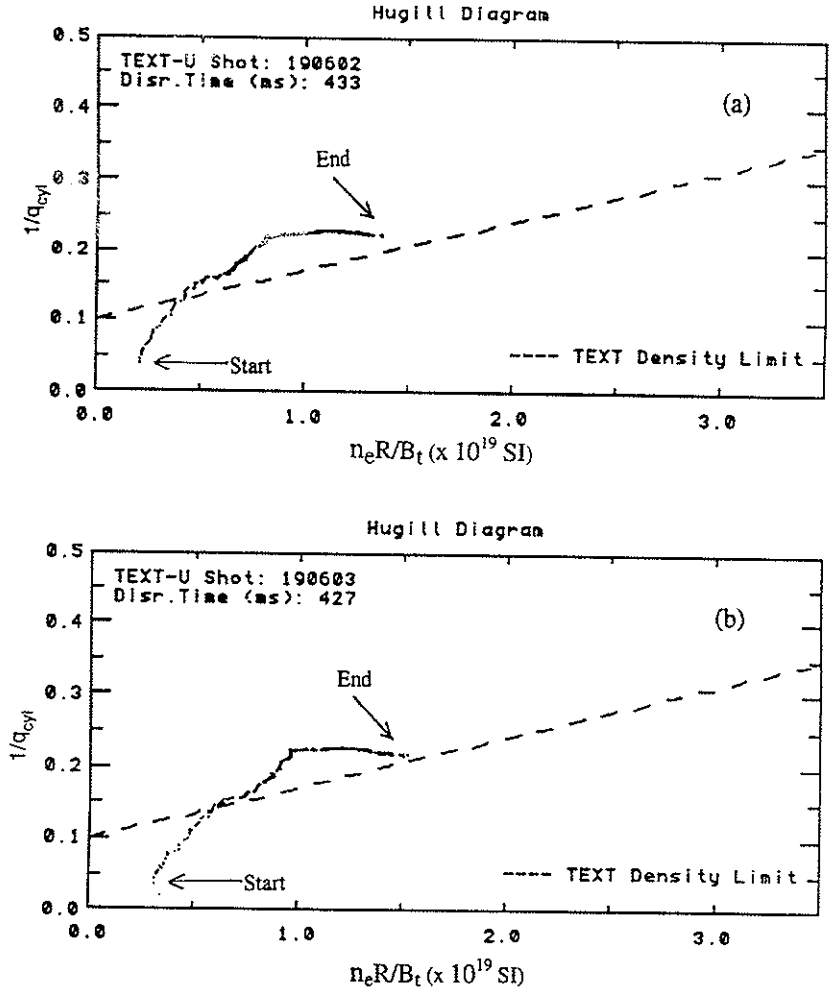

FIG. 19. Trajectories of two consecutive plasma disruptive pulses.

discharges and for discharges with impurity pellet injection. In those cases, which certainly represent a high Z_{eff} condition, the disruptions took place well beyond the normal density limit.

8. CONCLUSIONS

The triggering mechanism for major disruptions in TEXT-U circular plasmas has been investigated. The density limit delineated in a Hugill diagram was not useful by itself in determining the onset conditions for a major disruption, as disruptions were frequently observed within the Hugill limits. Also, strong radiation emission was often not identified as the probable cause for the plasma column to contract, lose confinement and ultimately disrupt. On the other hand, MHD mode coupling involving mainly the $m = 2$ and $m = 1$ components was identified as a good candidate for the main triggering mechanism for major disruptions. The plasma current decay time, during a disruption, was observed to vary substantially from shot to shot. The reason for this variation was investigated, in terms of the average Z_{eff}, plasma current, stored energy and plasma density, but no simple and direct correlation could be found.

On the other hand, the measurement of perturbed radial magnetic fields using two pairs of locked mode detecting coils has proven to be an important tool for investigating disruptions in TEXT-U plasmas. $\dot{\tilde{B}}_r$ signals with increasing amplitude were detected prior to most of the disruptions analysed. Because of the 6 kHz cut-off limit of the conducting vacuum chamber, the coils were able to measure the presence of fluctuating radial magnetic fields only after the characteristic $m = 2/m = 1$ mode coupling had occurred and the frequency of the Mirnov signals had dropped from approximately 10–12 kHz to 5–6 kHz. These oscillations on the locked mode coil signals, a

precursor to disruptions, were observed to last from a few milliseconds to several tens of milliseconds.

For some discharges, however, the oscillations on the Mirnov coil and soft X ray signals disappeared prior to the plasma disruption, when $\tilde{B}_r/B_\theta \approx$ 0.4–0.5%. These data, in conjunction with results obtained in other tokamaks, could be interpreted as a stopping of the rotation of the magnetic islands associated with the MHD modes. However, the signals obtained with the locked mode coils show that this is not the case, at least for TEXT-U plasmas. Even after the soft X ray and $\tilde{B}_\theta$ oscillations disappear, the modes still rotate in the toroidal direction but with a very low frequency, estimated to be around 50 Hz. This 'mode locking' was observed for both partial and major disruptions.

ACKNOWLEDGEMENTS

The authors would like to thank Dr. A. Wootton for many useful suggestions and for useful discussions. The first author is also very grateful to all of the FRC staff, for the support received on many occasions, and also to Drs R.M.O. Galvão and I.L. Caldas for helpful discussions. This work was performed under USDOE Grant No. DE-FG03-94ER54241 and with financial support from the Fundação de Amparo à Pesquisa do Estado de São Paulo (FAPESP).

REFERENCES

[1] VERSHKOV, V.A., MIRNOV, S.V., Nucl. Fusion **14** (1974) 383.
[2] WESSON, J.A., et al., Nucl. Fusion **29** (1989) 641.
[3] FINN, J.M., Nucl. Fusion **15** (1975) 845.
[4] DIAMOND, P.H., Phys. Fluids **27** (1984) 1449.
[5] STÄBLER, A., et al., Nucl. Fusion **32** (1992) 1557.
[6] BROWER, D.L., et al., Phys. Rev. Lett. **67** (1991) 200.
[7] KARGER, F., et al., in Plasma Physics and Controlled Nuclear Fusion Research 1976 (Proc. 6th Int. Conf. Berchtesgaden, 1976), Vol. 1, IAEA, Vienna (1977) 267.
[8] ROBERTS, D.E., et al., Nucl. Fusion **26** (1986) 785.
[9] McGUIRE, K.M., ROBINSON, D.C., Phys. Rev. Lett. **44** (1980) 1666.
[10] PIETRZYK, Z.A., et al., Nucl. Fusion **32** (1992) 1735.
[11] VANNUCCI, A., GILL, R.D., Nucl. Fusion **31** (1991) 1127.
[12] TSUJI, S., et al., Nucl. Fusion **25** (1985) 305.
[13] VANNUCCI, A., et al., Plasma Phys. Control. Fusion **31** (1989) 147.
[14] EDMONDS, P.H., et al., in Fusion Technology (Proc. 15th Symp. Utrecht, 1988), Vol. 1, North-Holland, Amsterdam (1988) 342.
[15] SNIPES, J.A., et al., Nucl. Fusion **28** (1988) 1085.
[16] HENDER, T.C., et al., Nucl. Fusion **32** (1992) 2091.
[17] SCOVILLE, J.T., et al., Nucl. Fusion **31** (1991) 875.
[18] KAYE, S.M., et al., Nucl. Fusion **28** (1988) 1963.
[19] LA HAYE, R.J., et al., Nucl. Fusion **32** (1992) 2119.
[20] NAVE, M.F.F., WESSON, J.A., Nucl. Fusion **30** (1990) 2575.
[21] PERSSON, M., BONDESON, A., Nucl. Fusion **29** (1989) 989.
[22] FITZPATRICK, R., HENDER, T.C., Phys. Fluids B **3** (1991) 2230.
[23] FITZPATRICK, R., et al., Nucl. Fusion **33** (1993) 1533.
[24] GREENWALD, M., et al., Nucl. Fusion **28** (1988) 2199.
[25] SMITH, B.A., Disruptions in TEXT Tokamak, Rep. FRCR 342, Univ. of Texas, Austin (1989).
[26] ISLER, R.C., Phys. Rev. Lett. **55** (1985) 2413.
[27] FERNANDES, A.S., HELLER, M.V.A.P., CALDAS, I.L., Plasma Phys. Control. Fusion **30** (1988) 1203.
[28] FINN, J.M., Nucl. Fusion **15** (1975) 845.
[29] WARD, D.J., WESSON, J.A., Nucl. Fusion **32** (1992) 1117.
[30] AXON, K.B., et al., in Plasma Physics and Controlled Nuclear Fusion Research 1978 (Proc. 7th Int. Conf. Innsbruck, 1978), Vol. 1, IAEA, Vienna (1979) 51.

(Manuscript received 12 July 1995
Final manuscript accepted 22 May 1997)

(E-mail address of A. Vannucci:
vannucci@if.usp.br)

Apêndice 4

Artigo publicado sobre a investigação da atuação de campos magnéticos externos no tokamak TBR-1

IL NUOVO CIMENTO VOL. 10 D, N. 10 Ottobre 1988

Influence of Resonant Helical Windings on the Mirnov Oscillations in a Small Tokamak (*).

A. VANNUCCI, O. W. BENDER, I. L. CALDAS(**), I. H. TAN, I. C. NASCIMENTO and E. K. SANADA

Instituto de Física da Universidade de São Paulo
C.P. 20.516, 01498 São Paulo, SP, Brazil

(ricevuto il 2 Giugno 1988)

Summary. — The influence of resonant helical perturbations on the plasma confined by the small tokamak TBR-1 was experimentally investigated. Strong attenuations of the Mirnov oscillations could be easily obtained by activating different resonant helical windings. The amplitudes of these oscillations were restored as the helical perturbation ended.

PACS 52.55 – Plasma equilibrium and confinement.
PACS 52.70 – Plasma diagnostic techniques and instrumentation.

1. – Introduction.

Since the first on pulsator(1), resonant helical windings (r.h.w.) have been widely used in other tokamaks to generate helical perturbations. Experiments with r.h.w. showed that macroscopic oscillations can be controlled and the nature of the disruptive instabilities can therefore be investigated(2,3). The ergodization of the plasma periphery, in order to control the edge plasma

(*) To speed up publication, the authors of this paper have agreed to not receive the proofs for correction.

(**) Partially supported by CNPq.

(1) F. KARGER, H. WOBIG, S. CORTI, J. GERNHARDT, O. KÜBER, G. LISITANO, K. MCCORMICK, D. MEISEL and S. SESNIC: *Proceedings of the V International Conference Plasma Physics Control. Nucl. Fus. Res.* (Tokyo, 1973), IAEA-CN-33/PD-2, 207 (1974).

(2) PULSATOR TEAM: *Nucl. Fus.*, **25**, 1059 (1985).

(3) D. C. ROBINSON: *Nucl. Fus.*, **25**, 1101 (1985).

parameters (4), and the detailed observations of the global modes in the tokamak discharges can also be achieved by using r.h.w. configurations (5).

The influence of r.h.w. perturbations on the plasma confinement was also investigated in the small low-beta tokamak TBR-1 of the Institute of Physics of the University of São Paulo. The minor and major radii of this device are 0.03 m and 0.11 m and the radius at the limiter is $a = 0.08$ m. The toroidal magnetic field ranges from 0.40 T to 0.45 T, the plasma current I_p from 6 kA to 12 kA, the mean electron density is $\bar{n} \simeq 5 \cdot 10^{18}\,\mathrm{m}^{-3}$ and the central electron temperature is $T_0 \simeq 200$ eV. The windings are externally positioned around the torus in such a way they circle the vessel completely. Their helicity can be selected to produce perturbations with $n = 1$ and $m = 2$, 3 or 4. The corresponding resonant helical field, created by the current I_{hel} in the coils (with opposite directions in adjacent conductors equally spaced), has a well-defined and dominant harmonic com-

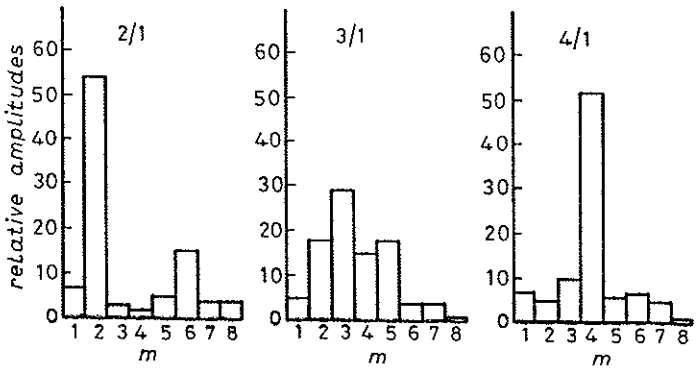

Fig. 1. – Fourier spectra associated with each m/n helical winding arrangement used in this work.

ponent (fig. 1) of the form $\cos(m\theta - n\phi)$, where θ and ϕ are the poloidal and toroidal angles, respectively. Two different pulse shapes of the helical current were used in this work.

2. – Experimental set-up and measurements.

The general confinement and stability conditions of the plasma in the TBR-1 tokamak and the main characteristics of the detected Mirnov oscillations were

(4) Z. YOSHIDA, K. OKANO, Y. SEIKE, M. NAKANISHI, M. KIJUSHI, N. INOUE and T. UCHIDA: *Proceedings of the IX International Conference Plasma Physics Control. Nucl. Fus. Res.* (Baltimore, 1982), IAEA, III, 273 (1983).

(5) J. Y. CHEN, Y. P. HUO, J. K. XIE, L. Z. LI, Q. C. ZHAO, G. Q. ZHANG, M. Q. WANG, D. Q. GUO, P. J. QUIN, G. X. LI, H. Y. FAN and C. B. DENG: *MDH studies on HT-6B and HT-6M Tokamak by active magnetic probes*, Report ASIPP/43 (1987).

reported previously (6). The equilibrium is maintained by a programmed external vertical field. Feedback control of the plasma position is not available yet and some horizontal plasma displacements occur during the discharges. The m.h.d. activity is usually intense and easily detected during the first three milliseconds, when the plasma is less sensitive to disruptive instabilities. The poloidal magnetic field oscillations $\dot{\tilde{B}}_\theta$ were detected through 16 coils equally spaced in the poloidal direction and 4 in the toroidal direction. The main detected modes were characterized by wave numbers $m = 2$, 3, 4 and $n = 1$ with frequencies ranging from 30 to 90 kHz.

The experimental results obtained with a $m = 3$, $n = 1$ helical winding and a current of 185 A are shown in fig. 2. The coils were activated 0.3 ms before the

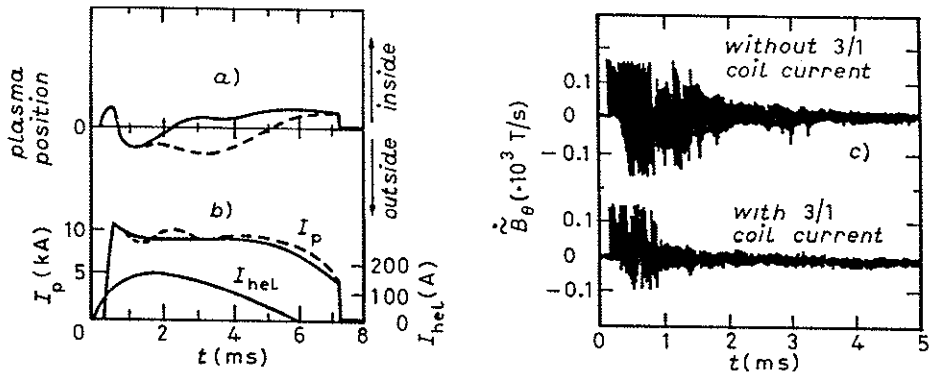

Fig. 2. – In *a*) the horizontal position of the plasma column is shown and in *b*) the plasma helical current time profiles are presented. The full line (——) corresponds to the discharge with 3/1 helical winding activated. In *c*) the corresponding m.h.d. activity is shown.

plasma discharge. The main observed effect was a strong reduction of the m.h.d. activity and this was noticeable mainly during the first 1.5 ms of the discharge. After this period an inward displacement is often observed and the activation of the helical coils tends to anticipate this displacement. This might be related to the instability against horizontal motions (7).

For a current distribution $j = j_0[(1 - r/a)^2]^{1.4}$, which corresponds to $q(a) = 3.8$, the island width of the 3/1 mode was about two times larger than that obtained after the windings were activated (8). The 3/1 coil has also a small $m = 2$ component and attenuation of both the dominant $m = 3$ and the side band $m = 2$ were obtained. The stochasticity parameter decreased from 0.5 to 0.3 with the

(6) I. H. TAN, I. L. CALDAS, I. C. NASCIMENTO, R. P. DA SILVA, E. K. SANADA and R. BRUHA: *IEEE Trans. Trans. Plas. Sci.*, PS-14, 279 (1986).
(7) M. Y. KUCINSKI and I. L. CALDAS: *Z. Naturforsch. A*, 42, 1124 (1987).
(8) A. S. FERNANDES, M. V. A. P. HELLER and I. L. CALDAS: *Plasma Phys. and Contr. Fus.* (1988), to be published.

activation of the coil. Field line tracing calculations for the modified equilibria with the helical windings show large distorted magnetic islands with large ergodic regions (8). The reduction of the m.h.d. activity is probably due to a plasma response to the external resonant perturbation applied rather than a consequent magnetic surface break-up.

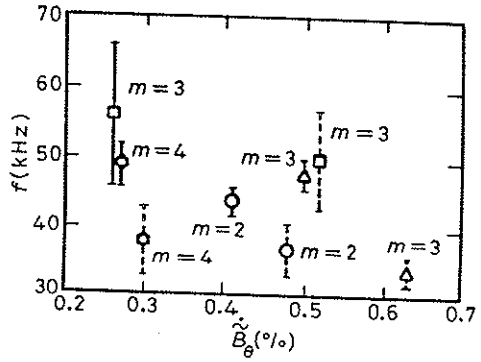

Fig. 3. – Dependence of the frequency with the normalized amplitude of the Mirnov oscillations. —— with coil current on, – – – with coil current off.

An increase of the oscillation frequency associated with an amplitude attenuation was often observed during the activation of the coil (fig. 3). This behaviour agrees with the property of the Mirnov oscillation observed in the TEXT Toxamak (9).

In fig. 4, it is shown the effect caused on the Mirnov oscillations by the activation of a 2/1 helical current with 260 A of amplitude and duration of 3 ms.

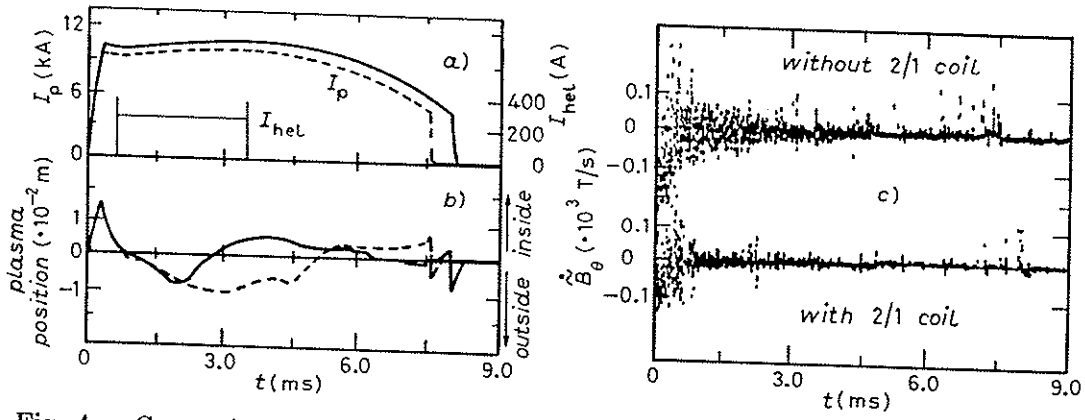

Fig. 4. – Curves in *a*) show the plasma and helical current time profiles and in *b*) the horizontal position displacements are shown. The full line (——) corresponds to the discharge in which the 2/1 helical winding was activated. In *c*) the corresponding m.h.d. signals are presented.

(9) S. B. KIM, T. P. KOCHANSKI and J. A. SNIPES: *A study of MHD oscillations in text using magnetic and soft X-ray diagnostic*, Report FRCR # 256 (1984).

Again in this case, in which a square wavelike current pulse is created, an inward displacement of the plasma column is verified. The poloidal perturbation field $\tilde{B}_\theta/B_\theta$ measured before and after the raise of the current pulse was about $(1.3 \pm 0.3)\%$ and $(0.8 \pm 0.2)\%$, respectively, for the 2/1 mode.

Shortening up the current pulse duration to 0.75 ms, the attenuation of the m.h.d. activity is once again obtained as is shown in fig. 5. After the end of the

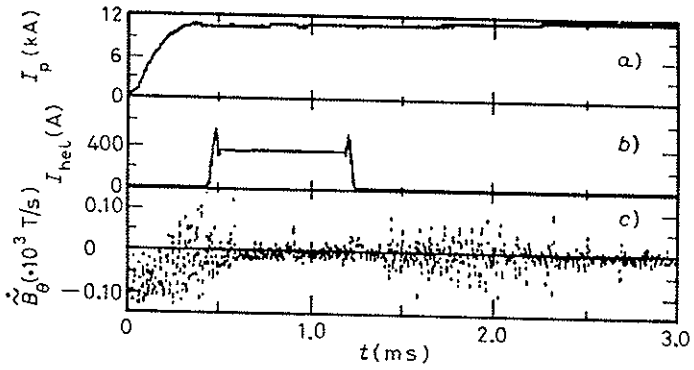

Fig. 5. – Profiles of plasma *a*) and 2/1 helical windings *b*) currents during a discharge in the TBR-1. In *c*) the corresponding m.h.d. activity is presented.

pulse, once the resonant helical-field influence at the plasma ceases, the initial intensity of the oscillations is promptly restored. The time lag observed between the current pulse formation at the helical windings and the attentuation of the m.h.d. activity (~ 200 μs) is consistent with the time penetration field through the steel wall of the vessel (3.1 mm thick).

Fourier analyses calculation of the relative amplitude of the perturbed poloidal field for three different time ranges of the discharge, *i.e.* before, during and after the current pulse application on the r.h.w. was performed. Right before the plasma is effectively submitted to the external-field influence, it could be verified that $\tilde{B}_\theta/B_\theta \sim (0.7 \pm 0.2)\%$. The dominant modes, with almost the same amplitudes, were $m = 3$ and $m = 4$, plus a small contribution of $m = 2$. During the next part the poloidal field oscillations become weaker with $\tilde{B}_\theta/B_\theta \sim (0.3 \pm 0.1)\%$ and the dominant m.h.d. mode is essentially $m = 3$. Finally, in the last region, the m.h.d. amplitude grows up again (with a growth rate $\gamma \simeq (4.3 \pm 0.6) \cdot 10^4\,\mathrm{s}^{-1}$) which corresponds almost entirely to the saturated $m = 2$ component. It was also seen that the oscillations detected during the activation of the r.h.w. still had $n = 1$ only. The frequencies associated with these three parts of the discharge were observed to have values of approximately 65 kHz and 30 kHz, respectively.

Finally, the coils were used as passive helical windings for the detection of particular mode structures. The frequencies of the detected oscillations were the same for all periodic structures with different m and the same $n = 1$.

3. – Conclusions.

The application of low-intensity resonant helical fields ($I_{hel}/I_p \simeq (2 \div 3)\%$) has shown to be an efficient method for attenuating and so for controlling the m.h.d. oscillations in the small low-β TBR-1 tokamak.

Fourier analysis of the magnetic pick-up coils' signals before, during and after the 2/1 helical pulse formation showed that the resonant field probably acted directly on the $q = 2$ island. This is supported by the fact that the $m = 2$ mode was observed only before and after the application of the helical windings. The pulse in fig. 5 illustrates very well this situation. The phenomenological mechanism through which the external field acts on the magnetic islands inside the plasma is not understood yet. A possible explanation could be a change in the current density profile caused directly by the m/n resonant fields on the magnetic islands of the same helicity. However, this consideration could not explain why the activation of a 3/1 helical winding would inhibit or produce sawteeth oscillations ([5]) since this fluctuation is well known to be related with the 1/1 oscillation mode.

* * *

The authors would like to thank Eng. A. G. Tuszel for projecting and constructing the square wavelike current pulse generator for the helical windings and Mr. A. N. Fagundes for developing the TBR-1 data acquisition system. Special acknowledgments are due to Dr. F. Karger (IPP) for suggesting us this work.

● RIASSUNTO (*)

Si è studiata in via sperimentale l'influenza delle perturbazioni elicoidali risonanti sul plasma confinato dal piccolo Tokamak TBR-1. Si sono potute facilmente ottenere forti attenuazioni delle oscillazioni di Mirnov attivando differenti avvolgimenti elicoidali risonanti. Si sono ripristinate ampiezze di queste oscillazioni nel momento in cui è terminata la perturbazione elicoidale.

(*) *Traduzione a cura della Redazione.*

Влияние резонансных спиралевидных обмоток на осцилляции Мирнова в малом токамаке.

Резюме (*). — Экспериментально исследуется влияние резонансных спиралевидных возмущений на плазму, удерживаемую в малом токамаке TBR-I. Можно легко получить сильное затухание осцилляций Мирнова с помощью различных резонансных спиралевидных обмоток. Амплитуды этих колебаний восстанавливаются, когда спиралевидные возмущения выключаются.

(*) *Переведено редакцией.*

Observation of disruptions in tokamak plasma under the influence of resonant helical magnetic fields (*)

M. S. T. ARAÚJO, A. VANNUCCI and I. L. CALDAS
Instituto de Física, Universidade de São Paulo
C.P. 66.318, 05389-970 São Paulo, SP, Brazil

(ricevuto il 19 Giugno 1995; approvato il 20 Febbraio 1996)

Summary. — Disruptive instabilities were investigated in the small-tokamak TBR-1 during the application of resonant helical magnetic fields created by external helical windings. Indications were found that the main triggering mechanism of the disruptions was the rapid increase of the $m = 2/n = 1$ mode which, apparently after reaching a certain amplitude, interacts with other resistive modes: the internal 1/1 mode in the case of a major disruption, or with higher m components, as the 3/1 or 4/1, in the case of minor disruptions. After the coupling, the growth of the associated islands would create a chaotic field line distribution in the region between the corresponding rational magnetic surfaces which caused the gross particle transport and, finally, destroyed the confinement. In addition, investigations on higher Z_{eff} discharges in which a mixture of helium and hydrogen was used resulted in much more unstable plasmas but apparently did not alter the basic characteristics of the disruptions.

PACS 52.30 – Plasma flow; magnetohydrodynamics.
PACS 52.70 – Plasma diagnostic techniques and instrumentation.
PACS 02.30.Nw – Fourier analysis.

1. – Introduction

The harmful consequences of disruptions in tokamaks are already well known. Depending on their strength, they significantly deteriorate the plasma confinement (minor disruptions) and can even lead to its complete loss (major disruptions). Furthermore, the rapid plasma current decay that follows a major disruption can cause severe stress on the electric-mechanic components of the tokamak. However, despite the intense study that has already been performed during the last decades [1-10], the causes associated to the occurrence of the disruptive instabilities are not yet well understood and, presently, this is still one of the main obstacles to the controlled-thermonuclear-fusion research. Accordingly, scaling analysis involving

(*) The authors of this paper have agreed to not receive the proofs for correction.

different tokamaks as the COMPASS, DIII-D, and JET, indicates that the solution to this problem will be of great importance to the next generation of even larger tokamaks [11].

The disruptive instabilities are usually preceded by a fast amplitude growth of MHD modes and, in particular, the major disruptions are commonly observed to be preceded by a sequence of minor disruptions. The main characteristics of major disruptions are: fast negative spike in the loop voltage signal, rapid loss of confined energy and sudden expansion of the plasma minor radius, with a diminution of the major radius.

Since the major disruptions lead to the complete destruction of the plasma confinement, they are the ones that had deserved more attention. Thus, the knowledge of the processes through which a major disruption is created has been the object of great concern and was specifically considered in several works in the literature; many of them present strong evidences that the $m/n = 2/1$ amplitude increase is mainly responsible for triggering this instability. In this context, the interaction of the $m/n = 2/1$ islands with the limiter [12], the coupling between the $m/n = 2/1$ and $m/n = 1/1$ modes [10, 13], and the destabilization of odd m-value modes, such as $m/n = 3/2$, by the growing $m/n = 2/1$ islands [7, 14], were some of the proposed mechanisms to explain the development of major disruptions.

However, despite all the experimental evidences and theoretical work that has been performed, several aspects concerning the major disruptions are still the object of strong controversy. The role played by impurities (Marfes, the rate of radiated power in relation to the input power, the influence of low-Z materials first wall coatings, etc.) and the absence of any precursors to some disruptions are, for example, features that still need further clarification [15-18].

In relation to mechanisms of controlling and possibly suppressing the onset of major disruptions, different processes and systems have already been proposed [19]. Among these, the use of resonant helical windings (r.h.w.) has produced interesting results. The first pioneer studies, showing how disruptive instabilities are affected by resonant helical magnetic fields (r.h.f.), were carried on the Pulsator tokamak discharges, which showed that the occurrence of a major disruption could be either delayed or activated, in response to a weak externally imposed magnetic perturbation created by an $m = 2/n = 1$ r.h.w. [20, 21]. After this work, other investigations involving the application of resonant helical magnetic fields in different tokamaks have been performed, extending the previous results to different discharges conditions and other perturbing helical modes [5, 6, 22-26]. Basically, these experiences showed that the application of r.h.f. could strongly attenuate the Mirnov oscillations amplitude. Therefore, this would mean that the intrinsic nature and the way the disruptive instabilities are triggered could then be investigated with this winding.

More recently, experimental data, supported by theoretical results [27-31], showed that locked modes could be created as a result of naturally existing (or artificially created) error fields. As a rule, when a mode locking occurs, the MHD perturbation amplitude is observed to decrease drastically, as a consequence of the fact that the magnetic islands stop rotating. This would mean that the attenuation of MHD activity, commonly observed during the application of resonant helical magnetic fields, could not be interpreted as a diminution in size of the magnetic islands but, rather, only as an indication that the magnetic islands are slowing down.

It should be noted, however, that whenever a locked mode occurs, the plasma has a strong probability to disrupt. High-current disruptive pulses in JET, for example,

were often observed to be preceded by a mode locking [13]. Therefore, if the condition of locked mode does exist, then degradation of the plasma, followed by a major disruption, should be expected. This is not, though, what one usually gets when resonant helical fields are properly applied; if the helical-currents intensity is below a certain threshold, major disruptions do not occur and they can even be postponed [21]. This is an indication that the application of r.h.f. might not necessarily create locked modes, but effectively decreases the magnetic-island dimensions.

Therefore, since the present knowledge about how disruptions are triggered and how they develop is still inconclusive, it seems worthwhile, in many aspects, to continue the investigations that have already started in the small, low-β, TBR-1 tokamak [8,22]. The characteristics of the major disruptions in this device are very similar, in many aspects, to those that have been observed in larger tokamaks such as JET [13], ASDEX [4], T-10 [10] and TEXT-U [32]. Thus, continuing the study of disruptions in small tokamaks, like the TBR-1, may provide support to larger-tokamak programs, helping to understand the physical processes that lead to the development of disruptions, and, consequently, making its control possible [11,33].

In this work we investigate the response of the plasma facing an external magnetic perturbation, caused by a set of helical windings externally and toroidally installed around the vacuum vessel. The measurement and identification of the precursor MHD modes, in relation to the observed disruptions in TBR-1, were performed using a set of Mirnov magnetic coils. For different kinds of discharge conditions, the analysis of the experimental data confirmed that an interaction between the $m = 2$ and $m = 1$ MHD components is mainly responsible for triggering the major disruptions in TBR-1, whereas the minor disruptions are caused by magnetic-island superposition involving the $m = 2$ and higher-m modes. These triggering mechanisms for minor and major disruptions in TBR-1 were also observed for more unstable plasma discharges, in which the MHD activity was enhanced by the injection of low-Z impurities in the plasma.

Altogether, this paper presents new evidences that disruptions are triggered by an interaction between precursor modes, namely a dominant $m = 2$ and other higher (minor disruptions) or lower (major disruptions) m modes. This overall picture is the same for both the spontaneous and the r.h.w. induced disruptions, and do not change even when low-Z impurity is injected in the plasma. The data presented show that even a small-scale device like the TBR-1 exhibits similar behaviour to larger-sized tokamaks, as far as disruptions are concerned. Thus, these results contribute to extend the observations of disruptions over a larger variety of tokamak operation regimes.

The experimental set-up used is described in sect. 2. The effects of the resonant helical windings on the disruptions and on the amplitude of the precursor modes are presented in sect. 3. The results concerning the influence of impurities in the disruptive instabilities are presented in sect. 4. Finally, discussions of the results and conclusions are given in sect. 5.

2. – Experimental set-up and measurements

TBR-1 (fig. 1) is a small ohmically heated tokamak (o.h.t.) with a complete poloidal limiter, which has minor radius $a = 0.08$ m, major radius $R = 0.30$ m, radius of the wall $b = 0.11$ m, toroidal field $B_\phi \simeq 0.4$ T and plasma currents that last up to 10 ms. For this

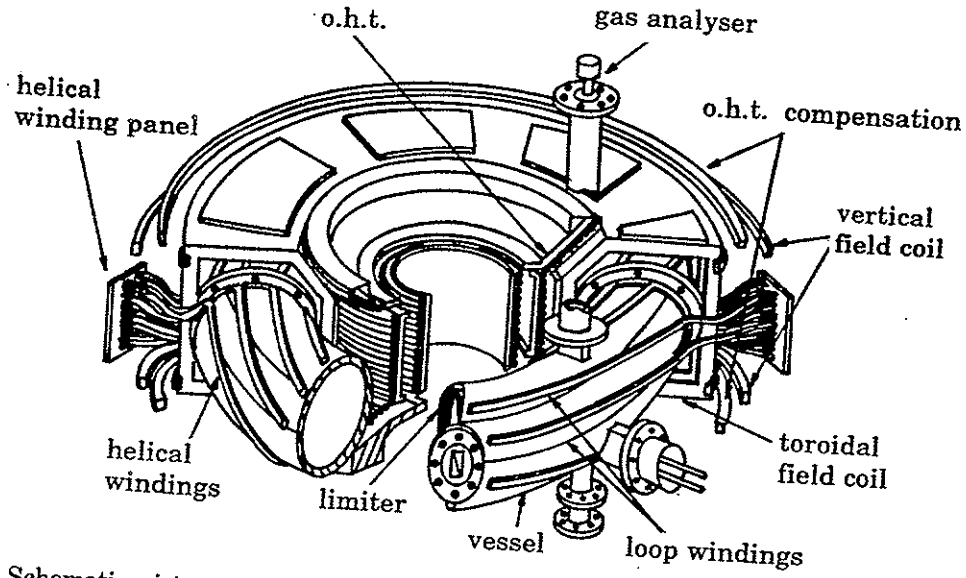

Fig. 1 – Schematic picture of the TBR-1 tokamak.

experiment, the plasma parameters were: central electron temperature $T_e(0) \simeq 150\,\text{eV}$ (estimated from soft–X-ray emission), central density $n(0) \simeq 6 \cdot 10^{18}\,\text{m}^{-3}$ (microwave interferometer measurements) and plasma current $I_p \simeq 9\,\text{kA}$. The two main diagnostics used were the soft–X-ray detection system and a set of Mirnov coils positioned inside the toroidal vacuum vessel. The soft–X-ray flux from the plasma was measured by an array of five surface-barrier detectors (ORTEC model CR019-50-100) installed inside an imaging camera. Each detector viewed a different central-plasma volume through a solid angle delimited by a beryllium- covered slot. The fluctuating poloidal magnetic field was measured by ten pick-up coils, poloidally distributed, and two others placed in toroidally opposite positions.

The output signals, after being amplified, were digitized at 400 kHz and recorded in a PC-386 microcomputer. Spectral analyses based on the fast Fourier transform were performed to identify the main MHD mode characteristics, *i.e.* the wave number, the frequency and the amplitude of the fluctuations. During the plasma discharges, the analysis of the experimental data was done at time intervals of 0.64 ms (256 data points), after the plasma current had reached an appropriate plateau. Similarly to other small- and medium-size tokamaks [5, 6], the dominant MHD modes during the TBR-1 discharges were observed to have the poloidal wave numbers $m = 1, 2, 3, 4$ and toroidal wave number $n = 1$. These modes showed broad frequency spectra with frequencies ranging from 20 kHz to 100 kHz, approximately.

The resonant helical windings, which were used to generate magnetic helical perturbations on the confined plasma, were externally positioned around the torus in such a way that they completely circled the vessel. Although in TBR-1 different r.h.w. helicity can be selected to produce distinct dominant m/n perturbations [22], this paper presents the results obtained only with the $m = 2/n = 1$ r.h.w. As a result, significant attenuation of the Mirnov oscillation amplitude was observed for low-intensity helical currents, $I_h/I_p \leqslant 0.03$, where I_h is the r.h.w. electric current.

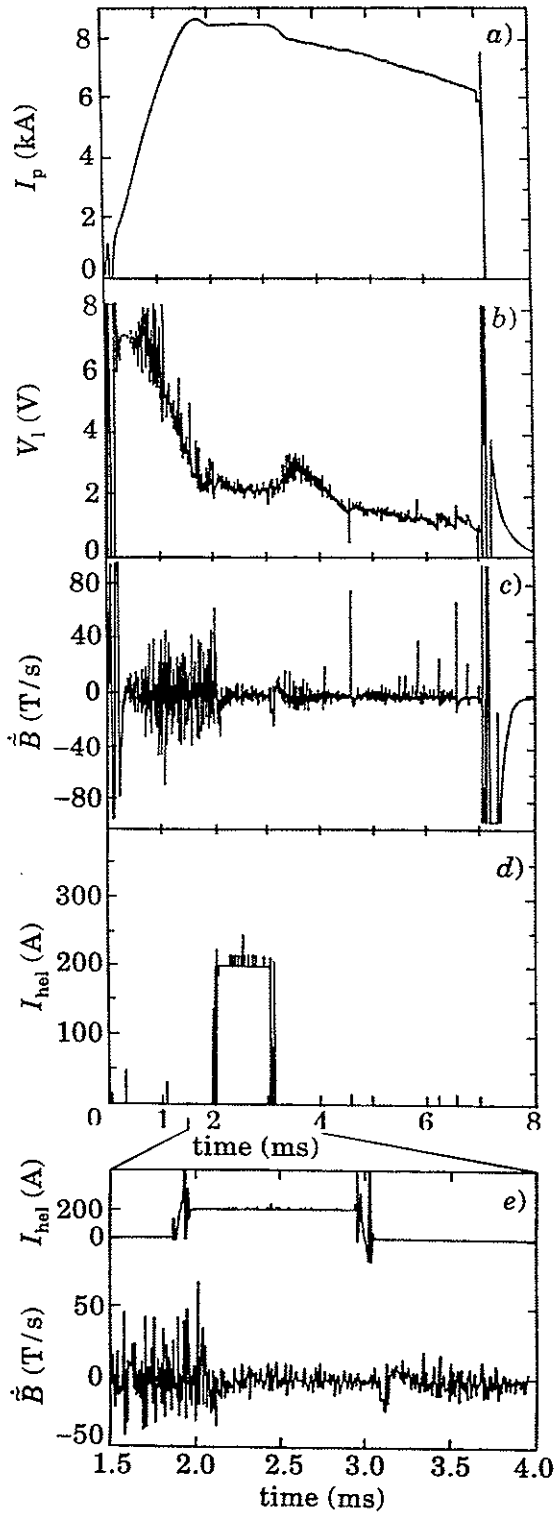

Fig. 2 – Plasma discharge in which a low-intensity r.h.f. was applied, causing a visible attenuation of the MHD activity. The experimental signals showed correspond to: *a*) plasma current, *b*) loop voltage, *c*) Mirnov oscillations, *d*) external helical current intensity and *e*) detail showing the MHD attenuation in a expanded time scale.

On the other hand, for more intense perturbing currents, in the range $0.03 \leqslant I_h/I_p \leqslant 0.05$, the Mirnov oscillations grew in amplitude and consequently triggered both minor and major disruptions.

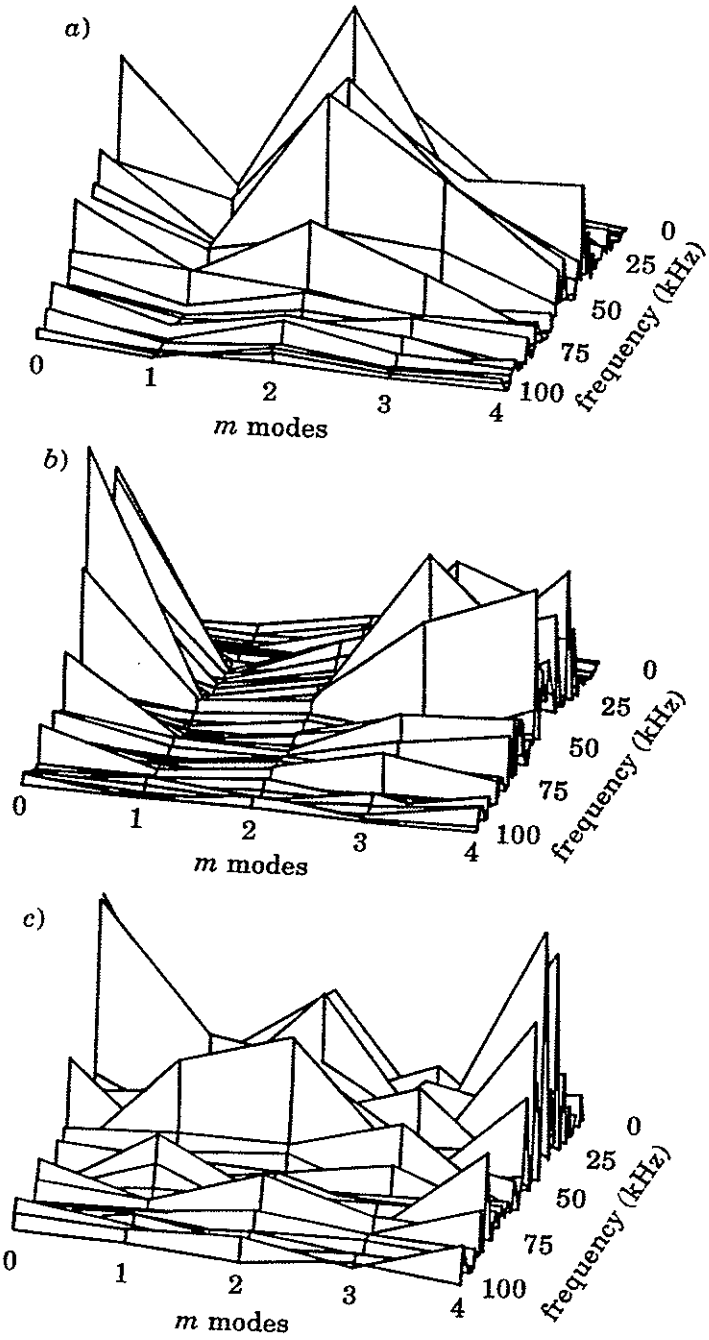

Fig. 3 – Power spectrum analysis of the MHD components before (*a*)), during (*b*)) and after (*c*)) the application of r.h.f., for the discharge showed in fig. 2.

3. – Influence of r.h.f.

The application of r.h.f. for short periods during the TBR-1 plasma discharges resulted either in an attenuation or in an activation of the MHD mode amplitudes, depending basically on the intensity of the applied helical current. In the latter case, major disruptions were subsequently triggered most of the time. The main characteristics concerning both situations will now be presented.

3·1. MHD *activity amplitude attenuation.* – A typical example of how r.h.f., with helicity $m/n = 2/1$, can attenuate the amplitude of the MHD activity is shown in fig. 2. It corresponds to an $I_p^{max} \simeq 8.5\,\text{kA}$ (fig. 2*a*)) plasma discharge that lasted for 7.2 ms, approximately. At $t \simeq 1.9\,\text{ms}$, when the loop voltage was relatively low (about 2.0 V) (fig. 2*b*)), a square wave-like r.h.w. current pulse of magnitude $I_{hel} \simeq 200\,\text{A}$, that lasted only 1 ms, was applied (fig. 2*d*)). This caused a strong attenuation of the oscillations measured by the Mirnov coils (fig. 2*c*)). The time delay of approximately 150 μs, as observed in fig. 2*e*), is due to the penetration time of the external helical field through the vacuum chamber walls. During the period in which the r.h.w. current pulse is on, an improvement on the plasma confinement conditions is obtained, as can be recognized by the relatively smooth loop voltage signal (fig. 2*b*)).

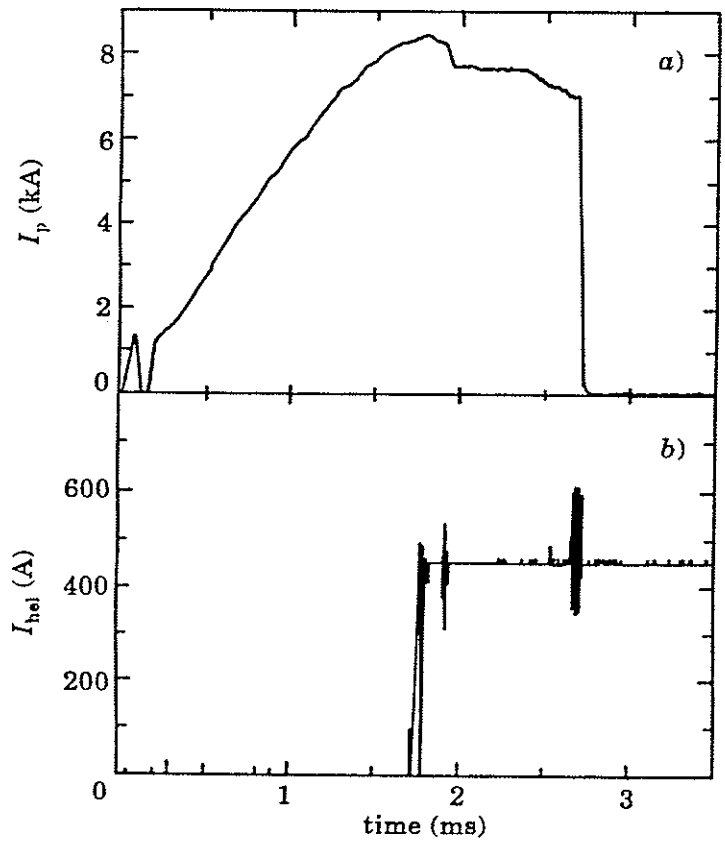

Fig. 4 – Plasma pulse which disrupted (*a*)) during the application of a strong external helical current (*b*)).

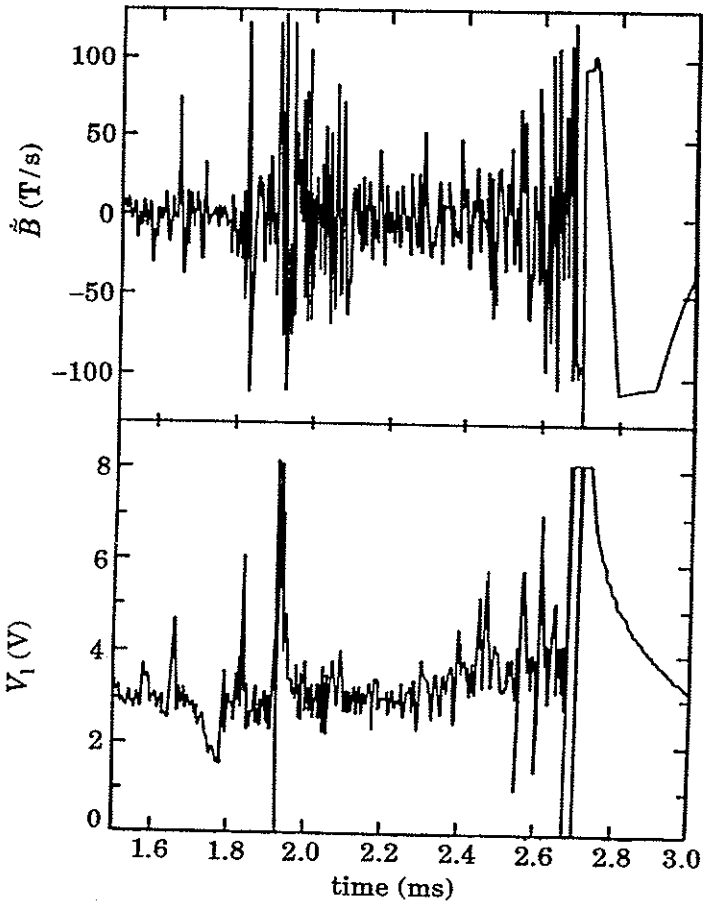

Fig. 5 – Detail showing the amplitude increase of the Mirnov oscillation and the loop voltage signals just before the major disruption showed in fig. 4.

Power spectral analyses of the poloidal MHD components, performed just before (fig. 3*a*)), during (fig. 3*b*)), and after (fig. 3*c*)) the application of helical magnetic perturbation, show that the attenuation on the $m = 2$ mode is much more effective than on the other components. However, these results should be already expected, since the perturbing helical current used has a 2/1 dominant helicity, and also because the $m = 2$ was the dominant mode just before the r.h.w. is activated. After the perturbation is turned off (fig. 3*c*)), the $m = 2$ mode grows and its amplitude becomes comparable to the other components.

3·2. MHD *mode activation.* – The plasma pulse shown in fig. 4 typically exemplifies a discharge in which an increase in amplitude of the MHD oscillations is observed after a strong r.h.w. current has been applied. The 2/1 helical current, with magnitude $I_{\text{hel}} \simeq 450\,\text{A}$, was applied at $t \simeq 1.8\,\text{ms}$ (fig. 4*b*)), which almost immediately triggered the minor disruption that took place at $t \simeq 1.9\,\text{ms}$ and caused the significant decrease of the plasma current at that time (fig. 4*a*)). Soon afterwards, the amplitude of the MHD activity is observed to increase again, as shown in fig. 5 (note the different time scale). These growing precursor oscillations ended up triggering the major disruption, that finally destroyed the plasma column at $t \simeq 2.7\,\text{ms}$.

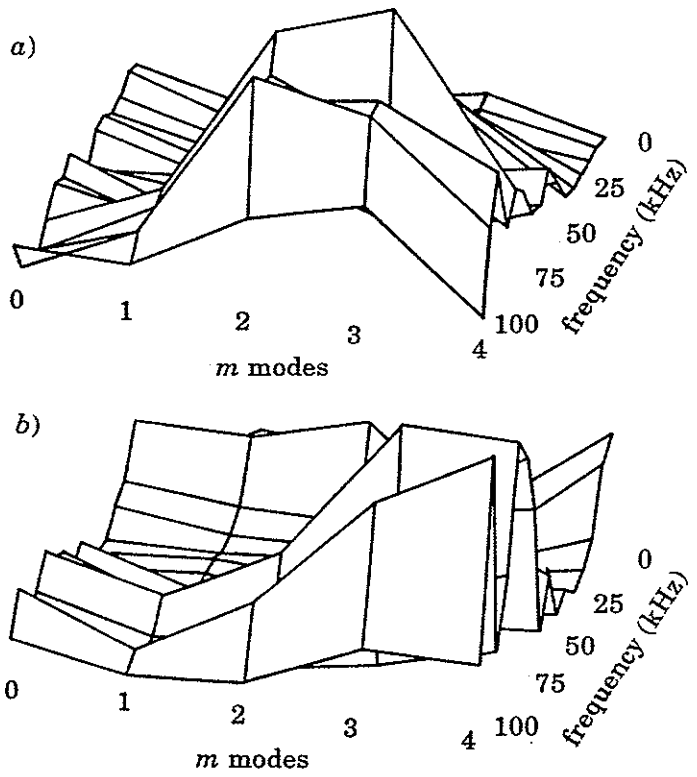

Fig. 6 – Power spectrum of the MHD activity before (a)) and right after (b)) the minor disruption showed in fig. 4 and 5.

In order to identify the main MHD components that were responsible for both the minor and major disruptions observed in this discharge, the derivative of the poloidal magnetic field, measured by the Mirnov coils, was Fourier-analysed. The frequency and the poloidal wave number power spectra, just before and right after the minor disruption, are showed in fig. 6. As one can note, there is a clear predominance of the

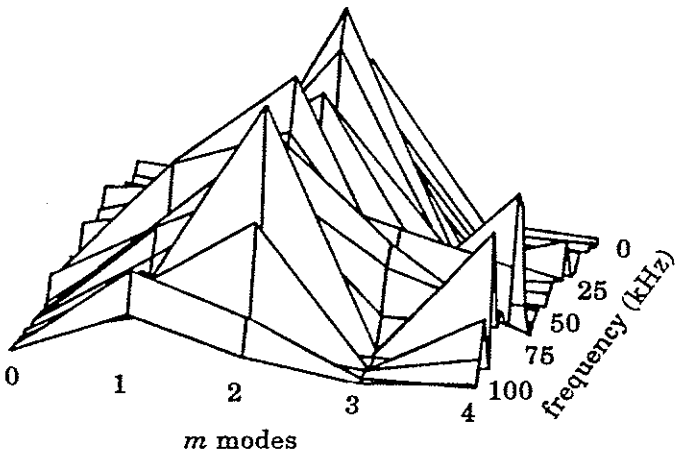

Fig. 7 – Power spectrum just before the major disruption showed in fig. 4 and 5. The predominance of the $m = 2$ component is very noticeable.

$m = 2$ mode, together with the $m = 3$ and $m = 4$ components, before the disruption (fig. 6*a*)). Furthermore, with the activation of the r.h.f., the $m/n = 2/1$ component (mainly the high-frequency part of the spectrum) is attenuated (fig. 6*b*)) and no minor disruption occurs. These observations indicate that the $m = 2$ mode plays an important role in triggering minor disruptions in TBR-1. The existence of a considerable amount of the $m = 3$ and $m = 4$ components, during the process, can be an indication that these secondary modes participate in the disruptive mechanism. These observations support the previously reported evidences that a global mode interaction may be associated to the occurrence of minor disruptions [8, 23, 25, 34].

The predominance of the $m = 2$ mode just before the occurrence of the major disruption is also remarkable (fig. 7); but in this case the $m = 1$ mode is also present, although no strong oscillations were observed on the central soft–X-ray signal. This situation might be understood if one considers the possibility that $q(0)$ is just slightly less than one at disruption time (allowing only a small island to be created at this rational magnetic surface, so no strong soft–X-ray emission would occur), while the intense $m = 1$ component, measured by the pick-up coils, would be caused by the toroidal effect side-band of the large islands at the $q = 2$ magnetic surface. The observation of dominant $m = 2$ and $m = 1$ components just before this disruptive instability might indicate that these two modes could be associated to the development of major disruptions in tokamaks, probably by creating secondary magnetic islands between the $q = 2$ and $q = 1$ magnetic surfaces, in a similar fashion as the mechanism proposed by Finn [34]. In addition, for the TBR-1 tokamak, strong $m = 1/m = 2$ mode coupling has already been reported just before the occurrence of a major disruption [8].

4. – Influence of low-Z impurities on the TBR-1 disruptions

A gas mixture of helium (5% to 16%) and hydrogen was used for investigating the influence of a low-Z impurity on the plasma confinement control with r.h.w. With the introduction of helium the MHD activity became more intense. Thus, for high helium concentration, between 12% to 16%, the plasma was very unstable and the discharge duration was usually short, in the range 2.5 ms–4.0 ms. In these cases, not even low intensity r.h.w. currents could be applied since the fast helical current transient would make the plasma column move rapidly towards the vacuum vessel walls.

On the other hand, for low-He concentrations, around 5%-8%, longer discharges could be obtained which permitted the application of r.h.w. currents. Most of the discharges, however, terminated in a major disruption as a result of the r.h.f. applied. One typical example of such discharges, in which He at 6% was introduced, is shown in fig. 8. It corresponds to an $I_p^{max} \simeq 8$ kA plasma pulse that lasted only 2.6 ms. The r.h.w. was turned on at $t = 2.0$ ms, when the loop voltage was relatively low, about 2.5 volts, and caused a visible attenuation of the MHD activity. Soon afterwards, a major disruption developed and destroyed the plasma at $t = 2.63$ ms. This disruption was preceded by two minor disruptions that occurred at $t_1 = 2.48$ ms and $t_2 = 2.57$ ms (these instants are indicated on the time axis of fig. 9), which led the plasma current to small decays. Concurrently, the loop voltage increased substantially during this period, indicating a higher plasma resistivity (fig. 9*b*)), while the plasma central temperature dropped, as shown by the soft–X-ray signal (fig. 9*d*)). The corresponding Mirnov and horizontal position signals are shown in fig. 9*c*) and 9*e*), respectively.

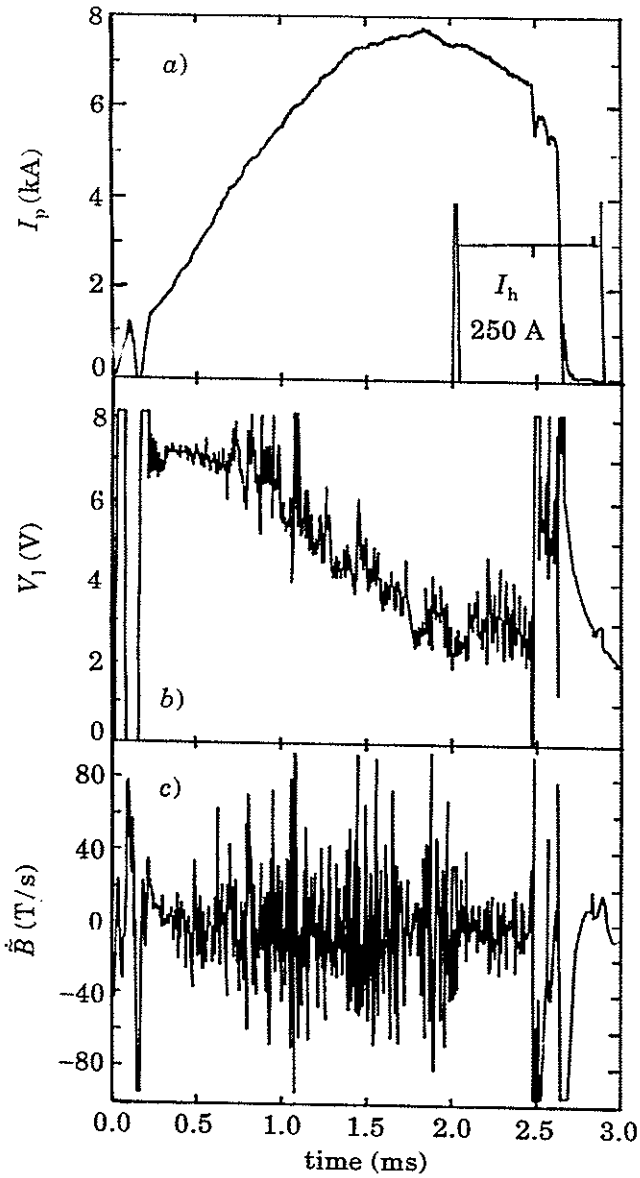

Fig. 8 – Plasma discharge in which a gas mixture of H and He at 6% was used. In *a*) the plasma current and the external helical-current pulse are showed. The loop voltage and the MHD activity signals are showed in *b*) and *c*), respectively.

The results of the power spectral analysis performed just before and right after the application of the r.h.w., in this case, are shown in fig. 10. As can be observed, a reasonable attenuation of the $m = 2$ mode was obtained. This situation, however, could not be sustained for a very long time. The intensity of the $m = 2$ component started increasing significantly soon afterwards and caused the sequence of minor disruptions observed. Also, this mode was identified as the dominant one and the prominent cause for triggering the disruptive process that, later on, destroyed the confinement.

Although the MHD activity increased and the plasma discharges became more unstable, due to the injection of helium, the disruptions triggering mechanisms

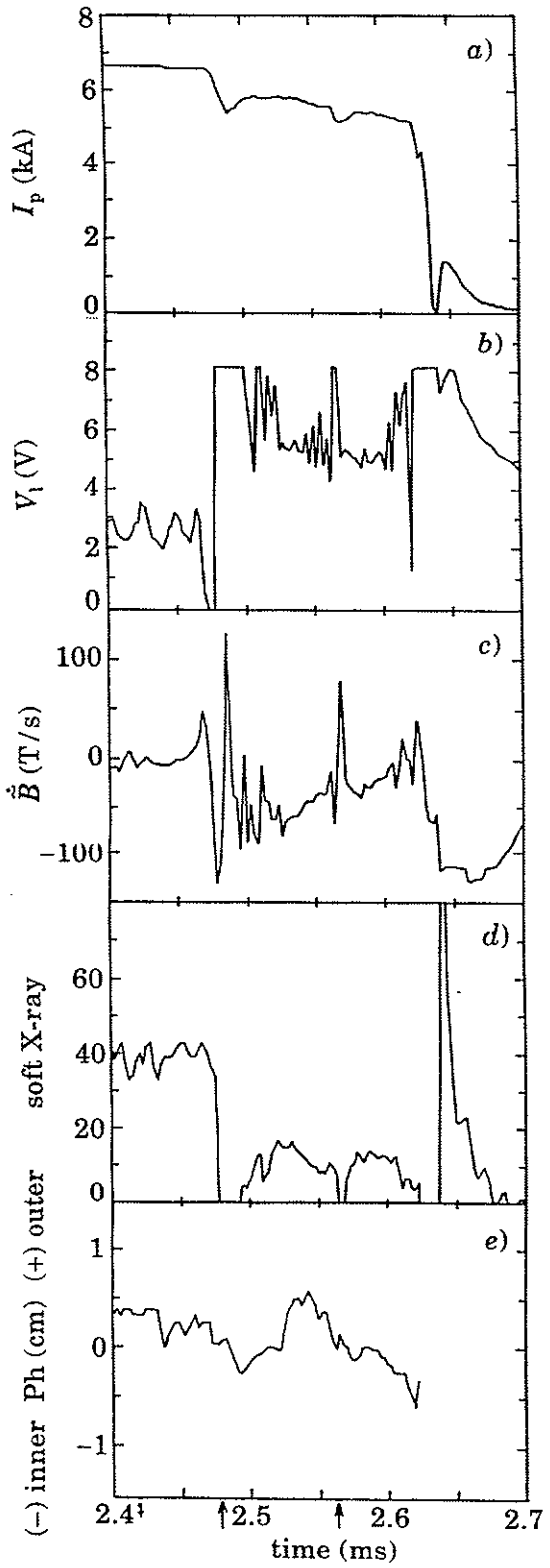

Fig. 9 – Expanded time scale of the discharge showed in fig. 8. The arrows indicate when the minor disruptions occurred, before the plasma collapses.

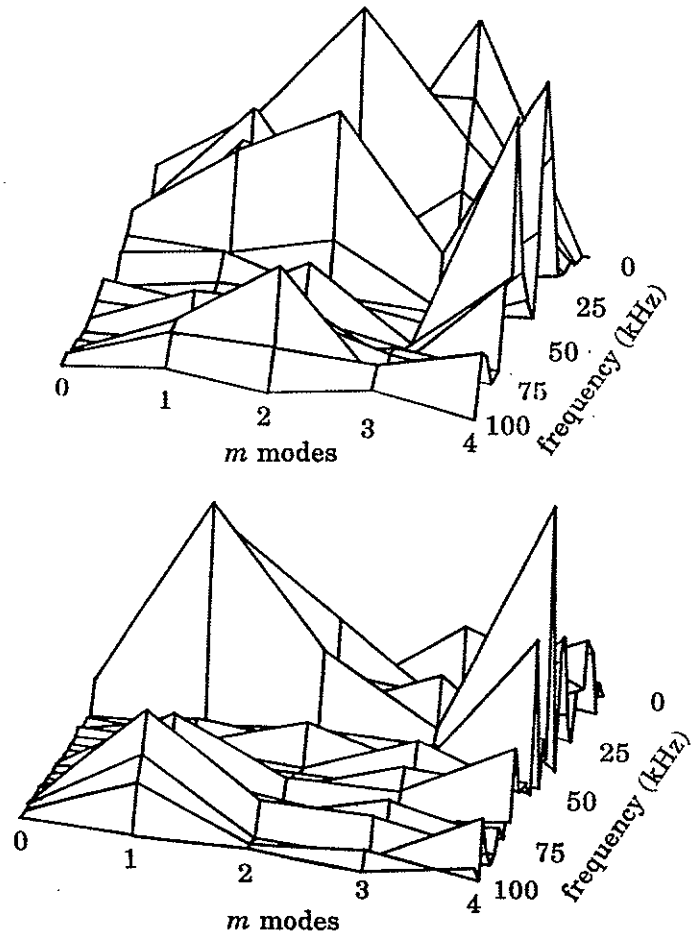

Fig. 10 – Power spectra before (*a*)) and after (*b*)) the activation of the r.h.w. for the pulse in which He was introduced.

observed in these discharges do not differ from those observed in normal discharges with pure hydrogen.

5. – Discussion and conclusions

The motivation of our work came from the apparent variety of conditions for tokamak disruptions to take place, as reported in the literature. There are strong controversies about which mechanisms would trigger a major disruption, although most of the authors emphasize the central role played by the $m = 2$ MHD precursor mode. However, the exact understanding of how and due to what causes the disruptive instabilities occurs, in order to achieve a disruption-free tokamak plasma regime, has not been reached yet. In this context, the basic contribution of this work is to increase the existing experimental database about the disruptive phenomena, grounded in observations obtained from different tokamaks and different plasma conditions.

In this respect, the consequences of applying r.h.f. to the TBR-1 small-tokamak discharges have been investigated. The MHD activity control with the $m/n = 2/1$

r.h.w. was observed to be effective for small helical currents, $I_h/I_p \leq 0.03$, whereas for higher currents, corresponding to perturbations in the range $0.03 \leq I_h/I_p \leq 0.05$, a tendency to increase this activity, and consequently lead minor and major disruptions to occur, was evident. Higher values of r.h.w. currents were then used to generate disruptions and investigate their origins.

Based on the experimental observations of the analysed discharges, indications were found that there are no major differences between spontaneous and r.h.w. induced disruptions. As has been observed in other tokamaks [5, 7, 13, 23], the MHD $m = 2$ mode is always present before the occurrence of any minor or major disruption, playing a decisive role whenever mode coupling or magnetic-island superposition are inferred. In TBR-1 discharges, calculations of the growth rate for this mode, $\gamma \simeq 1 \cdot 10^4\ s^{-1}$, indicate its resistive nature. Therefore, magnetic islands within the resonant magnetic surfaces may be accounted to play an important role in triggering both the major and the minor disruptions.

In order to evaluate a possible magnetic-surface destruction caused by magnetic-islands superposition, due to the growth of resistive modes just before a major disruption takes place, Chirikov's parameter was estimated from equilibrium parameters and mode amplitudes (modified by the r.h.w., whenever the resonant perturbations were used) [35]. These estimations indicated that the minor disruptions are preceded by island superposition, involving the $m = 2/n = 1$ and other higher m number components, as the $m = 3/n = 1$ or the $m = 4/n = 1$, which ergodizes the field lines mainly in the external portion of the plasma. However, concerning the major disruptions, these estimations indicated a significant field line ergodization in the plasma bulk, within the $q = 1$ magnetic surface. This seems to be the main difference between the triggering mechanisms of these two kinds of disruptions.

The effect of introducing helium, a low-Z impurity, in TBR-1 discharges was also investigated in this work. High helium quantities resulted in short discharges, with very unstable plasmas and intense MHD activity, which did not allow the activation of r.h.w. With lower He percentages, between 5% and 8%, longer discharges were obtained and r.h.w. currents could then be applied. Even so, for the majority of the cases, major disruptions were triggered when the r.h.w. was applied. Moreover, the addition of He for these discharges did not modify the disruption triggering mechanisms, as discussed before, for the normal pure-hydrogen discharges.

Finally, in TBR-1, the MHD activity attenuation during the application of r.h.f. was easily obtained without the observation of any major disruption. This is an indication that locked-mode processes, which would trigger a major disruption, are not induced by the applied external fields. However, only by installing locked-mode-detecting coils one would definitively confirm the non-existence of such processes in TBR-1 while r.h.f. are applied.

* * *

This work was partially supported by CNPq.

REFERENCES

[1] KADOMTSEV B. B., *Plasma Phys. Control. Fusion*, 26 (1984) 217.
[2] GREENWALD M., TERRY J. L., WOLFE S. M. *et al.*, *Nucl. Fusion*, 28 (1988) 2199.
[3] SYKES A. and WESSON J. A., *Phys. Rev. Lett.*, 44 (1980) 1215.

[4] ZOHM H., LACKNER K. and LUDESCHER C., *Nucl. Fusion*, **34** (1993) 655.
[5] ROBINSON D. C., *Nucl. Fusion*, **25** (1985) 1101.
[6] KARGER F. and KLUBER O., *Nucl. Fusion*, **25** (1985) 1059.
[7] TSUJI S., NAGAYAMA Y., MIYAMOTO K. *et al.*, *Nucl. Fusion*, **25** (1985) 305.
[8] VANNUCCI A., NASCIMENTO I. C. and CALDAS I. L., *Plasma Phys. Control. Fusion*, **31** (1989) 147.
[9] ITOH K., ITOH S. I., FUKUYAMA A. *et al.*, *Nucl. Fusion*, **32** (1992) 1851.
[10] SAVRUKHIN P. V., LYADINA E. S., MARTYNOV D. A. *et al.*, *Nucl. Fusion*, **34** (1994) 317.
[11] ROBINSON D. C., *Plasma Phys. Control. Fusion*, **35** (1993) B91.
[12] ROBERTS D. E., DEVILLIERS J. A. M., FLETCHER J. D. *et al.*, *Nucl. Fusion*, **26** (1986) 785.
[13] VANNUCCI A. and GILL R. D., *Nucl. Fusion*, **31** (1991) 1127.
[14] WADDELL B. V., CARRERAS B., HICKS H. R. *et al.*, *Phys. Rev. Lett.*, **41** (1978) 1386.
[15] GRANETZ R. S., *Phys. Rev. Lett.*, **49** (1982) 658.
[16] CHEETHAM A. D., HAMBERGER S. M., HOW J. A. *et al.*, in *Plasma Physics and Controlled Fusion Research, Proceedings of the X IAEA International Conference, London, 1984*, 1985, I, p. 347.
[17] WESSON J. A., GILL R. D., HUGON M. *et al.*, *Nucl. Fusion*, **29** (1989) 641.
[18] HEILHACKER R. and the JET TEAM, *Phys. Fluids B*, **2** (1990) 1291.
[19] TODD T. N., *Nucl. Fusion*, **32** (1992) 1071.
[20] KARGER F., WOBIG H., CORTI S. *et al.*, in *Plasma Physics and Controlled Fusion Research, Proceedings of the V IAEA International Conference, Tokyo, 1974*, 1975, I, p. 207.
[21] KARGER F., LACKNER K., FUSSMAN G. *et al.*, in *Plasma Physics and Controlled Fusion Research, Proceedings of the VI IAEA International Conference, Berchtesgaden, 1976*, 1977, I, p. 267.
[22] VANNUCCI A., BENDER O. W., CALDAS I. L. *et al.*, *Nuovo Cimento D*, **10** (1988) 1193.
[23] ROBERTS D. E., SHERWELL D., FLETCHER J. D. *et al.*, *Nucl. Fusion*, **31** (1991) 319.
[24] HUO Y., *Nucl. Fusion*, **25** (1985) 1023.
[25] CHEN J., XIE J., HUO Y. *et al.*, *Nucl. Fusion*, **30** (1990) 2271.
[26] MORI M., AIKAWA H., ASAHI Y., FUJITA T. *et al.*, *Proceedings of the XIV IAEA Conference on Plasma Physics and Controlled Nuclear Fusion Research, Wurzbeerg*, Vol. 2 (1992), p. 567.
[27] SMOLYAKOV A. I., HIROSE A., LAZZARO E., RE G. B. and CALLEN J. D., *Phys. Plasmas*, **2** (1995) 1581.
[28] SNIPES J. A., CAMPBELL D. J., HAYNES P. S. *et al.*, *Nucl. Fusion*, **28** (1988) 1085.
[29] HENDER T. C., FITZPATRICK R., MORRIS A. W. *et al.*, *Nucl. Fusion*, **32** (1992) 2091.
[30] LA HAYE R. J., HYATT A. W. and SCOVILLE J. T., *Nucl. Fusion*, **32** (1992) 2119.
[31] FITZPATRICK R. and HENDER T. C., *Phys. Fluids B*, **3** (1991) 2230.
[32] VANNUCCI A. and MCCOOL S. C., Major Disruptions in TEXT-U Tokamak Report FRCR#431, University of Texas, USA (1993).
[33] MORRIS A. W. and TODD T. N., *Nucl. Fusion*, **31** (1991) 1127.
[34] FINN J. M., *Nucl. Fusion*, **15** (1975) 845.
[35] FERNANDES A., HELLER M. V. P. and CALDAS I. L., *Plasma Phys. Control. Fusion*, **30** (1988) 1203.

Apêndice 5

Artigo publicado sobre a utilização de redes neurais na previsão das instabilidades de disruptura no tokamak TEXT

NEURAL NETWORK PREDICTION OF SOME CLASSES OF TOKAMAK DISRUPTIONS

J.V. HERNANDEZ, A. VANNUCCI[a], T. TAJIMA[b],
Z. LIN, W. HORTON, S.C. McCOOL[c]
Institute for Fusion Studies,
The University of Texas at Austin,
Austin, Texas,
United States of America

ABSTRACT. The use of neural network algorithms for predicting minor and major disruptions in tokamaks is explored by analysing disruption data from the TEXT tokamak with two network architectures. Future values of the fluctuating magnetic signal are predicted based on L past values of the magnetic fluctuation signal measured by a single Mirnov coil. The time step used (= 0.04 ms) corresponds to the experimental data sampling rate. Two kinds of approach are adopted for the network: the contiguous future prediction and the multi-time-scale prediction. Both networks are trained through the back-propagation algorithm with inertial terms and the strengths of the results are compared. The use of additional diamagnetic signals as a method of increasing the performance is suggested. The degree of success indicates that the magnetic fluctuations associated with the TEXT disruption data may be characterized by a low dimensional dynamical system.

1. INTRODUCTION

Disruptions in tokamak plasmas have been, for decades, a concern among fusion research scientists. In general, these harmful instabilities have been classified as major and minor disruptions, according to their potential for completely or partially destroying the plasma current. Owing to the fast decay of the plasma current following a major disruption, strong electromagnetic forces are produced that stress the whole tokamak structure. In large devices, such as JET, displacements of the whole mechanical structure by several millimetres have already been reported [1]. For future fusion reactors, such as ITER, requiring high plasma currents ($\gtrsim$20 MA) to be dealt with, mechanisms that can possibly predict, or even attenuate, the occurrence of major disruptions will be of critical importance.

Many investigations, both theoretical and experimental, have already been carried out in an attempt to understand better the physical mechanisms that are responsible for triggering plasma disruptions [2–9]. Magnetic islands contacting the limiter [2–3], MHD mode coupling [4–7] and ergodization of field lines within magnetic islands [8, 9], for example, are some of the explanations that have already been explored. Experiments based on the application of resonant [10] and non-resonant [11] magnetic fields, in an attempt to control the occurrence of major disruptions, have also been performed but only with some partial success.

In this paper, a different approach of how possibly to avoid the occurrence of fast disruptions, by means of using an adaptive algorithmic strategy called a neural network [12] to predict in advance the instant of time a disruption will occur, is being proposed. Since the $m = 2$ MHD mode, as is widely accepted, plays an important role in triggering the disruptive instabilities, the fluctuating magnetic field signal from one of the Mirnov coils installed in the TEXT tokamak was considered the appropriate experimental signal to be used as input to the neural network. Although neural networks have already been used for fitting plasma parameters and general data analysis [12–20], we believe that this is the first time that a neural network is used for predicting in advance the moment a disruption will take place.

[a] Instituto de Fisica, Universidade de Sao Paulo, Sao Paulo, Brazil.
[b] *Also at:* Advanced Science Research Center, Japan Atomic Energy Research Institute, Ibaraki, Japan.
[c] Fusion Research Center, The University of Texas at Austin, Austin, Texas, USA.

2. BACK-PROPAGATION NEURAL NETWORKS FOR TIME SERIES PREDICTIONS

In the presence of dissipation, the evolution of a high dimensional dynamical system may become trapped into a low dimensional region of the phase space, an attractor. If that is the case, then the underlying state of the system can be reconstructed from the observation of a time series $x(t)$ using time delayed vectors [12, 21–23],

$$X_t = (x_t, x_{t-1}, \ldots, x_{t-(n-1)}) \tag{1}$$

as long as the dimension $n > d$, where d is the dimension of the attractor, and $x_{t-j} \equiv x(t - j\tau)$, where τ is the time delay. This implies that there exists a smooth non-linear function Ψ that relates n past measurements of $x(t)$ to a future value of $x(t)$ [12, 21–23],

$$x(t + 1) = \Psi[x_t, x_{t-1}, \ldots, x_{t-(n-1)}] \tag{2}$$

In order to predict the future evolution of the system, it is necessary to find some way to approximate Ψ.

For this work, the TEXT magnetic fluctuation data are used in feedforward perceptron-type neural networks with non-linear activation functions [24] to approximate the smooth function Ψ and to perform the prediction task. Neural networks were originally used in a prediction context by Lapedes and Farber [25].

Neural networks are a flexible tool for approximating mappings between data sets.

In particular, back-propagation networks with at least one hidden layer of units with non-linear activation functions can be used as universal approximates to real-valued continuous functions. Another advantage of back-propagation networks is that they do not suffer from the 'curse of dimensionality' or combinatorial explosion in the parameters of the network as the number of inputs is increased. The generic architecture of a feedforward neural network contains L inputs, one or several hidden layers with one or several units each, and one output layer. A unit in one layer is fully connected with the units in the previous layer, and the output $h_i^{(k)}$ (unit i in the kth layer) is a function $g_i^{(k)}$ (the activation function) of the weighted sum of the outputs of all the units in the previous layer,

$$h_i^{(k)} = g_i^{(k)} \left(\sum_{j=1}^{N} W_{ij}^{(k-1)} h_j^{(k-1)} \right) \tag{3}$$

where $W_{ij}^{(k-1)}$ is the strength of the connection between unit j in the $(k-1)$th layer and unit i in the kth layer.

Supervised feedforward networks learn by example. The weights of the connections are determined by presenting to the network a set of actual input–output values (the training set) and comparing, through some error or cost function $\mathcal{E}(W)$, the output of the network $\hat{O}$ with the actual output O from the system. For this work, the cost function was chosen to be the mean square error,

$$\mathcal{E}(W) \equiv \frac{1}{M} \sum_{j=1}^{M} (O_j - \hat{O}_j)^2 \tag{4}$$

where M is the size of the data set (training, testing or validation) and the error is minimized by adjusting the weights according to the back-propagation algorithm [26, 27], which is a gradient descent recipe, and by including an inertial term to accelerate convergence. In particular,

$$W_{ij}^{\text{new}} = W_{ij}^{\text{old}} + \Delta W_{ij} \tag{5a}$$

$$\Delta W_{ij} = -\eta \frac{\partial \mathcal{E}}{\partial W_{ij}} + \alpha \Delta W_{ij} \tag{5b}$$

with η the learning rate, being a small positive constant ($0 < \eta \ll 1$), and with α the inertial term, a number between 0 and 1.

If a model-free estimator of Ψ in Eq. (2) is used to minimize the mean squared error $\mathcal{E}$ over the training set, then the resulting model might be complicated and complexity regularization might be necessary. Complexity regularization is often achieved by adding a non-negative penalty term and minimizing the resulting quantity. A penalty term can be added to obtain smooth estimators of Ψ or otherwise it may have to be settled on a network with a small number of weights. Instead of adding a penalty term to $\mathcal{E}$, we choose to minimize $\mathcal{E}$ over the training set, while monitoring the generalization ability of the network.

In order to characterize the goodness of the model, the average relative prediction error variation (ARV) given by

$$\text{ARV} = \frac{\sum_{j=1}^{M} (O_j - \hat{O}_j)^2}{\sum_{j=1}^{M} (O_j - \langle O_j \rangle)^2} \tag{6}$$

and the correlation coefficient ρ given by

$$\rho = \frac{\sum_{j=1}^{M} (O_j - \langle O \rangle)(\hat{O}_j - \langle \hat{O} \rangle)}{\sigma_O \sigma_{\hat{O}}} \quad (7)$$

are introduced. In these equations, $\langle O \rangle$ is the mean value of the set of M actual outputs, and σ_O and $\sigma_{\hat{O}}$ are the standard deviations of the actual and the predicted outputs, respectively.

3. PREDICTING DISRUPTIONS IN THE TEXT TOKAMAK

Two approaches are tried here for the evaluation of a method to predict disruptions in the TEXT tokamak. One is a supervised feedforward neural network that consists of 15 units in the input layer corresponding to the L past values of the fluctuating field $\dot{\tilde{B}}_{t-j}$ ($j = 1, \ldots, L$) and has two hidden layers (the first with nine units and the second with three) and one output unit for the predicted $\dot{\tilde{B}}_{t+1}$. The activation function for the hidden units are non-linear, $g(x) = \tanh(x)$, and the activation function for the output unit is linear, $g(x) = x$, in order to have a wide dynamical range. The number of hidden units was chosen by monitoring the out-of-sample performance of the network. The learning rate and the inertial term are $\eta = 0.001$ and $\alpha = 0.9$, respectively.

The training of the network was carried out by using two TEXT plasma discharges, one disruptive and the other non-disruptive. In order to stop the training of the network, we monitored its performance on a third (non-disruptive) shot (the validation set) so that the prediction error reached a minimum when evaluated over the validation set. Finally, the trained network was used on an independent (disruptive) shot.

In this work, the neural network was used to make both single and multistep predictions. In single step predictions, actual past values of the time derivative of the fluctuating poloidal magnetic field were used to predict its next value with a time step $\tau = 0.04$ ms, which corresponded to the sampling rate of the experimental data. In multistep predictions, the predicted output at time 1 is fed back into the input and is used to predict a new output, at time 2, and so on.

The other approach is a supervised feedforward neural network consisting of one hidden layer with eight hidden units, and one output unit. The activation function is $g(x) = \tanh(x)$ for all connections. The number of the input units will be five for the single frequency input organization and ten for the two frequency one. (For details, see Section 4.2.) Through monitoring the performance of the network, the learning rate and the inertial term are set to be 0.02 and 0.2, respectively, in this approach. The training of the network is done by using one TEXT tokamak data shot including both the general oscillating part and the disruption part. The number of passes through the training set is of the order of 10^6. For every 5000 times, a resulting set of weights are recorded and the value of the ARV and the correlation coefficient are calculated as a measurement of the performance of the network. The final resulting weights are chosen to be ones with a minimum of ARV and a maximum of the correlation function among the weights

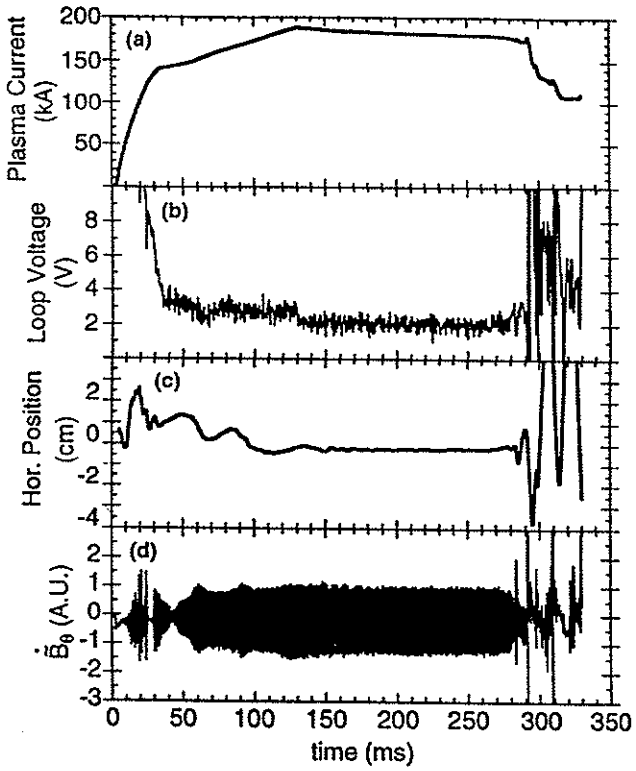

FIG. 1. A discharge corresponding to an $I_p \sim 180$ kA shot that disrupted at $t \sim 290$ ms and which was preceded by a minor disruption approximately 8 ms earlier. After the major disruption has taken place, the plasma position control system was unable to maintain the plasma column centred (horizontal position) and several minor disruptions occurred. The derivative of the fluctuating poloidal magnetic field from one of the Mirnov coils is also shown, which was used for feeding the neural network.

recorded. The real prediction work is done when this optimum weights set is applied to other data shots. Another scheme for multistep prediction is developed here. For example, for an L-step prediction, we will use the derivative magnetic field data before time t as the input source and take the data $\dot{\tilde{B}}_{t+L}$ as the target. Both the playing back onto the training data shot itself and the result of the trained network for other data shots are shown in the following.

4. RESULTS OBTAINED

4.1. First approach — contiguous future prediction

After the best architecture has been found and all the weights have been properly set, the neural network is used for forecasting disruptions in a plasma pulse other than those used for training. This is done for the discharge shown in Fig. 1. It corresponds to an $I_p \sim$ 180 kA shot that disrupted at $t \sim 290$ ms (Fig. 1(a)) and was preceded by a minor disruption, approximately 8 ms earlier. After the major disruption has taken place, the plasma position control system was no longer able to maintain the plasma column centred (Fig. 1(c)) and several minor disruptions occurred while the plasma current decayed. In Fig. 1(d) the derivative of the fluctuating poloidal magnetic field from one of the Mirnov coils that was used for feeding the neural network is shown.

The values of $\dot{\tilde{B}}_\theta(t + n\tau)$ predicted by the neural network for the last 200 ms of the discharge are shown in Fig. 2. In Fig. 2(a), the experimental data are plotted and can be compared with the results obtained for the single ($n = 1$) and multistep ($n = 15, 21, 28$) predictions, presented in Figs 2(b) to (e), respectively. These

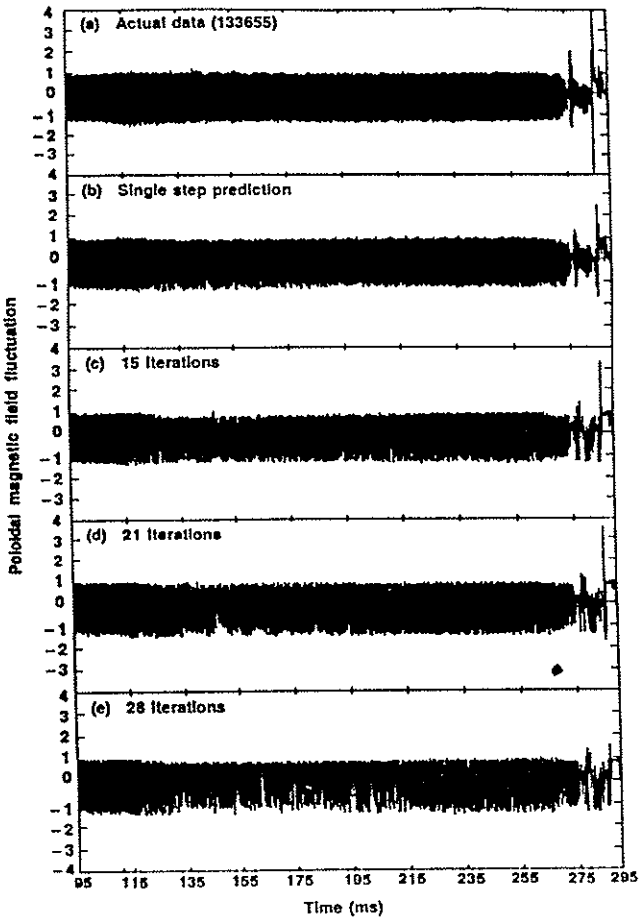

FIG. 2. Predicted $\dot{\tilde{B}}_\theta(t + n\tau)$ values from the contiguous past values for the final 200 ms of the discharge. In part (a), the experimental data are plotted for comparison with the results of single time step (n = 1) and multiple time step (n = 15, 21, 28) predictions, presented in parts (b) to (e), respectively. These values of n correspond to predictions made 0.04, 0.6, 0.84 and 1.12 ms earlier, respectively.

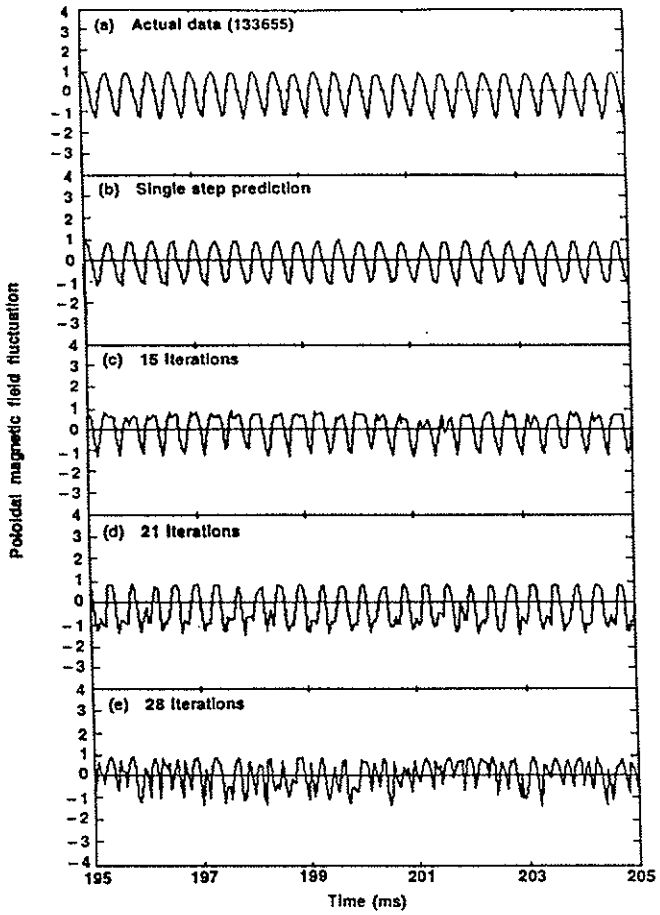

FIG. 3. Expansions of the experimental data (a) and contiguous future prediction results ((b) to (e)) in regions before the disruption time are shown to indicate the consistency of the neural network prediction.

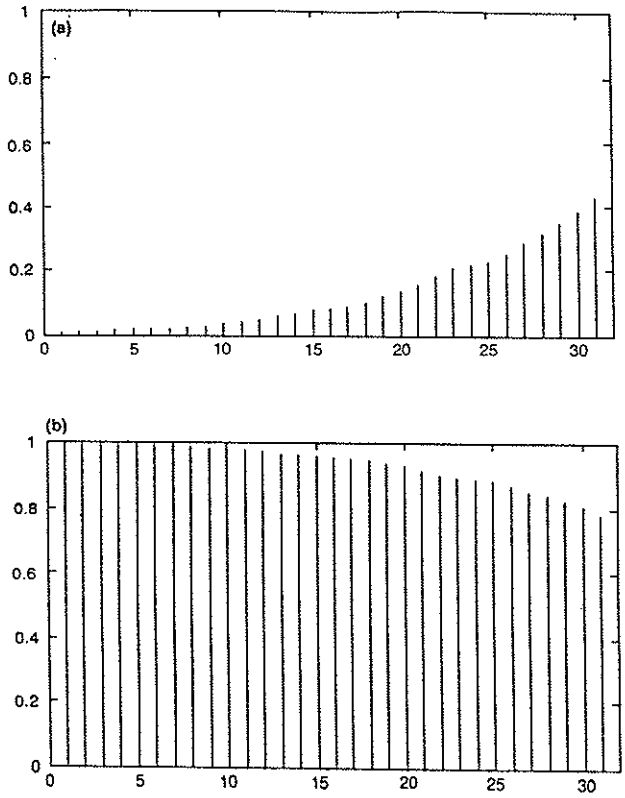

FIG. 4. For contiguous future prediction: (a) prediction error ARV and (b) correlation coefficient, as calculated from Eqs (6) and (7). As noted, the performance of the network degrades exponentially as the number of iterations increases.

values of n correspond to predictions made 0.04, 0.6, 0.84 and 1.12 ms earlier, respectively. Expansions of these signals in regions before the disruption time, as shown in Fig. 3, indicate that the predictions made by the neural network are consistent, even for higher values of n. In Figs 4(a) and (b) the corresponding prediction error and the correlation coefficient, as calculated from Eqs (5) and (6), are shown for a different number of iterations, which means the number of times the output of the predictor is fed back into its input before obtaining the final predictive output. As noted, the performance of the neural network, in determining the future values of the perturbed poloidal magnetic field, tends to degrade exponentially, as the number of iterations increases.

In Fig. 5, expansions of the signals shown in Fig. 2 are plotted within the disruption time region. Although there are some perceptible discrepancies between the waveforms of the experimental data (Fig. 5(a)) and the results of the prediction (Figs 5(b) to (e)), the occurrences of both the minor disruption (at $t \sim 276.7$ ms) and the major disruption (at $t \sim 289.5$ ms) are clearly identified by the neural network, even for the cases corresponding to higher numbers of iterations. It is interesting to note, on the oscillatory portions of the output results from the neural network, that the signal frequency tends to differ considerably from the actual data, as the number of iterations increases. This behaviour can probably be understood as being due to the typical frequency decrease of the Mirnov oscillations during the period of time that preceded a disruption. In TEXT-U, for example, close to a disruption, this frequency change varies from shot to shot, usually decreasing from about 12 kHz to 1–2 kHz; but in many cases reaching values of only some tens of hertz [27].

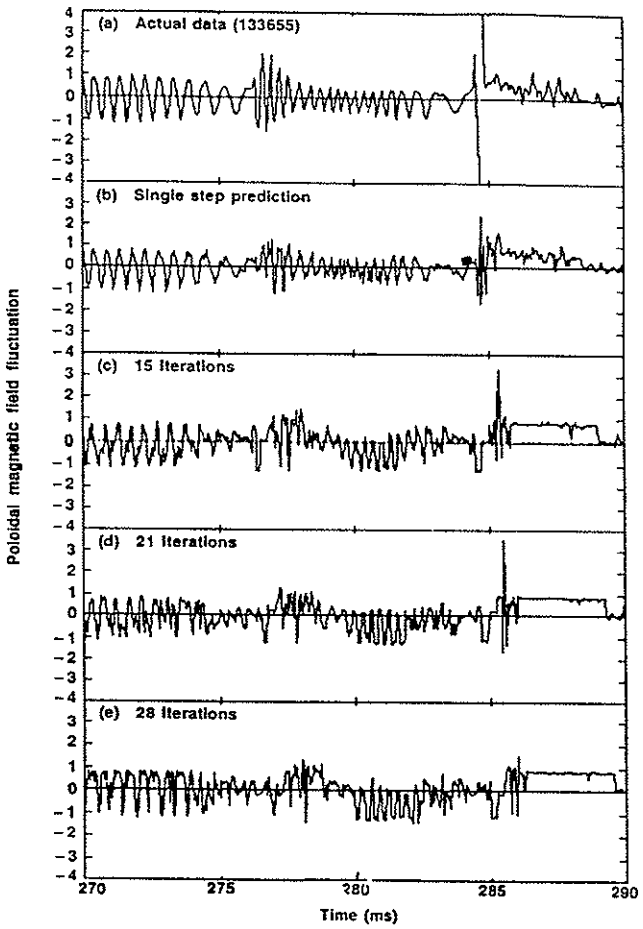

FIG. 5. Expansion of the signals shown in Fig. 2 plotted within the disruption range. It is noted that both the minor disruption (t ~ 277 ms) and the major disruption (t ~ 290 ms) are clearly identified by the neural network.

TABLE I. ARV AND CORRELATION COEFFICIENT
(For each weight the first value is the ARV and the second is the correlation coefficient.)

	Shot	Weights1	Weights2	Weights3	Weights4
SS1	133 651	0.20, 0.90	1.76, −0.21	0.28, 0.84	1.03, 0.35
SS2	133 652	5.30, −0.13	0.47, 0.73	9.45, −0.06	2.06, 0.08
SS3	133 654	0.25, 0.87	1.84, −0.29	0.21, 0.86	0.56, 0.65
SS4	133 655	1.61, 0.29	2.30, −0.41	2.41, 0.11	0.46, 0.71

The increasing lag in the predicted time for the major disruption shown in Fig. 5 in progressing from 15 iterations to 28 iterations is a problem that requires further investigation. It has been suggested that more advanced neural network models may succeed in eliminating or reducing this time lag problem.

4.2. Second approach — multi-time-scale prediction

In the second approach, for a simple short term prediction, the number of input units is set to be five, organized as follows:

$$\dot{\tilde{B}}(t),\ \dot{\tilde{B}}(t-\Delta t),\ldots,\dot{\tilde{B}}(t-4\Delta t)$$

The target output is $\dot{\tilde{B}}(t+5\Delta t)$ for the goal of five step prediction. We processed four data shots (SS1 to SS4), which contain about 7500 data points each, in this way, and four weight sets (weights1 to weights4) were properly obtained accordingly. We apply these weight sets to the data shots (SS1 to SS4) alternatively and the obtained ARV and correlation coefficient are given in Table I.

As the time resolution of the data shots is Δt = 0.04 ms, we achieved the 0.2 ms prediction using the five step model. From Table I, we can see that the performance of weights1 on SS3 and vice versa are better. Figure 6 shows that the playing back of weights2 on SS4 best reproduces the shape of SS4. By inspection of the original data SS1 to SS4, we find that SS1 and SS3 are similar to each other, while SS2 and SS4 are similar to each other. As expected, when the training data are similar to those forecast, the neural network is able to predict the essential characteristics more accurately.

Furthermore, we attempt to make a long term prediction. Following the procedure described above, we substitute the target output $\dot{\tilde{B}}(t+25\Delta t)$ to obtain a 25 step prediction. However, this leads to a failure, with the appearance of a phase shift in the oscillatory portion between the original data and the predictive data. The ARV is now up to 1 even for playing back on the training data itself. In this situation, we surmise that the data shot, even long before the disruption time, has more than one characteristic frequency. When we make the five step prediction, the prediction time is not long

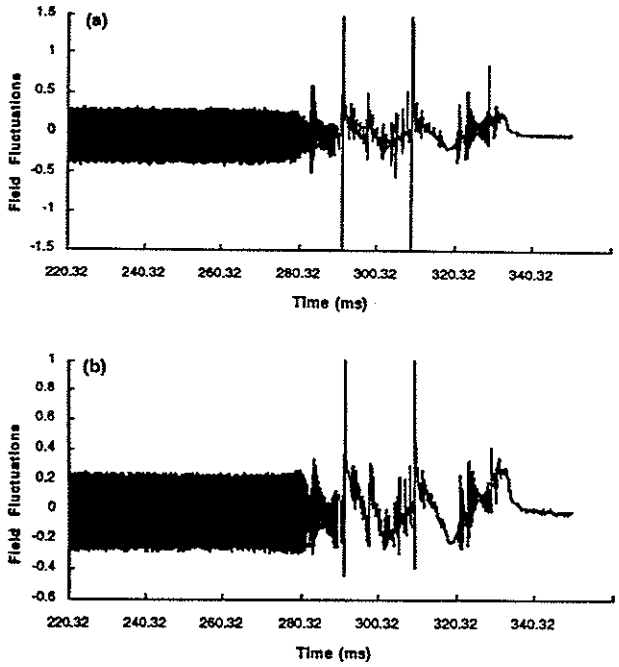

FIG. 6. With the single frequency input organization, the multi-time-scale prediction of (b) shot 133 655 is compared with (a) the experimental data. The predictive result is scaled here to the range [−1,1] for the sake of numerical stability. It is shown that both major disruptions and minor disruptions are identified, though there is a small time shift between the experimental data and the predictive one (Δt ~ 0.3 ms).

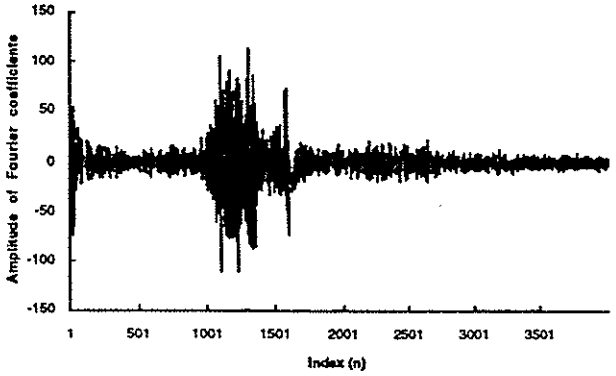

FIG. 7. Three peaks can be obtained from this figure: 1103, 1316 and 1590, which correspond to the frequencies 2298, 2714 and 3311 Hz.

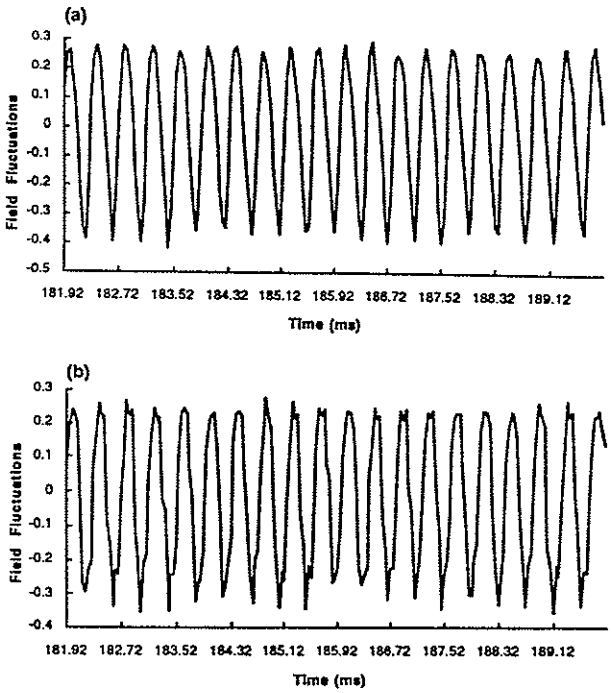

FIG. 8. Expansions of (a) the original data of shot 133 655 and (b) the multi-time-scale prediction with multifrequency input organization within the non-disruptive range. The prediction is 1.0 ms ahead in time. It shows that the adoption of the multifrequency input organization removes the time shift between the experimental data and the neural network prediction.

enough to cover one time period of the data shot, so that no out-of-phase phenomenon occurs, while it does in the 25 step prediction. This shows that our single frequency input organization can no longer accomodate the multi-frequency (wideband) data.

Solving this problem, we use Fourier analysis to calculate if there are any characteristic frequencies in the data shot and what they are. We first deal with SS4, which is shown to be the most difficult case to be modelled. The Fourier transform of SS4 is shown in Fig. 7. The index n (value of x axis) is related to the characteristic frequency we are searching for, $f = n/2N\Delta t$, where N is the total number of data points

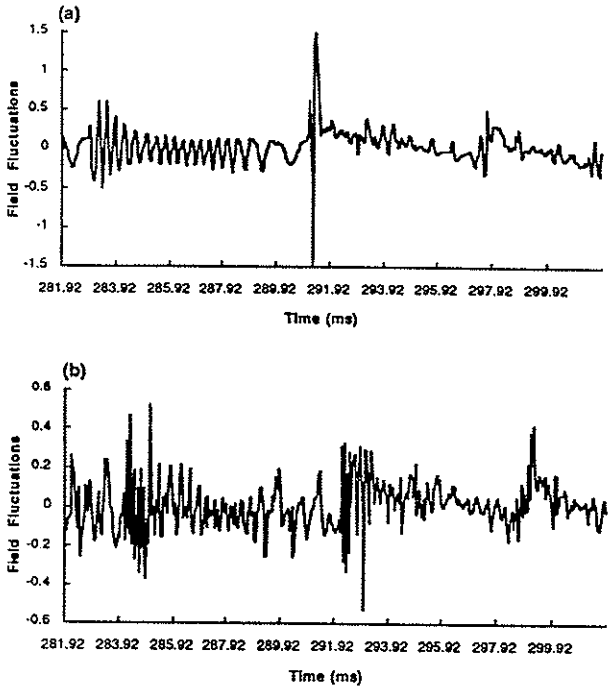

FIG. 9. Expansions of the signals in Fig. 8 within the disruption range. It shows that both the major disruptions and the minor disruptions are identified by the neural network and the time shift is reduced.

TABLE II. FOURIER TRANSFORM RESULTS FOR SS1 AND SS3 (N = 7000)
(f_1 and f_2 correspond to the two major characteristic frequencies of the data shot, respectively.)

Parameter	SS1 (133 651)		SS3 (133 654)	
	f_1	f_2	f_1	f_2
Index, n	844	2160	939	1953
Frequency (kHz)	1.58	3.86	1.68	3.49
Time period (steps)	15.84	6.48	14.91	7.17

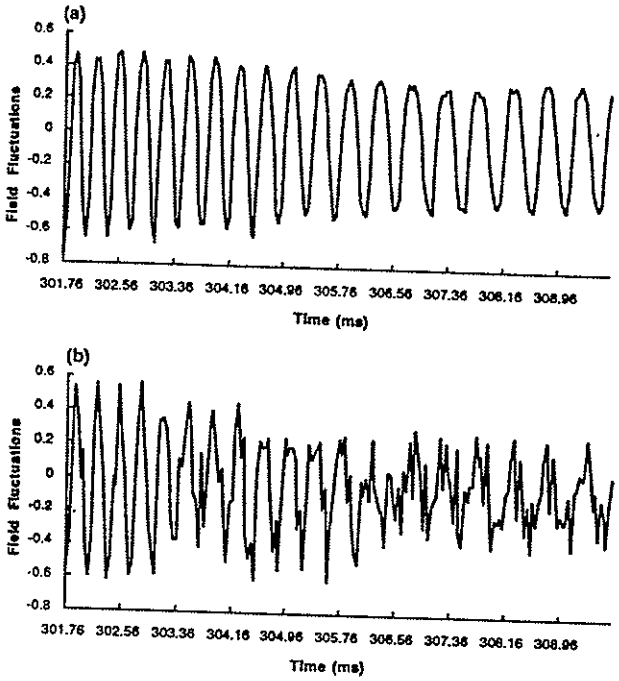

FIG. 10. The same neural network organization as used in Figs 8 and 9 is used for predictions for another shot (133 654). Expansions of experimental and predictive data are shown at the boundaries of the disruptive and non-disruptive portions. All major and minor disruptions are identified and the time shift is removed except for a small range ($\Delta t \sim 2.2$ ms) very close to the boundary point.

processed. In the case of SS4 ($N = 6000$) the indices n of the three peaks are 1103, 1316 and 1590, respectively; these correspond to the frequencies of 2298, 2741 and 3311 Hz. For convenience, we count the time period in step units; these correspond to 10.88, 9.12 and 7.55 steps, respectively. Considering this feature of the frequency spectrum, we introduce another sampling period with another five inputs in addition to the earlier five,

$$\dot{\tilde{B}}(t \times 6\Delta t),\ \dot{\tilde{B}}((t-2) \times 6\Delta t), \ldots, \dot{\tilde{B}}((t-5) \times 6\Delta t)$$

We choose six because the maximum time period is 10.88 steps and six will cover the half-period. With this introduction of multiple sampling periods, all the major characteristic frequencies of the behaviour of this system should be mastered by our model.

Training the network with this new input organization, we derive a new set of weights with SS4. Playing back on SS4 with multiperiods shows a great improvement over the earlier single sampling period. The ARV decreases to 0.39, compared with the unacceptable level of the order of unity before. With a detailed comparison of the general oscillatory portion, the phase shift appears to have vanished (Fig. 8). In the disruptive part, the phase shift is also reduced in comparison with the case with a single sampling period (Fig. 9). Fourier analysis of SS1 to SS3 is shown in Table II and the same procedure is used for SS1 and SS3. The result shows the multifrequency model actually works for the complicated disruptive data shot.

After several attempts, five is chosen to be the most convenient number of steps in our two frequency model. On training the network with SS1, the improvement is obvious and playing back onto SS1 itself, the ARV is now 0.13 and the correlation coefficient 0.92, even better than the results with the former five step prediction result. The result of applying weights1 onto SS3 is also promising (Fig. 10). The phase shift is absent and the ARV and correlation coefficient are accordingly 0.27 and 0.82, respectively.

Given these outcomes, we can conclude that at least the phase shift problem in disruption prediction can be partly solved with our new input organization. More data shots were then processed to confirm the effectiveness of the algorithm, while adjusting the usage of it for better results at the same time.

An attempt to feed the actual neural network program with recent data for the perturbed magnetic fields measured by an internal Mirnov coil in TEXT-U has already been made. However, the magnetic coils recently installed in TEXT-U were observed to pick up rather intense electromagnetic noise from the ambient environment, which made the prediction analysis by the neural network not very satisfactory.

The results presented here demonstrate the possibility of predicting the occurrence of disruptions in tokamak discharges more than 1 ms before they actually happen. This is encouraging. Certainly this prediction time period is not yet enough to allow, in the context of real time tokamak operation, any action to be taken to modify the plasma current profile in order to avoid the incipient disruption or, at least, minimize its harmful consequences. The predictive time span needs to be extended. For this purpose, plans are already on course to modify the program in order to include, together with the derivative of the fluctuating poloidal magnetic fields, other experimental signals, such as soft X ray emission, locked mode and H_α emission, so that more information about the dynamic evolution of the plasma discharge can be incorporated into the neural network input channel. This improvement hopefully will increase the input

dimensionality and the neural network ability to perceive immediately any change on the discharge conditions that could trigger a major disruption. Extending the prediction time to 3 ms, for example, would already be enough to forecast some of the major disruptions in TEXT-U (fast disruptions) before the characteristic amplitude growth of the $m = 2$ MHD precursor mode starts [28].

5. CONCLUSIONS

The utilization of a neural network for predicting plasma disruptions in TEXT discharges more than 1 ms before they actually take place has been successfully demonstrated. The neural network code constructed was of the feedforward type. Both one hidden layer and two hidden layer topologies are used with different multistep prediction strategies. The program was trained through the back-propagation algorithm with inertial terms by using plasma discharges (including both disruptive and non-disruptive parts) other than the one used for forecasting. The code will now be reconstructed to accept the input of other experimental signals, such as the soft X ray, locked mode and H_α, in an attempt to extend the prediction time even further.

The utility and power of the present approach are that an understanding of the physical mechanism of disruptions is not needed, and thus, the approach is general, flexible and independent of any idealized physics model. The success of neural network predictions for the rather stiff temporal phenomenon of tokamak disruptions is encouraging, as they are believed to be among the most difficult phenomena to predict.

ACKNOWLEDGEMENTS

The work was supported in part by the USDOE and in part by JAERI and FAPESP.

REFERENCES

[1] NOLL, P., et al., in Technology of Fusion (Proc. 8th Top. Mtg Salt Lake City, 1989) p. 259.
[2] KARGER, F., et al., in Plasma Physics and Controlled Nuclear Fusion Research 1976 (Proc. 6th Int. Conf. Berchtesgaden, 1976), Vol. 1, IAEA, Vienna (1977) 267.
[3] ROBERTS, D.E., et al., Nucl. Fusion **26** (1986) 785.
[4] TSUJI, S., et al., Nucl. Fusion **25** (1985) 305.
[5] VANNUCCI, A., et al., Plasma Phys. Control. Fusion **31** (1989) 147.
[6] VANNUCCI, A., GILL, R.D., Nucl. Fusion **31** (1991) 1127.
[7] WAIDMAN, G., KUANG, Guangli, Nucl. Fusion **32** (1992) 645.
[8] FINN, J.M., Nucl. Fusion **15** (1975) 845.
[9] ITOH, K., et al., Nucl. Fusion **32** (1992) 1851.
[10] HENDER, T.C., et al., Nucl. Fusion **32** (1992) 2091.
[11] VALLET, J.C., et al., Phys. Rev. Lett. **67** (1991) 2662.
[12] RUELLE, D., Ann. N.Y. Acad. Sci. **1** (1980) 357.
[13] ALLEN, L., BISHOP, C.M., Plasma Phys. Control. Fusion **34** (1992) 1291.
[14] LISTER, J.B., SCHNURRENBERGER, H., Nucl. Fusion **31** (1991) 1291.
[15] BISHOP, C.M., et al., Automatic Analysis of JET Charge Exchange Spectra Using Neural Networks, Rep. JET-P(92)90, JET Joint Undertaking, Abingdon (1992).
[16] HERNANDEZ, J.V., et al., Geophys. Res. Lett. **20** (1993) 2707.
[17] COCCORESE, E., et al., Nucl. Fusion **34** (1994) 1349.
[18] KUNG, S.Y., Digital Neural Networks, Prentice-Hall, Englewood Cliffs, NJ (1993).
[19] IEEE Trans. Neural Networks **NN-5** (1994) No. 2.
[20] WEIGEND, A.S., GERSHENFIELD, N.A. (Eds), Time Series Prediction: Forecasting the Future and Understanding the Past, Addison-Wesley, Reading, MA (1994).
[21] TAKENS, F., Dynamical Systems and Turbulence, Springer-Verlag, Berlin (1981).
[22] SAUER, T., et al., J. Stat. Phys. **65** (1991) 579.
[23] EKMAN, J.P., RUELLE, D., Rev. Mod. Phys. **57** (1985) 617.
[24] HERTZ, J., et al., Introduction to Theory of Neural Computation, Addison-Wesley, Reading, MA (1991) Ch. 6.
[25] LAPEDES, A.S., FARBER, R.M., Nonlinear Signal Processing Using Neural Networks — Prediction and System Modeling, Rep. LAUR-87-2662, Los Alamos Natl Lab., NM (1987).
[26] HORNIK, K., et al., Neural Networks **215** (1989) 359.
[27] RUMELHART, D.E., et al., Nature **323** (1986) 533.
[28] VANNUCCI, A., McCOOL, S.C., Major Disruptions on TEXT-U Tokamak, FRC Rep. 431, Univ. of Texas at Austin (1994).

(Manuscript received 2 November 1994
Final manuscript accepted 16 January 1996)

Submitted to Publication
in the Nuclear Fusion

Forecast of TEXT Plasma Disruptions Using Soft X-Rays as Input Signal in a Neural Network

A. Vannucci*, K.A. Oliveira*, T. Tajima

Institute for Fusion Studies
The University of Texas at Austin
Austin, Texas, USA - 78712-1068

* Instituto de Fisica
Universidade de Sao Paulo, C.P. 66318
Sao Paulo, 05315-970, SP - Brazil

Abstract:

A feed-forward neural network with two hidden layers is used in this work to forecast major and minor disruptive instabilities in TEXT tokamak discharges. Using the experimental data of soft X-ray signals as input data, the neural net is trained with one disruptive plasma discharge, and a different disruptive discharge is used for validation. After being properly trained the networks, with the same set of weights, it is then used to forecast disruptions in two others different plasma discharge. It is observed that the neural net is able to predict the incoming of a disruption more than 3 ms in advance. This time interval is almost three times longer than the one already obtained previously when magnetic signal from a Mirnov coil was used to feed the neural networks with. To our own eye we fail to see any indication of an upcoming disruption from the experimental data this far back from the time of disruption. Finally, from what we observe in the predictive behavior of our network, speculations are made whether the disruption triggering mechanism would be associated to an increase of the m = 2 magnetic island, that disturbs the central part of the plasma column afterwards or, in face of the results from this work, the initial perturbation would have occurred first in the central part of the plasma column, within the q = 1 magnetic surface, and then the m = 2 MHD mode would be destabilized afterwards.

I- Introduction

Disruptive instabilities in tokamaks are still a major concern and considered a great obstacle in achieving thermonuclear fusion using a tokamak reactor. The next large fusion devices, because of the large current values and high plasma temperature to be achieved [1], will have to be very carefully projected and properly constructed in order to support the occurrence of a large number of such instabilities if some proper mechanism has not been discovered by then to avoid them or at least minimize their harmful effects. Neural network forecasting, in this respect, might be one possible solution to this problem if it proves to be able to alert the incoming of a disruption in a period of time sufficiently long in order to allow defensive mechanisms to be turned on.

Nowadays, it is widely accepted that the m = 2 component of the magneto-hydrodynamic (MHD) activity of the plasma plays an important role in starting the disruptive process in tokamaks. Many papers have already suggested, for example, that a MHD mode coupling would be the main mechanisms for triggering both minor and major disruptions [2-7].

The first paper published exploring the idea of forecasting disruption using a neural network showed that major and minor disruptions could be forecasted more than 1 ms before they actually take place, when magnetic data obtained from one Mirnov magnetic coil was used to feed the neural net [8]. This period of time, however, was not considered to be sufficiently large to allow any proper controlling mechanism such as electron resonant heating [9,10], neutral beam [11], external resonant magnetic fields [12,13] or even impurity pellets injection [14] to be used in real time, in a possible attempt to suppress the upcoming disruption.

More recently, another paper was published reporting the use of neural network to estimate the high-β limit in DIII-D by combining signals from a large number of plasma diagnostics, resulting in a more accurate prediction of the high-β disruption boundary than that provided by the traditional Troyon limit [15]. After the instability boundaries has been accurately mapped, the neural network was reported to be able to alert in real time the controlling systems that those boundaries were about to be reached. The limitation of this method of forecasting disruption in a future reactor, for example, appears to be the necessary large number of

disruptions that would be necessary to occur beforehand in order to create a database that would then allows, afterwards, those instability boundaries to be properly set.

In this work, the result of forecasting disruptions in TEXT tokamak by feeding a neural networks with soft X-ray signals is presented. After being properly trained, the neural net was able to forecast the occurrence of disruptions more than 3 ms before it happens. This period of time is almost the triple of that obtained previously by using magnetic signal from a Mirnov coil [8].

II - Neural networks

Artificial neural networks are computer algorithms which simulate, in a very simplified form, the ability that brain neurons have to process information. A typical perceptron neural net is constituted by a certain number of binary units organized in layers, usually 3 or more. In a feedforward network, each neural unit is connected with all units from the previous layer and for each connection there is a specific statistical weight related to it [16,17]. Within each unit of the network, all the input weighted signals are summed and an excitatory or inhibitory signal is then fired to the next layer's units, depending whether the result of the sum has reached or not a certain threshold value, which is defined by the activation function chosen (Fig. 1). These weights are adjusted (or educated) to minimize error in prediction (back propagation [18]).

Observing the time delayed vector of a physical quantity X at time t, of the tokamak data:

$$X_t = [x_t, x_{t-\tau}, x_{t-2\tau}, \ldots, x_{t-n\tau}] \qquad (1)$$

then it is reasonable to suppose that the future state of the system, at time $t+\tau$, could be predicted by a smooth non-linear function F:

$$x(t+\tau) = F(X_t) \qquad (2)$$

where $\tau = 0.04$ ms corresponds, in this work, to the sampling rate of the CAMAC acquisition system. If the dynamics of the system under study is a low dimensional one, it is hoped that such

a function may be found even for stiff functions of dynamics such as the sudden onset of disruption.

However, since the function F is not known, the idea is to alternatively use a neural network to approximate F and, therefore, predict the future evolution of the system. In order to do its job, n in equation (1) must be smaller than the dynamical dimension d of the system, and the neural net must be trained first, that is, the correct set of weights for all connections must be found. When we start weights in *tabula rasa*, we need to "educate" these weights. The training process basically consists in feeding the neural net repeatedly with experimental data, from a given plasma pulse, and in comparing the output signal O (forecasted) with the real signal O (experimental data in our case). In this process, the back propagation algorithm [18] is used to minimize the error function for the current weights $\{W_{ij}\}$:

$$\varepsilon\{W\} = 1/M \sum (O_i - O_i\{W\})^2 \qquad (3)$$

which evaluates the efficacy of the training after each training epoch. The minimization process is basically that of the Newton method based on the gradient of ε with respect to the element of weight W_{ij}.

In a single-step process the soft X-ray data points are predicted one time step ahead only ($\tau = 0.04$ ms), while in multi-steps predictions the predicted output at time $t + \tau$ is fed back into the input and is used to predict a new output at time $t + 2\tau$, which is fed back into the input together with the values previously predicted, in order to predict a new output at time $t + 3\tau$, and so on.

The neural net architecture used in this work had the configuration (15 - 9 - 3 - 1), that is, 15 neural units in the input layer, 9 units in the first hidden layer, 3 units in the second hidden layer and only one unit in the output layer. The activation functions were chosen to be $g(x) = \tanh(x)$ for all the hidden units and $g(x) = x$ for the output unit. The training of the network and the disruption prediction was carried out over the last 200 ms of the plasma discharges.

III - Disruption forecast

In order to find the adequate weights for all the connections between the neural units, two different disruptive plasma pulses have been used: the training set and the validation set. The single and multi-step forecasting processes are performed, afterwards, over two others disruptive pulses, distinct from the ones used for training and validation.

In Fig. 2 the basic experimental signals, related to the first one of the plasma disruptive discharges used for forecasting, are shown. This pulse corresponds to an $I_p \approx 170$ kA plasma discharge that disrupted at $t \approx 470$ ms. About 18 ms before the major disruption a minor disruption occurred, as observed in the Mirnov magnetic signal (Fig. 2c), causing a significant drop on the average electron density (Fig. 2f) and electron temperature as observed through the X-ray emission signals (Fig. 2d). This same feature, that is, the major disruption being preceded by a minor disruption just before the plasma current collapse, is also observed on the plasma discharges used for validation and for training the net.

The result of the forecasting process for this particular plasma shot in shown in Fig. 3. As it can be observed, for one time step-prediction (Fig. 3a) the result obtained from the neural network agrees almost perfectly with the experimental signal. By increasing the forecast time interval, i. e., the number of time-steps, as showed in Fig. 3b for 25 time-steps, the shape of the sawteeth oscillations is observe to be somewhat deformed but the net is still capable of accurately predicting the instance of the minor disruption that takes place at $t \approx 452$ ms. The longest forecasting time achieved is obtained for 63 time-steps (Fig. 3c) for which the net still accurately predicts the occurrence of the minor disruption. This corresponds to a forecasting of the disruptive instability 2.52 ms before it actually takes place for the medium sized TEXT tokamak. For time-steps longer than that, the net continues predicting the disruption but now with a time shift delay, as shown in Fig. 2d for a 90 time-steps forecasting.

Examining in detail the result obtained for the 63 time-steps forecast (Fig. 3c), it can be observed that in order to make this prediction, the net used 15 experimental data points that are positioned around $t \approx 449.5$ ms. This particular time interval is located exactly in the oscillatory region of the last "typical" sawtooth oscillation, when our eyes are unable to perceive any peculiar occurring in the soft X-ray emission which would signal that an instability has started at that point (or before) and that a disruption in coming soon. Only after the crash of this sawtooth

at t ≈ 450.0 ms, when an strong fluctuation starts to build up afterwards, one can say that a disruptive instability indeed has been triggered.

As another test for the neural network, exactly the same set of weights obtained and used above is now used to forecast the disruption that occurred in a second plasma discharge (Fig. 4). This also corresponds to an $I_p \approx 170$ kA plasma discharge that disrupted at t ≈ 424 ms. Differently from the first discharge analyzed, however, in this particular plasma discharge the major disruption was not preceded by any minor disruption.

The results of the multi-step forecasting analysis done for this discharge are shown in Fig. 5. Once again, for a single time-step prediction the result of the net is observed to beautifully match the experimental signal (Fig. 5a). For longer forecast intervals (Fig. 5b) the net still accurately predicts the disruption time up to time-step 78 (Fig. 5c). This corresponds to a forecast of the occurrence of the major disruption 3.12 ms in advance, value which is nearly triple the time that has been obtained previously using only magnetic data to feed the neural net [8]. For larger time-steps, once again a time shift in prediction appears between the experimental signal and the result provided by the network (Fig. 5d).

Analyzing in more detail the result obtained for time-step 78 (Fig. 5c), we can verify that the experimental data points used by the net to make this prediction correspond to an instance of time around t ≈ 420.6 ms. This corresponds to about 0.5 ms earlier in time before the last sawtooth crash occurs, yielding the strong MHD precursor for the major disruption that follows.

Interestingly, in both prediction cases the experimental data points used by the net to accurately forecast the minor and major disruption (Figs. 3c and 5c) are located in time prior to the amplitude increase of the magnetic fluctuation in the corresponding magnetic signals, as can be seen in Figs 6 and 7, respectively.

Since the neural networks was able to forecast disruptions using data points related to some particular instances of time before the observation of an increase in amplitude of the MHD activity, this observation might suggest that it is not the growing magnetic islands related to the q = 2 magnetic surface that would consequently disturb the inner island at q = 1 magnetic surface. The results obtained in this work suggest that it is probably the other way around, i. e., some disturbance phenomena would develop first around the central part of the plasma column (visualized by the soft X-rays central detector) and then the plasma region within the q = 2 magnetic surface would be affected, destabilizing the m = 2 MHD mode. This interpretation

reminds us the works already done in tokamaks suggesting that the disruptive instabilities would be caused by a "cold bubble" moving towards the plasma center, as it could be experimentally observed in the electron temperature profile [19,20]. However, some more careful and further investigations must be done in order to give more confidence about the reality or not of this process.

IV - Forecasting the entire plasma discharge

Since the set of weights used to forecast disruptions in this work was obtained by training the neural network with the last 200 ms of the training and validation plasma discharges, it is reasonable to use only the last 200 ms of the forecasting plasma pulses for predicting the disruption time. Now, if that same set of weights previously obtained is applied to forecast the whole plasma discharge, instead of the last 200 ms only, some strong distortions in the net output signal are observed in comparison to the real signal. This result should be expected, however, once the experimental data corresponding to the ramping up phase of the soft X-ray signal is not used during the training section of the net.

In an attempt to improve the net performance over the whole plasma discharge, therefore, a new training section is performed by now using the entire soft X-ray experimental data of two disruptive plasma discharges. A third discharges is used for validation and finally a fourth one for forecasting. The best results obtained are showed in Fig. 8. For a single time-step prediction (Fig. 8b) the match with the experimental signal (Fig. 8a) can be considered perfect. For 13 time-steps prediction (Fig. 8c), the signal output from the neural net exhibits some oscillations during the ramping up phase of the signal and, very strongly, right after the occurrence of the minor disruption. However, by examining the 13 time-step result more closely in the neighborhood of the disruption time (Fig. 9) it can be observed that the net is still capable of determining the exact instance of time of disruption up to 0.52 ms in advance. Unfortunately, for longer time-step predictions a time shift occurs between the prediction by the net and the real disruption time. This indicates that the proper set of weights has yet to be found. Consequently, either a larger number of experimental data must be used to train the neural net, or the number of training epochs must be increased, or even a different net architecture might be necessary to be tested.

V - Conclusion

It has been shown that feed-forward neural networks can be effectively used to forecast both minor and major disruptive instabilities in tokamaks. It was demonstrated in this work that soft X-rays experimental signals are more appropriate than magnetic data from a Mirnov coil to be used as input signal to the net, for the purpose of disruption forecast. Our forecasting time of minor or major disruptions is almost three times the one based on magnetic data [8]. We also note that the future larger tokamaks have longer plasma time scales than the medium size machines such as TEXT. This opens up a possibility of using feed-back controlled auxiliary systems such as electron cyclotron heating, neutral beam, pellet injection, external magnetic fields, etc., to avoid the occurrence of the upcoming disruption or at least to minimize its harmful effects. Also, the forecasting neural net attached to a tokamak can learn by itself through a series of discharges and become "smarter" to be able to steer the plasma away from an unstable domain of operation [21]. We may call such an operation as a "neural tokamak".

Finally, observing that the soft X-ray experimental data points used by the net in the best forecasting cases are located prior to the instance of the amplitude increase in the Mirnov magnetic signals, we might be able to suggest that the perturbation which triggers the disruptions first initiates in the central part of the plasma column where the q = 1 magnetic surface is located and only afterwards this instability would reach the outer part of the plasma column, destabilizing the m = 2 MHD mode. Speculations can be made whether this process could be related to some already reported explanations of disruptions that an "cold bubble", pushed towards the center of the plasma, would trigger the disruptive instabilities in tokamaks.

In conclusion, the neural net is capable of predicting the time evolution of tokamak plasmas even for a sudden and violent disruptive occurrence. This predictive capability may be rather surprising, as the prediction time is well before an obvious visual pattern for "omen" appears. This predictive capability may be useful for large tokamaks which have long time scales of plasma evolution. The predictive behavior of the net shows that some of the underlying physics of the disruption, as the soft X-ray signals, are better equipped than the magnetic signals as an indicative of the possible origin of the disruptive instability. This could portend the discrimination of possible mechanisms of disruptions.

Acknowledgments:

The first author would like to thank all the FRC and IFS staff, in particular Don Patterson and Jim Dibble, for the support receive. Also the first author is grateful to FAPESP - Fundacao de Amparo a Pesquisa do Estado de Sao Paulo, for the financial support. The work was in part supported by U.S. DOE.

References

[1] - STACEY W.M. - Nucl. Fusion **35** (1995) 1369.

[2] - VANNUCCI A., NASCIMENTO I.C., CALDAS I.L. - Plasma Phys. Control. Fusion **31** (1989) 147.

[3] - McGUIRE K.M. and ROBINSON D.C. - Phys. Rev. Lett. **44** (1980) 1666.

[4] - VANNUCCI A. and McCOOL S.C. - Nucl. Fusion **37** (1997) 1229.

[5] - TSUJI S., NAGAYAMA Y., MIYAMOTO K., et al. - Nucl. Fusion **25** (1985) 305.

[6] - VANNUCCI A. and GILL R.D. - Nucl. Fusion **31** (1991) 1127.

[7] - PIETRZYK Z.A., POCHELON A., BEHN R., et al. - Nucl. Fusion **32** (1982) 1735.

[8] - HERNANDEZ J.V., VANNUCCI A., TAJIMA T., LIN Z., HORTON W., McCOOL S.C. - Nucl. Fusion **36** (1996) 1009.

[9] - HOSHINO K., MORI M., YAMAMOTO T., TAMAI H., et al. - Phys. Rev Lett. **69** (1992) 2208.

[10] - KISLOV D.A., ALIKAEV V.V., ESIPCHUK Yu.V., KAKURIN A.M., et al. - Nucl. Fusion **37** (1997) 339.

[11] - YOSHINO R., NEYATANI, Y., HOSOGANE N., WOLFE S.W., et al. - Nucl. Fusion 33 (1993) 1599.

[12] - HENDER T.C., FITZPATRICK R., MORRIS A.W., CAROLAN P.G., et al. - Nucl. Fusion **32** (1992) 2091.

[13] - ARAUJO M.S.T., VANNUCCI A., CALDAS I.L. - Il Nuovo Cim. **18 D** (1996) 807.

[14] - PAUTASSO G., BUCHL K., FUCHS J.C., GRUBER O., et al. - Nucl. Fusion **36** (1996) 1291.

[15] - WROBLEWSKI D., JAHNS G.L., LEUER J.A. - Nucl. Fusion **37** (1997) 725.

[16] - HERTZ J., KROGH A., PALMER R.G. - "Introduction to the Theory of Neural Computation", Addison-Wesley, Reading, MA (1991).

[17] - HINTON G. - Scientic American, Sept. issue (1992) 145.

[18] - RUMELHART D.E., HINTON G.E., WILLIAMS R.J. - Nature **323** (1986) 533.

[19] - FREDRICKSON E.D., McGUIRE K.M., BELL M.G., BUSH C.E., et al. - Nucl. Fusion **33** (1993) 141.

[20] - SCHULLER F.C. - Plasma Phys. Control. Fusion **37** (1995) A135.

[21] - YOSHINO R., et al. - Fusion Technol. **30** (1996) 237.

Figure Captions

Fig. 1 - Illustration of how the information is processed within one neuron unit of the neural net. All the input signal (V_i) from the units of the previous layer, after been properly weighted (W_{ij}), are summed and then an inhibitory or oscillatory signal is fired to the next layer's units as defined by the activation function g(x).

Fig. 2 - A TEXT disruptive discharge which was used for forecasting. The major disruption takes place at t ≈ 470 ms and was preceded by a minor disruption that occurs about 18 ms earlier. The signals corresponds to: (a) plasma current, (b) loop voltage, (c) Mirnov magnetic signal, (d) central soft X-ray intensity, (e) safety factor, (f) average electron density.

Fig. 3 - Results of the multi-step prediction carried out for the plasma discharge shown in Fig. 2. After properly trained, the neural network is capable of forecasting the occurrence of the disruption up to 2.52 ms ahead in time, corresponding to a 63 time-step prediction (c). For longer time-steps, a time shift is observed between the neural net result and the real soft X-ray signal (d).

Fig. 4 - Plasma discharge that was also used for forecasting, with the same set of weights used previously. Note that, in this case, the major disruption is not preceded by any minor disruption. The nomenclature is the same as that for Fig. 2.

Fig. 5 - Results of the multi-steps prediction carried out for the plasma discharge shown in Fig. 4. In this case, the neural net is able to predict the occurrence of the major disruption 3.12 ms ahead of time, corresponding to a 78 time-step prediction (c). Once again, a time shift between the result from the neural net and the experimental soft X-ray signal is observed for longer time predictions (d).

Fig. 6 - Expanded view of the soft X-ray intensity (a) and Mirnov magnetic signal (b) for the plasma discharge shown in Fig. 2, close to the disruption time ($t \approx 452$ ms). As can be observed, the experimental data used by the net in its best performance are located in time just before the MHD activity starts increasing in amplitude.

Fig. 7 - Expanded view of the soft X-ray intensity (a) and Mirnov magnetic signal (b) for the plasma discharge shown in Fig. 4, close to the disruption time ($t \approx 424$ ms). Once again it is observed that the experimental data used by the net in its best performance for this discharge are located in time before the MHD activity starts increasing in amplitude.

Fig. 8 - Using a different set of weights, obtained by choosing two disruptive pulses for training and a third one for validation, the neural networks was used to forecast the whole discharge over a fourth distinct plasma shot. The single step prediction (b) is observed to match very well the experimental signal (a) while for 13 time-steps (c), although the net is still capable of accurately predicting the exact instance the disruption occurs, some spurious oscillations appear in the beginning and, more strongly, just after the minor disruption at $t \approx 454$ ms.

Fig. 9 - Expanded view of Fig. 8c close to disruption time showing the accuracy of the prediction performed by net for a 13 time-steps forecasting. For longer time predictions a time shift appears, probably indicating that the net was not yet adequately trained.

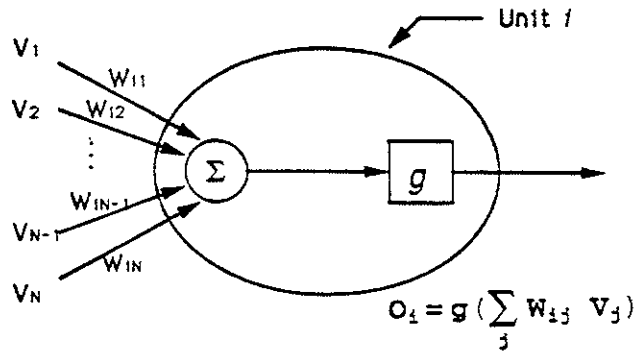

Fig. 1

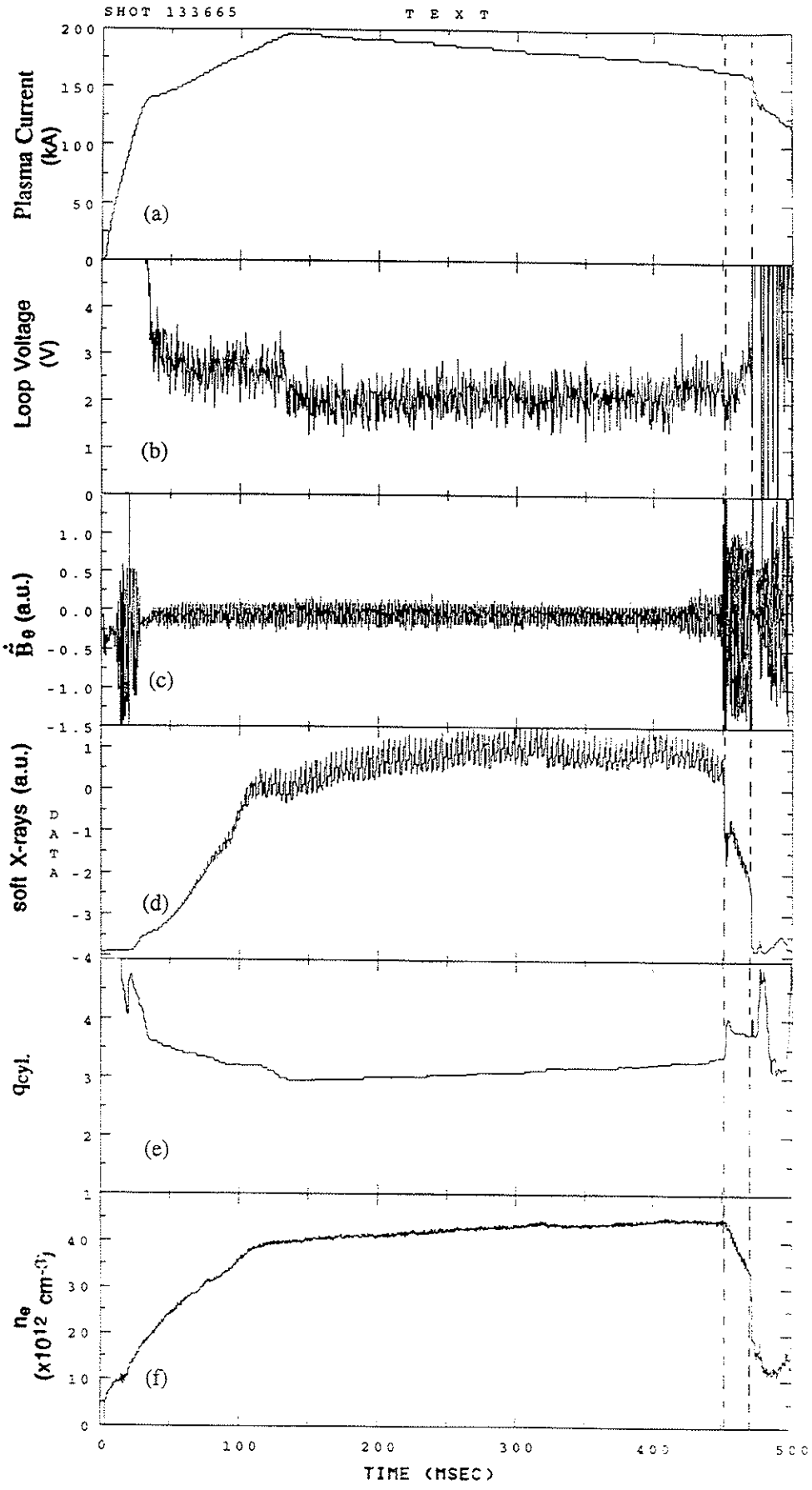
SHOT 133665
T E X T
Plasma Current (kA)
(a)
Loop Voltage (V)
(b)
$\tilde{B}_\theta$ (a.u.)
(c)
soft X-rays (a.u.)
D A T A
(d)
$q_{cyl.}$
(e)
n_e ($x10^{12}$ cm^{-3})
(f)
TIME (MSEC)

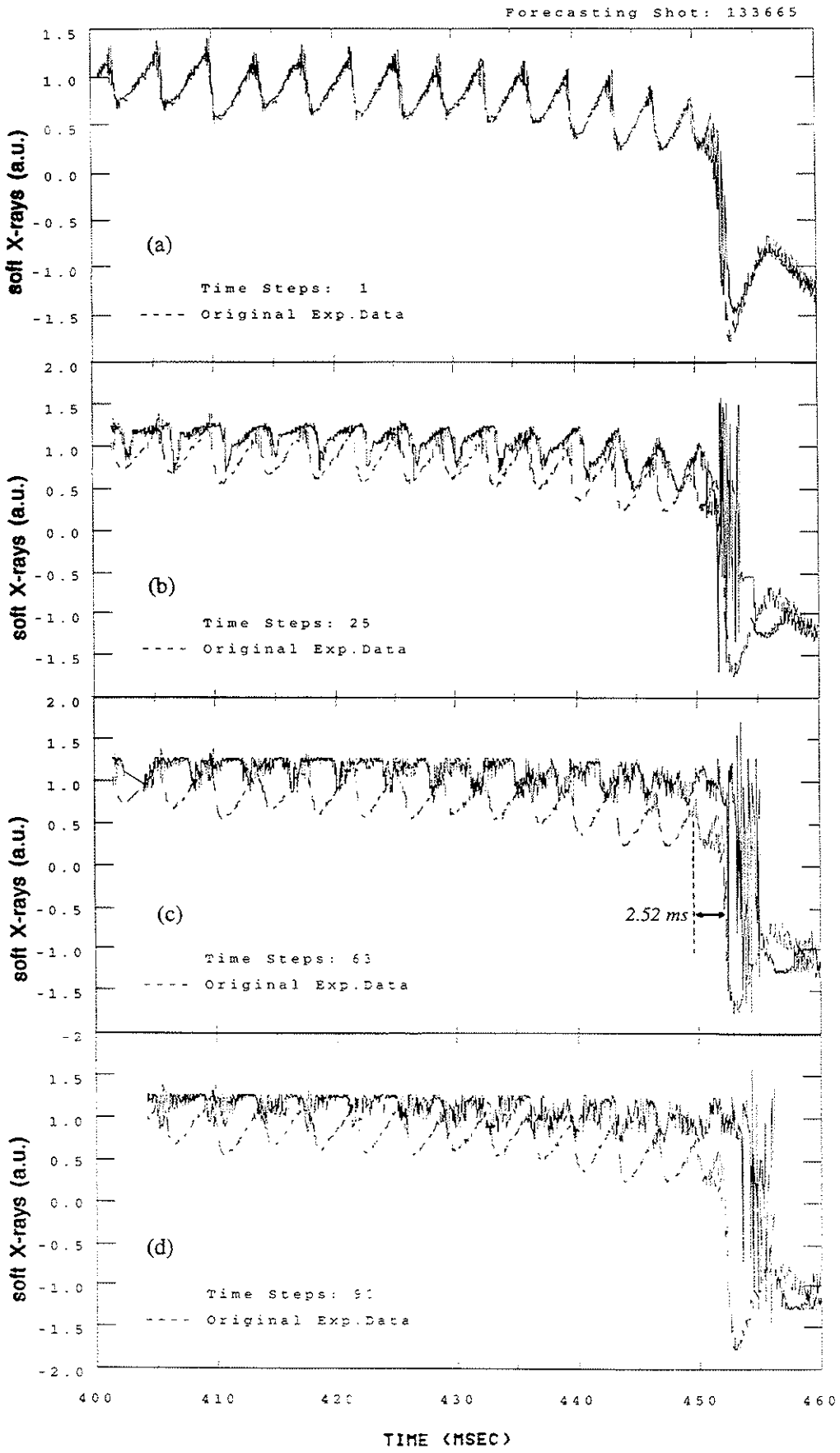
Forecasting Shot: 133665
soft X-rays (a.u.)
(a)
Time Steps: 1
---- Original Exp.Data
(b)
Time Steps: 25
---- Original Exp.Data
(c)
2.52 ms
Time Steps: 63
---- Original Exp.Data
(d)
Time Steps: 91
---- Original Exp.Data
TIME (MSEC)

Fig. 3

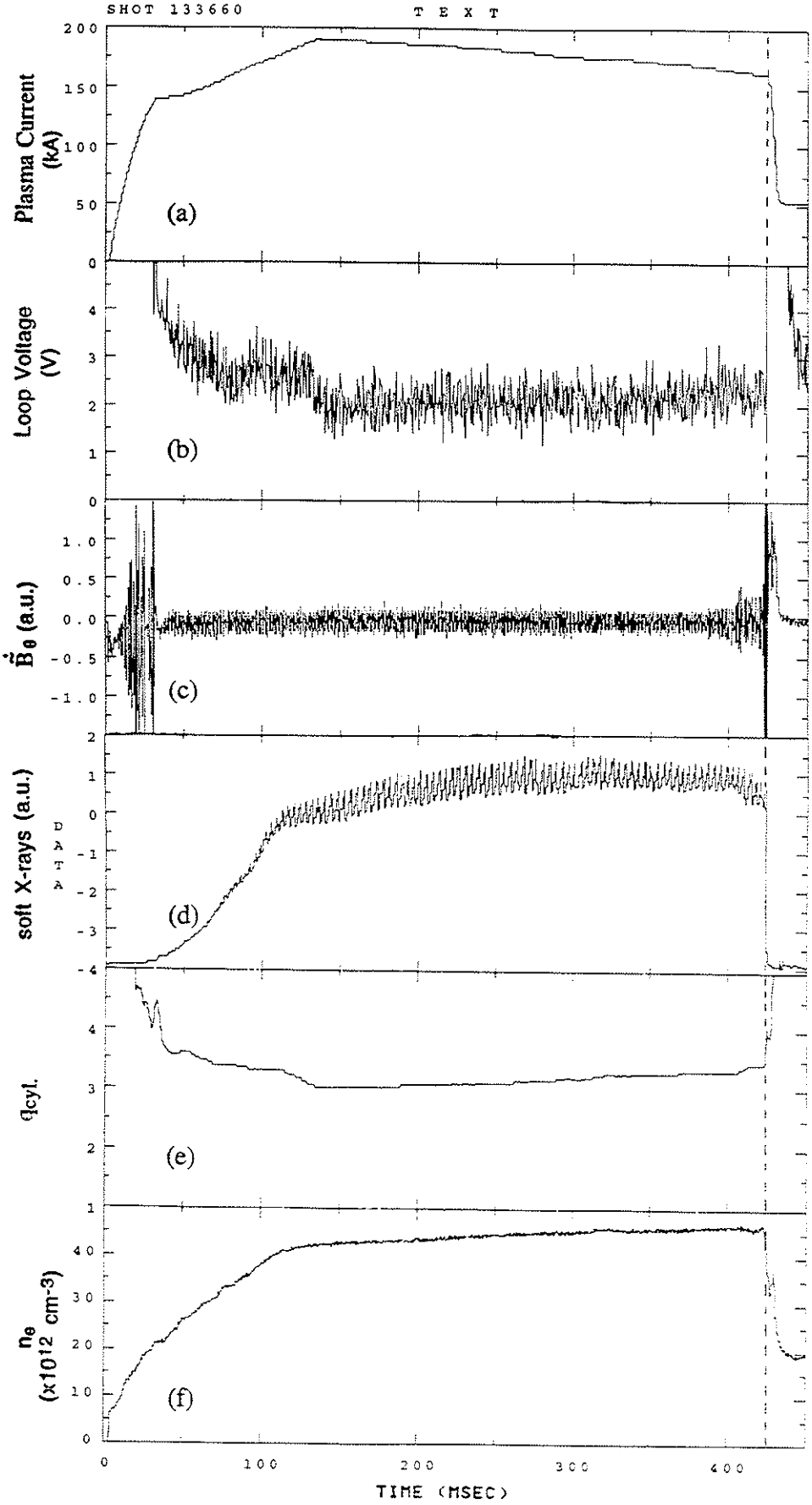
SHOT 133660
T E X T
Plasma Current (kA)
(a)
Loop Voltage (V)
(b)
$\tilde{B}_\theta$ (a.u.)
(c)
soft X-rays (a.u.)
(d)
$q_{cyl.}$
(e)
n_e ($\times 10^{12}$ cm^{-3})
(f)
TIME (MSEC)

F. 4

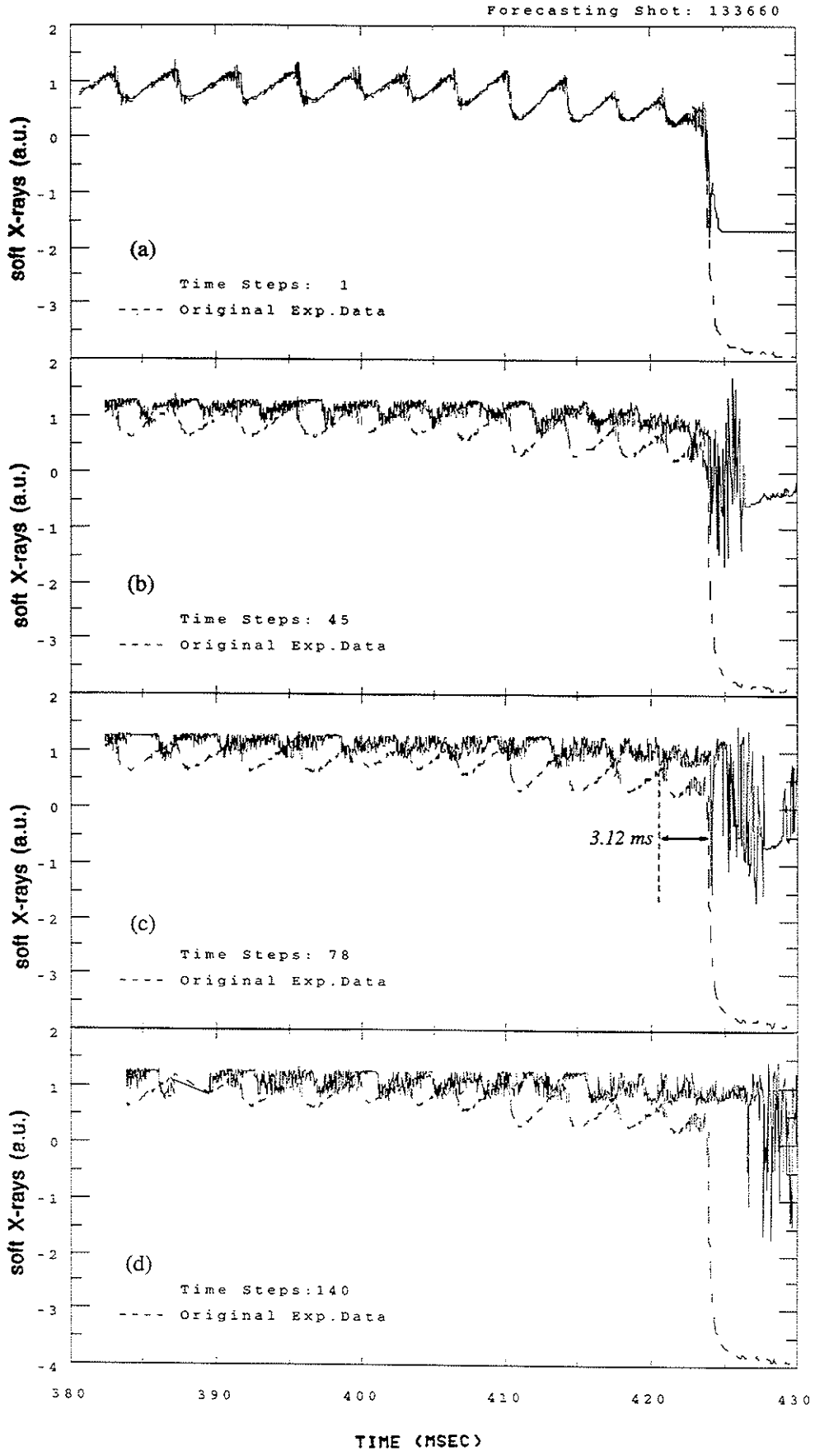
Forecasting Shot: 133660
soft X-rays (a.u.)
(a)
Time Steps: 1
---- Original Exp.Data
(b)
Time Steps: 45
---- Original Exp.Data
3.12 ms
(c)
Time Steps: 78
---- Original Exp.Data
(d)
Time Steps:140
---- Original Exp.Data
380
390
400
410
420
430
TIME (MSEC)

Fig. 5

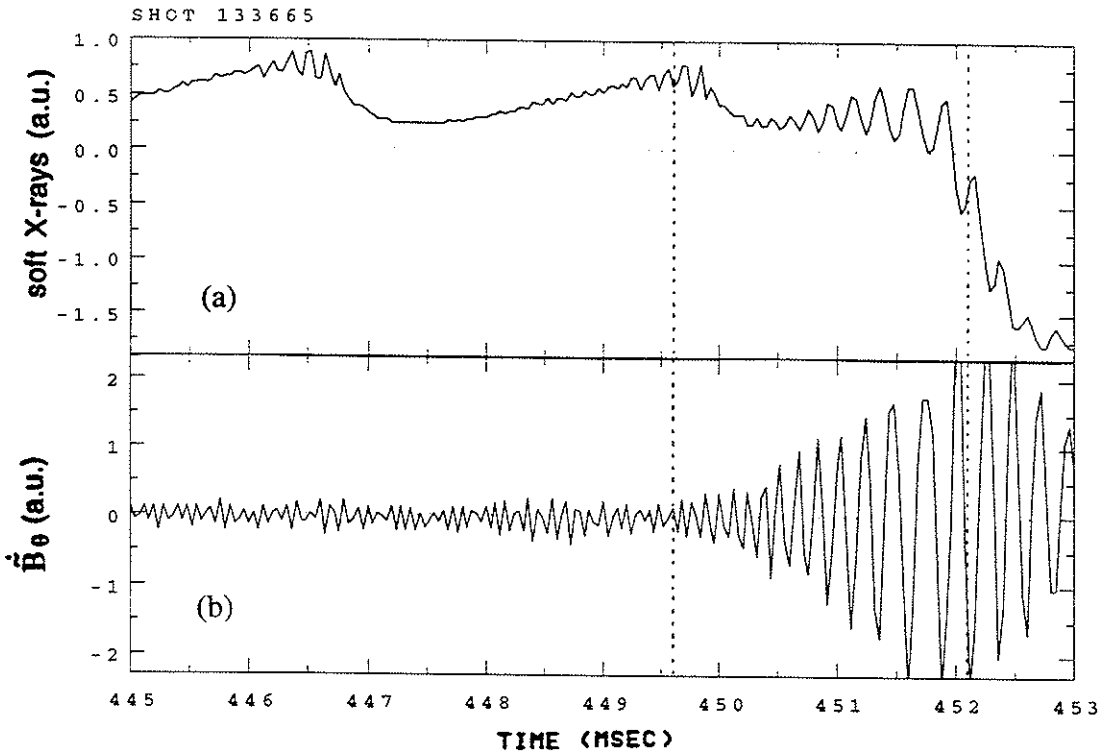
SHOT 133665
soft X-rays (a.u.)
1.0
0.5
0.0
-0.5
-1.0
-1.5
(a)
$\tilde{B}_\theta$ (a.u.)
2
1
0
-1
-2
(b)
445
446
447
448
449
450
451
452
453
TIME (MSEC)

Fig. 6

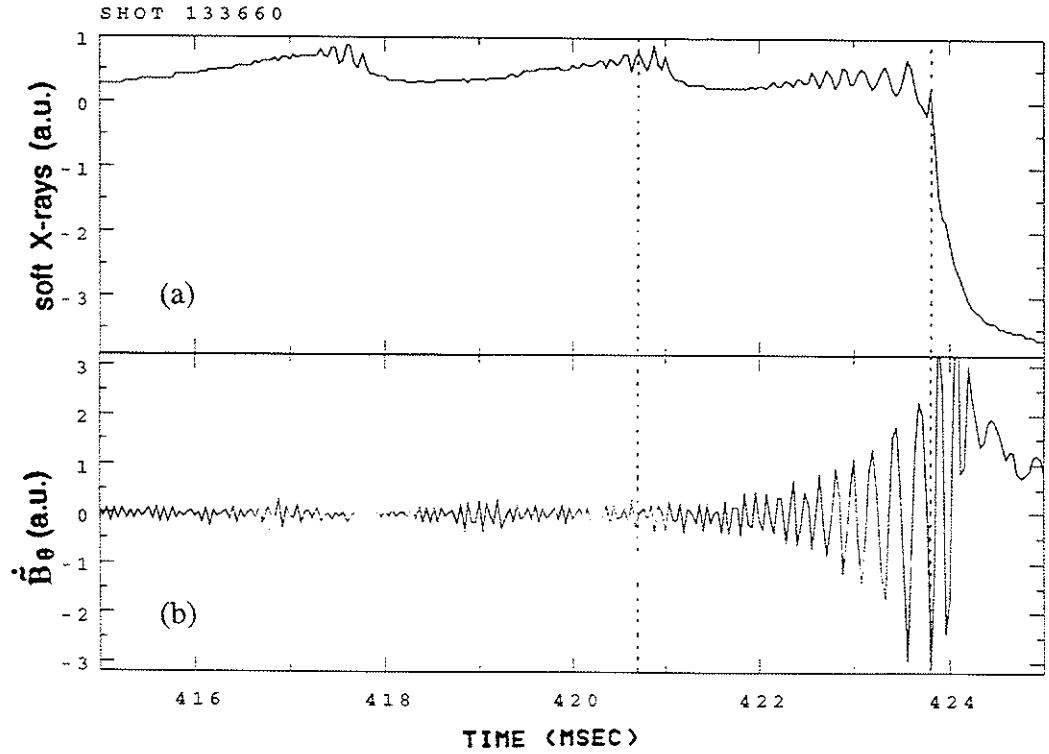
SHOT 133660
soft X-rays (a.u.)
1
0
-1
-2
-3
(a)
$\tilde{B}_\theta$ (a.u.)
3
2
1
0
-1
-2
-3
(b)
416
418
420
422
424
TIME (MSEC)

Fig. 7

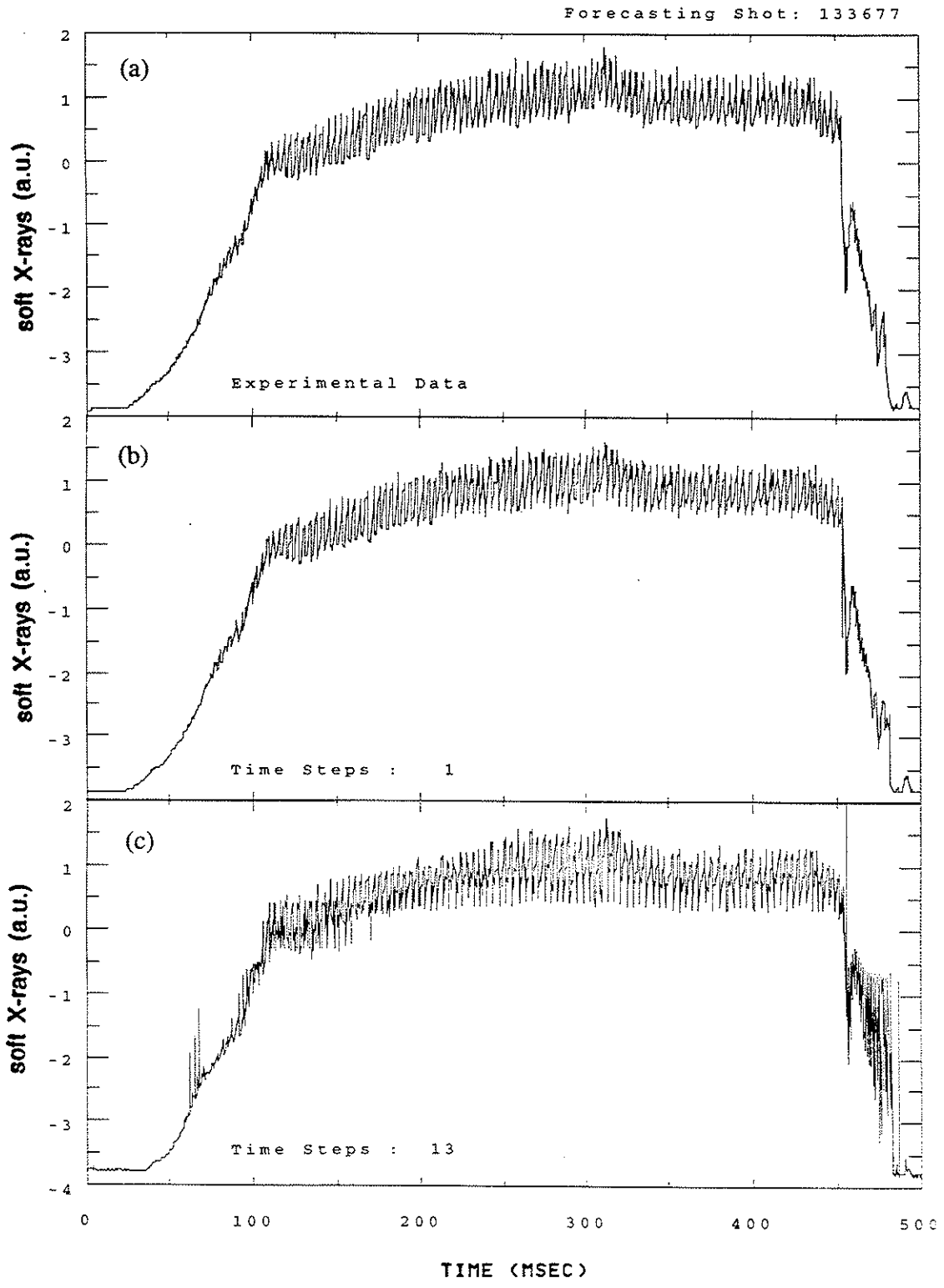
Forecasting Shot: 133677
(a)
Experimental Data
(b)
Time Steps : 1
(c)
Time Steps : 13
soft X-rays (a.u.)
soft X-rays (a.u.)
soft X-rays (a.u.)
2
1
0
-1
-2
-3
-4
0
100
200
300
400
500
TIME (MSEC)

Fig. 8

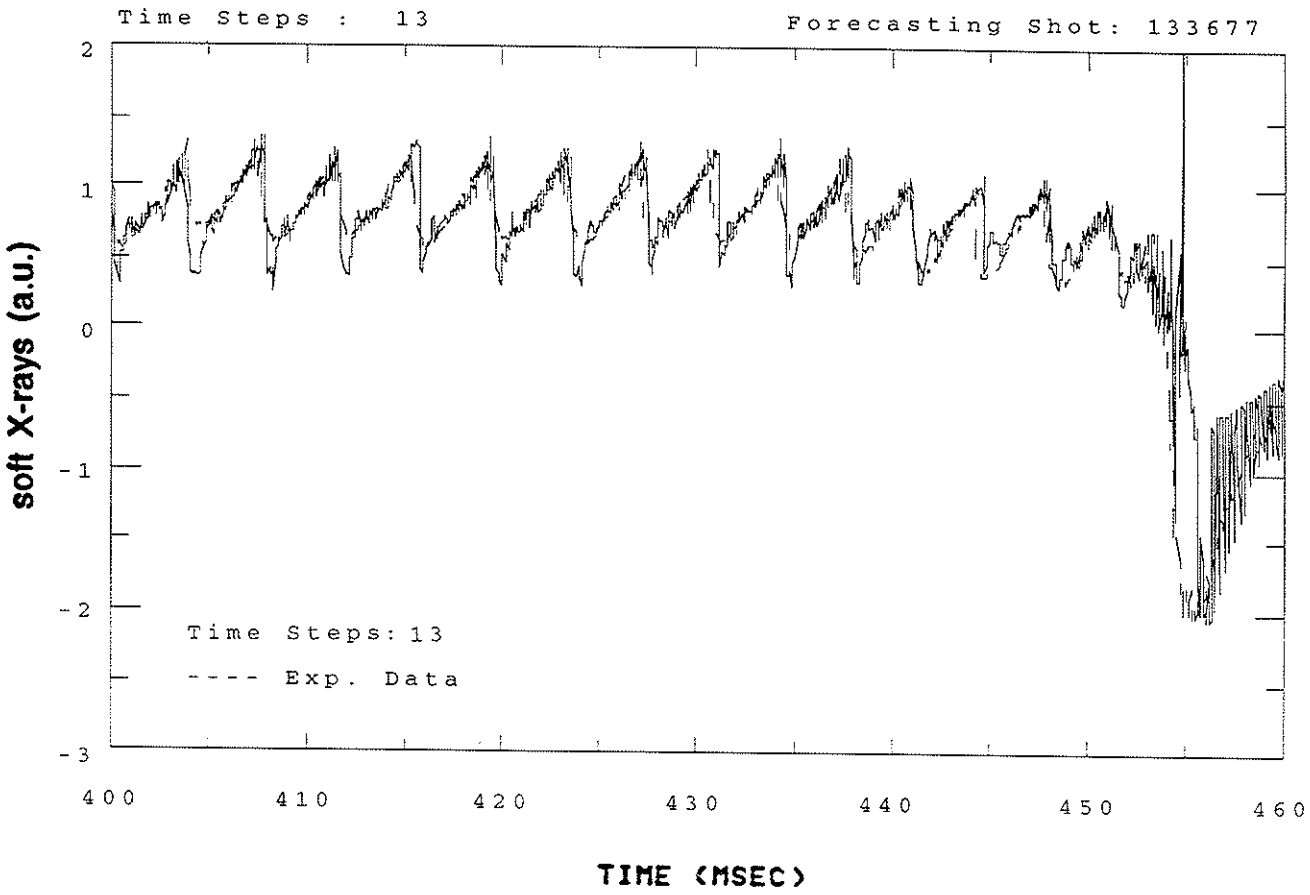
Time Steps : 13
Forecasting Shot: 133677
soft X-rays (a.u.)
2
1
0
-1
-2
-3
Time Steps: 13
---- Exp. Data
400
410
420
430
440
450
460
TIME (MSEC)

Fig. 9